FLUID-DRIVEN ROBOTIC SYSTEMS FOR INTRAOPERATIVE MRI-GUIDED INTERVENTIONS

Guo, Ziyan

Department of Mechanical Engineering

The University of Hong Kong

August 2018

This thesis is submitted to the University of Hong Kong in partial fulfilment of the requirements for the degree of Doctor of Philosophy. Except for where indicated, it presents entirely my own work and describes the results of my own research.

Abstract

Recent years have witnessed the rapid development and growing popularity of image-guided surgery. Magnetic resonance imaging (MRI) is well-known for its superior capability in providing non-invasive high-contrast images of soft tissues without ionizing radiation. It is also capable of monitoring the temperature changes during thermal therapies. These advantages have prompted MRI for vibrant applications ranging from biopsy, laser ablation, drug injection, to catheterization. Numerous patient trials have demonstrated the clinical values with the use of intra-operative (intra-op) MRI. However, these procedures could be still time-consuming and complicated by the lack of efficient manipulation with real-time navigation. It is timely to benefit from the recent advances in robotics for enhanced surgical manipulation and simplified workflow.

The main focus of this thesis is concerned with fluid-powered actuation and robotic manipulator designs that enable high-performance MR safe surgical manipulation under continuous intra-op MRI guidance. The use of ferromagnetic materials is forbidden in the strong magnetic field of MRI scanner. Conductive components, including electric wires and most metallic components, may generate heat by electromagnetic (EM) induction and induce image artefact/distortion. In this context, novel actuators driven by fluidic power, i.e. a customizable pneumatic stepper motor and high-fidelity master-slave hydraulic transmission, are proposed to provide intrinsically MR safe actuation. The kinematics and dynamics models have been studied, which facilitate the overall design optimization. The hydraulic transmissions have been integrated into a robotic manipulator for intra-cardiac electrophysiology (EP) catheterization. Multiple simulated clinical tasks have been carried out to validate the manipulation dexterity and efficiency. Furthermore, advanced MR-based *wireless* positional tracking markers have also been investigated, which can provide real-time instrument localization directly in the imaging domain. Incorporated with these *wireless* trackers and a novel fluid-tendon actuation mechanism, a neurosurgical robotic system has been developed to perform bilateral stereotaxy. Its compact design can be accommodated inside a standard head coil based on a single invasive anchorage. Transmission stiffness, targeting accuracy and MRI compatibility have been evaluated towards the application in deep brain stimulation (DBS). Pre-clinical trial has been conducted under the MRI to validate the proposed simplified workflow. A soft robotic manipulator powered by hydraulics has been designed for transoral laser dissection. Targeting accuracy at submillimetre level has been demonstrated in the path-following tests. MRI-guided navigation has been conducted for *ex vivo* tissue ablation.

In Loving Memory of My Grandma, 唐隽英 (1930.05-2012.10).

Acknowledgements

This four-year PhD study has been an amazing journey that is full of challenges. It is also a feast of experiences that have taken me across three continents in four countries, from the DRC in Los Angeles to the Surgical Robot Challenge in London to the ICRA presentation in Brisbane. Looking back to these four years, I feel deeply thankful to the people who have been accompanying and supporting me throughout.

I would like to express gratitude to my supervisor Dr. Ka-Wai Kwok for guiding me into the field of robotics. His enthusiasm and vision towards research has greatly inspired me. This thesis would not be made possible without his supports in all aspects.

Thank you to Dr. Danny Chan for his clinical inputs. His expertise seamlessly integrates the clinical and engineering researches. I am so grateful to have his generous help through this journey, which has widened my vision in MRI-guided robotic neurosurgery.

Thank you to Dr. Yue Chen for his sincere advices to my research, MR safe robotics, at the early stage of my PhD study.

I have gained such a great experience working in this research team, especially with my talented teammates. In no particular order, I would like to thank Ziyang Dong, Brian Lee, Chimlee Cheung, Justin Ho, Jacky Fu, Tim Lun, Jack Chan, Xiaomei Wang, Marco Chow, Martin Leong, Alan Tang, Haokun He, Ge Fang, Kui Wang, Angel Ng and Peggy Leung. It is always an enjoyable experience collaborating with and learning from my colleagues and collaborators. I would like to thank Prof. Wai-Sang Poon and Dr. Hao Su for their expertise in the neurosurgical robot project. I am thankful to have collaborated with Dr. Sai-Chun Tang, Dr. Su-Lin Lee, Yingjing Feng, and Dr. Chris Robert.

I would also like to thank my former supervisor Professor Yibing Li for his encouragement to my early-stage research study. He is my life model from many perspectives, which has invaluable influences on my life.

I am so grateful to have made so many good friends in Hong Kong. Special thank you goes to my Chi Sun squad, Dr. Kaifeng Liu, Dr. Sanyuan Niu, Yan Li and Jian Jin. As peer students, they are so outstanding that they can always amaze me by their wide and deep insights.

Last but not the least, I am so proud of having a very loving and supportive family. In numerous tough and frustrated moments, their unconditional love and boundless supports are always there to help me make it through. From my parents, I learned trust, patience, persistence, and the true happiness of life. My husband is my best friend and the most faithful cheerleader. His sunny optimism and peaceful spirits have accompanied me through the ups and downs of the entire PhD process.

Contents

CHAPTER 1 INTRODUCTION **24**

1.1 MOTIVATION AND OBJECTIVES 24

1.2 THESIS ORGANISATION AND MAIN TECHNICAL CONTRIBUTIONS 26

1.3 PUBLICATIONS, PATENTS AND INTERNATIONAL AWARDS DURING PH.D. STUDY 29

CHAPTER 2 MRI-GUIDED ROBOT-ASSISTED SURGERY **32**

2.1 INTRODUCTION 32

2.2 INTRA-OPERATIVE MRI 33

2.2.1 Interventional MRI (iMRI) Systems 33

2.2.2 Pulse Sequences for iMRI 35

2.2.3 MR Safety and Compatibility 38

2.3 CLINICAL MOTIVATION AND NEEDS FOR MRI-GUIDED SURGICAL ROBOTICS 41

2.3.1 Neurosurgery 41

2.3.2 Intra-cardiovascular Interventions 51

2.3.3 Head and Neck Surgery 53

2.4 CURRENT TRENDS AND PERSPECTIVES OF MRI-GUIDED ROBOTICS 55

2.4.1 Non-rigid Image Registration 56

2.4.2 MR-based 3D Positional Tracking 58

2.4.3 MRI-compatible Actuation 61

2.5 CONCLUSIONS 64

CHAPTER 3 CUSTOMIZABLE PNEUMATIC MOTOR **65**

3.1 INTRODUCTION 65

3.2 STATE-OF-THE-ART MRI-COMPATIBLE MOTORS AND UNMET TECHNICAL CHALLENGES 66

3.3 DESIGN METHODS 70

3.3.1 MR Safe Components and Materials 70

3.3.2 Working Principle of Stepping Actuation 72

3.3.3 Design Optimization 74

3.3.4 Self-locking Mechanism for Steady Positioning 77

3.3.5 Rapid Reconfiguration for Customizable Performance 78

3.3.6 Control Setup 81

3.4 EXPERIMENTS AND RESULTS 82

3.4.1 Parameter Analysis and Dynamic Performance *82*

3.3.2 MRI SNR Test *85*

3.4 Discussion 88

CHAPTER 4 HIGH-PERFORMANCE HYDRAULIC ACTUATION 90

4.1 Introduction 90

4.2 Design Methods 91

4.2.1 Master-slave Hydrostatic Transmission *92*

4.2.2 Integration Methods for Continuous Rotary Actuation *97*

4.2.3 Kinematics and Dynamics Modeling *103*

4.2.4 Design Optimization *109*

4.2.4.1 Stiffness 110

4.2.4.2 Latency 110

4.3 Experiments and Results 112

4.3.1 Force Transmission *112*

4.3.2 Hysteresis *113*

4.3.3 Dynamic Response *115*

4.3.4 SNR Test *116*

4.4 Conclusions 118

CHAPTER 5 APPLICATION OF HYDRAULIC ACTUATION ON STEREOTACTIC NEUROSURGERY 119

5.1 Introduction 119

5.1.1 MRI-guided High-Intensity Focused Ultrasound (HIFU) *119*

5.1.2 MRI-guided Deep Brain Stimulation (DBS) *121*

5.2 Robot Design Criteria 124

5.3 Methodology 126

5.3.1 Master-slave Actuation Mechanism *126*

5.3.2 Bilateral Manipulator Design *129*

5.3.3 Forward and Inverse Kinematics *130*

5.3.4 Needle Insertion *133*

5.3.5 MRI Distortion and Fiducial Marker System *134*

5.4 Experiments and Results 140

5.4.1 Transmission Stiffness and Steadiness Analysis *140*

5.4.2 Needle Targeting Accuracy *142*

5.4.3 MR-based Navigation *144*

5.4.4 MRI-compatibility Evaluation *146*

5.4.5 Pre-clinical Trial *147*
5.5 Discussion and Conclusions 149

CHAPTER 6 HYDRAULIC-POWERED ROBOTIC SYSTEM FOR INTRA-CARDIAC CATHETERIZATION **154**

6.1 Introduction 154
6.2 MR safe Catheter Robot 156
6.2.1 Motivation and Design Requirements *156*
6.2.2 Robot Description *158*
6.3 Proximity Query (PQ) Algorithm for Intra-Cardiac Catheter Navigation 161
6.3.1 Background *161*
6.3.2 PQ Formulation for Irregular Mesh Model *163*
6.3.2.1 Analytical Formulation of Edge-Segment Closest Point Pairs 163
6.3.2.2 Optimization-based Edge-Segment Closest Point Pair Estimation 165
6.3.2.3 Identification of Shortest Distance from Triangle to Segment 167
6.3.3 PQ Implementation for Catheter Navigation *169*
6.4 Experiments and Results 171
6.4.1 Cardiac Mapping *171*
6.4.2 Simulated Pulmonary Vein Isolation *173*
6.4.3 MRI-Compatibility Test *174*
6.5 Conclusion 175

CHAPTER 7 HYDRAULIC DRIVE SOFT MANIPULATOR FOR TRANSORAL ROBOTIC LASER ABLATION **177**

7.1 Introduction 177
7.1.1 Transoral Laser Microsurgery (TLM) *177*
7.1.2 Transoral Robotic Surgery (TORS) *178*
7.1.3 MR Thermometry *179*
7.2 Design Requirements 180
7.3 Methodology 183
7.3.1 Docking Module *183*
7.3.2 Advancement Mechanism *185*
7.3.3 Dexterous Laser Steering within Confined Workspace *186*
7.4 Experiments and Results 188
7.4.1 Path-following Test *188*
7.4.2 MRI-based Validation *193*
7.4.3 MRI-compatibility Evaluation *196*

7.5 Discussion and Conclusions 197

CHAPTER 8 CONCLUSIONS AND FUTURE WORK 199

8.1 Achievement of this Thesis 199

8.2 Future Directions 201

REFERENCES 203

List of Figures

Fig. 1.1 Three key components of the MR safe robotic systems presented in this thesis, namely MR safe actuation, dexterous manipulator design and *wireless* tracking technique. Robotic systems integrated with these three components have been tested and evaluated regarding the relevant clinical requirements for various applications, i.e. stereotactic neurosurgery, intra-cardiac catheterization or transoral laser ablation. This study may contribute a benchmark for the development of MRI-guided robotic devices, opening a new dimension for other procedures that may also benefit from intra-op MRI, such as breast biopsy and prostate intervention. 25

Fig. 2.1 **(a)** Low-field open iMRI system (0.5 Tesla Signa SP from GE Healthcare). Surgeon performs the operation standing in-between the double-donut magnets. **(b)** Dual-room suite with an MRI transfer system (VISIUS® system from IMRIS Inc.). Surgical table, navigation system, lights and camera are shown in the foreground, as in the typical positions for surgery. The equipment should be positioned outside the 5-Gauss line, before the magnet is entering the room. **(c)** Single-room system with a surgical table that can be pivoted (BrainSUITE® from BrainLAB Inc.). The surgical procedure is performed outside the 5-Gauss line (in red). And for MRI scanning, a central column can pivot the tabletop, lower it onto the MR table, and transfer it into the magnet. **Image source: GE Healthcare, IMRIS Inc., BrainLAB Inc.** 34

Fig. 2.2 Overview of the system setup for real-time MRI-guided interventions (assisted by robot). 36

Fig. 2.3 Schematic diagram of dynamic MRI. Images are continuously acquired at high frame rate. Image and instrument data return to the computing processor for graphical display with low-latency. The successive scanning schemes adapt to the real-time instructions from the computing processor [21]. 37

Fig. 2.4 **(a)** Safety hazards in the MR environment. The static magnetic field could strongly attract and rotate the objects that contain certain amount of ferromagnetic materials. Sagittal MR images in gradient-echo (GRE) sequence for patient **(b)** without and **(c)** with metal implant in brain [22]. Most area of the brain image is distorted, showing the large image artifacts caused by the metallic implant. **Image source: KOPP Development Inc.** 38

Fig. 2.5 MR labels defined by ASTM F2503 and IEC62570. Any implants, medical devices or other equipment used in or near the MR environment should be labeled. MR safe items can be placed anywhere inside the MRI room and pose no safety hazards. **Image source: ASTM F2503 – Practice for Marking Items for Safety.** 39

Fig. 2.6 **(a)** ACR Safety Zones within MRI facilities [24]. These zones are denoted as Zone I through IV. It corresponds to the levels of magnetic field exposure. **(b)** Strength of the static field. Within the 5–Gauss (0.5 mT) line area, unscreened personnel and ferromagnetic objects are strictly forbidden.

IMAGE SOURCE: MAGMEDIX INC., NATIONAL MRI-SHIELDING COMPANY. 40

FIG. 2.7 DEVELOPMENT MILESTONES OF IMAGE-GUIDED DEVICES FOR STEREOTACTIC NEUROSURGERY [38-41]. 43

FIG. 2.8 SIGNIFICANT MRI-GUIDED STEREOTACTIC PLATFORMS**.** **(A)** CLEARPOINT® SYSTEM BY MRI INTERVENTIONS, INC., USA. TWO FRAMES (SMARTFRAME®) ARE MOUNTED TO THE SKULL BILATERALLY AND MANUALLY ALIGNED TO THE PREDEFINED TRAJECTORIES; **(B)** MRI-COMPATIBLE SURGICAL ASSIST ROBOT BY AIST-MITI, JAPAN AND BRIGHAM AND WOMEN'S HOSPITAL, HARVARD MEDICAL SCHOOL, USA; **(C)** NEUROARM/SYMBIS® BY DEERFIELD IMAGING, USA; **(D)** NEUROBLATE® SYSTEM BY MONTERIS MEDICAL, INC., USA. **IMAGE SOURCE:** [37, 46-48] 45

FIG. 2.9 **(A)** SENSEI® X ROBOTIC SYSTEM, AND **(B)** AMIGO REMOTE CATHETER SYSTEM GUIDED BY PRE-OP IMAGES. **IMAGE SOURCE: HANSEN MEDICAL, CATHETER PRECISION INC.** 51

FIG. 2.10 SIGNIFICANT SYSTEMS FOR TRANSORAL ROBOTIC SURGERY (TORS) OR TLM: **(A)** DA VINCI SI SYSTEM, **(B)** FLEX® ROBOTIC SYSTEM AND **(C)** ACUPULSE® CO_2 FLEX FIBER SYSTEM. CURRENTLY, THERE IS NO ROBOTIC SYSTEMS IN THE MARKET FOR MRI-GUIDED TRANSORAL MICROSURGERY. **IMAGE SOURCE: INTUITIVE SURGICAL INC., MEDROBOTICS INC., LUMENIS, INC.** 54

FIG. 2.11 SURGICAL WORKFLOW OF **(A)** CONVENTIONAL STEREOTACTIC NEUROSURGERY. ERROR SOURCES OF THE CONVENTIONAL PROCEDURES HAVE BEEN LISTED AT THE LEFT; **(B)** MRI-GUIDED AND ROBOT-ASSISTED STEREOTACTIC NEUROSURGERY. IN THIS PROCEDURE, ERRORS CAN BE ELIMINATED THROUGH THE USE OF REAL-TIME MRI AND CLOSED-LOOP CONTROLLED ROBOTIC MANIPULATION. 55

FIG. 2.12 **UPPER ROW:** BRAIN DEFORMATION BEFORE AND AFTER THE CRANIOTOMY; **LOWER ROW:** GEOMETRIC DISTORTION IN DIFFUSION IMAGES. LARGE DISCREPANCY BETWEEN PRE-OP AND INTRA-OP IMAGES ARE OBSERVED IN THE OVERLAID IMAGE AT THE LAST COLUMN. **IMAGE SOURCE:** [97, 104] 57

FIG. 2.13 **UPPER ROW:** MRI-VISIBLE (GADOLINIUM-IMPREGNATED) CANNULA GUIDE ALIGNED TO THE PLANNED TRAJECTORY BY A SKULL-MOUNTED AIMING DEVICE (SMARTFRAME®, CLEARPOINT SYSTEM). MR IMAGES SHOW THE CANNULA AT THE COMPLETION OF ALIGNMENT, AND A CERAMIC MANDREL INSERTED SUBSEQUENTLY [111, 112]; **MIDDLE ROW:** SEMI-ACTIVE MARKER EMBEDDED AT THE TIP OF A 5F CATHETER, WHICH IS A RESONANT CIRCUIT CONTROLLED BY OPTICAL FIBER. REAL-TIME MR IMAGES ARE ACQUIRED WITH A RADIAL STEADY-STATE FREE-PRECESSION SEQUENCE. THE MR IMAGES SHOW THE SEMI-ACTIVE MARKER PRODUCES NO SIGNAL ENHANCEMENT IN THE DETUNED STATE AND AN INTENSE SIGNAL SPOT IN THE TUNED STATE [113]; **LOWER ROW:** BRACHYTHERAPY CATHETER MOUNTED WITH SEVERAL ACTIVE MARKERS ALONG THE METALLIC STYLET. THE HIGH-RESOLUTION MR IMAGE IS ACQUIRED WITH A 3D TSE SEQUENCE (RESOLUTION: $0.6\times0.6\times0.6$ MM^3) [114]. 59

FIG. 2.14 **(A)** NEUROARM MANIPULATOR (IN RED FRAME) MOUNTED ONTO AN EXTENSION BOARD FOR STEREOTAXY. IT IS DRIVEN BY ULTRASONIC PIEZOELECTRIC MOTORS (NANOMOTION, YOKNEAM, ISRAEL) (IN YELLOW FRAME). **(B)** CONCEPTUAL SETUP DIAGRAM OF ULTRASONIC-MOTOR INTEGRATED ROBOT. A CONTROLLER BOX PLACED INSIDE THE MRI ROOM MUST BE CAREFULLY SHIELDED TO ENSURE SAFETY AND MINIMAL INTERFERENCE TO THE IMAGING. 62

FIG. 2.15 **(A)** MRI-COMPATIBLE PROSTATE ROBOT (IN RED FRAME) DRIVEN BY PNEUMATIC STEPPER MOTORS (IN YELLOW FRAME). **(B)** CONCEPTUAL SETUP DIAGRAM OF PNEUMATIC-MOTOR INTEGRATED PROSTATE ROBOT. THE CONTROLLER BOX CAN BE PLACED OUTSIDE THE MRI ROOM AND CONNECTED WITH THE MOTOR BY HOSES. **IMAGE SOURCE:** [136, 137] 63

Fig. 3.1 (a) Low-power (max. 15mNm) piezoelectric motor, PAD7344 from Noliac Company, designed for applications requiring zero EMI. MR images generated by a Siemens 3T MRI scanner **(b)** without a piezoelectric motor and **(c)** with a piezoelectric motor placed 140 mm from the scanning centre. The image artifacts caused by the motor operation can be clearly observed, especially in the middle of the image. **Image source: Noliac Company [141]** 67

Fig. 3.2 Selected MR safe pneumatic stepper motors. **(a)** PneuStep developed by Stoianovici *et al.*; **(b)** Ø30-mm rotary motor developed by Sajima *et al.*; **(c)** High-torque motor developed by Chen *et al.*; **(d)** Unidirectional motor developed by Chen *et al.*, and **(e)** Linear stepper motor developed by Groenhuis *et al.* **Image source: [131, 132, 143, 144, 146]** 68

Fig. 3.3 **(a)** Computer-aided design (CAD) model of the presented pneumatic stepper motor; **(b)** Family of stepper motors with variable parameters, including diameter, tooth number and friction coefficient; **(c)** Exploded component view of the motor. 69

Fig. 3.4 **(a-h)** Manual assembly process of the presented air motor without using any tools. **(i)** Motor operating by three air tubes connected. 71

Fig. 3.5 Mechanics model of torque transmission in the 2-step process: **(a)** input gear actuated, and **(b)** output gear actuated. These gears are sequentially actuated by the pressurized air (in red) and vacuum (in light blue). In the input-gear-actuated step, output gear is passively pushed forward and gets out of the circumferential constraint of the directional gear. In the output-gear-actuated step, it is actively pressing on the direction gear. 74

Fig. 3.6 Illustration of three contact areas of the output gear. 76

Fig. 3.7 **(a)** Mechanics model of self-locking mechanism when power failure occurs; **(b)** Ratio of payload force F and axial friction Ff varying with friction coefficient μ. While the most existing air motors are back-drivable, this unique self-locking mechanism of the presented motor resolves this challenge and can maintain steady position with <2.50 Nm payload applied. 77

Fig. 3.8 Customization design workflow that incorporates geometrical parameters and manufacturing materials. 78

Fig. 3.9 Air pulses for input gear actuation (pi) and output gear actuation (po). The supplied pressure levels, pi and po, are the same. In the general settings, $T1 = 0.3T$, $T2 = 0.7T$ and $T3 = 0.1T$. Overlaid period $T3$ of pi and po is essential to avoid the sudden drop of torque output at this "shifting" moment. 81

Fig. 3.10 Dynamics performance of motors fabricated using **(a)** low-friction material ($\mu = 0.094$), and **(b)** high-friction material ($\mu = 0.194$). The "low-friction" motor can generate higher torque and remain more steady output at the four supply pressure levels, namely 2.8, 3.2, 3.6, and 4.0 bar. 83

Fig. 3.11 Linear relation between output torque and supplied air pressure of motors with three different friction coefficients, namely $\mu = 0.094, 0.157, 0.194$. At the same supply pressure, the motor

FABRICATED USING LOW-FRICTION MATERIAL PRODUCES HIGHER TORQUE AT LOWER MECHANICAL ENERGY LOSS. 83

FIG. 3.12 DYNAMICS PERFORMANCE OF MOTORS WITH DIAMETER OF **(A)** $\emptyset 35$ MM AND **(B)** $\emptyset 20$ MM. OUTPUT TORQUE OF Ø20-MM MOTOR CAN REMAIN STEADY WITHIN LARGER RANGE OF MOTOR SPEED (UP TO 350 RPM), WHILE THE Ø35-MM MOTOR MAY BE ALREADY UNSTABLE AT SPEED OF 110 RPM. WHEN THE SAME PRESSURE SUPPLIED, Ø20-MM MOTOR GENERATES LOWER TORQUE DUE TO THE REDUCED CROSS-SECTIONAL AREA. 84

FIG. 3.13 RELATION BETWEEN OUTPUT TORQUE AND SUPPLY AIR PRESSURE OF MOTORS WITH FOUR DIFFERENT DIAMETERS, NAMELY $\emptyset 20, \emptyset 25, \emptyset 30, \emptyset 35$ MM. DATA IS FITTED USING LEAST-SQUARES FIT. THIS LINEAR TREND CONFORMS TO THE THEORETICAL ANALYSIS, AND THE SLOPE CORRESPONDS TO THE SQUARE OF DIAMETER $d2$. 85

FIG. 3.14 EVALUATION SETUP FOR THE MRI COMPATIBILITY TEST. IT INCLUDES A PNEUMATIC MOTOR AND AN MRI PHANTOM PLACED INSIDE THE MRI BORE, AS WELL AS PNEUMATIC VALVES WITH ITS CONTROLLERS PLACED IN THE CONTROL ROOM. 86

FIG. 3.15 MR IMAGES OF THE PHANTOM WITH TWO SEQUENCES, T2-WEIGHTED TSE AND T1-WEIGHTED FFE, UNDER FOUR SCENARIOS: **1)** CONTROL - ONLY PHANTOM IS PLACED IN THE SCANNER; **2)** STATIC - MOTOR HAS BEEN INTRODUCED INTO THE SCANNER, BUT ALL THE POWER IS OFF; **3)** AIR POWERED - BOTH ELECTRIC AND PNEUMATIC POWER IS ON, BUT MOTOR IS STATIC; **4)** IN OPERATION - MOTOR IS OPERATING. OVERALL, NO EMI ARTIFACT IS OBSERVED EVEN WHEN THE MOTOR IS IN FULL OPERATION. 87

FIG. 3.16 SNR LOSS IN **(A)** T1-WEIGHTED FFE AND **(B)** T2-WEIGHTED TSE IMAGES UNDER THE FOUR DIFFERENT MOTOR CONDITIONS. 87

FIG. 4.1 **(A)** 3D MODEL OF A ROLLING-DIAPHRAGM-SEALED CYLINDER; **(B)** MRI SAGITTAL VIEW OF THE CYLINDER. THOUGH MOTOR IS SELDOM THE INTERESTS IN THE SCAN, MOTOR WAS PLACED AT THE ISOCENTER AND IMAGED BY A 1.5T PHILIPS SCANNER UNDER THE TYPICAL GRE SEQUENCE TO PROVE ITS MR SAFETY. SNR REDUCTION IS MINIMAL AND EVEN THE TINY STRUCTURE CAN BE CLEARLY VISUALIZED. THE LOCAL ARTIFACT (CIRCLED BY THE RED DASH LINE) IS INDUCED BY THE SUSCEPTIBILITY CHANGES AT THE AREA INVOLVING COMPLICATED SCREW THREAD STRUCTURES AND VARIOUS MATTERS, E.G. AIR, POLYMER AND RUBBER. 92

FIG. 4.2 **(A)** CONVENTIONAL O-RING SEAL. SIGNIFICANT SLIDING FRICTION MAY BE INDUCED DURING THE RECIPROCATING OPERATION. **(B)** MASTER-SLAVE HYDRAULIC TRANSMISSION WITH TWO-CYLINDER-PAIR DESIGN. ROLLING DIAPHRAGMS ARE USED FOR LOW-FRICTION MOTION TRANSMISSION. RACK-AND-PINION MECHANISM IS ADOPTED TO TRANSFER LINEAR TO ROTARY MOTION. THE CONTACT BETWEEN GEAR TEETH OF RACK AND PINION IS MAINTAINED CONSTANT BY PRELOADING THE FLUID, THUS MINIMIZING BACKLASH. 93

FIG. 4.3 CIRCUIT DIAGRAM OF HYDRAULIC DRIVING SYSTEM WITH *TWO* PAIRS OF CYLINDERS. A PRESSURIZATION SYSTEM IS INVOLVED FOR DEGASSED LIQUID SUPPLY AND PRE-LOADING, WHICH INCLUDES AN AIR PUMP, A TANK, A FILTER AND A PRESSURE GAUGE. THIS SYSTEM CAN PREVENT AIR BUBBLES TO BE INTRODUCED INTO THE HYDRAULIC CIRCUIT. TWO TRANSMISSION LINES ARE COUPLED, AND POWERED BY AN ELECTRIC MOTOR AT THE MASTER SIDE. 95

FIG. 4.4 HYDRAULIC CIRCUIT DESIGN FOR *THREE*-CYLINDER CONTINUOUS ACTUATOR. THREE PAIRS OF CYLINDERS ARE INVOLVED IN THIS EXAMPLE. THE METHODS OF INTEGRATION WITH THREE SLAVE CYLINDERS MAY VARY, DEPENDING ON THE APPLICATIONS. THE TRANSMISSION LINES ARE INDEPENDENTLY CONTROLLED BY THREE ELECTRIC MOTORS AT THE

MASTER SIDE. 97
Fig. 4.5 CAD MODEL OF THE INTEGRATED HYDRAULIC ACTUATION IN AXIAL ARRANGEMENT. TRUNNION IS THE PIVOTING CENTER FOR THE SWASH PLATE, WHICH IS THE BALL JOINT LOCATED AT THE HEAD OF SUPPORTING SHAFT................. 98
Fig. 4.6 KINEMATICS DIAGRAM OF THE AXIAL HYDRAULIC MOTOR. THE CYLINDERS NEED TO PITCH AND YAW ABOUT THE JOINTS Pi $(i = 1,2,3)$. THIS 2-DOF MOTION MAY INTRODUCE MUCH INSTABILITY DURING THE OPERATION.......... 99
Fig. 4.7 3D MODEL OF THE IN-LINE CONFIGURATION FOR HYDRAULIC ACTUATION. THIS CRANK-SHAFT MECHANISM IS COMMONLY USED IN AUTOMOTIVE ENGINES.. 100
Fig. 4.8 KINEMATICS DIAGRAM OF THE IN-LINE HYDRAULIC MOTOR.. 101
Fig. 4.9 CAD MODEL OF THE INTEGRATED HYDRAULIC TRANSMISSIONS IN RADIAL CONFIGURATION. SIMILAR WITH THE CRANK-SHAFT MECHANISM, A ROTATING PLATE AND ECCENTRIC SHAFT SERVE TO TRANSFER THE LINEAR PISTON MOTION TO ROTATION OUTPUT. 102
Fig. 4.10 KINEMATICS DIAGRAM OF THE RADIAL MOTOR. PISTON OF CYLINDER $C1$ IS FIXED WITH THE ROTATING PLATE, WHILE THE OTHER TWO MAY ROTATE ABOUT IT. BY APPLYING COSINE LAW FOR THE TRIANGLE ΔOAP IN SINGLE CYLINDER, THE PISTON DISPLACEMENT CAN BE CALCULATED AS **Eq. 4.1**. 103
Fig. 4.11 DYNAMICS PARAMETERS OF A SINGLE TRANSMISSION LINE. INPUT FORCE Fin IS APPLIED TO PUSH THE PISTON 1 AT CONSTANT VELOCITY. OUTPUT FORCE $Fout$ EQUALS TO ZERO. THE CROSS MARKERS “×” UNDER THE BLOCKS DENOTE THE FLUID DAMPING. 105
Fig. 4.12 HYSTERESIS OF THE PROPOSED HYDRAULIC TRANSMISSION. THE AVERAGE VALUES OF HYSTERESIS, 0.88MM, 0.93MM, 1.02MM AND 1.29MM ARE MEASURED, ON CONDITION OF PRELOADED PRESSURE 0.05 MPA, 0.1 MPA, 0.15 MPA AND 0.2 MPA, RESPECTIVELY.. 113
Fig. 4.13 **(A)** PERIODIC MOTION OF THE MASTER-SLAVE ACTUATION. THE SLAVE POSITION (DASH LINE) CAN PRECISELY FOLLOW THE SINUSOIDAL REFERENCE TRAJECTORY (CONCRETE LINE) OF THE MASTER UNIT AT 0.1 HZ. **(B)** ABSOLUTE ERROR HAS A MAXIMUM OF 0.67 MM. 114
Fig. 4.14 EXPERIMENTAL BODE PLOT SHOWING THE TORQUE RESPONSE OF THE MASTER-SLAVE HYDRAULIC TRANSMISSION AT FOUR LEVELS OF PRELOADED FLUID PRESSURE, NAMELY 0.05, 0.10, 0.15, 0.20 MPA. THE MAGNITUDE AND PHASE SHIFT ARE SHOWN IN THE TOP AND BOTTOM PLOTS RESPECTIVELY. THE DATA ARE COLLECTED AT THE STEADY STATE FROM 10 CYCLES. DESPITE THIS MASTER-SLAVE HYDRAULIC SYSTEM IS USUALLY OPERATING UNDER <1HZ (DELAY <45MS). MAXIMUM TEST FREQUENCY REACHES 13 HZ TO EXPLORE THE TRANSMISSION PERFORMANCE AT WIDER BANDWIDTH. 115
Fig. 4.15 **(A)** MR IMAGES OF AN SNR BOTTLE PHANTOM PLACED ASIDE, WHICH INDICATE NEGLIGIBLE EMI GENERATED DURING OPERATION. SNR TEST RESULTS OF TWO IMAGING SEQUENCES: **(B)** T1-WEIGHTED FFE, AND **(C)** T2-WEIGHTED TSE. SNR LOSSES IN BOTH SEQUENCES ARE WITHIN 2%. 117
Fig. 5.1 **(A)** EXABLATE NEURO® SYSTEM FOR MRI-GUIDED HIFU. PATIENT LYING AT THE MRI TABLE HAS TO WEAR A HELMET, WHICH CONTAINS A PHASE ARRAY TRANSDUCER SYSTEM COMPOSED OF OVER 1,000 INDIVIDUAL TRANSDUCER ELEMENTS. THE SPACE BETWEEN PATIENT HEAD AND TRANSDUCER IS A COOLING SYSTEM FILLED WITH CONSTANT-TEMPERATURE (APPROXIMATELY 18℃) WATER. IT IS TO PROTECT THE SKULL BONE TEMPERATURE REMAINING WITHIN

THE SAFE LIMITS. **(B)** FOCUSED ULTRASOUND GENERATING HEAT AND ABLATING TISSUE AT THE FOCAL POINT. **IMAGE SOURCE: INSIGHTEC LTD.** 120

FIG. 5.2 SLAVE MODULE OF THE PROPOSED MR SAFE ROBOT FOR INTRA-OP MRI-GUIDED BILATERAL STEREOTACTIC PROCEDURES. 122

FIG. 5.3 SINGLE MANIPULATOR SHOWN WITH TWO POSSIBLE CONFIGURATIONS. BOUNDARIES OF STN TARGETS HIGHLIGHTED IN GREEN, WHICH COULD BE REVEALED BY T2-WEIGHTED MRI. THE INSERTION PATH IS THE PRE-OPERATIVELY PLANNED TRAJECTORY. ITS ANGULAR INCLINATIONS (A_1 AND A_2) AND PROJECTION AT AXIAL/SAGITTAL PLANES ARE SHOWN IN THE BLOCK AT LOWER LEFT AND LOWER RIGHT CORNERS, RESPECTIVELY. 125

FIG. 5.4 KEY COMPONENTS (UPPER ROW) AND SCHEMATIC DIAGRAM (LOWER ROW) OF A 1-DOF ACTUATION DESIGN. .. 127

FIG. 5.5 **(A)** CAD MODEL SHOWING THE KEY COMPONENTS OF THE BILATERAL STEREOTACTIC MANIPULATORS. **(B)** LOWER LAYER OF THE MANIPULATOR POSITIONED ABOUT 30 MM ABOVE THE SKULL SURFACE, WHICH REMAINS THE SUFFICIENT SPACE FOR EASE OF OBSERVATION AROUND THE BURR HOLE. **(C)** OVERALL DIMENSIONS OBSERVED, WHICH DEMONSTRATES THE DESIGN IS SO COMPACT THAT TWO (BILATERAL) MANIPULATORS ATTACHED ON SKULL CAN BE FULLY STRETCHED IN TWO EXTREME CONFIGURATIONS WITHIN THE CONFINED SPACE OF A SIEMENS-STYLE MOCK HEAD COIL (INNER DIAMETER Ø265 MM). 128

FIG. 5.6 MANUAL ANCHORAGE OF THE ROBOT TO THE MOUNTING BASE WITHOUT THE USE OF ANY TOOL. THIS DESIGN MAY FACILITATE THE QUICK ROBOT REMOVAL, WHEN ANY ACUTE EMERGENCY OCCURS AND RESUSCITATION HAS TO BE PERFORMED FOR THE PATIENT. 129

FIG. 5.7 KINEMATICS DIAGRAM OF A SINGLE MANIPULATOR WITH COORDINATE FRAMES Ψ_O AND Ψ_E DEFINED AT THE HOUSING BASE AND THE NEEDLE TIP, RESPECTIVELY. 130

FIG. 5.8 LINEAR ACTUATOR FOR NEEDLE INSERTION DRIVEN BY THE TENDON-SHEATH MECHANISM. TWO ROLLERS ENCLOSED BY HIGH-FRICTION SOFT MATERIAL CAN ROTATE INWARDS/OUTWARDS AND GRIP THE NEEDLE FOR INSERTING/RETRIEVING MOTION. 134

FIG. 5.9 TWELVE FIDUCIAL MARKERS, FILLED WITH VITAMIN E OR FISH OIL, WHICH ARE FIXED ON THE MANIPULATOR HOUSING FOR IMAGE REGISTRATION. 135

FIG. 5.10 **(A)** FIDUCIAL RINGS FOR BURR HOLE LOCALIZATION AND TRAJECTORY PLANNING. SOFT HOLLOW RINGS ARE INJECTED WITH MRI-VISIBLE OIL (VITAMIN-E) AND SEWED WITH SKIN FOR FIXATION. **(B)** 3D MRI RECONSTRUCTION SHOWING THE FIDUCIAL RINGS CAN BE CLEARLY IDENTIFIED IN THE HIGH-RESOLUTION ANATOMICAL SCANNING. **(C)** LINE TRAJECTORY FOR INSTRUMENT INSERTION TRAJECTORY DEFINED BY THE SELECTED TARGET AND THE CENTER OF BURR HOLE, NAMELY THE CENTER OF FIDUCIAL RING. 136

FIG. 5.11 Z-FRAME FIDUCIAL MARKER SYSTEM FOR INSTRUMENT LOCALIZATION UNDER IMAGING SEQUENCE. **(A)** CAD MODELS OF THE MARKER SYSTEM DESIGN, SHOWING THE ARRANGEMENT OF SEVEN FIDUCIAL LINES. INTERSECTION BETWEEN THE SCANNING PLANE AND Z-FRAME SYSTEM, IN **(B)** ORTHOGONAL VIEW AND **(C)** SIDE VIEW. INTERSECTING POINTS ARE DEFINED AS $pm, (m = 1,2, \dots ,7)$. **(D)** PHOTO OF THE NEEDLE GUIDE EMBEDDED WITH BOTH Z-FRAME MARKER (RED DASH LINES) AND MR-BASED WIRELESS TRACKERS (RED DASH ELLIPSE). **(E)** 3D RECONSTRUCTED FRAME MARKER. **(F)** 2D MRI SHOWING A CROSS SECTION OF THE Z-FRAME. SEVEN INTERSECTING POINTS ARE VISIBLE IN THE

IMAGE AND ORDERED AS $pm, (m = 1,2, \ldots, 7)$. 137

FIG. 5.12 **(A)** DIMENSION AND COORDINATE SYSTEMS FOR THE FIDUCIAL MOTIF ($Z1$ PLANE). **(B)** THREE PARAMETERS, φ, γ, f, DESCRIBING THE RELATIONSHIP BETWEEN THE SCANNING PLANE AND FIDUCIAL MOTIF. IN THE PRESENTED Z-FRAME MARKER SYSTEM, $L1 = 20\,mm, L2 = 22\,mm, L3 = 18\,mm$. 138

FIG. 5.13 FORCE-DISPLACEMENT DIAGRAM SHOWING THE TRANSMISSION STIFFNESS OF THE ACTUATION MODULE AT FOUR LEVELS (0.5, 1, 1.5 AND 2 BAR) OF PRE-LOADED PRESSURE ON THE TRANSMISSION LIQUID. 141

FIG. 5.14 **(A)** NEEDLE GUIDE EMBEDDED WITH TWO MR-BASED TRACKING COIL UNITS, ONE OF WHICH IS SHOWN ON ITS SIDE WALL. **(B)** MR IMAGE OF THE BRAIN PHANTOM (IN THE CORONAL VIEW) REVEALING THE TWO TRACKING MARKERS BY THE CORRESPONDING BRIGHT SPOTS. DARK STRAIGHT LINE IS THE NEGATIVE ARTIFACT OF THE NEEDLE. THE TWO SPOTS ARE ZOOMED IN (ENCLOSED IN THE BLUE DASH ELLIPSE). TWO RED CROSSES PROBING AT THE SPOTS INDICATE THE SIGNAL INTENSITY OF THE COILS, IN CONTRAST TO THOSE INTENSITIES AVERAGE WITHIN OTHER TWO YELLOW CIRCLES: ON THE BACKGROUND AND AGAR-GEL BRAIN PHANTOM. **(C)** VIRTUAL CONFIGURATIONS OF THE INSTRUMENT AUGMENTED ON THOSE HIGH-CONTRAST MARKERS, WHICH ARE POSED ABOVE THE 3D RECONSTRUCTED BRAIN PHANTOM. ANY CHANGE OF THE INSTRUMENT POSE COULD BE DETECTED CONTINUOUSLY (AT 30-40HZ) UNDER THE REAL-TIME MR-TRACKING SEQUENCE. 145

FIG. 5.15 **UPPER:** T2-WEIGHTED FSE IMAGES OF AN SNR PHANTOM. THESE IMAGES ARE GENERATED AT DIFFERENT STAGES OF ROBOT OPERATION. A BINARY MAP FOR FSE SEQUENCE MARKED THE ARTIFACTS AS WHITE PIXELS. NO ARTIFACT IS OBSERVED WITHIN THE PHANTOM AREA. AS DEFINED BY THE ASTM STANDARD, IT INDICATED ZERO ARTIFACT WAS CREATED BY THE OPERATION OF ROBOT. **LOWER:** SNR TEST RESULTS. THE EXISTENCE OR OPERATION OF THE PROPOSED ROBOT IS DEMONSTRATED TO HAVE MINIMAL INFLUENCE TO SNR. 146

FIG. 5.16 SYSTEM SETUP OF THE PRESENTED MRI-GUIDED ROBOT-ASSISTED STEREOTAXY FOR CADAVER TRIAL. AN MRI-COMPATIBLE CAMERA WAS PLACED AT ABOUT 300 MM AWAY FROM THE SUBJECT TO MONITOR SUBJECT CONDITIONS AND ROBOT MOTIONS. 148

FIG. 5.17 GRAPHICAL USER INTERFACE FOR ROBOT POSE CONTROL. THE ROBOT IS REGISTERED WITH THE PATIENT'S ANATOMY, NAMELY THE SURGICAL TARGETS AND THE BURR HOLE CENTRE. THREE SMALL CIRCLES (IN GREEN, RED AND PURPLE) REPRESENT THE COORDINATES OF THREE MR-BASED *WIRELESS* TRACKERS, WHICH DETERMINE THE FOUR ROBOT JOINT ANGLES. CURRENT ROBOT POSE (COLOURED THICK LINES) AND THE PLANNED TRAJECTORY (BLACK DASH LINE) ARE SHOWN. ESTIMATED ERRORS AND COMPUTED ROBOT JOINT MOTIONS ARE DISPLAYED AT THE BOTTOM OF THE INTERFACE. THE TARGETING TRAJECTORY CAN BE MANUALLY ADJUSTED TO ALIGN WITH THE PLANNED TRAJECTORY. . 151

FIG. 5.18 PROPOSED WORKFLOW OF THE MRI-GUIDED STEREOTAXY WITH ROBOT ASSISTANCE, WHICH IS MUCH SIMPLER THAN THE CONVENTIONAL WORKFLOW (**FIG. 2.11A**). 152

FIG. 5.19 PROPOSED WORKFLOW OF THE MRI-GUIDED STEREOTAXY WITH ROBOT ASSISTANCE (CONTINUED TO **FIG. 5.18**). 153

FIG. 6.1 TYPICAL CATHETER EP ABLATION ROADMAP GUIDED BY FLUOROSCOPY. **(A)** LA ROADMAP (SYNGO® 3D ROADMAP) FORMED BY REAL-TIME 2D FLUOROSCOPY IMAGES AUGMENTED WITH PRE-OP 3D LA MODEL. **(B)** POSTERIOR VIEW OF THE LA ROADMAP FOR RF ABLATION. ABLATIONS LESIONS (RED DOTS) ARE CREATED AROUND THE VEIN OPENINGS TO isolate the abnormal electrical impulses from pulmonary veins. Pulmonary vein isolation (PVI) is a treatment for atrial fibrillation (AF). **Image Source: Siemens Healthcare and Hunter Heart [196].** 155

Fig. 6.2 Proposed robotic catheter platform with a clinically-used EP catheter installed. Master actuation unit in control room drives the slave unit in pair, both of which contain rolling-diaphragms for efficient mechanical energy transmission. The robot manipulates the catheter tip in 3-DoF motion, i.e. rotating, bending, coarse/fine insertion. 157

Fig. 6.3 Human-robot navigation interface for precise and effective catheterization. Circular lesion target (red) is indicated in the LA roadmap. Virtual camera is set at the catheter tip to provide endoscopic view from the tip. 159

Fig. 6.4 Two major performance indices in the left atrial EP catheterization procedures. **(a)** Accuracy, defined as the proximity distance (mm) measured from catheter tip to lesion target when RF ablation power is on. **(b)** Efficiency, total length (mm) of the completed lesion segments (red). 160

Fig. 6.5 **(a)** Basic structure of a single enclosing segment with two adjacent circular contours. Variables are defined for geometric analysis; **(b)** Newly-added variables following the previous iteration results. 162

Fig. 6.6 Exemplary configuration showing the closest point pairs of each iteration. It can be considered as an extreme case, which requires more than four iterations for convergence. 165

Fig. 6.7 **(a)** Four-vertex polygon extracted from the cross-sectional area of a single segment Ωj. It is to determine the distance calculation condition by identifying the region containing the point; **(b)** Voronoi Regions of triangle $\Delta\mathrm{ABC}$ in 2D space. 168

Fig. 6.8 Catheter configurations with two steering curvature. The catheter (7 segments) is inserted inside the LA model (10,658 mesh) for RF ablation during the intra-cardiovascular EP procedure. The sampling rate of PQ is maintained at 1kHz. 170

Fig. 6.9 **Upper row:** Experimental setup with the tele-operated robotic catheter system. **Lower row:** Mapping sequences with 52 target points, starting from red star and ending at red diamond. The dataset to be used in the experiment comes from expert mapping of the Tetralogy of Fallot (ToF) right ventricle phantom. The mesh at bottom left corresponds to the right ventricle outflow. And the mesh at bottom right corresponds to the triscupid valve. 172

Fig. 6.10 **(a)** Experimental settings of the simulated pulmonary vein isolation task. A clinically-used catheter is tele-manipulated by the proposed robot to perform "ablation" on the LA model. **(b)** Recorded locations (127 points) of ablation in the interior surface. 173

Fig. 6.11 **(a)** Experiment setup of MR-compatibility test. Key components are connected via eight pipelines between MRI and control room. The operator can tele-operate the catheter according to the navigation interface. **(b)** MR images of a SNR bottle phantom placed besides the robot. The EMI generated by the presence of robot or its operation is negligible. 174

FIG. 7.1 **(A)** TRANSORAL REGION OF INTEREST DELINEATED FROM CT IMAGES IN 3D; **(B)** T2-WEIGHTED FAST SPIN ECHO (FSE) MR IMAGE OF HEAD-AND-NECK REGION IN THE AXIAL SCANNING PLANE. RED ARROW INDICATES THE TUMOR LOCATED IN THE PARAPHARYNGEAL SPACE. YELLOW CIRCLES AND GREEN ARROWS, RESPECTIVELY, DENOTE THE CAROTID ARTERIES/NERVES AND PAROTID (SALIVARY) GLANDS; **(C)** HEAD-AND-NECK ANATOMY INDICATED WITH AN ACTUAL TUMOR ORIGINATED FROM THE OROPHARYNGEAL CAVITY. **IMAGE SOURCE: PEARSON EDUCATION INC.** 181

FIG. 7.2 FABRICATION PROCEDURE OF A PATIENT-SPECIFIC DENTAL GUARD (DOCKING MODULE); **(A)** UPPER AND LOWER IMPRESSIONS OF THE PATIENT TAKEN BY A DENTIST; **(B)** MASTER MODELS OF THE IMPRESSIONS; **(C)** PRECISE 3D SCANNED MODELS OF THE DENTAL ARCHES, INCLUDING UPPER AND LOWER IMPRESSIONS. SPECIFIC FEATURES (E.G. MR-FIDUCIALS, INSTRUMENT CHANNELS) ARE ACCOMMODATED INTO THE MODEL, OF WHICH THE SHAPES, SIZES AND LOCATIONS ARE OPTIMIZED; **(D)** DENTAL/SURGICAL GUARD PROTOTYPE FABRICATED USING BIOCOMPATIBLE MATERIAL (ACRYLIC RESIN). IT CAN FIX THE JAWS IN OPEN-MOUTH POSITION SO AS TO PROVIDE SUFFICIENT WORKSPACE ($> 25 \times 25 \times 20$ MM3) FOR TRANSORAL SURGICAL INTERVENTIONS. 183

FIG. 7.3 OVERVIEW OF THE PROPOSED TRANSORAL ROBOT (SLAVE). COORDINATE FRAMES ΨI, ΨII AND ΨIII ARE DEFINED AT THE DISTAL END OF SEGMENT 1, 2 AND 3, RESPECTIVELY. SEGMENT 1 IS A CONTINUUM STRUCTURE FOR ADVANCEMENT, WHICH IS DRIVEN BY THE 2-CYLINDER ACTUATOR AND CAN PASSIVELY ADAPT TO THE CURVATURE OF PATIENT NATURAL ORIFICE. SEGMENT 2 AND 3 ARE DESIGNED TO ACTIVELY STEER THE LASER COLLIMATOR, WHICH ARE ACTUATED BY HYDRAULIC POWER AS WELL. 184

FIG. 7.4 DESIGN AND OVERALL DIMENSION OF THE ROBOT SEGMENT 2. THREE CHAMBERS (BLACK) ARE ACTUATED BY REGULATED HYDRAULIC PRESSURES. REINFORCEMENT SPRINGS WITH PITCH OF 0.75 MM TIGHTLY ENCLOSE THE CHAMBERS TO CONSTRAIN THEIR RADIAL EXPANSION. AXIAL ELONGATION OF THESE PRESSURIZED SLENDER CHAMBERS ($\emptyset 3 \times 13.5$ MM) GENERATE COARSE BENDING MOTION, MAX. $\pm 60°$. 186

FIG. 7.5 3D MODEL OF THE ROBOT SEGMENT 3. ACTUATION METHOD OF SEGMENT 3 IS SIMILAR WITH THE ONE OF SEGMENT 2, BUT IS TO PROVIDE FINE ANGULAR ADJUSTMENT WITH SHORTER LENGTH OF ACTUATION CHAMBERS. THERE ARE TWO PARTITIONS DIVIDING THE REINFORCEMENT SPRING INTO THREE SEGMENTS, IN ORDER TO REDUCE THE TWISTING MOTION AND RADIAL INFLATION DURING ACTUATION. DIFFERENT FROM SEGMENT 2, A RIGID CAP ENCLOSES ALL THE ACTUATION STRUCTURES. THIS ENSURES MOBILITY WHEN THE CURVATURE OF THE WHOLE CONTINUUM ROBOT IS CONSTRAINED. A SEMI-SPHERE PLATE MAY INTERACT WITH THE INNER SPHERICAL SURFACE OF THE HOUSING CAP TO FORM A BALL JOINT. THE LASER COLLIMATOR IS FIXED WITH THE SEMI-SPHERE PLATE AND CAN BE PIVOTED TO PERFORM LASER PROJECTION ABLATION. 187

FIG. 7.6 EXPERIMENTAL SETUP OF THE PATH-FOLLOWING TEST. AN EM TRACKING SYSTEM (NDI MEDICAL AURORA) IS EMPLOYED TO PROVIDE THE REAL-TIME POSITION AND ORIENTATION DATA FEEDBACK. THE PROJECTION PLANE IS PLACED ABOUT 15-20 MM AWAY FROM THE PIVOTING CENTRE OF THE LASER COLLIMATOR. A CIRCULAR ABLATION TRACE ($\emptyset 5$ MM) CAN BE OBSERVED IN THE PROJECTION PLANE. 189

FIG. 7.7 **(A)** ISOMETRIC VIEW OF ROBOT SEGMENT 2 PROJECTING A SPIRAL TRAJECTORY AT THE PLANE; **(B)** PLOT OF DESIRED (BLACK) AND ACTUAL (RED) TRAJECTORIES ON THE PROJECTION PLANE. 191

FIG. 7.8 PRESSURE VARIATION OF THREE ACTUATION CHAMBERS THROUGH THE WHOLE JOURNEY OF SPIRAL PATH

FOLLOWING. 191

FIG. 7.9 PATH FOLLOWING ERRORS CALCULATED IN THE PROJECTION PLANE. TRACKING ERRORS ARE DEFINED AS THE DISTANCES BETWEEN THE TARGET AND ACTUAL PROJECTION POINTS. THE ACCURACY IS 0.266 ± 0.155 MM, WITH MAX. ABSOLUTE ERROR OF 0.843 MM. 191

FIG. 7.10 (A) ISOMETRIC VIEW OF ROBOT SEGMENT 3 PROJECTING A SPIRAL TRAJECTORY ON THE PLANE; **(B)** PLOT OF DESIRED (BLACK) AND ACTUAL (RED) TRAJECTORIES ON THE PROJECTION PLANE. 192

FIG. 7.11 PRESSURE VARIATION OF THREE ACTUATION CHAMBERS THROUGH THE WHOLE JOURNEY OF SPIRAL PATH FOLLOWING. 192

FIG. 7.12 PATH FOLLOWING ERRORS CALCULATED IN THE PROJECTION PLANE. THE ACCURACY IS 0.150 ± 0.084 MM, WITH MAX. ABSOLUTE ERROR OF 0.375 MM. 192

FIG. 7.13 SYSTEM SETUP IN A 1.5T MRI SCANNER (SIGNA™ HDXT, GE HEALTHCARE). TRANSORAL ROBOT OPERATED INSIDE AN MRI HEAD COIL FOR MRI-BASED TISSUE ABLATION TEST. 193

FIG. 7.14 **(A)** MR IMAGE OF ROBOT AND TARGET TISSUE UNDER THE IMAGING SEQUENCE, FLIP ANGLE = $10°$. THIS SCANNING WAS PERFORMED PRE-OPERATIVELY FOR TARGET LESION LOCALIZATION AND ROBOT PLANNING. TARGET TISSUE, WATER LINES, SUPPORTING MATERIAL OF THE DENTAL GUARD CAN BE ALL VISUALIZED UNDER THIS SCANNING SEQUENCE. **(B)** 3D MRI RECONSTRUCTION SHOWING THE DELICATE ROBOT STRUCTURES. 193

FIG. 7.15 **(A)** MR IMAGE UNDER THE TRACKING SEQUENCE, FLIP ANGLE = $2°$. THREE TINY BRIGHT SPOTS INDICATE THE 3D LOCATIONS OF TRACKING COILS. COMPARED TO THE IMAGES OBTAINED UNDER THE IMAGING SEQUENCE, THE SIGNAL OF TISSUE/WATER IS WEAKENED WHILE THE COIL SIGNAL IS BEING AMPLIFIED IN THE TRACKING SEQUENCE. **(B)** 3D ROBOT MODEL AUGMENTED IN IMAGE SPACE BASED UPON THE *ACTIVE* MR TRACKING FEEDBACK.................................. 194

FIG. 7.16 MR IMAGES OF THE TARGET LESION SHOWING THE ABLATION PROGRESS. THE ROBOT RAN TEN ABLATION CYCLES AND STOPPED FOR ONE IMAGING UPDATE. THIRTY ABLATION CYCLES WERE PERFORMED. TOTAL ABLATION TIME WAS 10 MIN. A SMOOTH, HOMOGENEOUS, AND CIRCULAR TRACE COULD BE READILY IDENTIFIED. 195

FIG. 7.17 POST-MORTEM EVALUATION. **(A)** 3D MRI RECONSTRUCTION, SHOWING THE CIRCULAR ABLATION TRACE. **(B)** *EX VIVO* TISSUE PHOTO WITH THE CIRCULAR LESION.. 195

FIG. 7.18 MR IMAGES OF FOUR DIFFERENT ROBOT OPERATING CONDITIONS, SCANNED BY TWO SEQUENCES: T1W- GRE AND T2W- FSE. 196

FIG. 7.19 RESULTS OF MRI COMPATIBILITY TEST. MAX. SNR LOSS REACHED 4.19% IN T1-WEIGHTED FSE SCANNING. THIS MAY DUE TO THE EXISTENCE OF ALUMINIUM COUPLER OF THE LASER COLLIMATOR.. 196

List of Tables

TABLE 2.1 EXISTING ROBOTIC SYSTEMS FOR MRI-GUIDED NEUROSURGERY 48
TABLE 3.1 COMPONENT FUNCTION OF PNEUMATIC STEPPER MOTOR 71
TABLE 3.2 WORKING PRINCIPLE OF CLOCKWISE AND COUNTER-CLOCKWISE ROTATIONS, TAKING A MOTOR WITH $N = 6$ TEETH AS AN EXAMPLE. NUMBERS HIGHLIGHTED IN WHITE INDICATE THE TOOTH NUMBER. GEARS IN YELLOW AND TRANSPARENT ARE DIRECTION GEARS, WHICH ARE FIXED WITH THE MOTOR HOUSINGS. 73
TABLE 3.3 SELECTED EXISTING MR SAFE AIR MOTORS 89
TABLE 4.1 SPECIFICATIONS OF THE HYDRAULIC TRANSMISSION 94
TABLE 4.2 KEY PARAMETERS OF *THREE*-CYLINDER DESIGN 104
TABLE 4.3 PARAMETERS OF DYNAMIC MODEL 105
TABLE 4.4 VALUES OF MAJOR PARAMETERS 105
TABLE 4.5 PHYSICAL PARAMETERS 111
TABLE 5.1 NEEDLE TARGETING ACCURACY TEST 143
TABLE 5.2 MRI SCAN PARAMETERS 143
TABLE 6.1 TOTAL TIME, TRAVEL DISTANCE AND OPERATION COST FOR THREE MAPPING SEQUENCES 172
TABLE 7.1 INCISION POWER DENSITY WITH ITS RESPECTIVE EFFECT ON TISSUE 182
TABLE 7.2 SCAN PARAMETERS FOR MRI-BASED ABLATION AND MRI COMPATIBILITY TEST 195

List of Acronyms

3D- Three-dimensional

AC-PC - Anterior Commissure-Posterior Commissure

AF - Atrial Fibrillation

ASTM - American Society for Testing Materials

BBB - Blood-brain Barrier

bSSFP - balanced Steady-State Free Precession

CAD - Computer-Aided Design

CSF - Cerebrospinal Fluid

CT - Computed Tomography

DBS - Deep Brain Stimulation

DC - Direct Current

DoF - Degree of Freedom

DTI - Diffusion-weighted Image

EA - Electro-Anatomic

EAM - Electro-Anatomic Mapping

ECG - Electrocardiogram

EM - Electromagnetic

EMI - Electromagnetic Interference

EP - Electrophysiology

EPI - Echo-Planar Imaging

ET - Essential Tremor

FDA - Food and Drug Administration

FFE - Fast Field Echo

FISP - Fast Imaging with Steady-state Precession

FLASH - Fast Imaging using Low Angle Shot

FLE - Fiducial Localization Error

FoV - Field of Volume

FPGA - Field-Programmable Gate Array

FSA - Frozen Section Analysis

GPi - Globus Pallidus interna

GPU - Graphics Processing Unit

GRE - Gradient Echo

HNC - Head and Neck Cancer

IE - Implicit Exploration

IEC - International Electrotechnical Commission

iMRI - Interventional MRI

Intra-op - Intra-operative

LA - Left Atrium

LITT - Laser Interstitial Thermal Therapy

LV - Left Ventricle

MCP - Mid-Commissural Point

MER - Microelectrode Recording

MIS - Minimally Invasive Surgery

MR - Magnetic Resonance

MRgFUS - MR-guided Focused Ultrasound Surgery

MRI - Magnetic Resonance Imaging

NEMA - National Electrical Manufacturer's Association

NPC - Nasopharyngeal Carcinoma

ONP - Oral and Nasopharyngeal

OS - Overall Survival

OT - Operating Theatre

PA - Polycaprolactam

PD - Parkinson's Disease

PEEK - Polyetheretherketone

PEI - Polyethylenimine

PET - Polyetherimide

PFS - Progression-Free Survival

PID - Proportion-Integration-Differentiation

POM - Polyoxymethylene

PQ - Proximity Query

Pre-op - Pre-operative

PRF - Proton Resonance Frequency

PTFE - Polytetrafluoroethylene

PU - Polyurethane

PVC - PolyVinyl Chloride

PVI - Pulmonary Vein Isolation

PWM - Pulse-width Modulation

RF - Radiofrequency

RFA - Radiofrequency Ablation

RV - Right Ventricle

sEEG - tereo Electroencephalography

SLA - Stereolithography

SMA - Shape Memory Alloy

SNR - Signal-to-Noise Ratio

SPGR - Spoiled Gradient

STN - Subthalamic Nucleus

TLM - Transoral Laser Microsurgery

ToF - Tetralogy of Fallot

TORS - Transoral Robotic Surgery

TRE - Target Registration Error

TSE - Turbo Spin Echo

VT - Ventricular Tachycardia

Chapter 1

Introduction

1.1 Motivation and Objectives

RECENT advances in imaging and surgery have contributed to early diagnosis, improved surgical outcomes and accelerated patient recovery. This entails the surgical procedures with further enhanced accuracy, efficiency, and safety. It can be made possible by high-quality intra-operative (intra-op) imaging combined with new surgical instrument designs. In the last decade, magnetic resonance imaging (MRI)-guided interventions have drawn much attention. It is accredited to several advantages of MRI: **i)** no ionizing radiation, unlike computed tomography (CT) or X-ray; **ii)** high-contrast soft tissue imaging; **iii)** intra-op visualization of physiological or pathological changes; and **iv)** volumetric imaging and three-dimensional (3D) localization in real time. These also give rise to the demand for precise manipulation of surgical instruments and simplified workflow. It is timely for robotic technology to find its way into more complex MRI-guided procedures. Robots have superior capabilities over human in certain tasks, which are constrained by limited workspace (i.e. MRI bore), demanding on accuracy, and intensive operation. Improved surgical outcomes of adopting robot assistance have been demonstrated in numerous studies [1-3]. Despite these benefits reported, a number of technical challenges still remain to be resolved. For instance, issues related to the strong magnetic field (1.5T or 3T) of MRI scanner, tissue deformation/patient movement, robotic operation without degrading imaging quality, manipulation within the confined workspace of imaging coil/patient anatomy, and real-time positional tracking feedback are some of the main obstacles that need to be tackled.

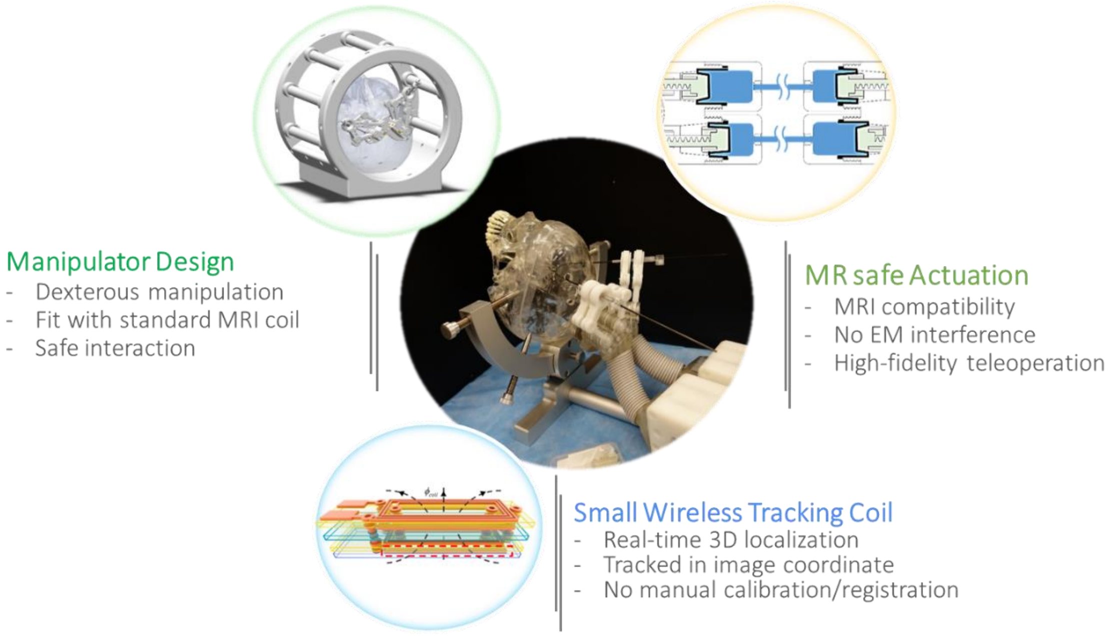

Fig. 1.1 Three key components of the MR safe robotic systems presented in this thesis, namely MR safe actuation, dexterous manipulator design and *wireless* tracking technique. Robotic systems integrated with these three components have been tested and evaluated regarding the relevant clinical requirements for various applications, i.e. stereotactic neurosurgery, intra-cardiac catheterization or transoral laser ablation. This study may contribute a benchmark for the development of MRI-guided robotic devices, opening a new dimension for other procedures that may also benefit from intra-op MRI, such as breast biopsy and prostate intervention.

I propose to address these challenges by three novel components, i.e. MR safe fluidic actuators, dexterous manipulators, and miniaturized MR-based tracking coils. The main objectives include:

1) To design and fabricate high-performance magnetic resonance (MR) safe actuation systems that their operation induces minimal electromagnetic interference (EMI) to the MR imaging. High-power and high-fidelity teleoperation can be achieved by fluidic actuators over a long distance (>10m).
2) To develop compact and dexterous robotic manipulators that can be accommodated inside the constraint workspace of MRI scanner or patient's anatomy. Three manipulators have been designed towards different MRI-guided interventions, namely stereotactic neurosurgery, intra-cardiac catheterization and transoral laser ablation.
3) To incorporate miniaturized *wireless* MR-based tracking coil for intra-op MRI navigation. Robotic instrument can be localized directly in imaging coordinates in real-time. There is no need for any calibration or co-registration between the imaging and tracking domain. It substantially reduces any error due to the manual selection of fiducials on the images.

4) To validate the entire robotic system's potential clinical values in lab- and MRI-based experiments. Performance indices relevant to the surgical benefits are also investigated.

Currently, there is no existing MRI-guided robotic system that is integrated with all these techniques. The proposed three robotic systems, i.e. neurosurgical robot, catheter robot and transoral soft robot, are all the first of its kind to continuously navigate MR-tracked instruments under intra-op MRI roadmap. These systems can be implemented in commonly-used diagnostic MRI facilities without having to transfer patients or scanners during the procedures. This study may contribute a benchmark for the development of MRI-guided robotic devices, opening a new dimension for other procedures that may also benefit from intra-op MRI, such as breast biopsy and prostate intervention.

The success of this study would represent a major step toward several ultimate goals:

- **i)** To enhance the accuracy by coping with dynamic surgical environments using intra-op MRI and MR-tracked instruments;
- **ii)** To increase the safety by using EMI-free MR safe robotic systems under MRI;
- **iii)** To decrease the risks of damaging critical functional or anatomical structures;
- **iv)** To save the operation time from complicated workflow, such as post-resection margin evaluations in transoral laser tumor dissection. The overall healthcare expenditure could be significantly reduced, also compensating the cost of using MRI.

1.2 Thesis Organisation and Main Technical Contributions

In **Chapter 2**, I have introduced the basic concepts and recent advances of interventional MRI (iMRI) systems, pulse sequences, MR safety and compatibility. These advancements and the wide accessibility of MRI have facilitated its further applications for surgical guidance. An overview of the state-of-the-art intra-op MRI-guided robotic platforms is provided, especially towards the applications of stereotactic neurosurgery. Although currently there is no commercial MR safe/conditional robotic system for intra-cardiac catheterization or transoral laser microsurgery (TLM). These two procedures are of great potential to be assisted by MRI-guided robotic systems to improve the surgical outcomes. The clinical considerations and key technical challenges of these three applications, namely stereotactic neurosurgery, intra-cardiac catheterization and TLM, are outlined. In this context, three key enabling techniques are proposed to improve the surgical workflow and achieve greater clinical penetration, namely *non-rigid* registration, MR-based tracking and MR safe actuation. Their current status, limitations, and future trends have been discussed. In the following technical chapters of this thesis, the development of two novel MR safe fluidic actuators have been detailed (**Chapter 3&4**). Incorporated with the *wireless* MR-based tracking coils, three fluid-powered robotic systems for intra-op MRI-guided interventions are developed and evaluated based on the clinical requirements of its corresponding application (**Chapter 5-7**).

Chapter 3 introduces a novel customizable pneumatic stepper motor that features with its compactness and simplicity. It comprises of seven components only, which are fabricated by 3D printing in homogeneous material. Parameters of each component are standardized to facilitate the rapid reconfiguration by three initial inputs, i.e. motor dimension, motion resolution and stall torque. Alternating bursts of the compressed air drive the motor rotate stepwise with a max. torque of 5.16 mNm and max. speed of 170 RPM. Theoretical modelling and experiments have been carried out to evaluate the motor performance under different parameter combinations and supplied pressures. MR-compatibility has been verified in a 1.5T MRI scanner. It was less than 3% signal-to-noise ratio (SNR) loss even when the motor was in full operation.

In **Chapter 4**, integrated hydraulic transmission methods using rolling-diaphragm-sealed cylinders are presented. Novel integration methods, e.g. *three*-cylinder design, have been introduced to provide *continuous* bidirectional rotation at unlimited range. Kinematics and dynamics models have been studied for overall design optimization. Force transmission, hysteresis, dynamic response, and SNR test have been experimentally evaluated. Such MR safe, high-performance hydraulic transmissions have been integrated into three robotic platforms for various applications, i.e. stereotactic neurosurgery, intra-cardiac catheterization and transoral laser ablation. These robots are introduced with details in the following **Chapter 5-7**.

Chapter 5 introduces an intra-op MRI-guided robot for bilateral stereotactic procedures. Its compact design enables robot operation within the constrained space of standard imaging head coil. A maximum transmission stiffness coefficient of 24.35 N/mm can be achieved with transmission fluid pre-loaded at 2 bar. Sufficient targeting accuracy (average within $\leq$1.73mm) has been demonstrated in a simulated targeting task of deep brain stimulation (DBS). A novel MR-based *wireless* tracking technique is adopted. It is capable to offer real-time and continuous 3D localization of robotic instrument under the proper MR tracking sequences. It outperforms the conventional method of using low-contrast passive fiducials that can only be revealed in the MR image domain. These *wireless* tracking units/markers are integrated with the robot, which are miniaturized coil circuits fabricated on flexible thin films. A navigation test was performed under the standard MRI settings in order to visualize the 3D localization of the robotic instrument. MRI-compatibility test was also carried out to prove the minimal interference to MR imaging of the presented hydraulic robotic platform.

Chapter 6 presents a robotic catheter system that integrates an MR safe robotic manipulator and corresponding techniques to enable MRI-guided intra-cardiac electrophysiological interventions, such as intra-op image processing, real-time positional tracking of catheter tip and human-robot control interface. The robot is driven by hydraulic actuators for effective electrophysiology (EP) catheterization. The master-slave hydraulic actuation system with small hysteresis has enabled the precise tele-manipulation even at a long distance (e.g. 10 m). Slave robot is made of non-metallic and non-conductive materials; therefore, it can operate close to or even inside the MRI scanner without adversely affecting the imaging quality. It has been demonstrated that the robot can perform high-fidelity tele-manipulation of a standard EP catheter in multiple simulated clinical tasks, such as cardiac mapping and radiofrequency ablation (RFA).

In **Chapter 7**, a soft continuum robot for MRI-guided transoral laser ablation is introduced. It can be anchored firmly onto a surgical dental guard, avoiding the complications of instruments docking through intraoral cavity using conventional retractors. The continuum robot can be divided into three segments regarding their functionalities. Segment 1 is a continuum structure for advancement, which can passively adapt to the natural orifice curvature. Six water tubes and one laser fiber are channelled through. Segment 2 and 3 are designed for actively steering. They feature with a hybrid structural design, comprising of both soft actuation chambers and rigid spring enclosure for reinforcement. Miniaturized RF-semi-active coils are adopted to provide low-error high-frequency positional tracking. Along with online ablation temperature monitor offered by MR thermometry, reliable intra-op guidance can be achieved in the forms of *in situ* visual feedback. Steady, smooth and consistent motion control of this long, thin and flexible continuum robot has been validated. MRI compatibility test has also been performed to prove the minimal imaging interference during robot operation.

1.3 Publications, Patents and International Awards during Ph.D. Study

The work during my Ph.D. study has resulted in the following publications in peer-reviewed international journals and conference proceedings, book chapter, patents and awards:

Journals:

1) Z. Guo, Z. Dong, K.H. Lee, C.L. Cheung, H.C. Fu, J.D.L. Ho, H. He, W.S. Poon, D.T.M. Chan, K.W. Kwok. *Compact Design of a Hydraulic Driving Robot for Intra-operative MRI-guided Bilateral Stereotactic Neurosurgery[J]*. **IEEE Robotics and Automation Letters**, 2018, 3(3): 2515-2522.
   [Best Conference Paper Award in IEEE International Conference on Robotics and Automation 2018 (ICRA'18) out of 2,2539 papers]
   [Finalist of Best Medical Robotics Paper Award in IEEE International Conference on Robotics and Automation 2018 (ICRA'18)]

2) Z. Guo, M.C.W. Leung, H. Su, K.W. Kwok, D.T.M. Chan, W.S. Poon. *Techniques for Stereotactic Neurosurgery: Beyond the "Frame", Towards the Intraoperative MRI-guided and Robot-assisted Approaches[J]*. **World Neurosurgery**, 2018, 116: 77-87.

3) Z. Dong, Z. Guo, K.H. Lee, G. Fang, W.L. Tang, H.C. Chang, D.T.M. Chan, K.W. Kwok. *High-performance Continuous Hydraulic Motor for MR Safe Robotic Teleoperation[J]*. **IEEE Robotics and Automation Letters**, 2018. (under review)

4) Y. Feng, Z. Guo, Z. Dong, X.Y. Zhou, K.W. Kwok, S. Ernst, S.L. Lee. *An Efficient Cardiac Mapping Strategy for Radiofrequency Catheter Ablation with Active Learning[J]*. **International Journal of Computer Assisted Radiology and Surgery**, 2017, 12(7): 1199-1207.

5) K.H. Lee, D.K.C. Fu, Z. Guo, Z. Dong, M.C.W. Leong, C.L. Cheung, A.P.W. Lee, K.W. Kwok. *MR Safe Robotic Manipulator for MRI-Guided Intracardiac Catheterization[J]*. **IEEE/ASME Transactions on Mechatronics**, 2018, 23(2): 586-595.

6) S.C. Tang, T.T.L. Lun, Z. Guo, K.W. Kwok, N. McDannold. *Intermediate Range Wireless Power Transfer with Segmented Coil Transmitters for Implantable Heart Pumps[J]*. **IEEE Transactions on Power Electronics**, 2017, 32(5): 3844-3857.

[First Place Prize Paper Award for 2017 in the IEEE Transactions on Power Electronics out of 789 papers and letters]

Peer-reviewed international conference proceedings:

7) Z. Guo, T.T.L. Lun, Y. Chen, H. Su, D.T.M. Chan, K.W. Kwok. *Novel Design of an MR-safe Pneumatic Stepper Motor for MRI-guided Robotic Intervention*, Proceedings of **Hamlyn Symposium on Medical Robotics 2016**. London, UK, pp.50-51.

8) K.H. Lee, Z. Guo, G.C.T. Chow, Y. Chen, W. Luk, K.W. Kwok. *GPU-based Proximity Query Processing on Unstructured Triangular Mesh Model[C]*. **IEEE International Conference on Robotics and Automation 2015** (**ICRA'15**), pp.4405-4411.

9) S.C. Tang, T.T.L. Lun, Z. Guo, K.W. Kwok, N. McDannold. *Mid-range wireless power transfer with segmented coil transmitters for implantable heart pumps[C]*. **IEEE International Workshop on Electromagnetics: Applications and Student Innovation Competition (iWEM)**, 2016: 1-3.

10) C.L. Cheung, K.H. Lee, Z. Guo, Z. Dong, M.C.W. Leong, Y. Chen, A.P.W. Lee, K.W. Kwok. *Kinematic-Model-free Positional Control for Robot-assisted Cardiac Catheterization*, Proceedings of **Hamlyn Symposium on Medical Robotics 2016**. London, UK, pp.80-81.

Book chapter:

11) Z. Guo, M.C.W. Leung, H. Su, K.W. Kwok, D.T.M. Chan, W.S. Poon. *Prospective Techniques for MRI-guided Robot-assisted Stereotactic Neurosurgery[M]*. **Handbook of Robotic and Image-guided Surgery**, Elsevier, 2019. (to appear)

Patents published (or filed):

1) *MRI Tracking Device Design, Fabrication, and Methods of use for MRI-guided Robotic System*, US Prov. Patent: **US62/640,798**. [Filed on Mar. 9, 2018]

2) *Fluid-powered Transmission for MRI-guided Interventions*, US Prov. Patent:

US62/640,302. [Filed on Mar. 8, 2018]

3) *Robotic Stereotactic System for MRI-guided Neurosurgery*, US Prov. Patent: **US62/623,280**. [Filed on Jan. 29, 2018]

4) *Robotic Catheter System for MRI-guided Cardiovascular Interventions*, US Utility Patent: **US15/630,406** [Filed on Jun. 22, 2016]
PCT Patent: **PCT/CN2017/089701** [Filed on Jun. 23, 2017]
Licensed by Signate Life Sciences (HK) Limited, which includes MRI Interventions Inc. as its portfolio company.

International awards:

1) Aug. 2018

   First Place Prize Paper Award for 2017 in the *IEEE Transactions on Power Electronics*, selected from 789 papers and letters.

2) May 2018
   Best Conference Paper Award in IEEE International Conference on Robotics and Automation 2018 (**ICRA'18**), selected in 2539 papers from 61 countries.

3) Mar. 2018
   Finalist of Best Medical Robotics Paper Award in IEEE International Conference on Robotics and Automation 2018 (**ICRA'18**).
   [sponsored by Intuitive Surgical]

4) Jun. 2017
   Merit Poster Award in IEEE International Conference on Robotics and Automation 2017 (**ICRA'17**) Workshop on Surgical Robots.
   [sponsored by Intuitive Surgical]

5) Jun. 2016
   Best Live Demonstration in Surgical Robot Challenge 2016, London, UK.

Chapter 2

MRI-guided Robot-assisted Surgery

2.1 Introduction

THE introduction of computer-based image navigation systems allows intra-op guidance based on pre-operative (pre-op) images since 1990s [4]. Provided with the advanced imaging and navigation assistance, minimally invasive surgery (MIS), established as an alternative to the conventional open procedures, is thus playing an increasingly important role in the current clinical practice. The main purposes of these procedures can be summarized as targeting, marking, access to specific anatomical areas, lesions removal, and tumor treatment by applying radiation, electrical field, thermal energy or therapeutic agent.

MRI is well-known for its superior capabilities in providing non-invasive, non-ionizing radiation and high-contrast images of soft tissues. It is also capable of monitoring the temperature changes during thermal therapies [5]. These advantages have prompted MRI for vibrant adoption of guidance for interventions ranging from biopsy [6], thermal therapy for tumor ablation [7, 8], drug injection [9, 10] to catheter-based procedures within cardiovascular system [11, 12]. Biopsy is currently one of the most frequent clinical interventions under MRI guidance [13]. A number of studies have demonstrated increased targeting accuracy with the assistance of robotic platforms under intra-op MRI [14-17]. Fast MRI scanning sequences (such as radial fast imaging using low angle shot (FLASH) sequence with a temporal resolution of 20-30 ms [18]) have been widely available in the current MRI facilities and permitted the procedural guidance involving soft tissue deformation. The field is ready for MRI-guided robots to find its way into more complex procedures by offering precise treatment and delivering image-guided therapy, such as devices implantation or tissue ablation.

In this chapter[1], an overview of the robotic surgical platforms for MRI-guided interventions will be provided. It presents a historical perspective of MRI-compatible mechanical designs and discusses how they are used in robot-assisted MIS and their potential pitfalls. Technical challenges are outlined, particularly regarding the clinical requirements of three surgical procedures. This chapter provides the basis for the technical issues to be addressed in this thesis.

2.2 Intra-operative MRI

2.2.1 Interventional MRI (iMRI) Systems

There are mainly three types of intraoperative or interventional MRI (iMRI) suites in the market, regarding the layout of operating and MRI rooms: **1)** single-room design with collocated environments, surgery is conducted inside the MRI scanner (**Fig. 2.1a**); **2)** dual-room design with moving patient or magnet (**Fig. 2.1b**); and **3)** single-room design with separate areas for operation and scanning (**Fig. 2.1c**). **Fig. 2.1a** shows a double-donut open MRI system (Signa SP, GE Healthcare), which is a single-room design with operation performed inside the scanner. There is 58-cm gap between the split superconducting magnets with 60-cm bore diameter. The imaging isocenter is located at the middle of the gap, coaxial with the magnets. The patient can be transferred into the magnet bore along the axis as in the diagnostic scanner, and a wide variety of positions can be adopted for the imaging. The physician would stand in the gap and approach the patient from sides to perform the surgery. This design eliminates the needs for patient transfer and facilitates quick MRI-guided interventional procedures. Despite the advantages of iMRI guidance, such confined workspace still impedes the broad acceptance of this scanner. It is especially difficult for those long and complicated surgical procedures to be performed, which

---

[1] The work presented in this chapter has been published in:

[1] <u>Z. Guo</u>, M.C.W. Leung, H. Su, K.W. Kwok, D.T.M. Chan, W.S. Poon. *Techniques for Stereotactic Neurosurgery: Beyond the "Frame", Towards the Intraoperative MRI-guided and Robot-assisted Approaches[J].* **World Neurosurgery**, 2018, 116: 77-87.

[2] <u>Z. Guo</u>, M.C.W. Leung, H. Su, K.W. Kwok, D.T.M. Chan, W.S. Poon. *Prospective Techniques for MRI-guided Robot-assisted Stereotactic Neurosurgery[M].* **Handbook of Robotic and Image-guided Surgery**, Elsevier, 2019. (to appear)

may require intensive cooperation of physicians. In addition, manipulation capabilities of surgeons and image quality are greatly sacrificed to collocate the surgical and imaging fields. This scanner is limited to the first fifteen systems and has been no longer commercially-available.

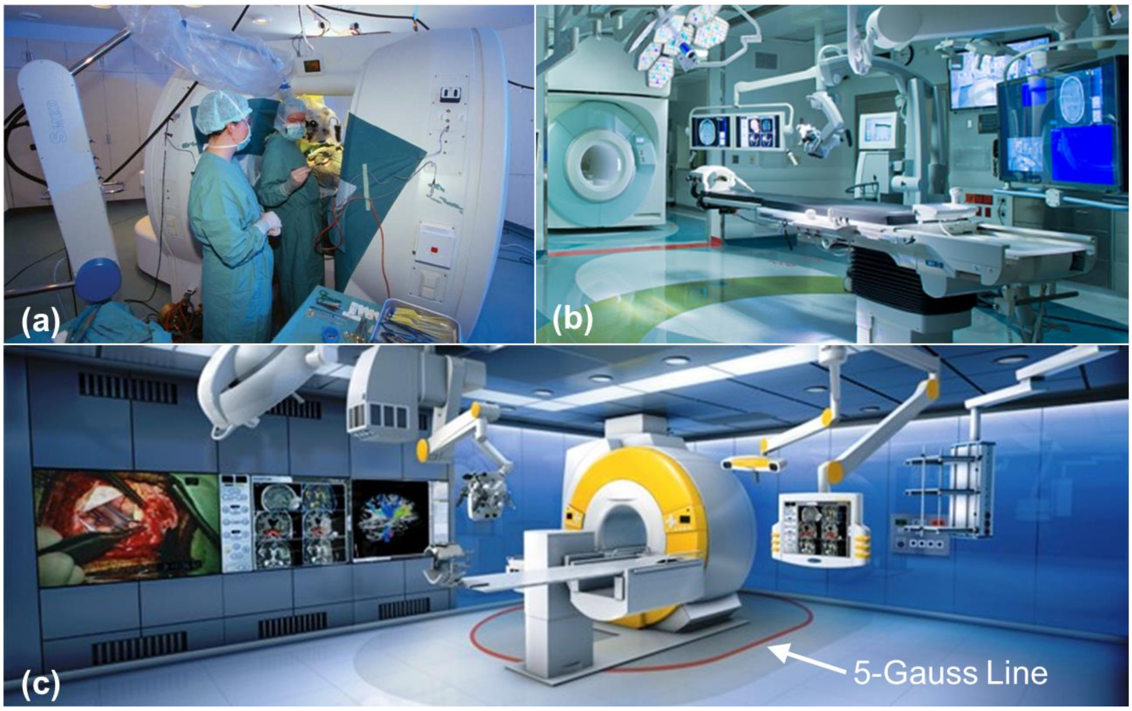

Fig. 2.1 **(a)** Low-field open iMRI system (0.5 Tesla Signa SP from GE Healthcare). Surgeon performs the operation standing in-between the double-donut magnets. **(b)** Dual-room suite with an MRI transfer system (VISIUS® system from IMRIS Inc.). Surgical table, navigation system, lights and camera are shown in the foreground, as in the typical positions for surgery. The equipment should be positioned outside the 5-Gauss line, before the magnet is entering the room. **(c)** Single-room system with a surgical table that can be pivoted (BrainSUITE® from BrainLAB Inc.). The surgical procedure is performed outside the 5-Gauss line (in red). And for MRI scanning, a central column can pivot the tabletop, lower it onto the MR table, and transfer it into the magnet.
Image source: GE Healthcare, IMRIS Inc., BrainLAB Inc.

Dual-room design separates imaging and operating environments, which requires transitions of patient/scanner between two rooms for imaging. Such design may avoid many issues, especially regarding the surgical tools (**Fig. 2.1b**). Most of the standard surgical instruments, e.g. microscope and cautery, can be still employed in the operating room. Note that all the non-MR-compatible equipment must be removed from patient and beyond the 5-Gauss line prior to the magnet/patient transitions. The travel distance of magnet/patient is usually up to 18 m. However, such transitions during the operation are considerably time-consuming and laborious. The patient-handling systems have to be MR-compatible and meet both surgical/imaging imperatives. Anaesthesia machines demand on cautious management, especially during the patient travel, to prevent any tension of the airway/intravenous lines and disconnect/reconnect the gas supplies. Siting and RF-shielding of these dual-room suites can also be complicated and costly.

Fig. 2.1c shows a single-room suite with an operating area in the MRI room. The patient anatomy of interest is positioned outside the 5-Gauss line during the normal surgery, allowing the use of variety of standard surgical instruments. For imaging, the handling system may be pivoted and the patient is moved into the magnet. This transitions are relatively easy. Since anaesthesia machines can reside at the pivoting column of the handling system, so that it can support the patient at both operating and imaging location. Compared to the normal diagnostic MRI suites, larger rooms are required for additional operating space outside the 5-Gauss line and equipment with surgical-grade infection control systems. These single-room suites are cost-effective especially for short-duration procedures.

In summary, the major goal of an iMRI suite is to offer image guidance for interventional or surgical procedures. After reviewing the existing iMRI systems, the major challenge appears to be the integration of the MRI system with the surgical equipment. Open low-field MRI systems may provide relatively unrestricted access to patient, but the image quality and surgeon operation capabilities have to be compromised. Closed-bore MRI scanners can usually provide sufficient imaging quality with high magnetic field. But the interventions have to be performed by iterative cycles, i.e. repeatedly moving the patient in-and-out of the magnet bore for imaging update/manual operation. The field is evolving. The recent surge of MR-compatible robotic systems may represent the next stage in this revolution. These robotic systems have great potential to provide a systematic approach to address the major issues of intra-op MRI-guided interventions, such as improved access/manipulation, tracking/localization, and energy delivery control for thermal therapies. A detailed review on existing MR-compatible robotic systems is presented in **Section 2.3**.

2.2.2 Pulse Sequences for iMRI

Pulse sequences for interventional MRI guidance differ from the diagnostic MRI in two main manners: **i)** Besides high-contrast image generation, interventional imaging sequences also serve for device tracking and therapeutic monitoring. Interventional imaging typically interleaves and swaps several pulse sequences, e.g. active tracking sequence and continuous roadmap imaging for endovascular procedures. **ii)** These pulse sequences and the corresponding reconstruction algorithms are designed to minimize the time between imaging acquisition start and reconstructed output display, especially for those applications demanding on latency. These challenges have driven the dynamic MRI evolution during the past years [19], which is formed rapidly and successively by continually acquiring the image data. Recent advances on $k - space$ trajectory schemes, rapid contrast generation, and interventional software platforms have laid the foundation enabling the flexible configurations to meet the challenges.

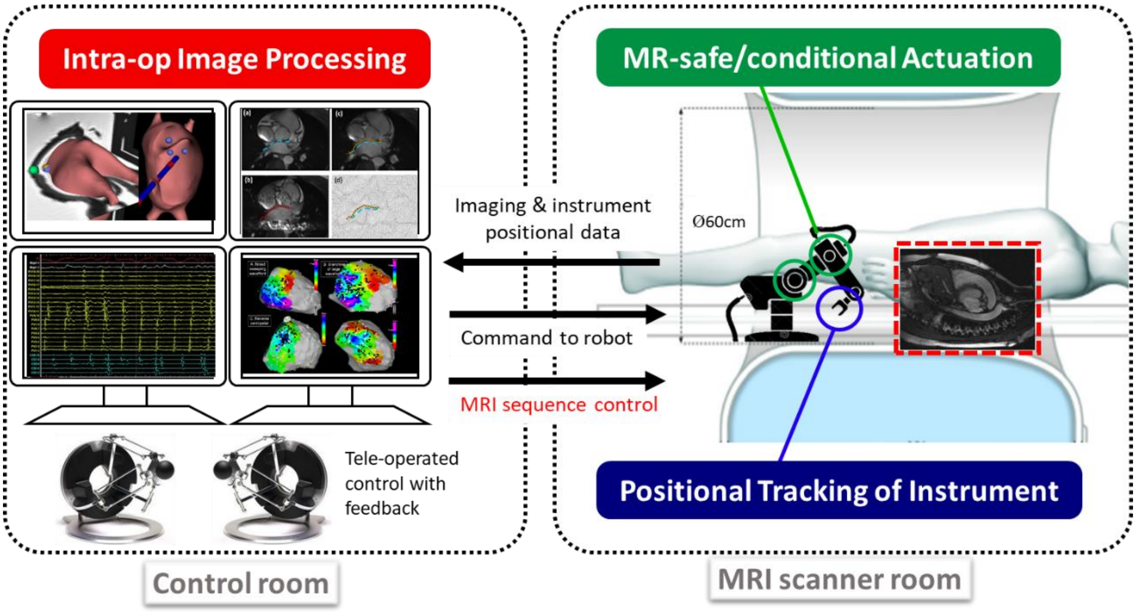

Fig. 2.2 Overview of the system setup for real-time MRI-guided interventions (assisted by robot).

Gradient-recalled steady-state imaging can provide many imaging tools for interventional MRI procedures, such as T1-weighted fast field echo (FFE), T1-weighted FLASH, T1-weighted spoiled gradient (SPGR) and fast imaging with steady-state precession (FISP). Quick switch among these tools can be achieved by making minor changes in the gradient spoiling and setting the radiofrequency (RF) phase between echo location and excitations. T2-weighted imaging is typically employed for tumour visualization with positive contrast [20]. Fully balanced steady-state free precession (bSSFP) sequences can provide fast repetition time and good blood-myocardium contrast, such as bright images of water-based fluid (e.g. blood and cerebrospinal fluid (CSF)) rather than void. Even though this sequence usually provides T2/T1 weighting. The undesired T1 contamination can be removed in the bSSFP images by adding unequally-spaced

180° pulses to balance the readout. The frame rate can be up to 10 frames/s with parallel imaging of standard Cartesian bSSFP. T1-weighted gradient-recalled imaging is usually adopted to guide endovascular catheterization with active tracking. Alternatively, small amounts of diluted contrast medium can be injected periodically through the catheter, to highlight its location without active positional tracking. **Fig. 2.2** depicts the system setup of this real-time intra-op MRI-guided interventions with robot assistance.

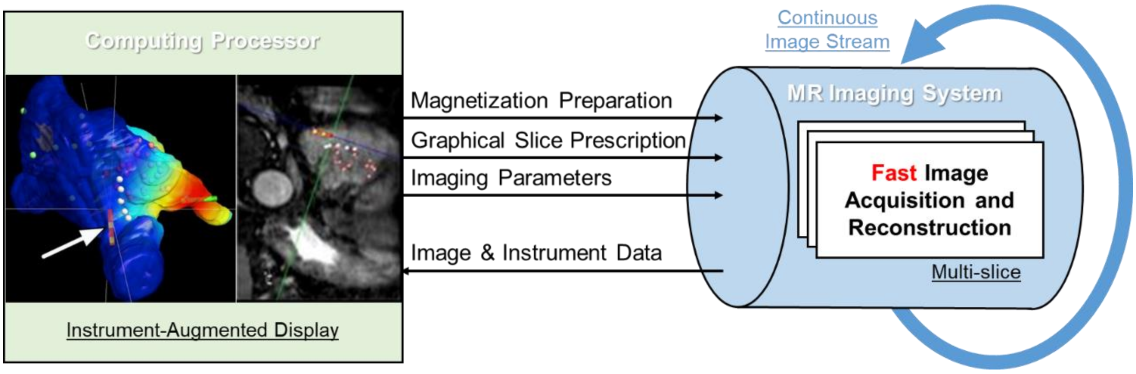

Fig. 2.3 Schematic diagram of dynamic MRI. Images are continuously acquired at high frame rate. Image and instrument data return to the computing processor for graphical display with low-latency. The successive scanning schemes adapt to the real-time instructions from the computing processor [21].

Throughout the MRI-guided interventional procedures, dynamic imaging control of frame rate, slice geometry and image contrast is usually carried out. The schematic diagram of dynamic imaging is shown in **Fig. 2.3**. Such interactive modification is beneficial to trade-off the image quality and frame rate as required during the procedures. By adaptively selecting the scanning planes, interventionists can precisely localize and track the surgical instruments. The tracked instruments may be displayed/augmented to the acquired images for online device navigation. Image contrast is typically controlled by an additional magnetization preparation module prior to each single shot image. This module can be toggled on or off interactively. For instance, saturation pulses can highlight T1 contrast of gadolinium-filled devices; flow-sensitive saturation pulses are used to generate bright-tissue/dark-blood images for enhanced anatomical context [21].

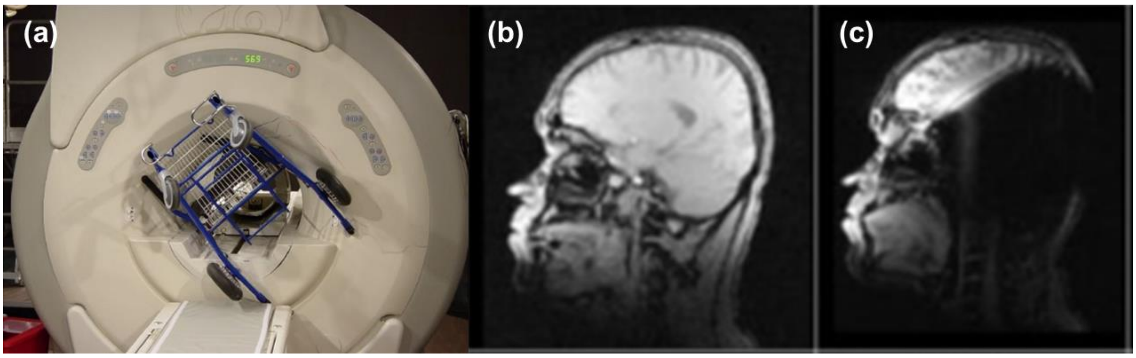

Fig. 2.4 **(a)** Safety hazards in the MR environment. The static magnetic field could strongly attract and rotate the objects that contain certain amount of ferromagnetic materials. Sagittal MR images in gradient-echo (GRE) sequence for patient **(b)** without and **(c)** with metal implant in brain [22]. Most area of the brain image is distorted, showing the large image artifacts caused by the metallic implant.
Image source: KOPP Development Inc.

2.2.3 MR Safety and Compatibility

MR environment may pose unique safety hazards for accessory devices and patients with metallic implants (**Fig. 2.4a**). Ferromagnetic materials are forbidden in the MR environments. Even objects made of materials with susceptibility differences from soft tissue may produce inhomogeneity of static magnetic field and cause severe image artifacts/distortion (**Fig. 2.4b**). Certain degree of image artefacts or distortion (e.g. several millimetres) is allowed in the diagnosis and has not much influence on the outcome. However, the discrepancies induced by this artefact/distortion can lead to mistargeting or undertreatment in MRI-guided interventions, e.g. tumor biopsy or laser ablation. Especially for the robot operating inside the magnet bore, it should maintain minimal EMI to the imaging. Referring to guidelines of the American Society for Testing and Materials (ASTM) F2503 and the International Electrotechnical Commission (IEC) 62570, any items used in or near the MR environment should be labelled (**Fig. 2.5**), i.e. MR safe, MR conditional and MR unsafe.

MR safe items are made of materials that are electrically non-conductive, non-metallic, and non-magnetic. It can be determined by scientific rationale rather than the test data. MR safe labelling has to match with the MRI system for static field strength, maximum spatial field gradient, dB/dt limitations (usually only applicable to active implants). Items intended to enter the magnet bore should be MR safe.

MR conditional items are those demonstrated safety in the MR environment under defined conditions. It may safely enter the MRI scanner room but only under very specific conditions provided in the labelling. These items should have minimal impact on static magnetic field, RF field, and switched gradient magnetic field.

MR unsafe items should not enter the MRI scanner room. Patients with MR unsafe devices should not be scanned.

Additional information, such as expected temperature rise and artefact extent inflation, should be clarified in advance for specific applications. For instance, heating effect should be strictly diminished for the devices that have direct contact with patients. For items not intended to enter the magnet bore, there is gauss-line positioning restriction or requirement to tether or affix the device to an unmovable part of the room.

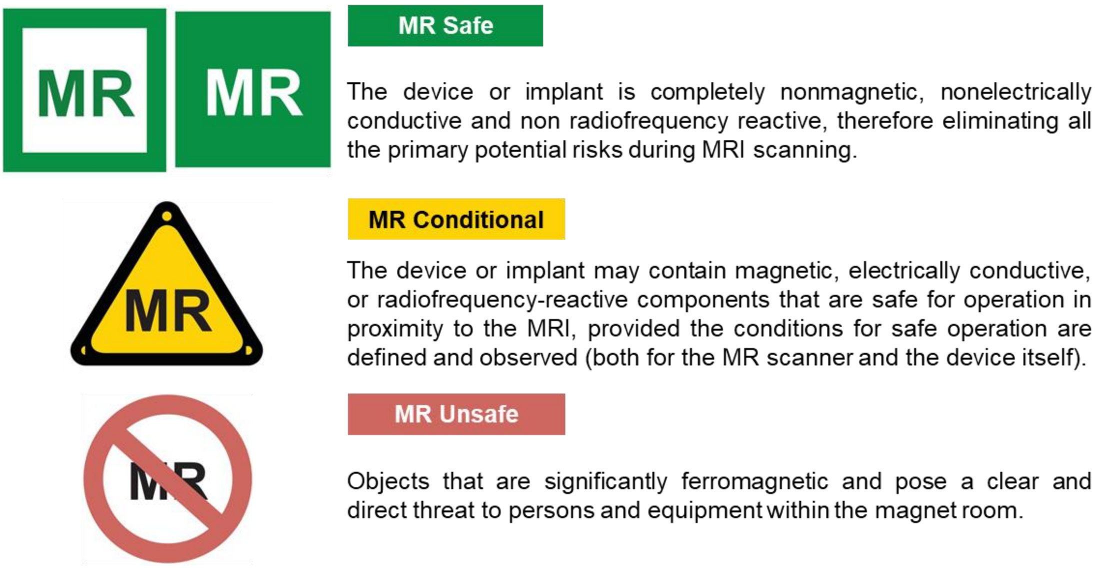

Fig. 2.5 MR labels defined by ASTM F2503 and IEC62570. Any implants, medical devices or other equipment used in or near the MR environment should be labeled. MR safe items can be placed anywhere inside the MRI room and pose no safety hazards.
Image source: ASTM F2503 – Practice for Marking Items for Safety.

The American College of Radiology (ACR) has defined four zones regarding the magnetic field exposure within MRI facilities. These four zones are denoted as Zone I through IV (**Fig. 2.6a**).

Zone I is a freely-accessible area for general public. It is the area for patients and healthcare personnel accessing the MR environment.

Zone II is an interface area between the uncontrolled *Zone I* and the strictly-controlled *Zones III/IV*. Patient actions in this area are usually supervised by MR personnel.

Zone III is usually called a controlled area. Access is strictly restricted. Entrances should all display the "restricted access" notices and be supervised by MR personnel.

Zone IV is the inner controlled area, which is typically the MRI room. This zone is always located inside *Zone III* and should be clearly marked due to the presence of strong magnetic fields.

The controlled area as mentioned above is in the general vicinity of the MRI system. It is defined as the areas where the static magnetic field exceeds 0.5 mT (5 Gauss). Within the 5-Gauss line, the MR environment is considered as the 3-D space volume surrounding the scanner (**Fig. 2.6b**) [23]. When the fringe magnetic field strength is lowered to 0.1 mT (1 Guass), magnetic-field-sensitive equipment can be placed in this area to ensure its performance, e.g. computer monitors, image amplifiers.

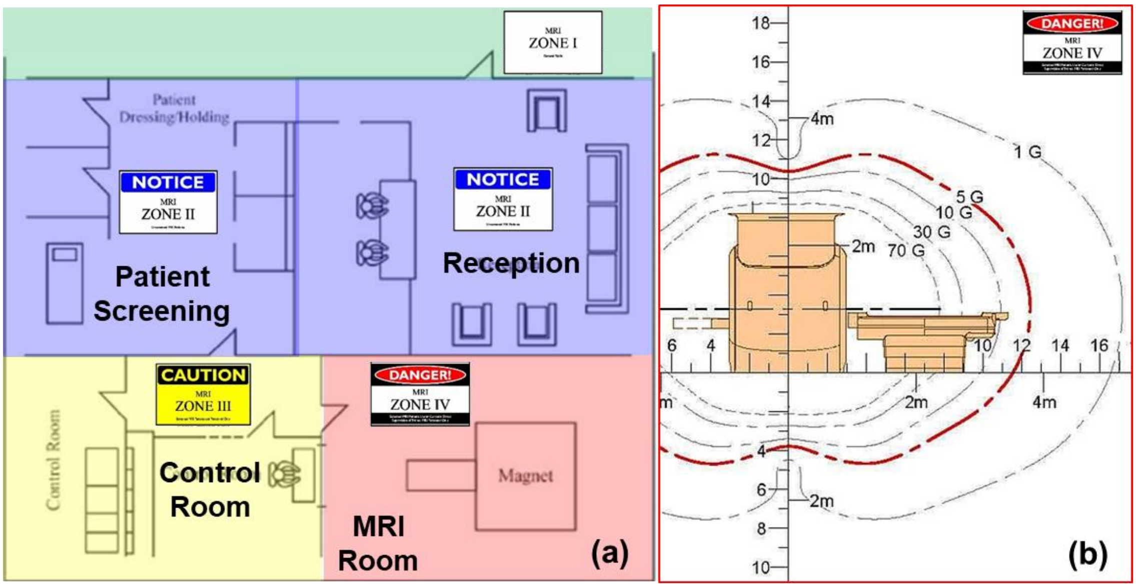

Fig. 2.6 **(a)** ACR Safety Zones within MRI facilities [24]. These zones are denoted as Zone I through IV. It corresponds to the levels of magnetic field exposure. **(b)** Strength of the static field. Within the 5−Gauss (0.5 mT) line area, unscreened personnel and ferromagnetic objects are strictly forbidden.
Image source: Magmedix Inc., National MRI-Shielding Company.

2.3 Clinical Motivation and Needs for MRI-guided Surgical Robotics

2.3.1 Neurosurgery

Stereotactic neurosurgery is a technique that can locate targets of interest within the brain using a 3D coordinate system [25]. Stereotactic approaches have been widely used in a variety of procedures, such as biopsy, injection, ablation, catheter placement, stereo electroencephalography (sEEG) and deep brain stimulation (DBS). The current workflow for stereotaxy comprises three primary stages: **i)** *Pre-op planning*, which requires imaging conducted before operation. CT and/or MRI (e.g. gadolinium-enhanced volumetric MR imaging) are the two common imaging modalities that can offer precise lesion localization. In targeting of deep brain structures for functional disorders diagnosis, MRI is advantageous to visualize tissue such as deep brain nuclei in high tissue resolution and special sequences, as well as functional imaging techniques. Together with its high sensitivity in detection of pathological/physiological changes, MRI is preferred in surgical planning; **ii)** *Immediate planning with frame*, which is a stage involving 3-D coordinate registration between the images and the stereotactic frame. Image-fusion technology is commonly adopted in this step, where CT imaging is usually fused with the pre-op MRI for surgical planning in a computer station; **iii)** *Intra-op refinement*, which includes setting up the platform for the coordinates and trajectories. Burr hole and dural puncture is made. Conventional stereotaxy for DBS includes microelectrode recording (MER) and macro-stimulation for physiological validation.

Despite the standard workflow has been established for about half a century (**Fig. 2.7**), the surgical manipulation still remains challenging, particularly due to the high demand for precision and minimum invasiveness. Imprecise positioning of instruments would result in deviated trajectory and targeting error, which would significantly increase the risk of hemorrhage. Registration at the planning stage may provide a one-time calibration for surgical roadmap based on the pre-op images. However, it cannot compensate for the changing conditions during surgery without continuously updating and tracking. Errors induced during registration come from various sources: **i)** differences in patient positioning during scanning (i.e. in supine) and surgery (i.e. in prone); **ii)** lead-time between scanning and surgery; **iii)** mechanical error of the frame; **iv)** number of sampling fiducial points for registration; and **v)** the intrinsic error in the image fusion step. During the procedure, brain deformation occurs in response to many factors of surgical manipulation and anesthesia procedures such as intracranial pressure changes, postural and gravitational forces, tissue removal, administration of pharmaceuticals and edema caused. Once dura is opened, such brain shift is inevitable, which will possibly cause the changes of both critical brain structures and target positions. Therefore, using only pre-op images as the roadmap seems to be the major disadvantage in the current workflow for stereotaxy.

Frameless stereotaxy uses landmarks or fiducial markers to replace the “frame” for registration between images and operation space. This technique relies on the references of fiducial markers or facial contours to provide real-time positional information of the imaged brain and surgical instruments. Its accuracy [26-29], diagnostic yield, morbidity rate and mortality rate [30] are comparable to those of frame-based approach. Reduced anesthetic time and fewer complications are also reported in frameless stereotactic neurosurgery [31].

Although the instrument navigation can be provided via frameless technique, further requirement on clearly visualizing and continuously updating the surgical progress still remains a challenge [32-34]. In this light, MRI possesses several advantages over other imaging modalities (such as ultrasound or CT): It is highly sensitive for intracranial pathology and is capable of visualizing soft tissue in high-contrast 3D images without ionizing radiation. For example in some cases of DBS, fluoroscopy/CT and MER are adopted frequently to confirm the acceptable placement of electrodes while assessing the corresponding symptoms with the awake patient under local anesthesia [35]. Provided with intra-op MRI guidance, DBS can be performed under general anesthesia and verified *in situ* with MR images [36]. The resultant imaging models in 3D enable the navigation system to offer real-time visualization of the actual tissue targets relative to the instrument. In particular, the incorporation of frameless technique in MRI guidance is an appealing method which could greatly simplify the procedure by performing general anesthesia, reducing the co-registration errors in different imaging modalities and monitoring the progress during surgical manipulation [37].

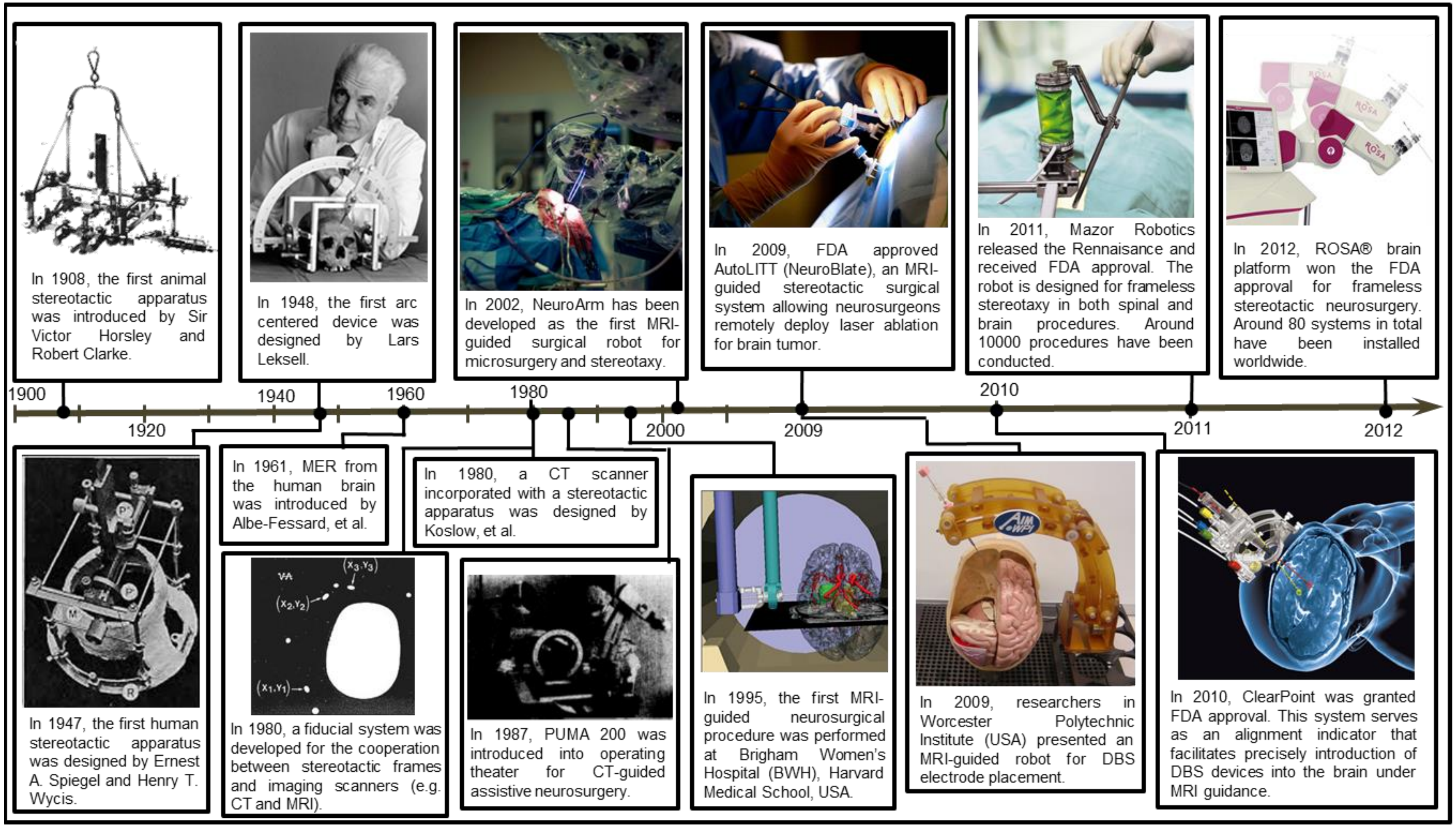

Fig. 2.7 Development milestones of image-guided devices for stereotactic neurosurgery [38-41].

Numbers of clinical trials have been conducted through the use of manually-operated MR-safe/conditional stereotactic platforms, e.g. NexFrame® (Medtronic, Inc., Ireland) and SmartFrame® (Clearpoint, MRI Interventions, Inc., USA) [42]. Clearpoint® system (as shown in **Fig 2.8a**) has been deployed in several therapeutic approaches, e.g. electrode placement [43], focal ablation [44] and direct drug delivery [45]. A clinical study [36] using frameless approach in DBS for 27 patients with movement disorders was reported. All of the procedures were performed with diagnostic MRI scanners (1.5T and 3T), while patients could be moved between isocenter and the bore edge. The aiming device (SmartFrame®) could be adjusted by surgeons remotely to the prescribed trajectory, when the patient was at the isocenter. A ceramic stylet was then inserted and oblique MR images were obtained along the trajectory. A second pass would be performed when the radial error was deemed unacceptable by the implanting surgeon. In this study, no case required more than 2 passes. The radial errors observed were 0.68 ± 0.42 mm (1.5T procedures) and 0.78 ± 0.38 mm (3T procedures). The procedure duration was counted between the initial skin incision and final skin closure. It was approximately 3.5-4 hours for bilateral procedures, 217.1 ± 33.3 min (1.5T procedures) and 247.6 ± 44.7 min (3T procedures).

However, these systems still require intensive manual operation and surgeons are reaching their physical limits of accuracy and coordination with regards of the narrow neurosurgical corridors. In addition, the procedures could be complicated and time-consuming. Patients or machines (e.g. intra-op MRI scanner) need to be transferred for each scanning to update the surgical progress, which greatly increases the operation time and disrupts the surgery rhythm. These challenges have directed the increasing attention to developing intra-op tele-operated manipulators and further translating robotic technologies into neurosurgery. Robots have superior capabilities over human in certain tasks, especially those which are limited by space, accuracy demanding, intensive and tedious. The clinical benefits have been shown in the recent surge of robot-assisted surgical interventions. These studies have implied the increasing demands on development of intra-op MRI-guided robotic platforms for stereotactic neurosurgery.

In the context of current neurosurgical challenges, the incorporation of real-time visualization and precise manipulation is imminent for brain shift compensation and workflow simplification. In this section, insights regarding the state-of-the-art MRI-guided neurosurgical robots will be provided, as well as three key enabling techniques with emphasis on their current status, limitations and future trends.

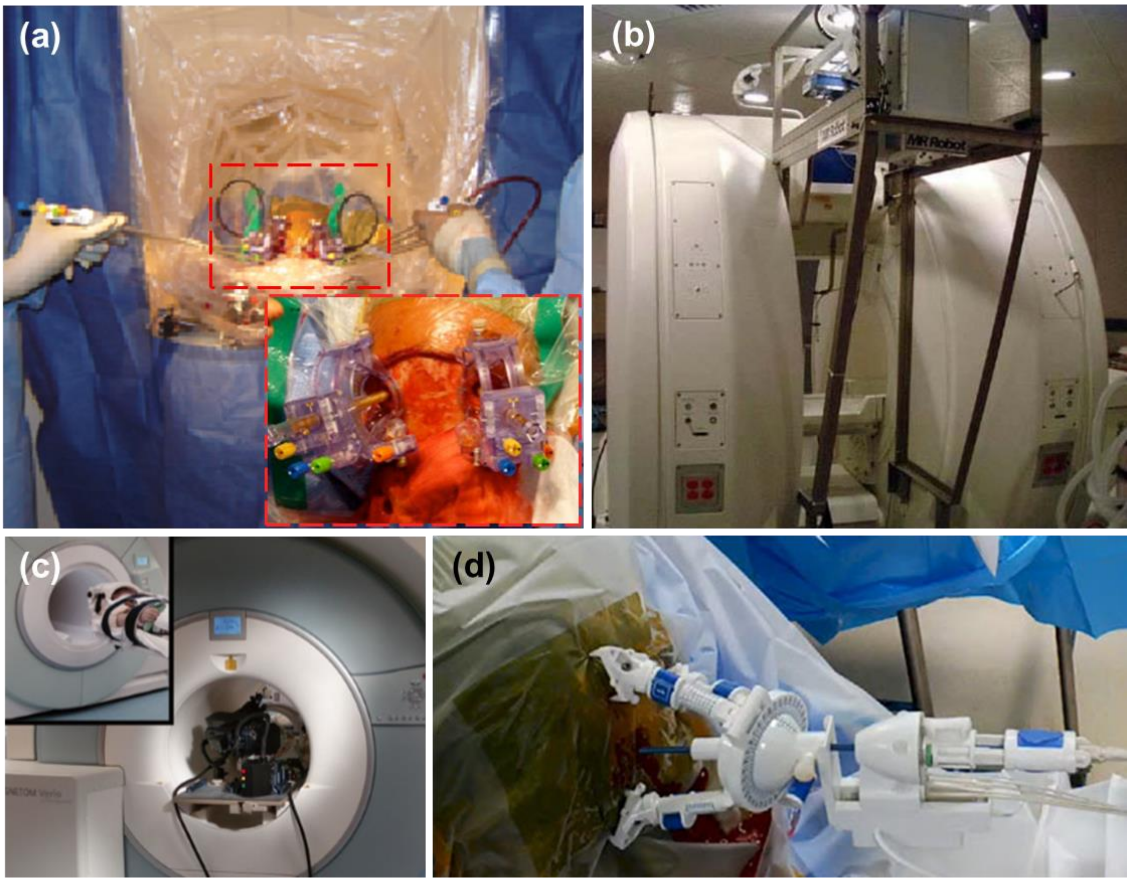

Fig. 2.8 Significant MRI-guided stereotactic platforms**. (a)** ClearPoint® system by MRI Interventions, Inc., USA. Two frames (SmartFrame®) are mounted to the skull bilaterally and manually aligned to the predefined trajectories; **(b)** MRI-compatible surgical assist robot by AIST-MITI, Japan and Brigham and Women's Hospital, Harvard Medical School, USA; **(c)** NeuroArm/SYMBIS® by Deerfield Imaging, USA; **(d)** NeuroBlate® system by Monteris Medical, Inc., USA.
Image Source: [37, 46-48]

The first MRI-compatible manipulator was built by Masamune *et al.* [49] towards stereotactic neurosurgical applications and tested *in vitro*. Chinzei *et al.* [46, 50] developed an MRI-compatible surgical assist robot (as shown in **Fig. 2.8b**) based on a low-field, open-bored, interventional MRI (iMRI) scanner (i.e. Signa SP 0.5T, GE Medical Systems, USA). It is the first one integrated with optically-linked frameless stereotactic tracking system [51]. However, surgeons have to operate inside the MRI room. The confinement of iMRI operation workspace may affect their performance, especially for those long and complicated procedures. Moreover, the use of open or large bore scanners often comes with the sacrifice of image quality. Any metallic components in robots may even further degrade the image quality. The cost of installation and maintenance of such suites is considerably high.

NeuroArm/SYMBIS® surgical system (Deerfield Imaging, USA) is an MRI-compatible robotic system for tele-operated microsurgery and stereotactic brain biopsy [52, 53] (as shown in **Fig. 2.8c**). It consists of two 7+1 degrees of freedom (DoFs) manipulators, and operates with the maximum workload of 0.5 kg, force output of 10N and the speed of end effector ranging from 0.5-5 mm/sec [54]. They are semi-actively controlled by a remote workstation, integrated with hand tremor filter and movement scaling. Image-guided neurosurgery, in general, is performed by the two manipulators outside the magnet bore. Different from the general neurosurgical procedures, stereotaxy will be conducted within the bore by a single MRI-compatible robotic arm. To ensure its MRI compatibility, this arm is fabricated from titanium, polyetheretherketone (PEEK), and polyoxymethylen [47]. The arm is directly attached to the magnet bore, in order to provide constant spatial relationship with the magnet's isocenter and therefore patient's pathology. It was reported that the NeuroArm system has been used in 56 patient cases, primarily for central nervous system neoplasia and cavernous angioma [52]. The surgical tasks included a combination of manipulation, coagulation, pick and place motions of cotton strips. To increase safety and operation performance, techniques namely virtual fixture, augmented force feedback and a haptic high-force warning system were adopted. A case study showed the total duration of robot-assisted glioma surgical operation, excluding craniotomy and wound closure, was about 33 min.

Monteris stereotactic platform, shown in **Fig. 2.8d**, is an MRI-based stereotactic surgical system designed to permit the neurosurgeon to remotely operate a 2-DoF robotic device and deploy laser to ablate the brain tumors. The NeuroBlate® laser probe is oriented by a separate stereotactic frame (AXiiiS stereotactic miniframe) that is compatible with and visible to the MRI machine. This frame consists of three linearly translating legs, a ball-socket and a 360-degree directional interface, which is disposable. The probe mates with a piezomotor-driven robotic driver, which remotely controls the translation and rotation of the laser ablation fiber. Surgeons can monitor the probe positioning and the ablation profile according to real-time MRI and thermometry data, ensuring safe boundaries from surrounding structures [55]. For multiple trajectories, a patient may be required to return the operation room for probe removal, frame relocation/realignment and possible new craniotomy. Clinical results of NeuroBlate® system were reported in a multicenter study [56]. It evaluated 24 glioblastoma and 10 anaplastic glioma patients who had undergone laser interstitial thermal therapy (LITT) with a primary focus on progression-free survival (PFS) using precise volumetric analysis. After 7.2 months of follow-up, 71% of cases demonstrated progression and 34% died. The median overall survival (OS) for the cohort was not reached;

however, the 1-year estimate of OS was 68.9%. The median PFS was 5.1 months.

A flexible continuum robot comprising three serially connected 2-DoF segments, named minimally-invasive neurosurgical intracranial robot (MINIR), was reported [57, 58]. The robot is remotely driven by actively-cooled shape memory alloy (SMA) springs via pulling tendons. An compressed-air cooling system for the SMA is incorporated to accelerate the heat dissipation (e.g. 6s taken for the heated spring to recover its original position from 5 mm elongation) and increase the actuation bandwidth. However, the robot is still at early development stage and research effort is continued to improve the SMA actuation performance [59]. Another research prototype developed by Fischer *et al.* [60, 61] was designed specifically for needle-based neural interventions inside the MRI bore. The system features with 7 DoFs driven by piezoelectric ultrasonic motors, in which a 2-DoF needle driver is implemented for rotating and inserting an interstitial ultrasound-based ablation probe. The robot mechanism is based on the functionality and kinematic structure of the conventional stereotactic frame (e.g. Leksell frame). It could reach targets with accuracy of 1.37±0.06 mm in tip position and 0.79°±0.41° in orientation. The SNR reduction in imaging reached 10.3% when the needle driver was running. Proper shielding of cables and DC-power lines of robot was remained for further improvements to ensure the imaging quality.

Table 2.1 Existing robotic systems for MRI-guided neurosurgery

Emerging Platforms	Degree-of-freedom	Number of end effector	Actuator *	Accuracy	HMI	Features	Key references
NeuroArm/SYMBIS® **(Deerfield Imaging, USA)**	7+1	2	E	sub-millimeter	√	- Tele-operated microsurgery and stereotaxy; - Only one manipulator can fit into the magnet bore; - Haptic feedback; - 3D image reconstruction for navigation; - Phase: FDA approved, commercial.	[47, 62, 63]
NeuroBlate® **(Monteris Medical, Inc., USA)**	2	1	E	1.57 ±0.21mm	√	- Laser ablation; - Patient under general anesthesia; - Continuous MR thermography acquisition; - Phase: FDA approved, commercial.	[56, 64]
Pneumatic MRI-compatible needle driver **(Vanderbilt University, USA)**	2	1	P	1.11mm	-	- Transforamenal ablation; - Pre-curved concentric tube; - 3T closed-bore MRI scanner; - Phase: clinical trial.	[17, 65]
MRI-guided surgical manipulator **(AIST-MITI, Japan & BWH, Harvard University, USA)**	5	1	E	0.17mm/ 0.17deg	-	- Navigation and axisymmetric tool placement; - 0.5T open MRI scanner; - Pointing device only; - Phase: *in vivo* test with a swine brain.	[50, 66]

MR safe bilateral stereotactic robot (The University of Hong Kong, Hong Kong)	**8**	**2**	**H**	**1.73 ±0.75mm**	**√**	- **Bilateral stereotactic neurosurgery;** - **Skull-mounted;** - **MR safe/induce minimal imaging interference;** - **SNR reduction ≤ 2.5%;** - **Phase: preclinical trial**	[67]
MRI-compatible stereotactic neurosurgery robot (Worcester Polytechnic Institute, USA)	7	1	E	1.37 ±0.06mm	-	- Needle-based neural interventions; - Mounted at the MRI table; - SNR reduction in imaging less than 10.3%; - Phase: research prototype.	[60, 61]
Mesoscale neurosurgery robot (Georgia Institute of Technology, USA)	†	1	‡	About 1mm	-	- Tumor resection, intracerebral hemorrhage evacuation; - Skull-mounted; - Phase: research prototype.	[57-59]
Multi-imager compatible needle-guide robot (Johns Hopkins University, USA)	3	1	P	1.55 ±0.81mm	-	- General needle-based interventions; - Table-mounted; - Intraoperative MRI scanner (iMRIS); - Phase: research prototype.	[68]
MRI-compatible needle insertion manipulator (University of Tokyo, Japan)	6	1	E	3.0mm	-	- Needle placement; - 0.5T MRI scanner; - Phase: research prototype.	[49, 69]
Endoscope manipulator (AIST, Japan)	4	1	E	About 0.12mm/ 0.04deg	-	- Endoscope manipulation for transnasal neurosurgery; - Vertical field open MRI; - Large imaging noise caused by ultrasonic motors; - Phase: research prototype.	[70]
Tele-robotic system for MRI-guided neurosurgery (California State University, USA & University of Toronto, Canda)	7	1	P/H	-	√	- Brain biopsy; - 1.5T MRI scanner; - Mounted at the surgical table; - Phase: research prototype.	[71]

Open-MRI compatible robot (Beihang University, China)	**5**	**1**	**E**	**-**	**-**	**- Biopsy and brachytherapy; - 0.3T intraoperative MRI scanner; - Phase: research prototype.**	[72]

HMI, Human Machine Interface; FDA, Food and Drug Administration.
***. Actuator: E – Non-magnetic electric actuator, such as piezoelectric motor or ultrasonic motor, P – Pneumatic actuator, H – Hydraulic actuator.**
†. A flexible continuum robot, of which the degrees of freedom depend on the number of segments.
‡. Shape memory alloy spring-based actuators remotely driving the manipulator via pulling tendons.

2.3.2 Intra-cardiovascular Interventions

(a) **(b)**

Fig. 2.9 **(a)** Sensei® X Robotic System, and **(b)** Amigo Remote Catheter System guided by pre-op images. **Image source: Hansen Medical, Catheter Precision Inc.**

More than 2.6 million people experience heart rhythm disorders (arrhythmia) in the US alone each year. Certain types of arrhythmia, such as ventricular tachycardia (VT), can cause sudden cardiac death, which kills more than half a million people a year in the US. These numbers are increasing as the population ages. At least 80% of these deaths could be avoided through better diagnosis and treatment. Cardiovascular EP is an effective surgical treatment that is attracting increased interest. In EP procedures, electrophysiologists insert a 1.5-m long catheter from the femoral vein to the heart chamber where RFA is conducted via the catheter tip on the lesion tissue to isolate the abnormal electrophysiological signals that cause arrhythmias.

There are two key procedures repeated in EP when the catheter has been inserted into heart chamber: **i)** *Electro-anatomical mapping* (EAM) – electrode at the catheter tip will be maneuvered in contact with the atrial/ventricle tissue. Numerous catheter-tissue contact points, combined with the measured electrical signals and tracked location of the tip, are collected at different phases of cardiac cycle. However, the contact points form an electro-anatomic (EA) map which would not be anatomically correct and consistent with the cardiac roadmap obtained by the pre-op imaging. **ii)** *RFA* – electrode at the catheter tip will transfer the RF energy to destroy various small areas of tissue which are supposed to be the origins of arrhythmia as indicated on the EA map. In conventional EP, fluoroscopy and ultrasound are adopted to visualize the catheter configuration inside the heart chamber. The progress of RFA can only be roughly estimated on the basis of the catheter-tissue contact force, intra-cardiac surface electrocardiograms (ECGs), ablation temperature and impedance decay at the catheter tip [73].

Even with catheter navigation via a cardiac EP roadmap, manipulating the catheter to the desired location remains challenging. The control of a thin (Ø2.67mm), long (1.5-m), flexible EP catheter can be extremely inconsistent, especially within rapidly deforming cardiovascular tissue, such as the left ventricle (LV) and left atrium (LA). The challenges have drawn attention to the development of tele-operated robotic platforms, such as a well-known commercial platform – Sensei® Robotic System [74] (**Fig. 2.9a**), that improves the dexterity and accuracy of catheter manipulation for intra-cardiac EP intervention. However, the catheter navigation can still be complicated by the lack of real-time and continuous updates of patient-specific cardiac EP roadmaps. The electrophysiologists may not feel sufficiently confident to perform effective RFA, due to the possibly large misalignment (>5mm) of the actual position of catheter tip with respect to the roadmap or EA map. This poses significant disadvantages in using the industry-leading EP robots (**Fig. 2.9**), including Hansen Sensei™ X [74], Amigo Remote Catheter System [75], as well as Stereotaxis Niobe® [76] even with highly-steerable catheter tip driven by magnetic force. Furthermore, either insufficient RFA of the lesion or inaccurate verification of electrical-circuit isolation [77] can cause edema instead of necrosis, increasing the chances of arrhythmia recurrence. In contrast, excessive heating of tissue would also cause "steam pops", increasing the risk of wall perforation by catheter.

MRI offers excellent images contrast for cardiovascular soft tissue, forming a cardiac roadmap [78, 79] in 3D. Late gadolinium enhancement T2-weighted cardiac MRI [80, 81] can also readily visualize the scar tissue [82] and edema [81] arising from successful or incomplete RFA. Intra-op visualization of RFA-induced physiological changes is already made possible by MRI, thus allowing the electrophysiologist to promptly determine whether the treatment of particular lesion is complete or requires further ablation. Many research groups (e.g. [83-86]) have already conducted numerous patient trials and demonstrated the significant clinical value with the use of intra-op MRI for EP in clinical routine.

However, development of the MRI-guided robotic EP system is still in its infant stage. Even with the MRI-based real-time tracking techniques [80, 87, 88] that can localize the catheter tip relative to the MR image/roadmap coordinates, the ablated lesions on intra-op MR images are still not necessary well-aligned with the roadmap. Rigid image co-registration [89] between the pre- and intra-op images would help compensate the 6D-offset due to patient positioning and motion, but rapid morphological changes of LA and LV that occur prior to, during or after ablation, is also the major factor causing the misalignment. *Non-rigid* 3D image registrations [90, 91] are used in the conventional EP, but mostly applied only once after the EAM for improved integration between the EA map and the pre-op roadmap. The significant clinical benefit of using *non-rigid* registration has been demonstrated [92-94]. None of the existing MRI-guided EP can be used for frequently and rapidly updating the roadmap based on intra-op T2/real-time MR images. Processing of such *non-rigid* registrations is normally computationally intensive. Long computation time (>5 s) will make such applications clinically impractical. Currently, there is no commercial robotic catheterization platform is MR-safe/conditional.

2.3.3 Head and Neck Surgery

Transoral surgery is an approach to treat the head and neck cancers (HNCs) on nasopharynx, oropharynx, larynx and hypopharynx through the intra-oral cavity. HNCs originated from squamous cell affect ~550,000 people worldwide and is the 5th most common cancer worldwide. Currently in Hong Kong, as of 2013, nasopharyngeal carcinoma (NPC) alone is the 10th most common cancer, and the 6th most common in males with the absolute numbers continuing to increase. Transoral surgery is the least toxic treatment modality toward HNCs compared to radiotherapy and chemotherapy. But this open approach is usually associated with significant morbidity. To limit the surgical trauma and long-term injury, minimally invasive robotic approaches may offer the possibility to preserve the functionalities of critical structures, such as speech, swallowing and facial cosmesis.

Surgical robotic platforms, da Vinci robot (Intuitive Surgical Inc.) and Flex® Robotic System (Medrobotics) (**Fig. 2.10**), are currently FDA approved for transoral surgical resection of T1/2 oropharyngeal lesions. However, maneuvering instruments in confined space, such as oral and nasopharyngeal (ONP) cavities, closed to the critical neurovascular and muscle structures remains very demanding tasks. This poses great needs for more precise and less invasive approaches to dissect the carcinoma with an adequate margin away from the critical structures through the oral access. Current minimally invasive approaches to HNCs mostly lack the ability to adequately plan for the surgery in 3D. It heavily relies on the surgeons' experience while ablating/dissecting the tumors, particularly their deep aspect that are not readily visible. This situation still lags far behind the clinical requirements for effectively monitoring the change of tissue morphology in 3D.

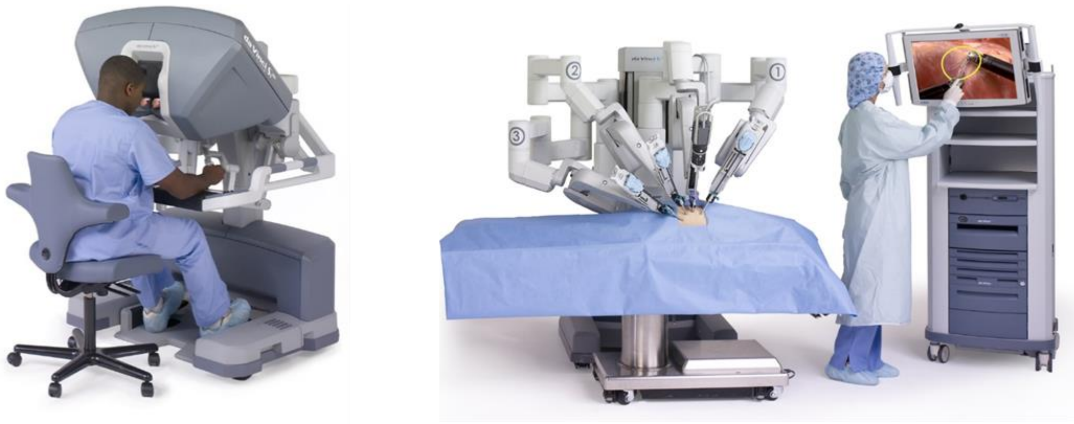

(a)

(b) **(c)**

Fig. 2.10 Significant systems for transoral robotic surgery (TORS) or TLM: **(a)** Da Vinci Si System, **(b)** Flex® Robotic System and **(c)** AcuPulse® CO_2 Flex Fiber System. Currently, there is no robotic systems in the market for MRI-guided transoral microsurgery.
Image source: Intuitive Surgical Inc., Medrobotics Inc., Lumenis, Inc.

With the recent advancements of MRI, intra-op 3D visualization of the HNCs, as well as the laser-induced physiological changes, can be made possible by T2-weighed/diffusion-tensor MRI. Thus the surgeons are allowed to promptly determine whether the tumor resection is complete or conducted safely from the critical structure; however, development of the MRI-guided laser resection interface is still in its infant stages. Currently, there is no well-established robotic interface capable of continuously controlling the laser beam projection on lesion regions based on intra-op MRI data, despite the advances of optics technologies which enable to endoscopically introduce high-intensity (e.g. thulium) laser through an optic fiber. It couples with an increasing demand on development of an MR safe/conditional robot platform which could provide precise, effective and reliable laser navigation in confined ONP cavities. This robotic navigation needs to involve MR-compatible actuation dedicated for dexterous manipulation, as well as its close-loop control realized by real-time MR thermometry data.

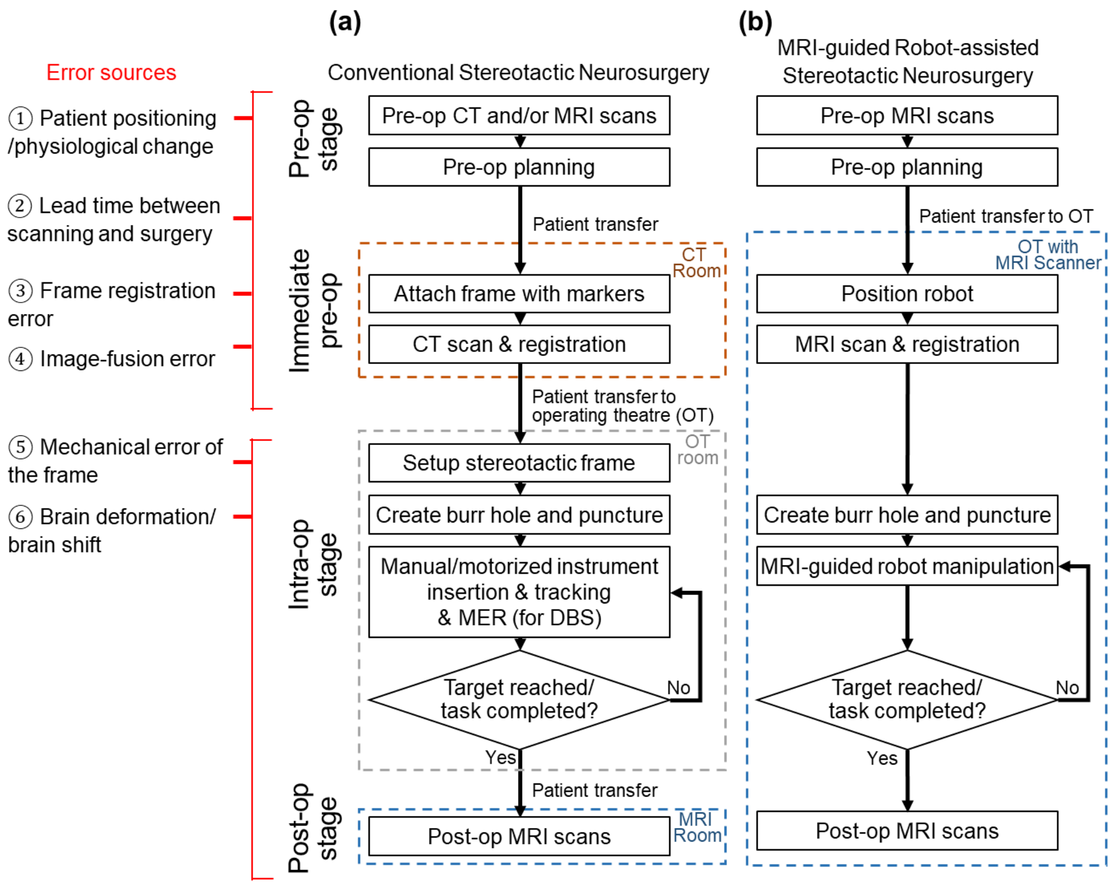

Fig. 2.11 Surgical workflow of **(a)** conventional stereotactic neurosurgery. Error sources of the conventional procedures have been listed at the left; **(b)** MRI-guided and robot-assisted stereotactic neurosurgery. In this procedure, errors can be eliminated through the use of real-time MRI and closed-loop controlled robotic manipulation.

2.4 Current Trends and Perspectives of MRI-guided Robotics

Despite the emergence of many MRI-guided robotic systems (as listed in **Table 2.1**), only a few are in widespread clinical use. The common technical challenges in conjunction with the use of robotics in MRI include the confined workspace inside scanner bore, MRI compatibility of the robot, real-time imaging with sufficient quality for targets/instruments localization and navigation. Most of previous works only address part of these challenges and still lack of effectiveness, in which the longer procedure time (e.g. transferring patient in-and-out frequently) probably lead to the higher cost. The surgical costs for patient could also involve MRI scans, the use of robot/MRI-compatible instruments and the extra manpower for robot operation [31]. This high cost may be the vital factor that restricts the wide application of robotics technology in healthcare [95]. In this section, three key enabling technologies, *non-rigid* image registration, MR-based tracking and MR safe actuation, are proposed for high-performance intra-op MRI-guided robotic platforms. A detailed review is provided with emphasis on their current status, limitations and future trends. A robotic system integrating with these technologies may greatly simplify the workflow (e.g. stereotactic neurosurgery as shown in **Fig. 2.11**), increase accuracy and potentially reduce the clinical expenditure.

2.4.1 Non-rigid Image Registration

Image registration enables precise localization of the preoperatively segmented critical/target regions on the rapidly acquired intra-op image in order to establish/update the surgical planning accordingly. To date, many commercial navigation systems only employ *rigid* registration to realign the both sets of images. However, it cannot compensate for any image discrepancy resulting from the actual brain deformation and the MR image distortion. For example, it cannot tackle the severe misalignment (~10-30 mm [96]) caused by brain shift after craniotomy (**Fig. 2.12**). This large-scale brain deformation inevitably makes the surgical plan inconsistent to the actual anatomy during the procedure. *Non-rigid* image registration has been proposed to mitigate such misalignment. In particular, the biomechanical finite-element-based registration schemes are specifically developed to estimate and predict the extension of any brain shift of different regions. The relative stiffness model of intracranial structures has to be constructed so as to deduce deformation caused by gravity [97-99].

Apart from non-linear image discrepancy due to the tissue deformation, spatial distortion of MR images would also hamper the accuracy in MR-guided stereotactic surgery [100]. The cause of MR distortion is multiform and incalculable. Let alone base (static) field inhomogeneity, chemical shift and susceptibility artifacts, the nonlinearity of the B1 gradient field contributes most to such distortion. It has been reported that the spatial distortion can be as much as 25mm at the perimeter of an uncorrected 1.5T MR image; the error would still remain within the 1% range (typically ~4mm) even after correction of using standard gradient calibration (e.g. grid phantoms) [101, 102]. This error is significant in regards of the supreme accuracy requirement in robotic MIS. Worse still, the distortion may even aggravate under higher magnetic field inhomogeneity that presents in 3T MRI scanners [100]. The combined effect of these variables often results in very complex and nondeterministic image distortion, particularly affecting the images obtained by advanced excitation sequences. For example, the echo-planar imaging (EPI) sequence used in the acquisition of diffusion-weighted images (DTI) is vulnerable to susceptibility-induced distortions, resulting in heavy distortion at the tissue margins where the magnetic susceptibility is rapidly changing in 3D space (**Fig. 2.12**) [103].

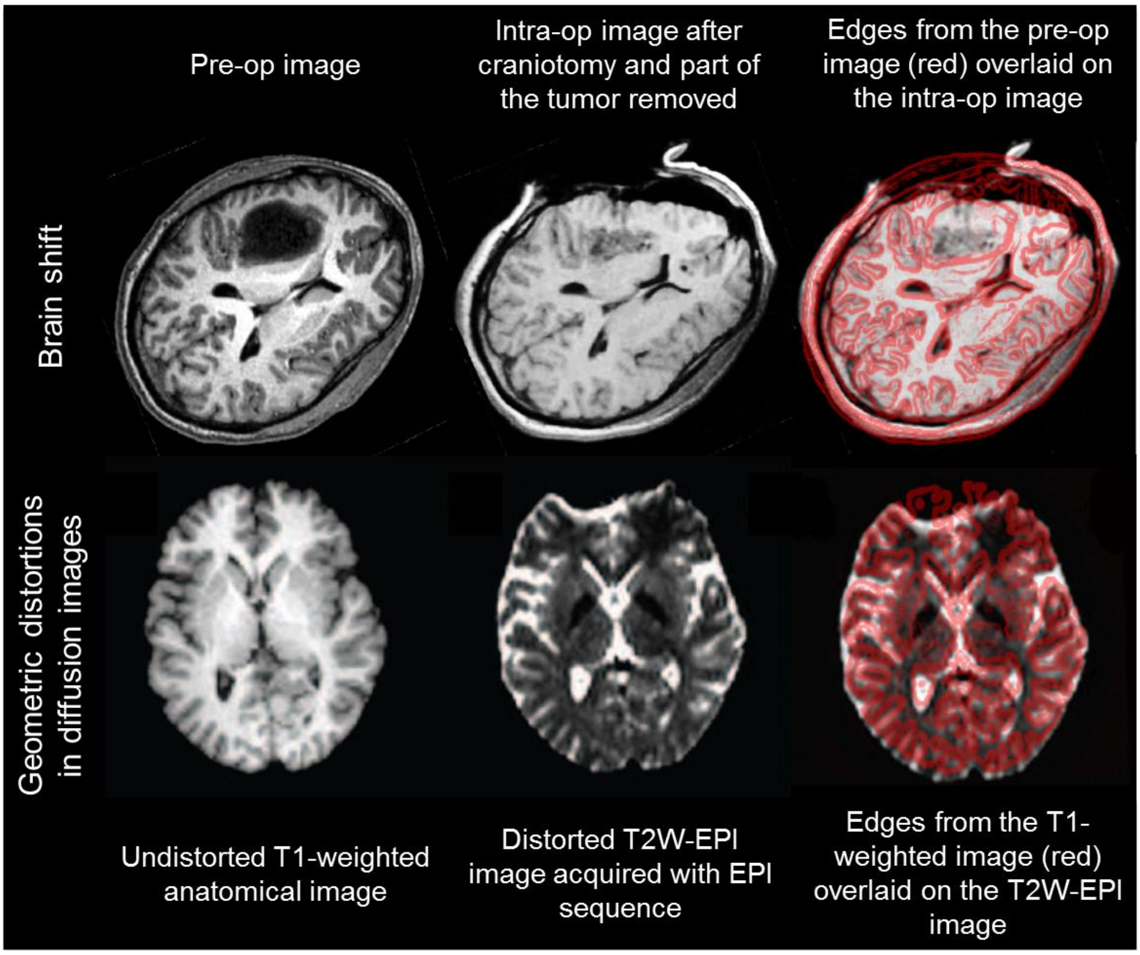

Fig. 2.12 **Upper row:** brain deformation before and after the craniotomy; **Lower row:** geometric distortion in diffusion images. Large discrepancy between pre-op and intra-op images are observed in the overlaid image at the last column.
Image source: [97, 104]

Considering such gradient field nonlinearity, gradient-based excitation sequences were set back despite its widespread usefulness. *Non-rigid* registration schemes can correct the distortion in gradient-based image while retaining any useful anatomical information. This can be achieved by registering the distorted image to a standard MR image obtained at the same imaging instance, e.g. T2-Turbo Spin Echo (TSE) images that exhibits little image distortions. As a result, the image correspondence in 3D obtained by *non-rigid* registration can reliably restore the misalignment caused by image distortion. Recent research demonstrated significant (>10%) accuracy improvement has been archived by resolving such misalignment [105]. However, complex computation involved in *non-rigid* registration schemes impedes its efficacy to be used in the intra-op scenarios. This motivates the development of high-performance image registration schemes using scalable computation architectures such as graphical processing units (GPU), field-programmable gate arrays (FPGA), or computational clusters. Recent works [106-108] have demonstrated substantial computation speed-up, in which the registration process can be accomplished within seconds, even with a large image dataset in 3D (~27M voxels) being used.

2.4.2 MR-based 3D Positional Tracking

Real-time tracking enables *in situ* positional feedback of surgical instruments inside the MRI scanner bore. Not only does it act as the feedback data to close the control loop of robot, but it also allows the operator to visualize the instrument position/configuration w.r.t. the brain roadmap. Sufficient number of tracked markers are required to pinpoint the instrument in the image coordinates [109]. However, real-time positional tracking of instrument inside the MRI scanner is challenging for several reasons: **1)** conventional instruments can either be invisible or create serious susceptibility artifacts on MR images; **2)** restricted space of the scanner bore, or complicated EM-shielding limit the use of external tracking devices in MRI room, e.g. stereo-optical cameras; **3)** and image reconstruction is time-consuming (e.g. 9.440 seconds required for acquisition of a slice of T2-weighted MR image with field of volume (FOV) of 220×220 mm [110]). When only a few numbers of 2D images can be obtained; it is hard to localize multiple marker points on image domain in relatively large 3D space.

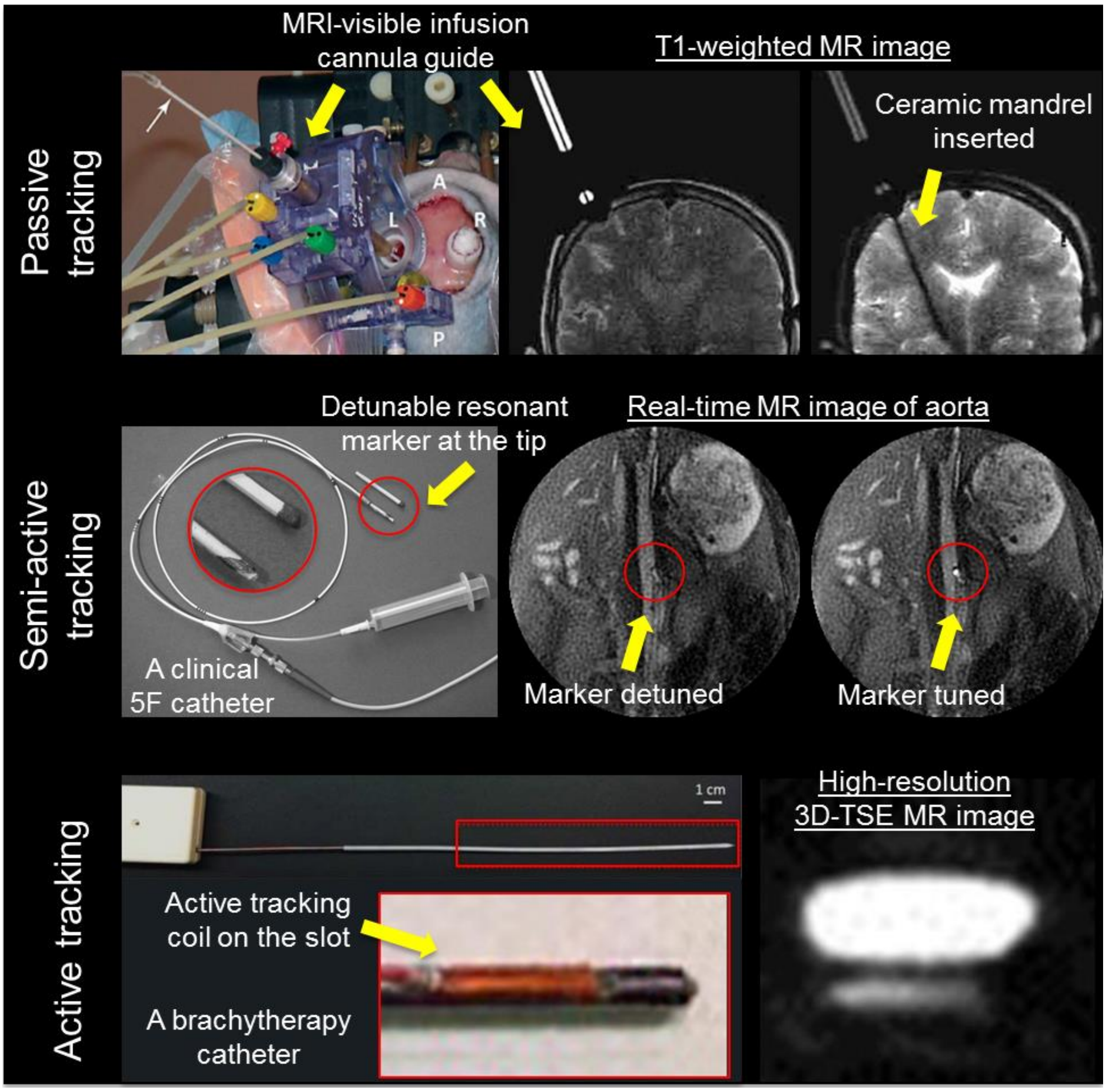

Fig. 2.13 Upper row: MRI-visible (gadolinium-impregnated) cannula guide aligned to the planned trajectory by a skull-mounted aiming device (SmartFrame®, ClearPoint system). MR images show the cannula at the completion of alignment, and a ceramic mandrel inserted subsequently [111, 112]; **Middle row:** Semi-active marker embedded at the tip of a 5F catheter, which is a resonant circuit controlled by optical fiber. Real-time MR images are acquired with a radial steady-state free-precession sequence. The MR images show the semi-active marker produces no signal enhancement in the detuned state and an intense signal spot in the tuned state [113]; **Lower row:** Brachytherapy catheter mounted with several active markers along the metallic stylet. The high-resolution MR image is acquired with a 3D TSE sequence (resolution: 0.6×0.6×0.6 mm^3) [114].

Passive tracking (**Fig. 2.13, upper row**) is the most commonly-used method, in which passive markers are incorporated with the surgical instruments and directly visible in MR images by changing the contrast. No additional hardware is necessary. The markers are either filled with paramagnetic agents (e.g. gadolinium compounds) that can produce positive MR image contrast, or diamagnetic materials (e.g. ceramic) that generates negative contrast. The shape of these markers can be customized into spheres, tubes or other desired structures for the ease of recognition on the images. Passive tracking is simple and safe, that can be performed under various MR field strengths without inducing any heat. However, passive markers may be invalid when the markers are in close proximity, or out of the imaging slice [115]. Thus, the configuration of marker system needs to be specially designed for readily identification [116]. In addition, the localization of passive markers is challenging to be performed automatically and also in real-time. Their visualization relies on 2D image reconstruction, which is time-consuming and may not be reliable because the MR images can be intrinsically distorted [117]. Image-based algorithms are required to post-process the images and localize the markers, which are sensitive to the marker intensity.

To resolve the problems in passive tracking, much research attention has recently drawn to the development of MR-based active tracking techniques (**Fig. 2.13, middle and lower row**). Active marker is a small coil serving as antennas individually connected with the MRI scanner receivers, and actively respond to the MR gradient field along three principal directions. Without the need for image reconstruction, the markers can be rapidly localized using 1D projection technique [118]. This localization is automatic, since the marker can be independently identified through its own receiving channel [119, 120]. The obtained coordinates may then be immediately used for adjustment or selection of further scanning plane [121]. Specific MR sequences are designed to incorporate and interleave both tracking and imaging. Delicate heat control is in need because of the resonating RF waves and storage of electrical energy caused by the conductive structure [122]. Therefore, semi-active tracking system is also preferable, in which there is no electrical wire connected between the coil marker and the MRI machine. It avoids the potential problem of heat generated by the wires. This marker unit acts as an RF receiver to pick up the MR gradient signal, as well as an inductor to resonate with the signal transmitted to the MRI scanner receiver [123]. Thus, resonance frequency of this coil marker needs fine tuning to adapt with the scanners of different field strengths (i.e. 63.8MHz and 123.5MHz, respectively, for 1.5T and 3T MRI scanners), while 1.5T is more popular for the current common practice and 3T can provide images with lower noise and less acquisition time. Without its individual receiving channel in MRI, the identification among multiple semi-active trackers may require specific algorithm or extra control components. An optical unit may be incorporated to resolve this challenge by controlling the resonant circuit and switching on/off the signal of a single tracking coil [113] (**Fig. 2.13, Middle row**).

It is foreseen that such MR-based tracking coils could be implemented to realize real-time instrument tracking. Promising results have been reported in an MR-active tracking system for intra-op MRI-guided brachytherapy. Three active micro-coil markers (1.5×8mm^2, **Fig. 2.13**) are mounted on a brachytherapy stylet (with diameter of Ø1.6mm) [124]. Both the tracking and imaging are in the same coordinate system, the stylet configuration can be virtually augmented on the MR images *in situ*. High-resolution (0.6×0.6×0.6 mm^3) stylet localization at high sampling rate of 40Hz, with low-latency <1.5ms, could be achieved.

2.4.3 MRI-compatible Actuation

Actuator as one of the key components in a surgical robot, its performance determines the surgery safety and accuracy. These two factors are particularly demanding for instrument manipulation, which generally involves precise coordination of 3 DoFs at least. Conventional high-performance actuators mostly consist of magnets and are driven by electromagnetic (EM) power. However, the use of ferromagnetic materials is forbidden under the strong magnetic field. This poses a strong incentive to develop motors that are safe and compatible with MRI environment.

Piezoelectric/ultrasonic motors actuated by high-frequency electric current have been extensively applied for interventional MRI applications [125-127]. Such motors are usually small in size (e.g. 40.5×25.7×12.7 mm^3, Nanomotion® motor as shown in **Fig 2.14**), and can provide fine movement at the nanoscale. However, the motion range and speed of these motors are generally insufficient for some long-stroke DoFs (e.g. inserting ablation catheter for tumors located in the deep brain area) without additional transmission mechanisms. EMI is inevitably induced by the high-frequency electrical signal. Tailor-made EM-shielding of the motor and its electronic drivers usually degrades the motor compactness [126, 128]. Nevertheless, the image quality will be more or less deteriorated by the presence of electric current while the motors operate inside the scanner bore during the image acquisition, thus affecting the visualization of small targets (e.g. DBS targets with diameter of approximately 4-12 mm).

In this light, intrinsically MR safe motors driven by other energy sources, e.g. pressurized air/water flow, are preferable. Minimal EMI is generated by this fluid-driven actuation [129-132]. **Fig. 2.15** shows a general setup of a pneumatically-actuated MRI robot. Long transmission air pipes connect the robot with its control box, which are placed in MRI/control rooms respectively.

Pressurized air at 0.2-0.4 MPa can be supplied from the medical air system which is commonly available in hospital rooms. This air in robot may not be tightly-sealed and allowed to exhaust into the atmosphere, which will generate unfavorable noises and vibration in the operating room. The compressibility of air results in limited torque/force output and low-stiffness transmission, making the positional accuracy hard to reach millimeter level and satisfy the clinical requirement [133].

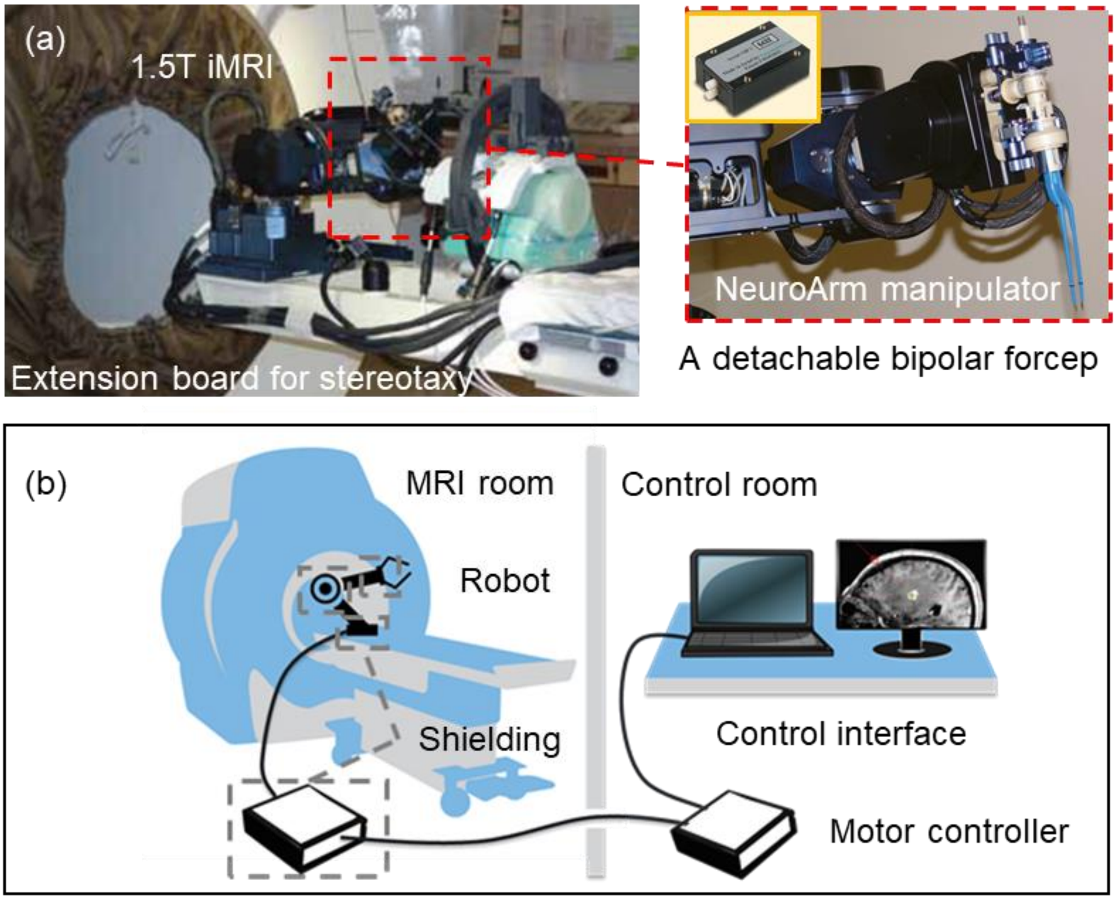

Fig. 2.14 **(a)** NeuroArm manipulator (in red frame) mounted onto an extension board for stereotaxy. It is driven by ultrasonic piezoelectric motors (Nanomotion, Yokneam, Israel) (in yellow frame). **(b)** Conceptual setup diagram of ultrasonic-motor integrated robot. A controller box placed inside the MRI room must be carefully shielded to ensure safety and minimal interference to the imaging.
Image source: [134, 135]

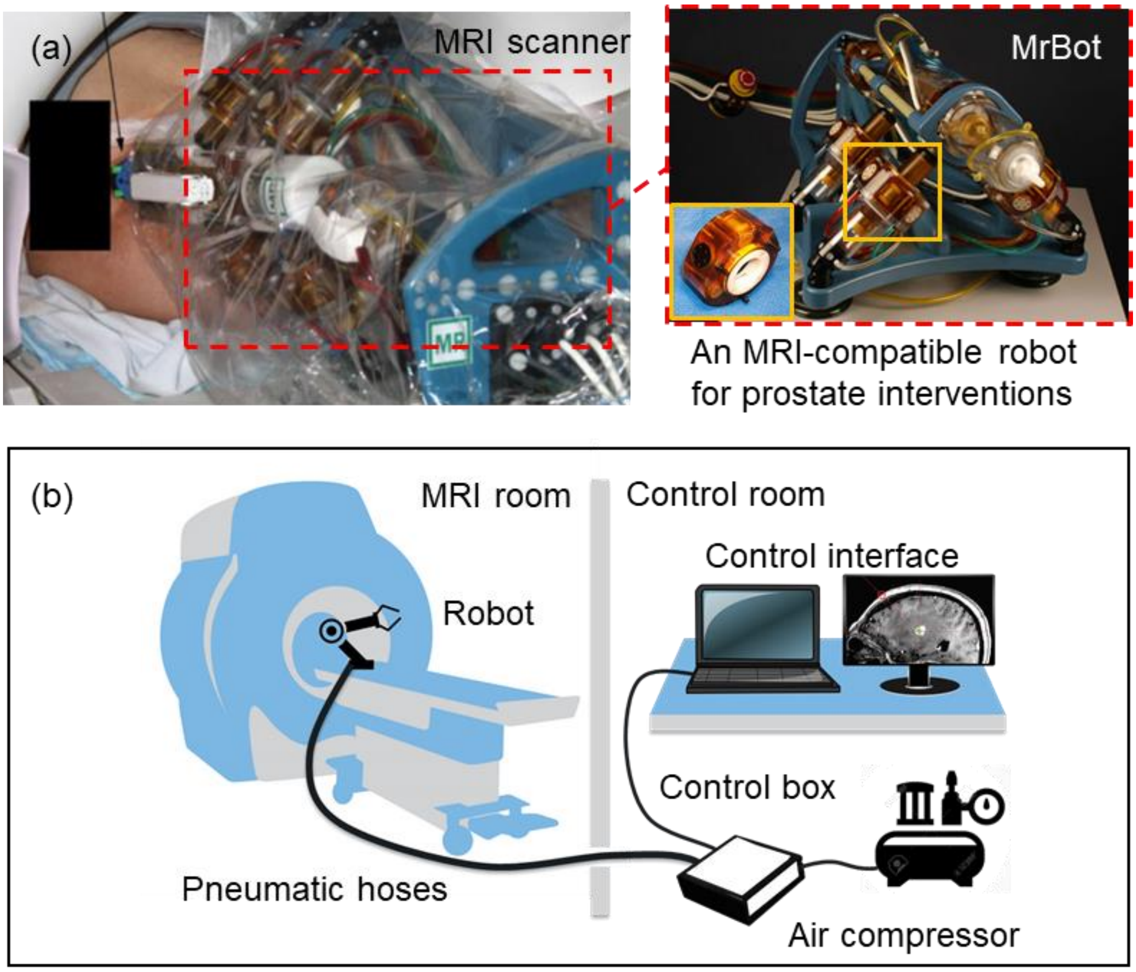

Fig. 2.15 **(a)** MRI-compatible prostate robot (in red frame) driven by pneumatic stepper motors (in yellow frame). **(b)** Conceptual setup diagram of pneumatic-motor integrated prostate robot. The controller box can be placed outside the MRI room and connected with the motor by hoses.
Image source: [136, 137]

In contrast, incompressible liquid (e.g. water, oil) in hydraulic motors offers relatively accurate, responsive and steady mechanical transmission. They can typically render large output power. Master-slave design is usually adopted in hydraulic systems. The master unit is placed in the control room, which is driven by electric motors; the slave unit works near or inside the MRI scanner bore, which is made of MR-safe/conditional materials. Power is transmitted from the master unit via long hydraulic tubes. Discreet sealing may be the main concern of such actuation as to prevent liquid leakage for all the connectors in hydraulic system. This can pose difficulties in setting up the robot, e.g. in disconnecting/reconnecting the hydraulic tubes through the waveguide (with diameter of ~Ø100mm) in between the MRI room and control room. Referring to Clearpoint® system, four semi-rigid shafts are used to connect the trajectory guide and control knobs, permitting the surgeons to manipulate the aiming device without reaching to the bore (as shown in **Fig 2.8a**) [37]. Remote manipulation with submillimeter accuracy has been demonstrated in this manual system. The result indicates the promising incorporation of this method in a remotely-actuated robot system, by connecting the motors with the manipulator's joints through the flexible driving shaft. This method can enable the use of high-power hydraulic motors without adding extra weight/dimension to the manipulators.

2.5 Conclusions

In this chapter, I have introduced the basic concepts of iMRI systems, pulse sequences, MR safety and compatibility. These advancements and the wide accessibility of MRI have facilitated its further applications for surgical guidance. An overview of the state-of-the-art intra-op MRI-guided robotic platforms is provided, especially towards the application of stereotactic neurosurgery. Although there is currently no commercial MR safe/conditional robotic system for intra-cardiac catheterization or TLM. These two procedures are of great potential to be assisted by MRI-guided robotic systems to improve their surgical outcomes. The clinical considerations and key technical challenges of these three applications are outlined. To improve the surgical workflow and achieve greater clinical penetration, three key enabling techniques are proposed with emphasis on their current status, limitations, and future trends. These three techniques are related to image registration, positional tracking and MR-compatible actuation. *Non-rigid* image registration can facilitate more accurate anatomical roadmap by tackling the challenges of soft tissue deformation/shift and MRI distortion during the surgery. MR-based tracking can provide real-time positional instrument tracking with high resolution and update rate, which should also be incorporated to realize intra-op online navigation. Fluid-powered actuation has been proved with great potential of offering high-performance actuation under MRI, without adversely affecting the imaging quality. These technology developments may all serve to exploit the information and augment the surgeon's capabilities, by providing enhanced visualization and manipulation. In the following chapters of this thesis, two novel designs of MR safe fluidic motors are first introduced. Integrated with the fluidic motors and the other two aforementioned techniques, three MRI-guided robotic platforms are developed and validated regarding their corresponding clinical requirements.

Chapter 3
Customizable Pneumatic Motor

3.1 Introduction

IN the last chapter, I have outlined the needs for MRI-guided robotic interventions and its associated requirements. Fundamental challenges confronted in MRI-compatible mechatronics have been discussed, e.g. to maintain zero EMI of robot operation during the imaging. To resolve this, a novel MR safe customizable pneumatic stepping motor is presented in this chapter[3]. Its design can be flexibly customized for various actuation requirements. The presented stepper motor composes of only seven key components with homogeneous material and can be directly 3D printed out for the ease of reconfiguration. The stepper motor is of low cost (less than 8 USD) and could be disposable thus averting the complication of any sterilization process. The prototype has small size (e.g. Ø20×51 mm) and can be rapidly reconfigured to meet the actuation requirements at different application scenarios. It can generate high-speed rotation (up to 170RPM) in both directions. Steady torque can also be preserved within a wide range of speed. This torque-speed performance distinguishes itself from the commonly declining ones. All in all, the major novelties of the work presented in this chapter are as follows:

---

[3] The work of this chapter has been presented in the following paper:

Z. Guo, T.T.L. Lun, Y. Chen, H. Su, D.T.M. Chan, K.W. Kwok. *Novel Design of an MR-safe Pneumatic Stepper Motor for MRI-guided Robotic Intervention,* Proceedings of **Hamlyn Symposium on Medical Robotics 2016**. London, UK, pp.50-51.

1) Design of a stepper motor that comprises of only seven components and can be directly fabricated by 3D printing process. The motor is low-cost and can be disposable to eliminate the needs for complicated sterilization;

2) A small-size and self-lockable pneumatic motor designed to operate inside the limited space of MRI scanner. It can be incorporated with the robotic systems for applications demanding on high stall torque/steady positioning;

3) Easy reconfiguration/customization of the motor with regards to its dynamic performance. Mapping between design parameters and dynamic performance has been established. It is believed that a family of motors can be easily generated and cover a wide range of application scenarios.

4) Experimental validation on motor performance and MRI compatibility. A unique feature of the presented motor is, compared to the existing air motors, torque output at a certain pressure supply level does not compromise with the increasing speed.

3.2 State-of-the-art MRI-compatible Motors and Unmet Technical Challenges

As the key component for robotic surgical manipulation, two types of MRI-safe/conditional actuations have been mainly investigated [138]: **1)** electricity-powered actuation, such as piezoelectric motors and ultrasonic motors, and **2)** fluid-powered actuation, namely pneumatic motors and hydraulic motors.

Unlike the conventional electric motors actuated by the interaction force between magnetic field and winding currents, piezoelectric motors operate based on the converse piezoelectric effect. The piezoelectric material deforms or vibrates when the electric field is applied, thus generating linear or rotary motion stepwise. Currently, piezoelectric motors have been extensively studied and tailor-made for many iMRI applications [125, 139]. This may attribute to its compactness (e.g. 42.2×42.2×21.5 mm^3, as shown in **Fig. 3.1**), fine motion resolution and high dynamic fidelity.

Krieger *et al.* [125] utilized Shinsei harmonic motors (Shinsei Corporation, Japan) for transrectal prostate biopsy with 40-80% SNR reduction. Bannan *et al.* [126] presented a custom-made piezoelectric motor. It combines both linear and rotary motion using the inchworm principle. But no SNR result was reported. To attenuate the image artifact caused by EMI, Su *et al.* [139] customized the driving electronics of a piezoelectric motor based on direct digital synthesizer. Even though the SNR test shows promising results with less than 15% reduction, it still presents formidable barrier to minimize the deterioration of image quality (**Fig. 3.1**). Electrical current inevitably generates EM waves and causes imaging artifacts, e.g. stripes or dot-type artifacts, due to the RF interference. Regarding the MR safety issues of such motors, proper shielding and location inside the MR room are required. According to the definition in ASTM standard F2503-05 [140], electric devices (thus piezoelectric/ultrasonic motors) could be MR conditional at best. These disadvantages have naturally shifted the research focus towards inherently MR safe motors, namely hydraulic and pneumatic motors [132].

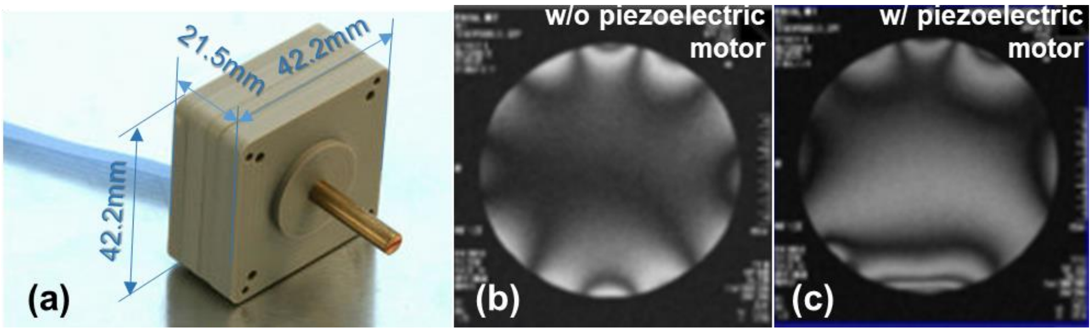

Fig. 3.1 (a) Low-power (max. 15mNm) piezoelectric motor, PAD7344 from Noliac Company, designed for applications requiring zero EMI. MR images generated by a Siemens 3T MRI scanner **(b)** without a piezoelectric motor and **(c)** with a piezoelectric motor placed 140 mm from the scanning centre. The image artifacts caused by the motor operation can be clearly observed, especially in the middle of the image.
Image source: Noliac Company [141]

In terms of image quality and MR safety, pneumatic motors are advantageous over piezoelectric counterparts. From the material considerations, pneumatic motors can be non-magnetic and non-conductive, thus reducing their impact on the field inhomogeneity and nonlinearity. From the energetics perspective, fluidic power is intrinsically “clean” energy while electricity (i.e. piezoelectric motors) already excludes the MR safe option. Pneumatic motor can be designed MR safe with minimal image quality reduction. Unlike hydraulic motor, fluid leakage of air motor is not a concern. As these motors are usually powered by the pressurized medical air, which is commonly available in hospital rooms. The medical air itself is guaranteed not to affect the MR imaging physics [142]. However, they are typically not ideal for continuous position control due to the friction issue and non-linear dynamic characteristics [139]. To meet this challenge, air stepper motors are developed (**Fig. 3.2**) [131, 132, 143-147]. They can produce stepwise motion without the necessity to incorporate feedback sensors/encoders.

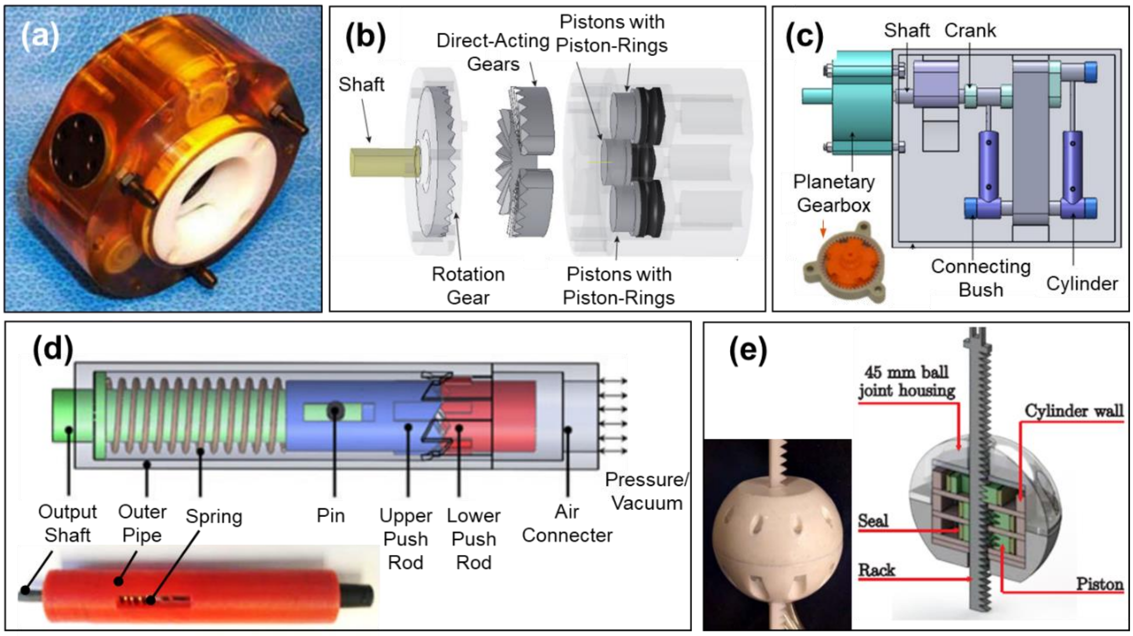

Fig. 3.2 Selected MR safe pneumatic stepper motors. **(a)** PneuStep developed by Stoianovici *et al.*; **(b)** Ø30-mm rotary motor developed by Sajima *et al.*; **(c)** High-torque motor developed by Chen *et al.*; **(d)** Unidirectional motor developed by Chen *et al*., and **(e)** Linear stepper motor developed by Groenhuis *et al.* **Image source: [131, 132, 143, 144, 146]**

Stoianovici *et al.* [143] are the pioneers who invented the first MR safe pneumatic stepper motor, called *PneuStep* (**Fig. 3.2a**). It mainly comprises three diaphragm cylinders, a group of internal gears and cranks. The working principle of *Pneustep* is to sequentially actuate three cylinders so as to drive an off-centered gear, which is fixed with the output shaft. It can generate stepwise motion with resolution of 0.055mm (linear) and 3.33° (angular). **Fig. 3.2b** shows another stepper motor mechanism developed by Sajima *et al.* [144]. It requires only half the component quantity (~10) of *PneuStep* and has considerably smaller size (Ø30×35mm^3). The motor is driven by pushing one of three direct-acting gears successively against the rotation gear at a time. As there is a certain stagger angle between the direct-acting gear and rotation gear, the rotation gear rotates at this angle every time to mesh with the direct-acting gear.

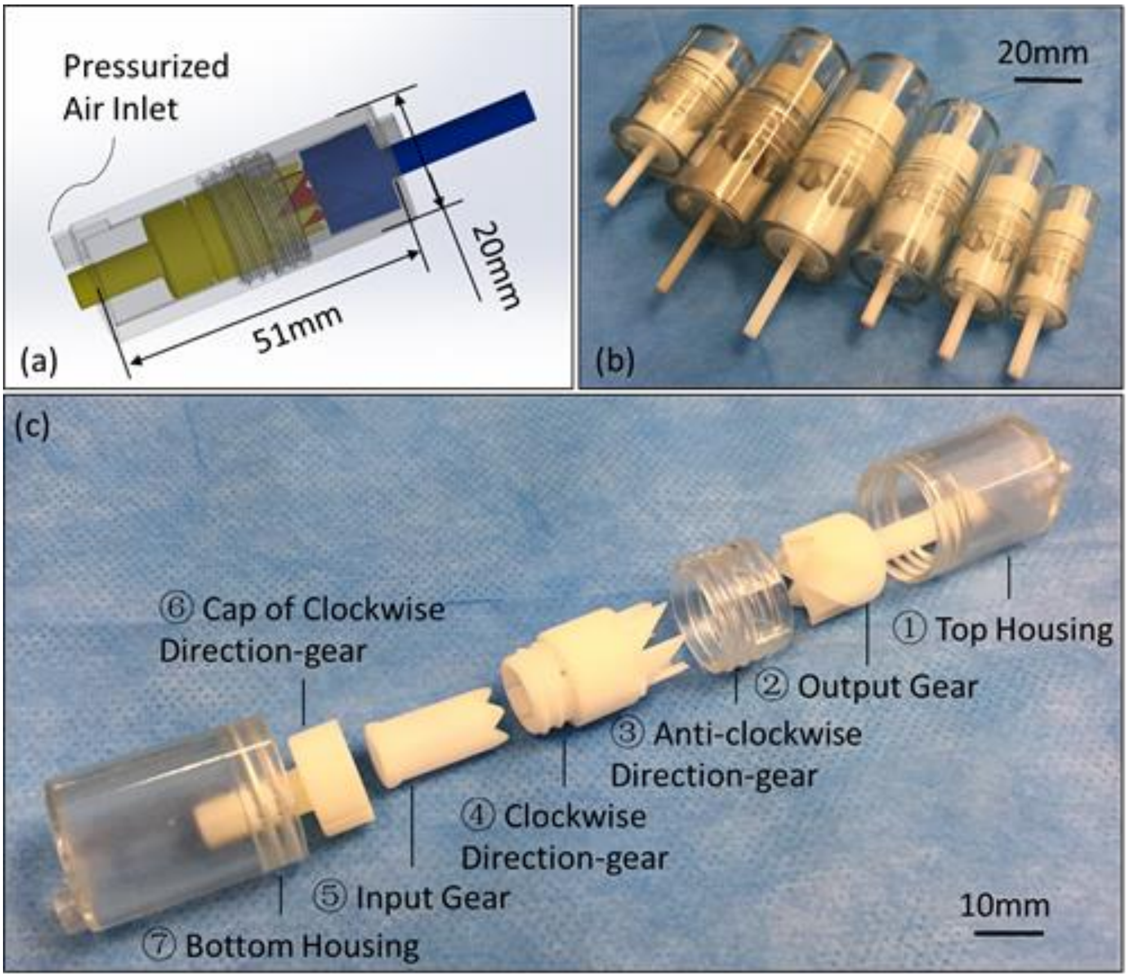

Fig. 3.3 **(a)** Computer-aided design (CAD) model of the presented pneumatic stepper motor; **(b)** Family of stepper motors with variable parameters, including diameter, tooth number and friction coefficient; **(c)** Exploded component view of the motor.

Chen and Kwok *et al.* [132] designed a high-torque stepper based on the principle of a two-stroke engine as shown in **Fig. 3.2c**. The crank mechanism transforms the linear motion of air cylinders to the rotary motion of output shaft. Incorporated with a planetary gearbox, this motor can generate 3.6° rotation at each step with max. torque of 230 mNm. The main limitation of this motor is its bulky size (95×60×35 mm^3) and back-drivability, due to the air compressibility and the lack of locking mechanism. Another design presented by Chen *et al.* [131] is a compact air motor with only 10 mm in diameter (**Fig. 3.2d**). It relies on the intermeshing interactions of upper and lower push-rod gears, which are pushed by a spring and air pressure respectively. Only unidirectional rotation can be realized by this motor. A novel stepper motor (**Fig. 3.2e**) proposed by Stramigioli *et al.* [148, 149] has been incorporated with an MRI-guided robotic system for breast biopsies. Fine rotational/translational motion (i.e. 0.25°/0.25 mm) can be achieved via pushing the pistons towards a curved/straight rack. However, the motion stroke is greatly limited by the rack length. Though it can exert max force of over 60 N at 6.5 MPa air supply pressure. The transmission distance is short (0.5 m) and not yet meets the required distance (at least 8m, from control room to MRI table) for MRI-guided robotic interventions.

3.3 Design Methods

3.3.1 MR Safe Components and Materials

The presented motor design is composed of seven components and weighs 70g only. All the components can be tightly enclosed in a cylindrical structure with minimal total dimension of Ø20×51mm. **Fig. 3.3** shows the exploded component view of the motor. The basic functions of those seven components are listed in **Table 3.1**. Only four of them take effects on the rotary motion/torque transmission, namely the input gear, direction gear and output gear. All the components are fabricated by a rapid prototyping machine (Objet260 Connex, Stratasys, USA) with polymer materials, e.g. acrylic compounds (VeroWhitePlus, Stratasys, USA). Such acrylic compounds can provide sufficient structure rigidity, as well as smooth surface without post-processing (a friction coefficient obtained from pre-experiment is $\mu = 0.157$). The completion time in printing one prototype is approximately 4 hours. The assembly can be accomplished manually without any tools within one minute (as shown in **Fig. 3.4**). Small amount of additional semisolid lubricant can further smoothen the motion and reduce the friction loss in heat dissipation. By plugging three air tube in, the motor can start operating.

Table 3.1 Component Function of Pneumatic Stepper Motor

Part		FUNCTION
①	-	Covering the output gear, guiding and limiting its motion.
②	-	Meshing with input gear and two direction gears
	-	Generating torque.
③	-	Meshing with the output gear to induce anti-clockwise rotation.
	-	Connecting top and bottom housings.
④	-	Meshing with the output gear to induce clockwise rotation
	-	Guiding and limiting the motion of input gear.
⑤	-	Meshing with the output gear to actuate rotation.
⑥	-	Creating close space for actuation of input gear.
	-	Switching direction.
⑦	-	Covering the input gear, guiding and limiting its motion.

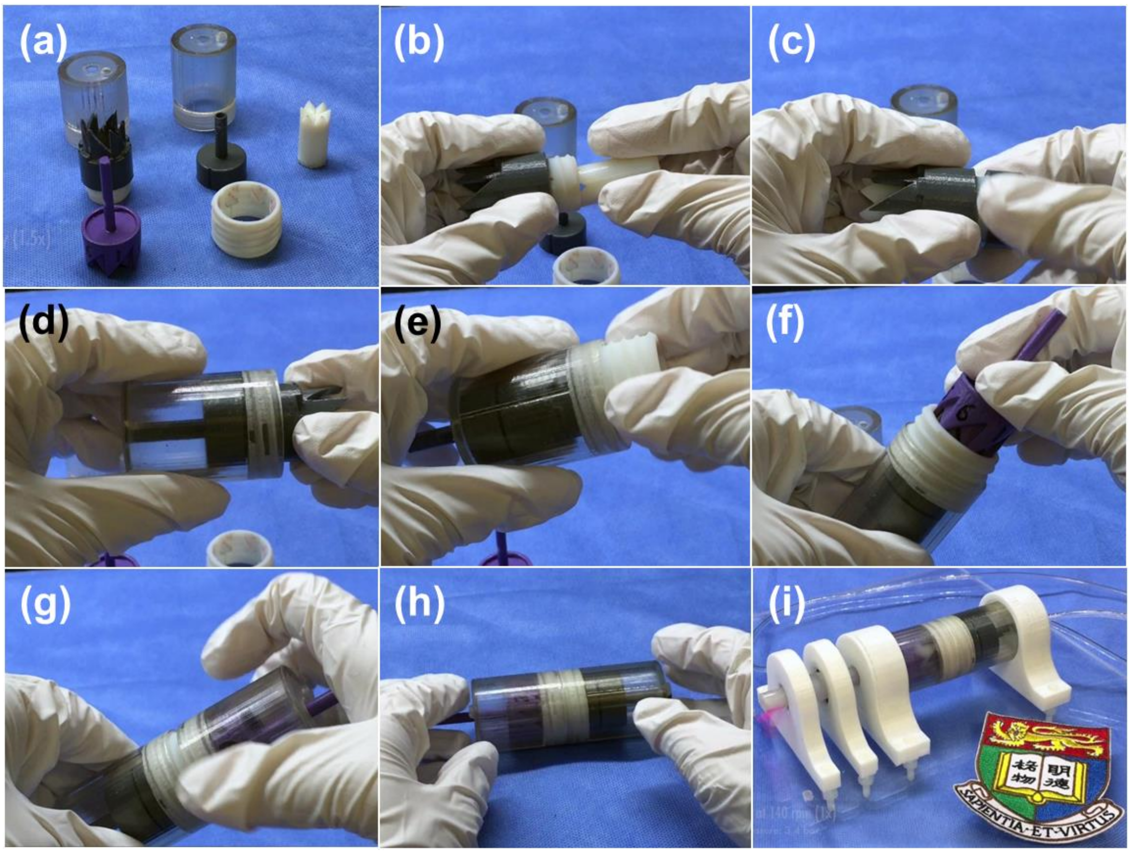

Fig. 3.4 **(a-h)** Manual assembly process of the presented air motor without using any tools. **(i)** Motor operating by three air tubes connected.

3.3.2 Working Principle of Stepping Actuation

Besides fabrication and assembly process, simplicity of the presented motor is also in the operation itself. The basic working principle of this motor is to complete one step by utilizing the circumferential offsets between output and input/direction gears. These gears are actuated by three independent air chambers. Regulated pressurized air pulses in chambers serve as the impulsion driving the gear moving axially. Interaction forces among gears induce rotation. As illustrated in **Table 3.2**, input gear (in red) can only move axially; output gear (in blue) is capable of axial motion and rotation; and direction gear is relatively fixed with the housing during one step. When the gear has N teeth, rotation by 360°/N per step will then be generated.

The switch between bi-directional rotations can be achieved by an air switch, when the input gear pushes the output gear away from the direction gears adjoined (Stage 3, **Table 3.2**). Relative position between clockwise direction gear and anti-clockwise direction gear will be altered. The direction gear, that the output gear first gets in touch with at Stage 4 (**Table 3.2**), provides an angular moment in the corresponding direction and thus determines the rotary direction. The advantages of this mechanism, such as high accuracy and simplicity, have been investigated in previous pneumatic stepper motor designs [131].

Table 3.2 Working principle of clockwise and counter-clockwise rotations, taking a motor with $N = 6$ teeth as an example. Numbers highlighted in white indicate the tooth number. Gears in yellow and transparent are direction gears, which are fixed with the motor housings.

Clockwise	Stage 1	Counter-clockwise
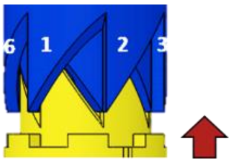	Input gear (red) is pushed by air pulse and moves axially forward.	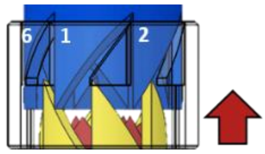
	Stage 2	
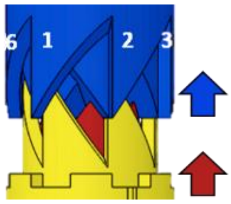	Input gear meets output gear (blue) and pushes it axially forward as well.	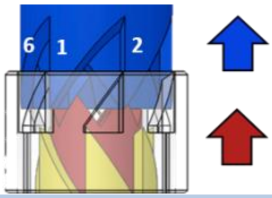
	Stage 3	
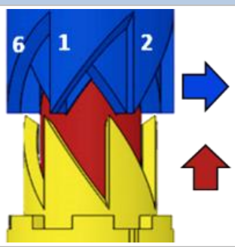	Output gear gets rid of the circumferential constraints of direction gear, such that it can fully mesh with the input gear and rotates $90°/N$ (i.e. 15°).	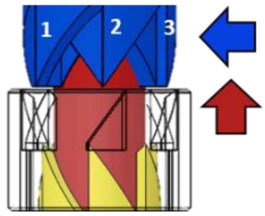
	Stage 4	
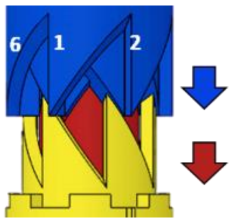	Output gear is pushed by the other air pulse, moving axially backward. It meets the direction gear again (yellow or transparent).	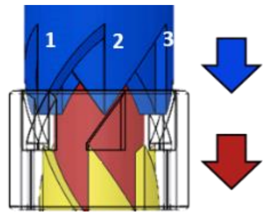
	Stage 5	
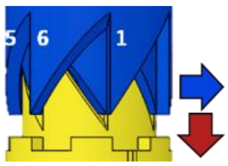	Output gear gets fully engaged with direction gear. This results in $270°/N$ (i.e. 45^o) rotation at this stage and $360^0/N$ rotation in total.	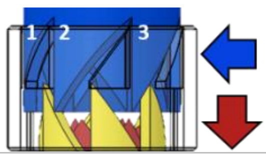

: Motion direction of input gear;

: Motion direction of output gear.

3.3.3 Design Optimization

The torque transmission can be sequenced into two processes: **i)** firstly, output gear is *passively* pushed away by input gear from direction gear, as shown in the Stage 3 of **Table 3.2**. **Fig 3.5a** also illustrates the geometric details of the resultant status; **ii)** secondly, output gear is *actively* pressing on direction gear and meanwhile rotating itself by the reactive force F_o'. This process can refer to the Stage 5 of **Table 3.2**. The detailed kinetics of torque transmission is illustrated in **Fig. 3.5**.

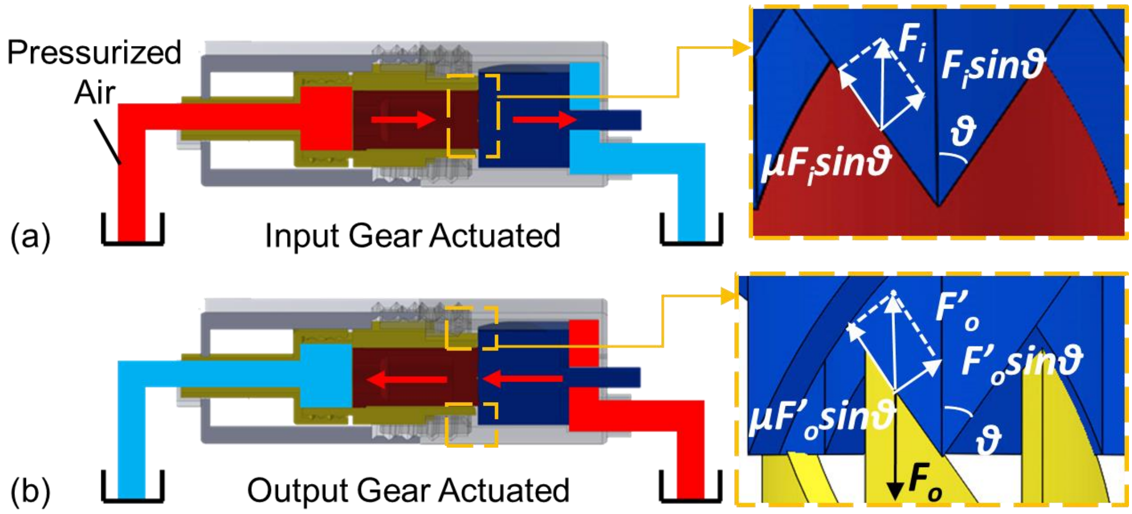

Fig. 3.5 Mechanics model of torque transmission in the 2-step process: **(a)** input gear actuated, and **(b)** output gear actuated. These gears are sequentially actuated by the pressurized air (in red) and vacuum (in light blue). In the input-gear-actuated step, output gear is passively pushed forward and gets out of the circumferential constraint of the directional gear. In the output-gear-actuated step, it is actively pressing on the direction gear.

Process I: In **Fig. 3.3a**, angle θ is a half of the tooth angle on output gear. The friction coefficient is denoted by μ, and F_i denotes the axial force driven by input gear, but which is originated by the air pulse acting on the bottom of input gear, s.t. $F_i \propto \pi r_i^2 p_i/4$, where r_i is the radius of input gear, and p_i is the air pressure acting on input gear. The optimized tooth angle θ, $\theta = 1/2\tan^{-1}(1/\mu)$, is determined by the surface friction coefficient μ, which depends on the choice of material. Without the trivial expression of rotational force deduction, torque T_{o1} is as follows:

$$F_{ri} = F_i \sin\theta\cos\theta - \mu F_i \sin^2\theta \quad \textbf{(3.1)}$$

$$T_{o1} = r_{ei}F_{ri} = r_{ei}F_i(\sin\theta\cos\theta - \mu\sin^2\theta) \quad \textbf{(3.2)}$$

where r_{ei} is the effective radius of F_{ri}. By having the correlation of $r_{ei} \propto r_i$, the torque output T_{o1} at **Process I** could be simplified as:

$$T_{o1} \propto r_i^3 p_i(\sin\theta\cos\theta - \mu\sin^2\theta) \quad \textbf{(3.3)}$$

Thereby, the output gear rotates by $90°/N$ with torque T_{o1}, where N is tooth number.

Process II: Similarly, the geometry of the output gear is symmetric to the input one (**Fig. 3.3b**), s.t. $F_o \propto \pi r_o^2 p_o/4$; therefore, the sexpression of the force and torque can be obtained:

$$F_{ro} = F_o \sin\theta\cos\theta - \mu F_o \sin^2\theta \quad \textbf{(3.4)}$$

$$T_{o2} = r_{eo}F_{ro} = r_{eo}F_o(\sin\theta\cos\theta - \mu\sin^2\theta) \quad \textbf{(3.5)}$$

$$T_{o2} \propto r_o^2 r_d p_o(\sin\theta\cos\theta - \mu\sin^2\theta) \quad \textbf{(3.6)}$$

where r_o is the radius of output gear, $p_o$is the air pressure acting on the output gear. Effective radius of force F_{ro} is r_{eo} s.t. $r_{eo} \propto r_o$. As a result, the output gear rotates by $270°/N$ with torque T_{o2}. Referring to equations **3.3** and **3.6**, seven parameters in total, $(\theta, \mu, r_i, r_o, r_d, p_i, p_o)$, are closely related to the output torque.

Referring to [131], which adopts the similar meshing design for generating rotation, tooth angle is a crucial parameter in torque transmission. This angle can be optimized to maximize the achievable torque while the pushing gear forces F_i and F_o keep the same. It is straightforward that the torque gradient at its peak should maintain zero:

$$\frac{\partial T_{o2}}{\partial \theta} = 0 \text{ and } \frac{\partial T_{o1}}{\partial \theta} = 0 \quad \Rightarrow \quad \theta = \frac{1}{2}\tan^{-1}\left(\frac{1}{\mu}\right) \tag{3.7}$$

Friction coefficient μ is determined by the choice of material and post-process, so is the optimized tooth angle θ. Note that during the transmission, direction gear accounts for 75% rotation in each step. With the radii of three gears (r_i, r_o, r_d) all in positive correlation with the output torque, the radius distribution of gears could be tailor-made with respect to the required dynamic performance.

Three contact areas of output gear (**Fig. 3.6**) are created to mesh with the input gear and two direction gears. The areas contacted with the direction gears are larger than the area contacted with input gear ($r_d > r_i$). It is because the direction gears stay still while input gear and outer gear rapidly moving forwards and backwards, thereby giving rise to most rotating degrees ($90°/N$) of the output gear in each step. Hence, such area distribution can tactically enlarge the rotating force acting on the output gear. The larger the diameter, the more stable of such contacts. All in all, this functional distribution on output gear enhances both the stability and dynamic performance of the motor. The effect of pressures p_i and p_o is positively correlating with the output torque, which will be further discussed in **Section 3.4**.

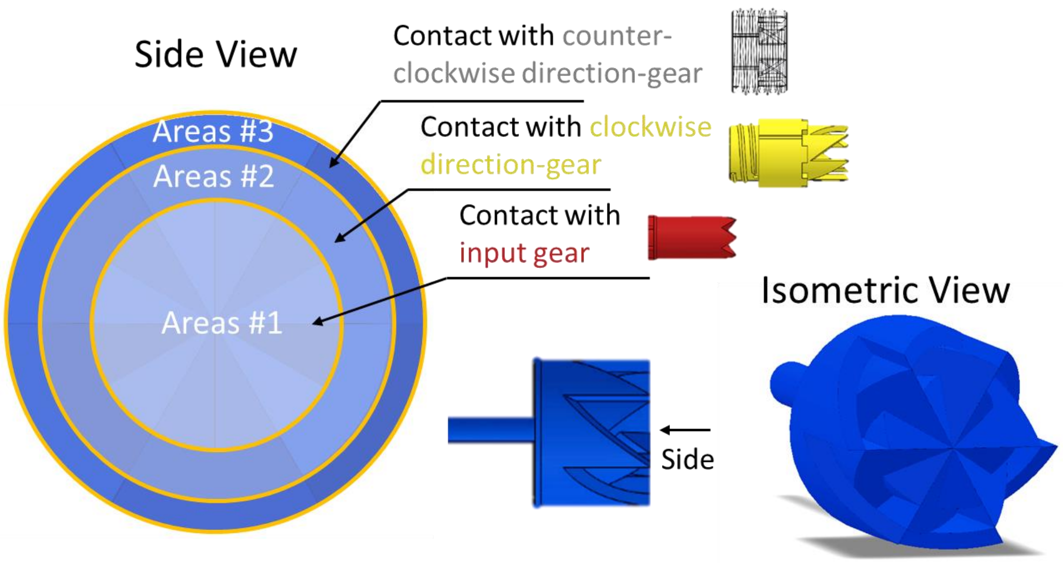

Fig. 3.6 Illustration of three contact areas of the output gear.

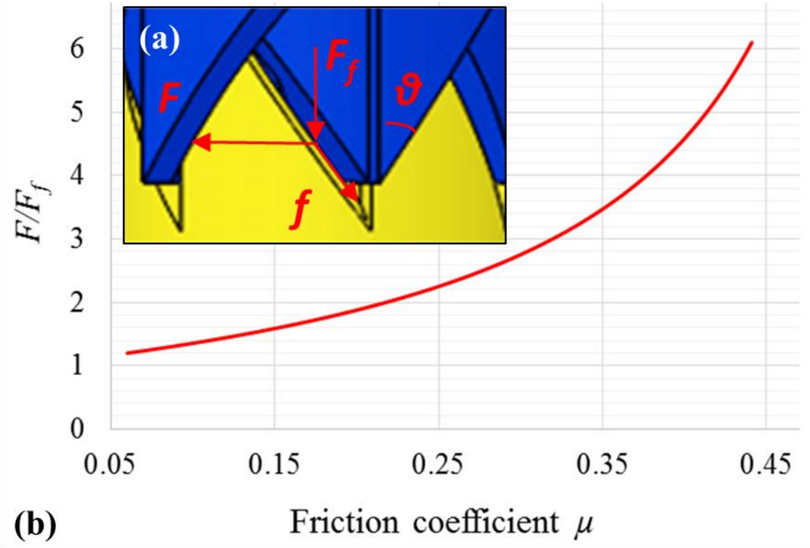

Fig. 3.7 **(a)** Mechanics model of self-locking mechanism when power failure occurs; **(b)** Ratio of payload force F and axial friction F_f varying with friction coefficient μ. While the most existing air motors are back-drivable, this unique self-locking mechanism of the presented motor resolves this challenge and can maintain steady position with <2.50 Nm payload applied.

3.3.4 Self-locking Mechanism for Steady Positioning

Fig. 3.7 shows the statics when power failure occurs. The motor is self-lockable as the deep meshing between output and direction gear limits the rotation. F denotes the axial force driven by output gear, which can be calculated by the distributed payload torque on each tooth. Thereby, $F = T/Nr$, where r is the radius of direction gear and N is the tooth number. Angle θ is half of the tooth angle on output gear. To generate the relative motion between output gear and direction gear, the ratio of payload force F and axial friction F_f must fulfill:

$$\frac{F}{F_f} > \frac{1+\mu\tan\theta}{\tan\theta-\mu} \tag{3.8}$$

In the presented prototype, it could maintain its position when no more than 2.5 Nm payload applied at the output gear (result obtained from repeated tests). This mechanism resolves a common concern of using air motors, as they are usually easily back-drivable. This self-locking mechanism of the presented air motor indicates its feasibility for systems with high demands on steady positioning.

3.3.5 Rapid Reconfiguration for Customizable Performance

Dynamics capability of a motor is of paramount importance to its ultimate performance. The aforementioned considerations on design parameters may improve its output torques. In addition, dimension is also a decisive factor regarding the implementation in various robots. To simplify the reconfiguration process, all the dimensions of components are standardized, as described in **Table 3.3**.

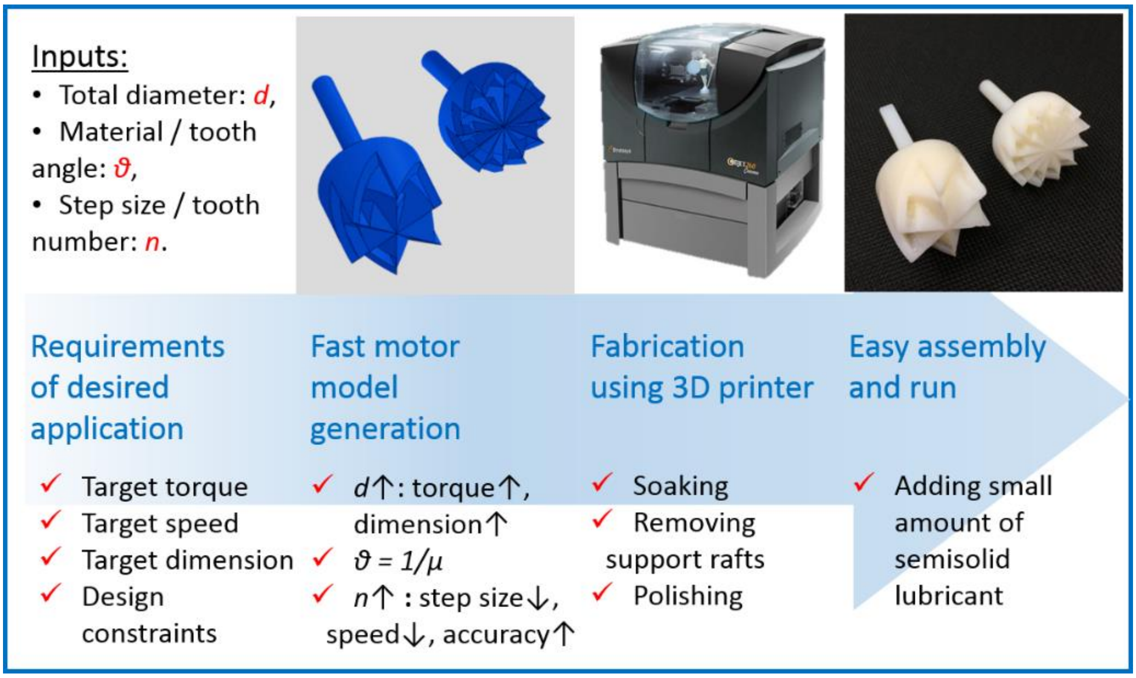

Fig. 3.8 Customization design workflow that incorporates geometrical parameters and manufacturing materials.

The number of tooth N can be customized from three to more, depending on the desired output speed, resolution and manufacturing precision. Not having to incorporate with gearbox, the transmission ratio could be adjusted with N while remaining the same torque. This could eliminate the additional transmission loss and axial dimension. The larger N, the higher rotary resolution (less step size) can be. The backlash can be also decreased by reducing the step size; however, the aggressive increase on N may raise a concern of motion reliability. That means the stagger angles among gears are even smaller. Motion vibration may be induced by misalignment of gear meshing even due to the tiny manufacturing error.

The dimensions of all the components are standardized, as described in **Table 3.3**. To reconfigure the motor, initial inputs consist of total diameter a, tooth angle θ, tooth number N, while a is related to output torque, θ to material and N to output speed. Then the parameters of all the parts can be determined, thus generating a new motor model in seconds. Followed by fast additive manufacturing and easy assembly, the reconfigured motor could be immediately implemented in desired applications. The whole development process (as illustrated in **Fig. 3.8**) could be limited in 4.5 hours.

Table 3.3 Standardized parameters* regarding the three initial inputs, namely total diameter *d*, tooth angle θ and tooth number *N*. Thus, the design parameters of a reconfigured motor can be generated.

①	②	③
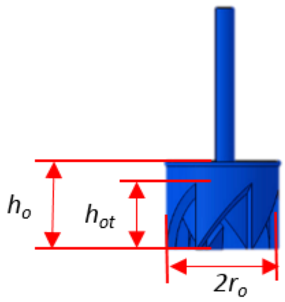	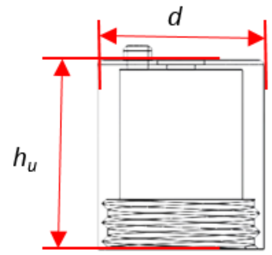	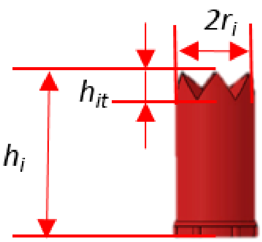
$h_o = h_{ot} + 5$	$h_u = h_o + h_{ct} + 5$	$h_i = h_{it} + h_{ct} + 4$
$h_{ot} = 2\pi r_o / (N \cdot tan\theta)$	d = *Initial input*	$h_{it} = \pi r_i / (N \cdot tan\theta)$
$r_o = (d-9)/2$		$r_i = r_{dc} - 2.5$
④	⑤&⑥	⑦
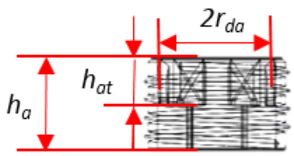	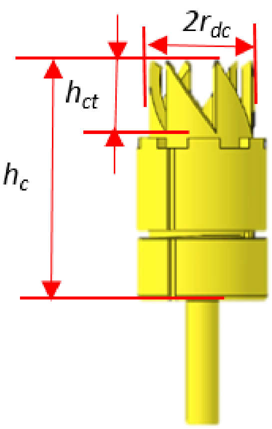	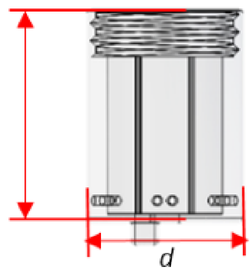
$h_a = h_{at} + 11$	$h_c = h_i + h_{ct} - h_{it}$	$h_l = h_c + 2$
$h_{at} = \pi rd_a / (N \cdot tan\theta)$	$h_{ct} = 2\pi r_{dc} / (N \cdot tan\theta)$	d = *Initial input*
$r_{da} = (d-9)/2$	$r_{dc} = r_{da} - 2.5$	

*The unit is mm. Tolerance might be minor adjusted considering various factors, including material and fabrication.

3.3.6 Control Setup

Control setup of the pneumatics is as shown in **Fig. 3.9**. Three air passages are created three chambers. Correspondingly, three 2-way and 2-position solenoid valves are used to distribute the air pulses for step motion. Valves are triggered by relays that receive signals from microcontroller. One valve is used for changing directions. The other two valves generate pulse-width modulation (PWM) signals to actuate the motion of input gear and output gear alternatively. The rotary speed is set as ω (RPM). PWM period T can be thus calculated as $T = 60/\omega N$. Duty cycles are used to control the duration of different gears actuated by the pressurized air, e.g. the duty cycle D_i of input gear is $D_i = T_1/T$, and duty cycle D_o of output gear is $D_o = (T_2 + T_3)/T$. Generally, the initial duty cycles are set as, $D_i = 0.3$ and $D_o = 0.8$. Minor adjustment of the duty cycles might be needed for different motor models. There is a period that both input and output gears are actuated and pushed against each other. This overlay is to avoid the sudden torque drop when shifting the actuated gears.

.

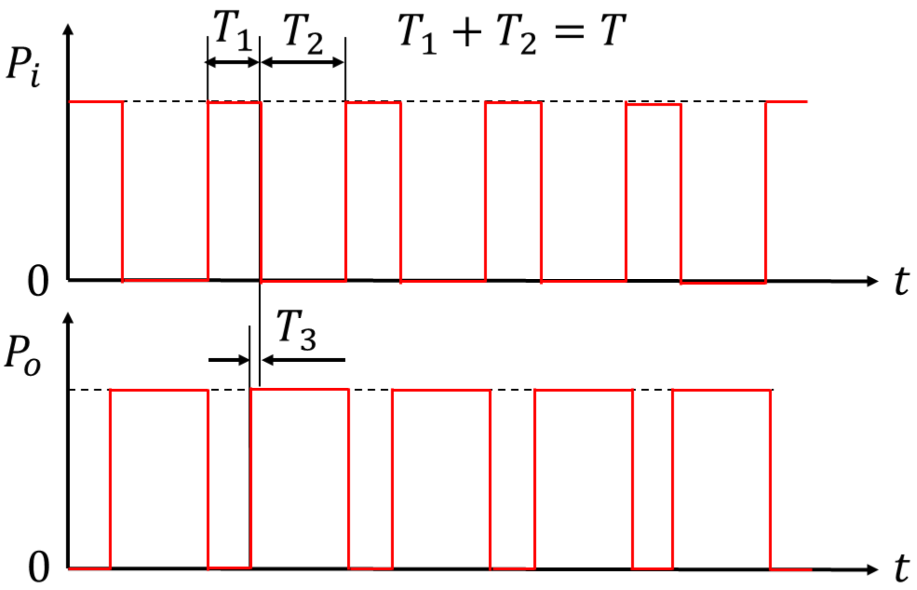

Fig. 3.9 Air pulses for input gear actuation (p_i) and output gear actuation (p_o). The supplied pressure levels, p_i and p_o, are the same. In the general settings, $T_1 = 0.3T$, $T_2 = 0.7T$ and $T_3 = 0.1T$. Overlaid period T_3 of p_i and p_o is essential to avoid the sudden drop of torque output at this "shifting" moment.

3.4 Experiments and Results

3.4.1 Parameter Analysis and Dynamic Performance

Torque and speed are two key metrics to characterize the actuator performance. As the working principle explained in **Table 3.2**, to overcome the internal friction and actuate both input and output gears, a threshold pressure is required. Despite the threshold pressure of presented motor is around 1.5 bar, the torque output is relatively low. Therefore, the data collection was initiated from a level of pressure with the torque output beyond 0.5 mNm, i.e. 2.8 bar. A gearbox (gear ratio = 400:1) was incorporated. A digital torque gauge (range: 0-3 Nm; resolution: 3 mNm) was adopted to measure the torque amplified by the gearbox. Torque without gearbox was calculated and presented in the following plots. Each data point was obtained from the average of three repeated tests.

Fig. 3.10 depicts the torque-speed performance of two motors fabricated with low-friction material ($\mu = 0.094$, **Fig. 3.10a**) and high-friction material ($\mu = 0.194$, **Fig. 3.10b**). The material friction coefficients were obtained from pre-tests. These labels, "high-friction" or "low-friction", are based on their relative numerical values among the tested motors. The supplied air pressure was ranging from 2.8 bar to 4.0 bar by 0.4 bar. Given the same pressure supply, the output torque of the "low-friction" motor was generally higher than the "high-friction" motor, so as the efficiency. This is explicit that the energy loss of "low-friction" motor during the gear interactions is much lower than the "high-friction" one. Additional to the two examples shown in **Fig. 3.10**, torque-speed performance of a motor with "mid-friction" ($\mu = 0.157$) material was also tested. The relation between the material friction coefficient and the torque output is summarized in **Fig. 3.11**. Data was fitted using least-square method.

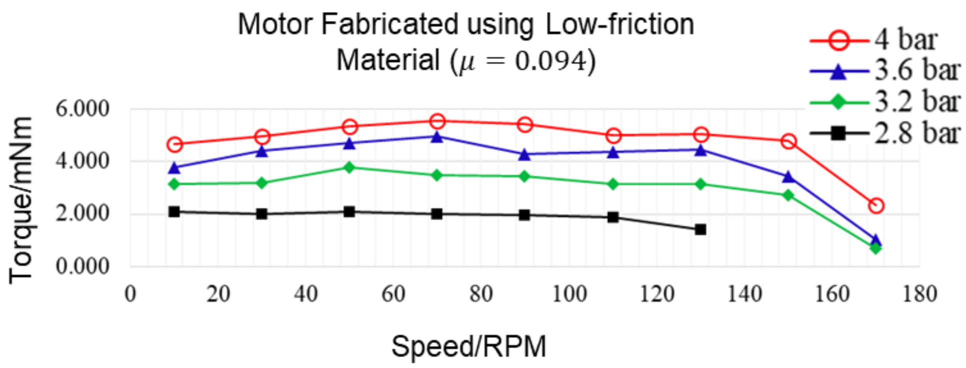

(a)

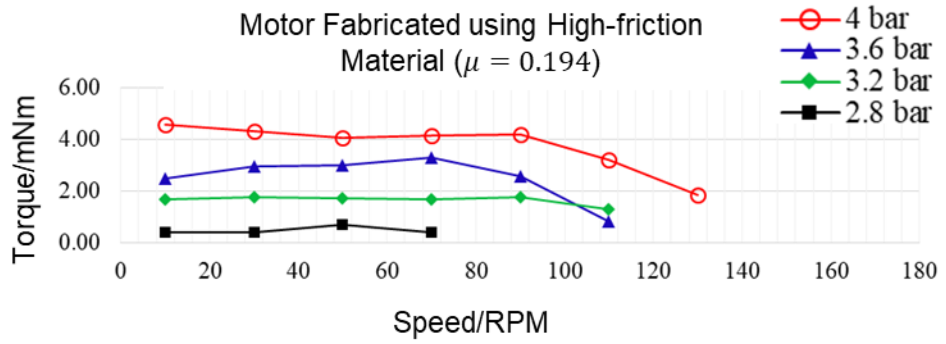

(b)

Fig. 3.10 Dynamics performance of motors fabricated using **(a)** low-friction material ($\mu = 0.094$), and **(b)** high-friction material ($\mu = 0.194$). The "low-friction" motor can generate higher torque and remain more steady output at the four supply pressure levels, namely 2.8, 3.2, 3.6, and 4.0 bar.

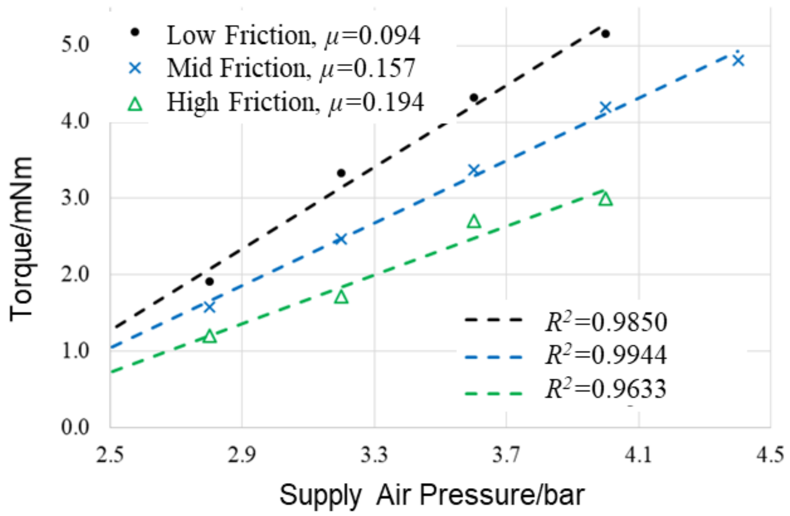

Fig. 3.11 Linear relation between output torque and supplied air pressure of motors with three different friction coefficients, namely $\mu = 0.094, 0.157, 0.194$. At the same supply pressure, the motor fabricated using low-friction material produces higher torque at lower mechanical energy loss.

The torque of the motor with low friction could operate at a stable level within a relative wider range of speed (130 RPM for low friction, 70 RPM for high friction). This may due to the instability introduced by the stronger interaction between high-friction gears. Beyond this speed limit, output torque was declining. One potential explain is that the duty cycle in each step was fixed. But the actual duration was varying along with the velocity (pulse supply frequency) change. When reducing the duration, there was not sufficient diffusion time and the disturbances between two pulses got severe. Shorter duration also implied the insufficient accumulative air pressure to provide the required force for gear driving, thus resulting in the decreasing torque. Apart from design parameters, the steady output torque within the linear regime of a motor is solely dependent on the supplied air pressure.

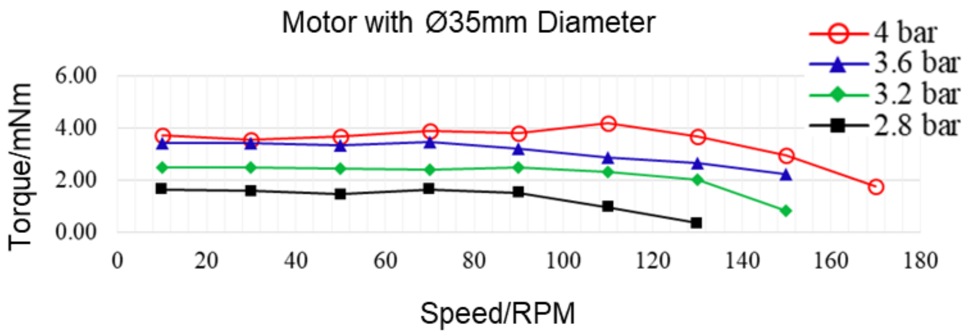

(a)

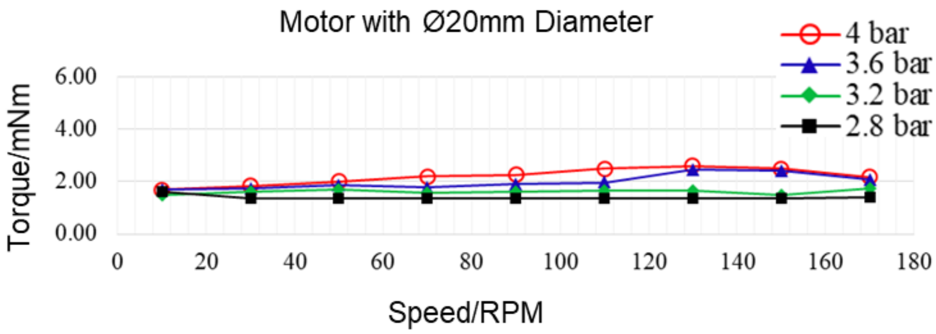

(b)

Fig. 3.12 Dynamics performance of motors with diameter of **(a)** Ø35 mm and **(b)** Ø20 mm. Output torque of Ø20-mm motor can remain steady within larger range of motor speed (up to 350 RPM), while the Ø35-mm motor may be already unstable at speed of 110 RPM. When the same pressure supplied, Ø20-mm motor generates lower torque due to the reduced cross-sectional area.

Fig. 3.12 depicts torque-pressure performance with motors of two different diameters, Ø20 and Ø35. **Fig. 3.13** illustrates the relation between torque outputs and motor diameters, ranging from 20 mm to 35 mm by 5 mm. With the same air supply pressure, the output torque is increasing with the motor diameter. The reason is when the motor chambers are filled with pressured air, the axial pushing force at the gears increases with larger cross-section area. Each motor could cover a certain range of output torque and speed. For example, the smallest prototype could output steady torque of 1.6-2.1 mNm within the range of 10-230 RPM. The motor with smaller size tends to get higher max. speed. It is because the travel distances per cycle of each gear are scaled down. The minimum time required for one cycle is thus decreased. The above experimental results support the theoretical analysis and demonstrates the dynamic capability of the presented motor. Moreover, motor torque could be greatly increased by enlarging pulse pressure/motor diameter or embedding gearbox.

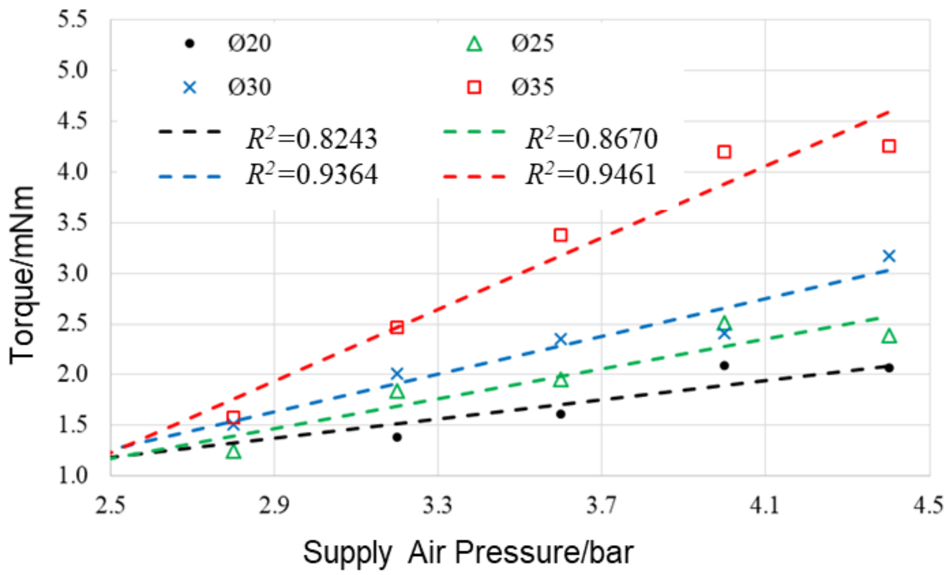

Fig. 3.13 Relation between output torque and supply air pressure of motors with four different diameters, namely $\emptyset 20, \emptyset 25, \emptyset 30, \emptyset 35$ mm. Data is fitted using least-squares fit. This linear trend conforms to the theoretical analysis, and the slope corresponds to the square of diameter d^2.

3.3.2 MRI SNR Test

To quantify the MRI-compatibility, imaging tests with motor running under MRI have been conducted. The motor was placed closely to a commercial MRI phantom cylinder

(#452213095955, CadMed+, USA), which was located at the isocenter of the scanner. The experimental setup is as shown in **Fig. 3.13**. To measure SNR and the max. width of image artifacts, two common image sequences, T1- weighted FFE and T2-weighted TSE were applied to generate the phantom images under different motor operation scenarios (as shown in **Fig. 3.14**). The SNR value of the MR image can be calculated [150] as follows:

$$SNR = \frac{M_{center}}{SD_{corner}} \tag{3.9}$$

where M_{center} is the mean value of image pixel within the 40×40 region located at the image center, and SD_{corner} is the standard deviation of the intensity values within the 40×40 pixel region at the image corner.

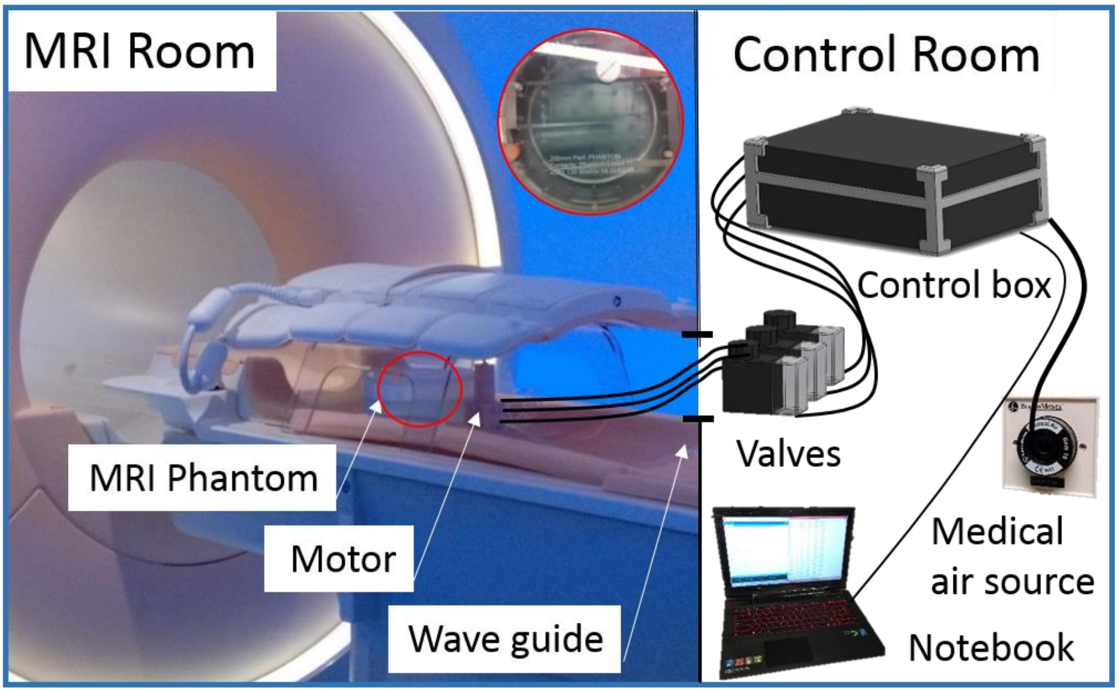

Fig. 3.14 Evaluation setup for the MRI compatibility test. It includes a pneumatic motor and an MRI phantom placed inside the MRI bore, as well as pneumatic valves with its controllers placed in the control room.

Fig. 3.15 shows the SNR generated with respect to four scenarios, which are: **1)** control: only phantom is placed in the scanner; **2)** static: motor has been introduced into the scanner, but all the power is off; **3)** air powered: both electric and pneumatic power is on, but motor is static; **4)** In operation: motor is in normal motion. **Fig. 3.16** shows that the proposed stepper motor does not cause significant SNR loss (<3%). No image artifact is observed even on the delicate line structures inside the SNR phantom (**Fig. 3.15**).

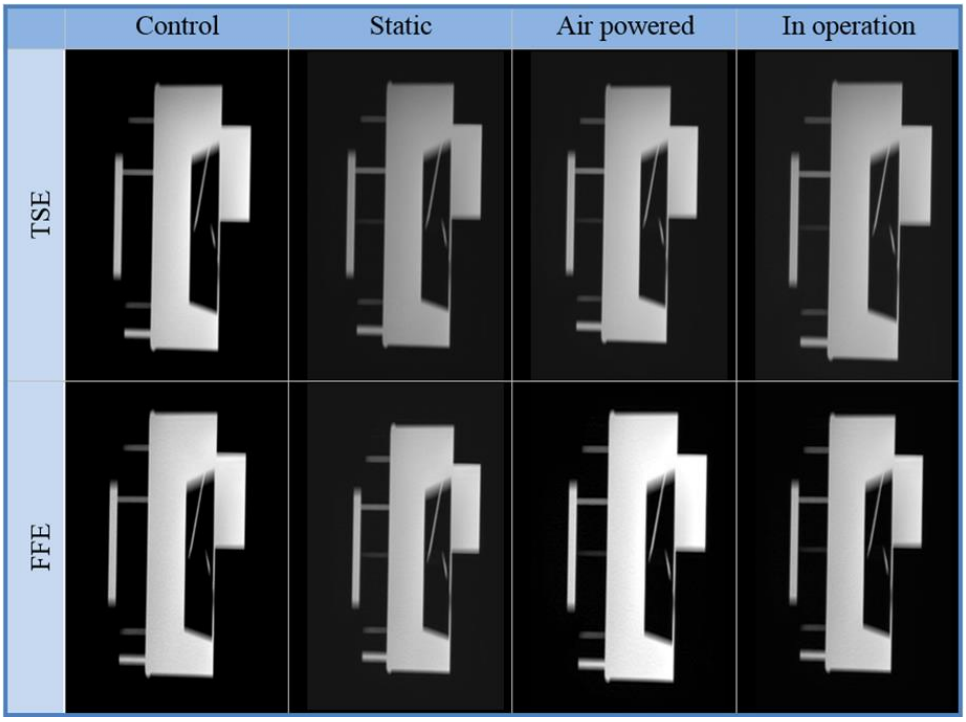

Fig. 3.15 MR images of the phantom with two sequences, T2-weighted TSE and T1-weighted FFE, under four scenarios: **1)** Control - only phantom is placed in the scanner; **2)** Static - motor has been introduced into the scanner, but all the power is off; **3)** Air powered - both electric and pneumatic power is on, but motor is static; **4)** In operation - motor is operating. Compared to scenarios 1 and 2, no EM artifact is observed even when the motor was in full operation (scenario 3 and 4).

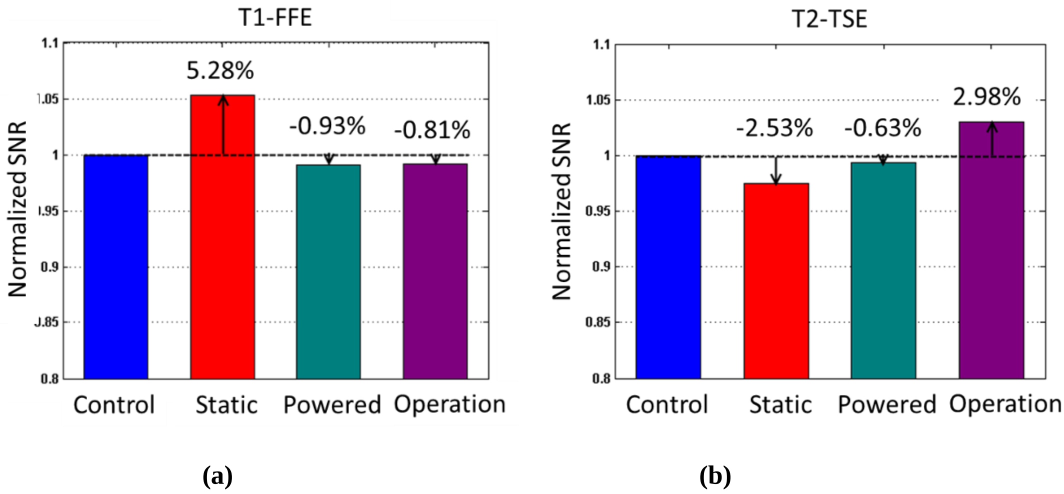

Fig. 3.16 SNR loss in **(a)** T1-weighted FFE and **(b)** T2-weighted TSE images under the four different motor conditions.

3.4 Discussion

In this chapter, the design, theoretical analysis and experimental validation of a pneumatic motor has been presented. The proposed motor features with its compactness (e.g. Ø20×51 mm) and simplicity with only seven components made of homogeneous 3D-printed material. MRI compatibility tests have been conducted. SNR loss is less than 3% and no observable image artifact is generated. These features are important for actuation in the strong magnetic field and confined workspace.

Key design parameters and their influence on dynamics performance have also been discussed. A standardized design flow has been presented to enable fast reconfiguration in regards to different application requirements. The cost of this motor, including manufacturing and raw material, is only approx. 8 USD. Such that, it could be disposable after each surgical procedure without having to deal with the complex sterilization. Continuous long-time (>10 hours) motor operation without performance degradation has been observed, which could already cover the procedural time of most surgeries. Further durability tests may be conducted in the future to validate its operation stability and safety.

Working principle of the motor has been introduced in this chapter. Alternating bursts of the pressurized air flow drive the motor rotating stepwise. It can generate steady torque (max. 5.16 mNm at 4 bar) within a relatively wide range of speed (0-170 RPM). **Table 3.3** presents a comparative study between the proposed pneumatic motor and the existing MR safe counterparts, mainly regarding design complexity and dynamic performance. Since the testing environments among these motors are rather different, e.g. air supply pressure and hose length, which are the critical factors determining the power output. It is hard to compare their dynamic performance solely based on the presented max. speed/torque or power density. Noting the high rotary speed of the proposed motor, users have much flexibility to choose input air pressure and gear ratio combinations to meet a range of torque-speed requirements. Bandwidth is another key performance criterion. However, this technical data of the listed air motors is still unknown. These motors are mainly incorporated in robots for needle-based interventions, which may not require frequent and high-speed manipulation. At a rough estimate, the bandwidth of the presented air motor may not exceed 0.5 Hz due to the extra air pulses required for bi-directional switch and lock. A new mechanism for quick switch may be investigated in the future to improve this aspect. Further study on air dynamics will be also useful to enhance motor bandwidth. The presented motor is self-lockable with deep meshing between output gear and direction gear. This highlights its capability of steady positioning, even when power failure occurs.

Table 3.3 Selected Existing MR Safe Air Motors

	Stoianovici *et al.* [126]	Sajima *et al.* [127]	Groenhuis *et al.* [142]	Proposed air motor
Size/mm^3	Ø85×30	Ø30×35	Ø45	Ø20×51
# of components	~25	~10	>20	7
Resolution	3.33°	4.19°	0.25mm	60°
Speed/RPM	166.6	50	2.5mm/s†	170
Torque/$mN \cdot m$	640	150	60N‡	5
Air supply pressure/bar	8	8	4	4
Hose length/m	3	n/a	0.5	10
Power density /$W \cdot mm^{-3}$	483.7×10^{-6}	7.6×10^{-6}	0.3×10^{-6}	1.8×10^{-6}

†. Speed of the linear motor depends on the stepping frequency, namely the frequency of air pulse supply.

‡. Maximum force exerted of the linear motor.

However, air is compressible. In a remote-operating robotic system, the transmission distances between MRI and control rooms are commonly over 10 m. The output force/torque of air motor can be greatly decreased through such long hoses. Moreover, the high-frequency air pulses (>1 Hz) inevitably generate vibration and noises. It is particularly unfavorable in the operating environment. It is also difficult to deal with the air dynamics and the transmission delay. In this light, pneumatic motors may be excluded from certain applications that are demanding on responsive manipulation, e.g. intra-cardiovascular EP catheterization in dynamic environments. To achieve wider application, my research attention is thus shifted to the development of another fluid-powered motor using incompressible liquid, which will be detailed in **Chapter 4**.

Chapter 4

High-Performance Hydraulic Actuation

4.1 Introduction

IN the previous chapters, I have overviewed the state-of-arts in MRI compatible actuation for safe operation in the MR environment without degrading the imaging quality. I have outlined the limitations and unsolved technical challenges. Motivated by the pneumatic motor presented in **Chapter 3**, hydraulic actuation is developed to enhance the long-distance (10 m) transmission performance. The purpose of this chapter is to introduce a novel design for low-friction hydraulic transmission with rolling-diaphragm-sealed cylinders. Multiple integration methods, e.g. two-cylinder or three-cylinder configurations at the slave side, are presented in regard to the requirements of dimension, motion range, and output torque, etc. Such methods can form the high-performance robotic actuation for MRI-guided interventions. In this chapter[4], the generic kinematic and dynamic models of these integration methods is introduced. Key design parameters are identified and optimization scheme is presented with emphasis on the transmission stiffness

---

[4] The work presented in this chapter has been submitted to or published in:

[1] Z. Dong, Z. Guo, K.H. Lee, G. Fang, W.L. Tang, H.C. Chang, D.T.M. Chan, K.W. Kwok. *High-performance Continuous Hydraulic Motor for MR Safe Robotic Teleoperation[J]*. **IEEE Robotics and Automation Letters**, 2018. (under review)

[2] K.H. Lee, D.K.C. Fu, Z. Guo, Z. Dong, M.C.W. Leong, C.L. Cheung, A.P.W. Lee, K.W. Kwok. *MR Safe Robotic Manipulator for MRI-Guided Intracardiac Catheterization[J]*. **IEEE/ASME Transactions on Mechatronics**, 2018, 23(2): 586-595.

[3] *Fluid-powered transmission for MRI-guided interventions*, US Prov. Patent: **US62/640,302**. [Filed on Mar. 8, 2018]

and response. In sum, the major contributions of this chapter are listed as follows:

1) Design of low-friction hydraulic transmission, allowing high-fidelity quick-response master-slave manipulation over a long (10 m) distance;

2) Integration methods, which can be customized for different robot DoFs. Novel three-cylinder designs can provide smooth bidirectional rotation with unlimited range. Both position and torque controls can be further applied on it;

3) Dynamics model for design optimization. Experimental validation of transmission force, hysteresis, dynamic response is performed to ensure dexterous robotic manipulation.

4.2 Design Methods

Hydraulic motor driven by incompressible fluid, such as water or oil, usually has high power transmission density and fast response [151]. However, liquid leakage is a common concern of hydraulic systems. Large frictional forces may also exist with the utilization of conventional sealing approach, e.g. sliding seal. O-ring seal may be the most commonly adopted approach, which consists of a toroid with a circular cross-section and is made of elastomers, e.g. Silicone and Neoprene. O-rings are installed in a groove, which is usually machined in the piston side surface. When the diameters of two surfaces (cylinder and piston) are properly sized, the clearance in-between is slightly less than the difference of outer diameter and inner diameter of the O-ring. Then it forms a gland, mechanical deformation of O-ring may result forces to ensure the surface contact and create a barrier to the potential liquid leakage path. Inevitably, high sliding friction and substantial mechanical losses are introduced during the operation. Other problems related to this high friction operation may include material shears and extrusion gaps, in particular for the high-pressure dynamic circumstances.

For the introduction of rolling-diaphragm seal, there is no such MRI-compatible actuation reported so far. An efficient passive fluid transmission is developed by Whitney *et al.* [152] based on the rolling-diaphragm seals for haptics device. On account of the friction-free transmission, a self-contained system can be formed to ensure the bidirectional operation and input-output synchronization. However, metallic components are used for enhanced torque output and durability, e.g. steel-cord belt. This prevents its direct use in MR environments [153]. In addition, the range of rotation (135°) in previous designs are limited due to the relatively short stroke (24mm, DM3-20-20, IER Fujikura) of the diaphragms. To this end, there is a strong incentive to develop novel integration methods of these hydraulic transmissions, which are intrinsically MR safe, capable of bi-directional rotation, and have infinite range.

4.2.1 Master-slave Hydrostatic Transmission

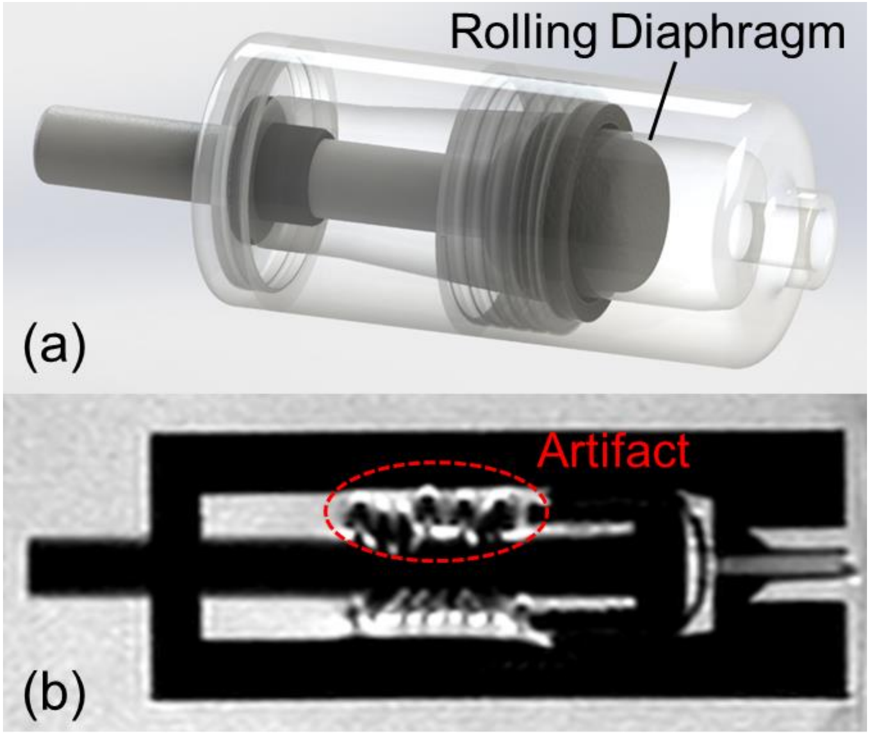

Fig. 4.1 **(a)** 3D model of a rolling-diaphragm-sealed cylinder; **(b)** MRI sagittal view of the cylinder. Though motor is seldom the interests in the scan, motor was placed at the isocenter and imaged by a 1.5T Philips scanner under the typical GRE sequence to prove its MR safety. SNR reduction is minimal and even the tiny structure can be clearly visualized. The local artifact (circled by the red dash line) is induced by the susceptibility changes at the area involving complicated screw thread structures and various matters, e.g. air, polymer and rubber.

Each cylinder unit (as shown in **Fig. 4.1**) contains a rolling diaphragm (FEFA Inc., Germany). Such diaphragm seals are usually utilized in heavy-duty and frequent-cycling applications, such as automotive and aerospace industries. They are made of moulded fabric-reinforced elastomer to withstand the high fluid pressure, making them inherently MR safe. Rolling diaphragms can act like pressure vessels with flexible sidewalls and a variable volume. The diaphragm is fixed with the cylinder groove. Its hat tightly encloses the piston head, frequently flips inside-out and rolls over with the piston to generate linear motion. The length of linear motion depends on the effective stroke of rolling diaphragm. Such working principle intrinsically avoids the static contact/sliding friction between the cylinder and seal [152], thus reducing the mechanical energy loss during actuation. Moreover, rolling-diaphragm seals are less prone to hysteresis compared to the other sealing methods, e.g. O-rings (**Fig. 4.2a**), U-cups, die-cut diaphragms and metal bellows. Additional advantages of rolling diaphragms may include accurate, repeatable motion, minimal spring rate and no lubricant or maintenance required.

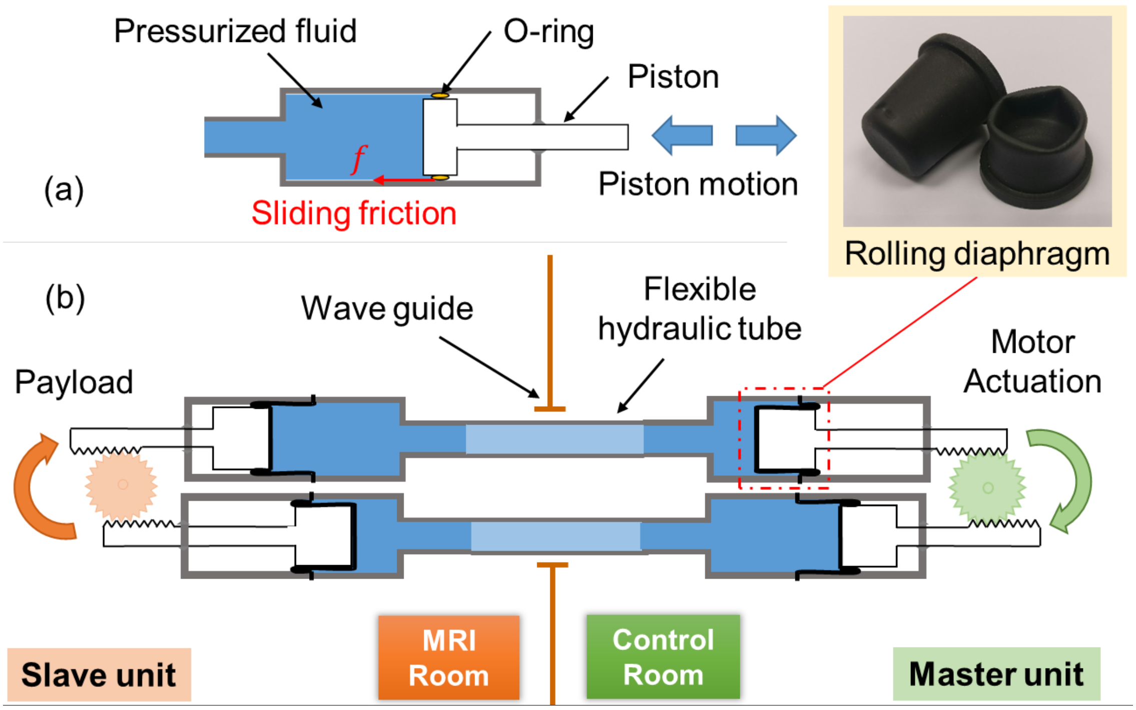

Fig. 4.2 **(a)** Conventional O-ring seal. Significant sliding friction may be induced during the reciprocating operation. **(b)** Master-slave hydraulic transmission with two-cylinder-pair design. Rolling diaphragms are used for low-friction motion transmission. Rack-and-pinion mechanism is adopted to transfer linear to rotary motion. The contact between gear teeth of rack and pinion is maintained constant by preloading the fluid, thus minimizing backlash.

Diaphragm seals are typically used in heavy-duty and high-cycling applications, such as automotive and aerospace industries. Common causes leading to early failure include abrasion against the piston, circumferential compression and machining flaws. To this end, the shapes of the cylinder wall and piston head are designed to properly fit with the diaphragm. The clearance can only accommodate single diaphragm folding, so as to prevent undesired ballooning and ensure symmetric rolling of the diaphragm. As a result, the fluid pressure can be efficiently applied on the piston, rather than stretching the diaphragm.

Master-slave actuation is adopted, with a pair of cylinders as one transmission line/unit. A long pipe (about 10 m), passing through the waveguide in-between MRI room and control room, connects the pair of cylinders. Slave part operates on the MRI table near the patient. Master part is driven by electric direct current (DC) motors. All the electronics are located in the control room. Such separation assures minimal EMI to the MRI scanning. It also allows simple and compact design of slave part. **Table 4.1** lists out the specifications of the hydraulic transmission.

Table 4.1 Specifications of the Hydraulic Transmission

Hydraulic pipeline	Length ≈10 m; Outer/Inner diameter = 6/4mm (Nylon Tubes: DG-5431101, Daoguan Inc,)
Transmission fluid	Pressurized distill water ≤ 0.3 MPa
Rolling diaphragm	Diameter Ø18mm; Thickness 0.3mm; Stroke length 35mm (FEFA Inc.)
Power source	DC motor with 500 pulses encoder (HFmotor-40150, Chengdu Hangfa Hydraulic Engineering Co., Ltd, China) (Max. torque 278 mNm; Gear ratio 14:1)

Incompressible fluid, such as mineral oil or water, must be fully filled in the pipes without any air bubble and preloaded. This can ensure stiff, responsive and accurate motion transmission in both directions. Semi-rigid nylon pipes (outer/inner diameter of Ø6/4 mm, DG-5431101, Daoguan Inc., China) are selected, in regard to the trade-offs between stiffness and pliability for 10-m long transmission. The transmission fluid is usually preloaded at 0.2 MPa. During the operation, this fluid pressure can be even higher (less than 0.3 MPa). Radial expansion of these pipes should be minimal under loading. The main components, such as cylinders and piston rods, are all 3D-printed using polymer composites (Stratasys, US). Other MR safe materials (e.g. polyethylenimine (PEI), polyoxymethylene (POM)) with higher stiffness and strength can be further explored to enhance the structural robustness and rigidity.

However, the motion of one transmission line can only take place in one direction, namely the piston cannot pull the diaphragm back. Therefore, only one transmission line (pair of cylinders) is *incapable* to generate bidirectional transmission. To solve this, a variety of integration methods of multiple cylinder pairs are proposed. An exemplary configuration is presented in **Fig. 4.2b**, with *two* pairs of cylinders arranged in *parallel*. Rack-and-pinion mechanism is adopted to transfer piston linear motion to output shaft rotation. The pinion gear is placed at the center and coupled with two racks of the piston rods. *Bidirectional rotation* can be thus generated, with a range $\theta = x/R$ of 95.6°, where x is the stroke length (25 mm) and R is the radius of pitch circle (15 mm). The pinion gear at slave side is connected to the output shaft, while the one at master side is coupled with an electric motor. An alternative is to drive the two master cylinders separately using two electric motors, so as to independently control the two transmission lines. But it may require complicated control. For simplicity, symmetric designs are adopted for master and slave parts.

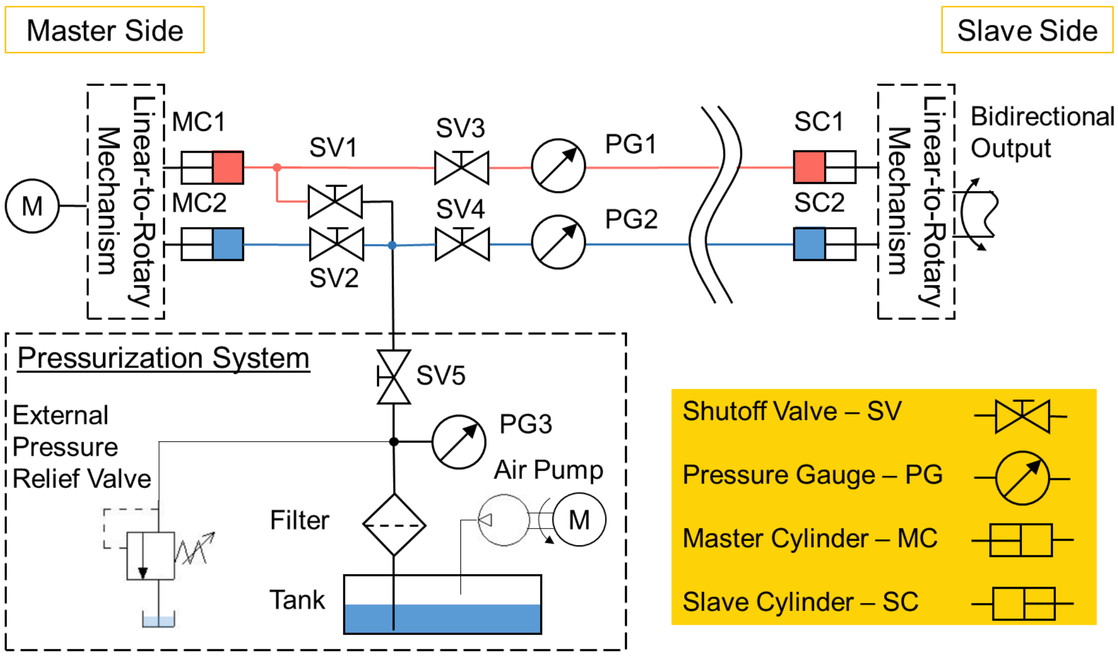

Fig. 4.3 Circuit diagram of hydraulic driving system with *two* pairs of cylinders. A pressurization system is involved for degassed liquid supply and pre-loading, which includes an air pump, a tank, a filter and a pressure gauge. This system can prevent air bubbles to be introduced into the hydraulic circuit. Two transmission lines are coupled, and powered by an electric motor at the master side.

The transmission liquid in pipelines is preloaded at the same pressure (0.05-0.20 MPa). This can be achieved by opening all the valves for preloading and shutting SV1/SV5 for operation, as shown in the circuit diagram (**Fig. 4.3**). Generally, the main switch valve SV5 is closed first before the motion. Other valves remain open for the adjustment of zero position of both master and slave parts. Considering the liquid leakage management, each branch of the hydraulic system has at least one valve to isolate it from the circuit. For example, if leakage occurs in slave cylinder-1, the liquid flow can be easily stopped by shutting the valve SV3. Pressure gauges are also incorporated in each main line to monitor the operation and ensure no liquid leakage (sudden drop of the pressure). The whole hydraulic system is pressurized indirectly via an air pump, which is connected with a closed reservoir. The inlet pipe of the hydraulic system is placed at the bottom under the water. While the air in the reservoir is pressurized by the air pump, the water will be pushed into the pipe. This setup can ensure minimal air bubbles introduced into the circuit. In addition, such preloading can enhance the transmission efficiency and minimize the backlash. This enhancement can be achieved by three manners:

1) Compressing the tiny air bubbles existing in the pipelines;

2) Pre-stretching the rolling diaphragm and stiffening the nylon pipes;

3) Pushing the gear teeth of rack to keep constantly contact with the teeth of pinion and preloading all the couplers.

In an attempt to enlarge the range of motion, the two cylinders can be arranged at an acute angle. Therefore, the diameter of the pinion's reference circle can be reduced, but this will also inevitably sacrifice the accuracy of transmission, as well as the maximum output torque tolerated by the gear structure [154]. By tuning the cross-sectional areas of master and slave cylinders, a certain transmission ratio can be naturally formed without embedding additional gearbox. However, this increased range of motion stroke may not be optimal for high-precision application, and also still lag far behind the actuation requirement for long-range instrument insertion, e.g. for breast needle biopsy (>100 mm [155]) or EP catheterization from the femoral veins to LA. To this end, diaphragm-based hydraulic transmission in the novel configuration of *three* cylinders is proposed to resolve the unmet technical requirements.

4.2.2 Integration Methods for Continuous Rotary Actuation

Fig. 4.4 shows a generic hydraulic circuit design for integrated continuous actuation with three (or more) pairs of cylinders. Different from the two-cylinder actuation design, the three master cylinders are usually driven by three independent electric motors. This setup adds the flexibility of further implementing positional or torque control on the proposed actuator. For each transmission line, there are two valves to separately control the master and slave cylinders. In case of any leakage accident occurs, it can be rapidly stopped and isolated from the main circuit by closing the corresponding valves. Pressure gauges are also installed for each transmission line. They are used to ensure the pre-loading level of each line is reached, and monitor the pressure change during the operation. If there is a sudden pressure drop, the system will stop immediately to check any leakage or mechanical failure happens. Similar with the hydraulic circuit for two-cylinder configuration, the pre-loading pressure is 0.05-0.2 MPa in this setup. After the preloading completing, main valve SV4 is closed first. While the other valves remain opened, zero positions of each cylinder are adjusted. Then valves SV1-3 are closed, the actuator can start running.

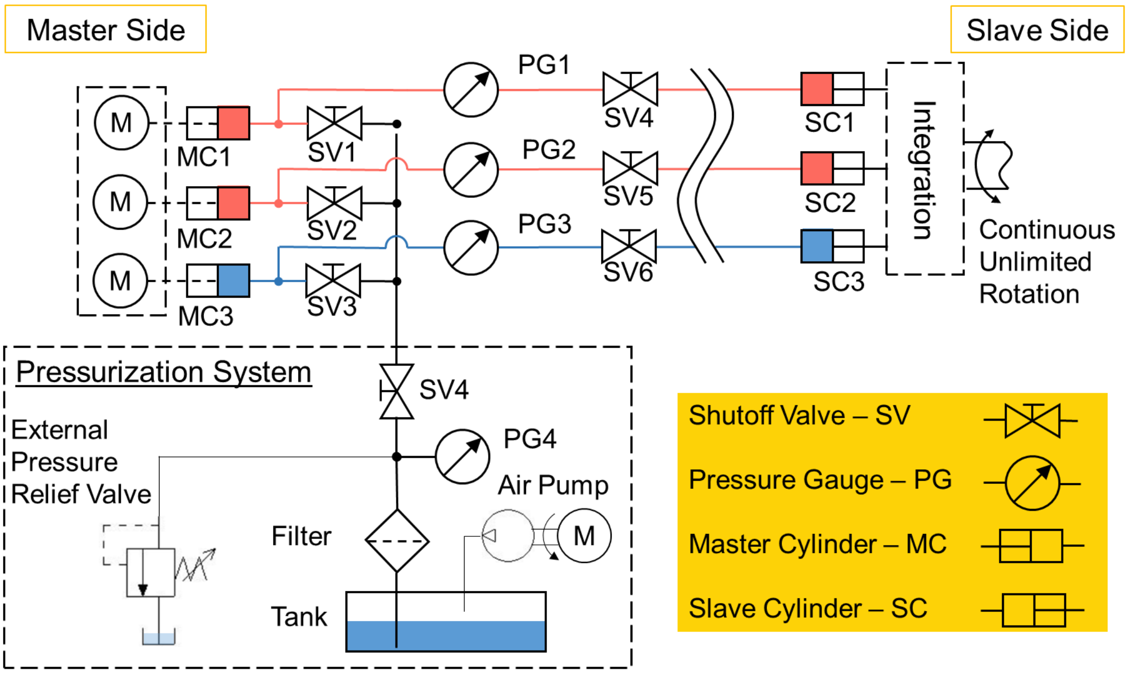

Fig. 4.4 Hydraulic circuit design for *three*-cylinder continuous actuator. Three pairs of cylinders are involved in this example. The methods of integration with three slave cylinders may vary, depending on the applications. The transmission lines are independently controlled by three electric motors at the master side.

Three integration methods on the basis of cylinder arrangement and rotation output direction are proposed in this section, namely axial, in-line, and radial arrangements. In each arrangement, three or more cylinders can be integrated to generate continuous bidirectional rotation. Here takes three cylinders as examples. **Fig. 4.5** illustrates the CAD model of the integrated hydraulic actuation in axial arrangement.

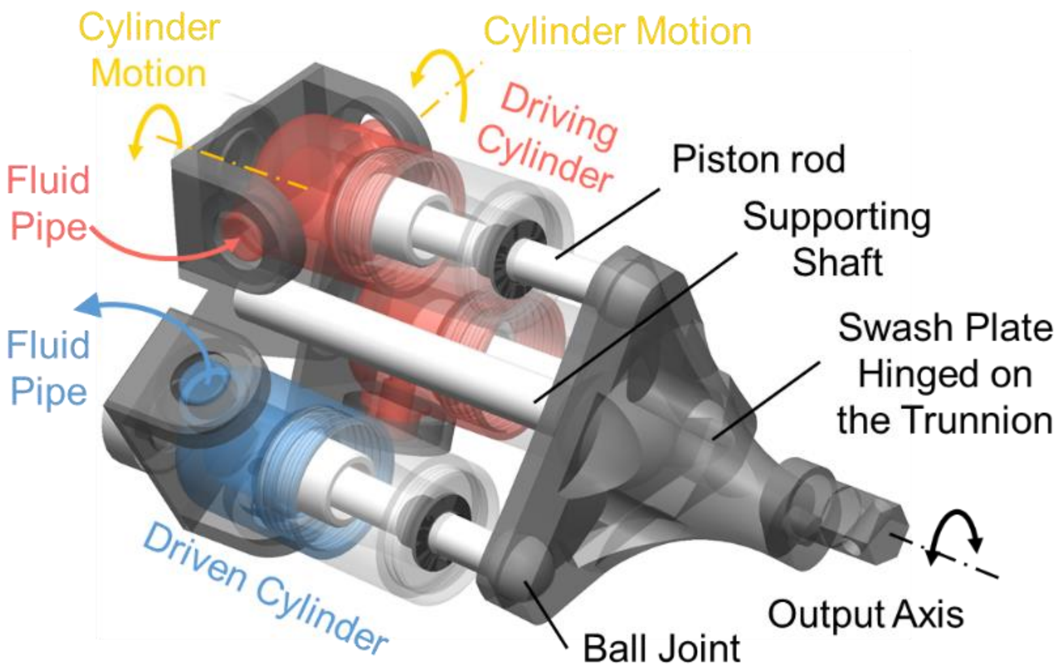

Fig. 4.5 CAD model of the integrated hydraulic actuation in axial arrangement. Trunnion is the pivoting center for the swash plate, which is the ball joint located at the head of supporting shaft.

The swash plate, first invented in the 1920s [156], is a long-known mechanism translating the piston reciprocating motion to shaft rotation. It is firstly invented to replace the crankshaft, but becomes popular only in the recent years thanks to the manufacturing advancements for improved durability. A swash plate consists of a disk hinged by a trunnion to the supporting shaft. An oblique angle τ is remained constant between the disk and supporting shaft during its operation (**Fig. 4.6**). The smaller this angle τ, the larger stroke is required for the piston-motion. A series of pistons driven by the hydrostatic power are placed coaxially with the supporting and output shafts. These piston rods have ball joints at heads and are coupled with a swash plate via these joints. Each cylinder is accommodated on a 2-DoF base fixed with the supporting structure. During the actuation, the cylinder may have pan-tilt motion about the axes of the base. The motor operation requires the mobility of cylinders/hydraulic tubes, which may inevitably introduce more moving components and cause instability. The main advantages of this axial design with swash-plate mechanism are the high power-to-volume density [157], and the variability of displacement. This mechanism has been used in Stirling engines and Duke engines [158, 159].

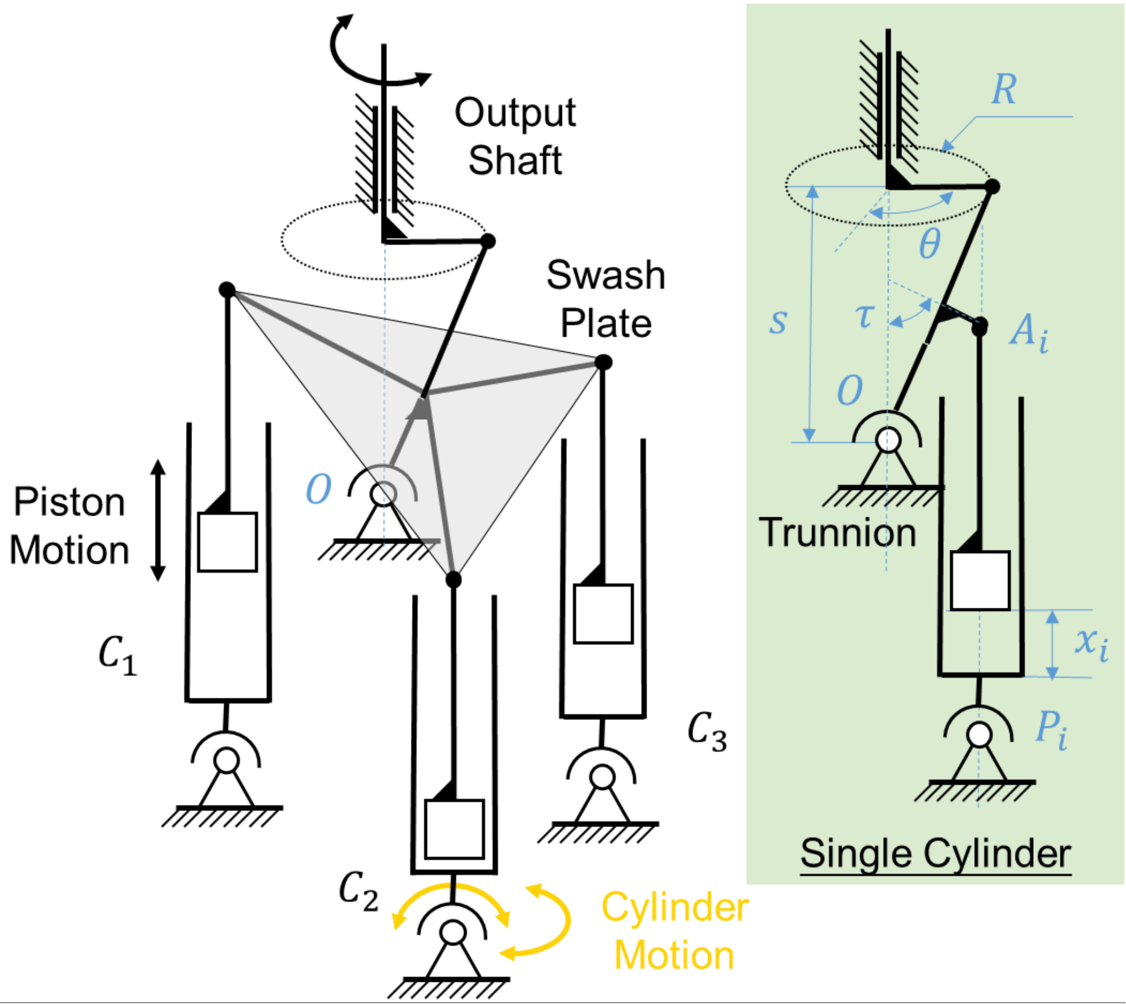

Fig. 4.6 Kinematics diagram of the axial hydraulic motor. The cylinders need to pitch and yaw about the joints P_i $(i = 1,2,3)$. This 2-DoF motion may introduce much instability during the operation.

Crank-shaft mechanism (**Fig. 4.7**) for in-line cylinder arrangement is a typical engine design in automotive. Three cylinders are mounted to the supporting structure via bearings, with small-range swaying motion during actuation. Each cylinder has one port for pressurized fluid supply in different time phase. The pressure phase difference is $120°$ in the proposed design, which is determined by the circumferential crank angle. This ensures that at least one cylinder is exerting driving force, defined as driving cylinder, throughout the actuation cycle, while the remaining cylinder(s) is (are) being contracted, defined as driven cylinder(s) (**Fig. 4.7**). Counterweights are incorporated to the crankshaft to balance the inertia effect and reduce vibration especially in the high-speed applications. To fine tune the counterweight parameters, there are screw holes in the shaft for adding or removing the weights. **Fig. 4.8** shows the kinematics diagram of this in-line hydraulic motor.

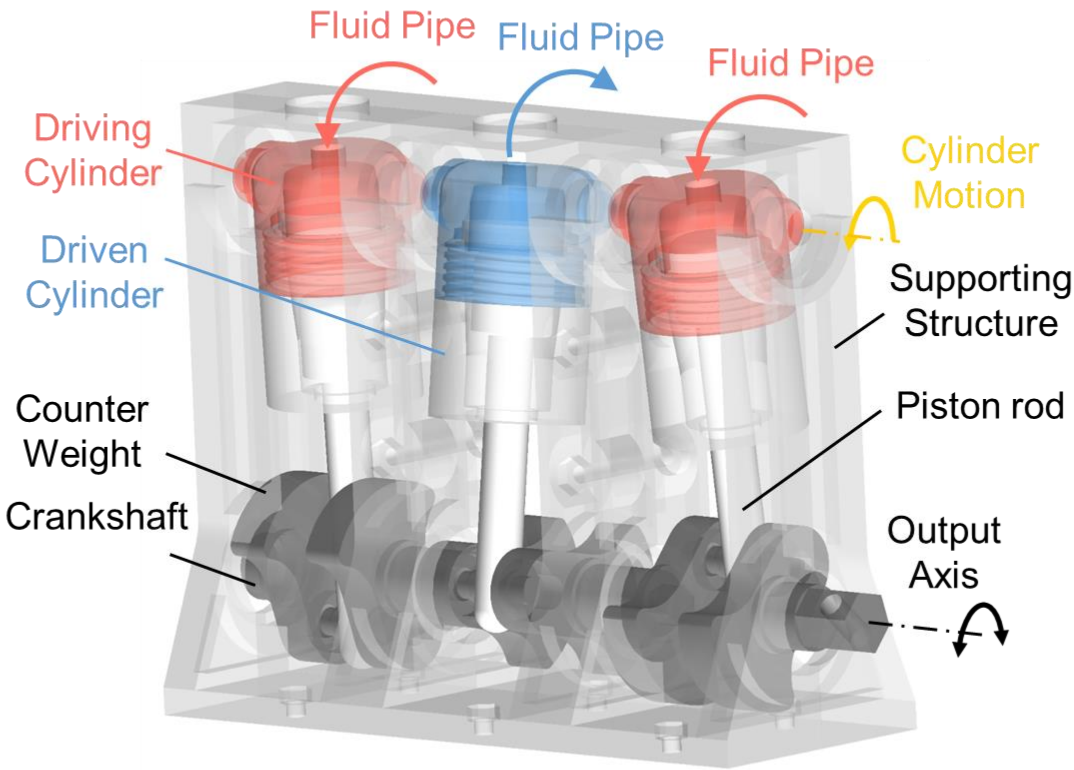

Fig. 4.7 3D model of the in-line configuration for hydraulic actuation. This crank-shaft mechanism is commonly used in automotive engines.

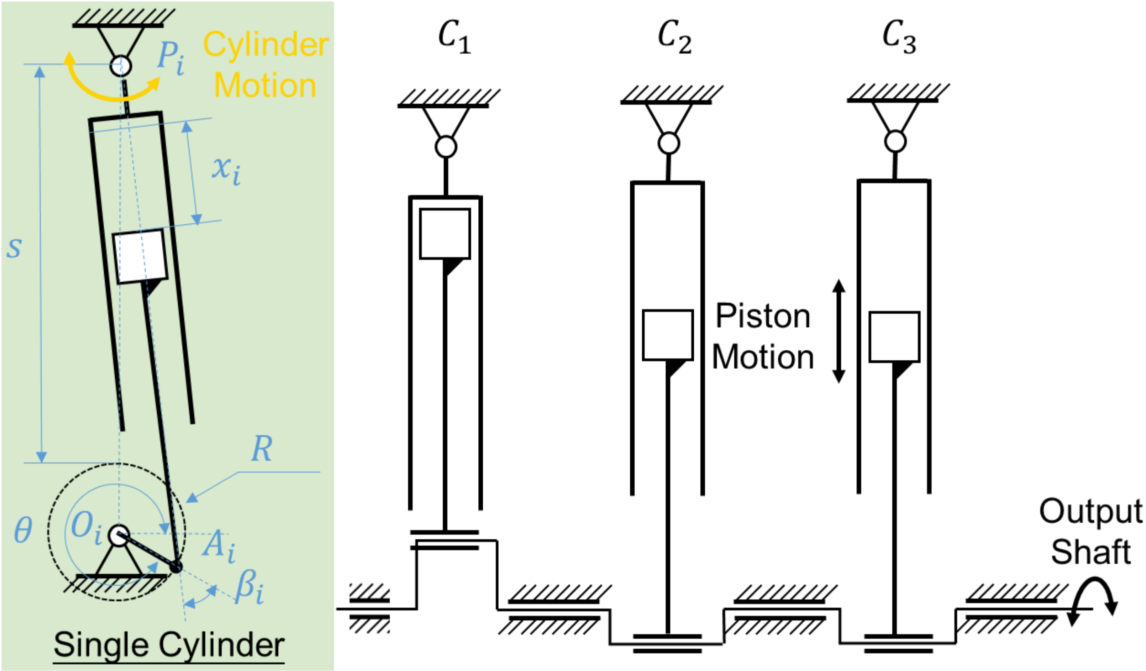

Fig. 4.8 Kinematics diagram of the in-line hydraulic motor.

Fig. 4.9 shows the CAD/CAM model of the radially-integrated three-cylinder actuation unit, in which three cylinders are placed about the central output axis at 120° intervals. This three-cylinder design can avoid singularity, which is the configuration that the input force from cylinders cannot be translated into output torque. It usually occurs in the similar crank-shaft mechanism with one or two cylinder(s), when all the piston rods pass through the center of output axis. This singularity would introduce uncertainties of motion control, particularly when the actuator is rotating at low speed without sufficient momentum to overcome such a singularity position and sustain its motion direction. When it is configured with more cylinders (>3), the output torque would also be increased in theory. However, size and weight of the slave actuator are always the design tradeoff to balance the selection of cylinder number.

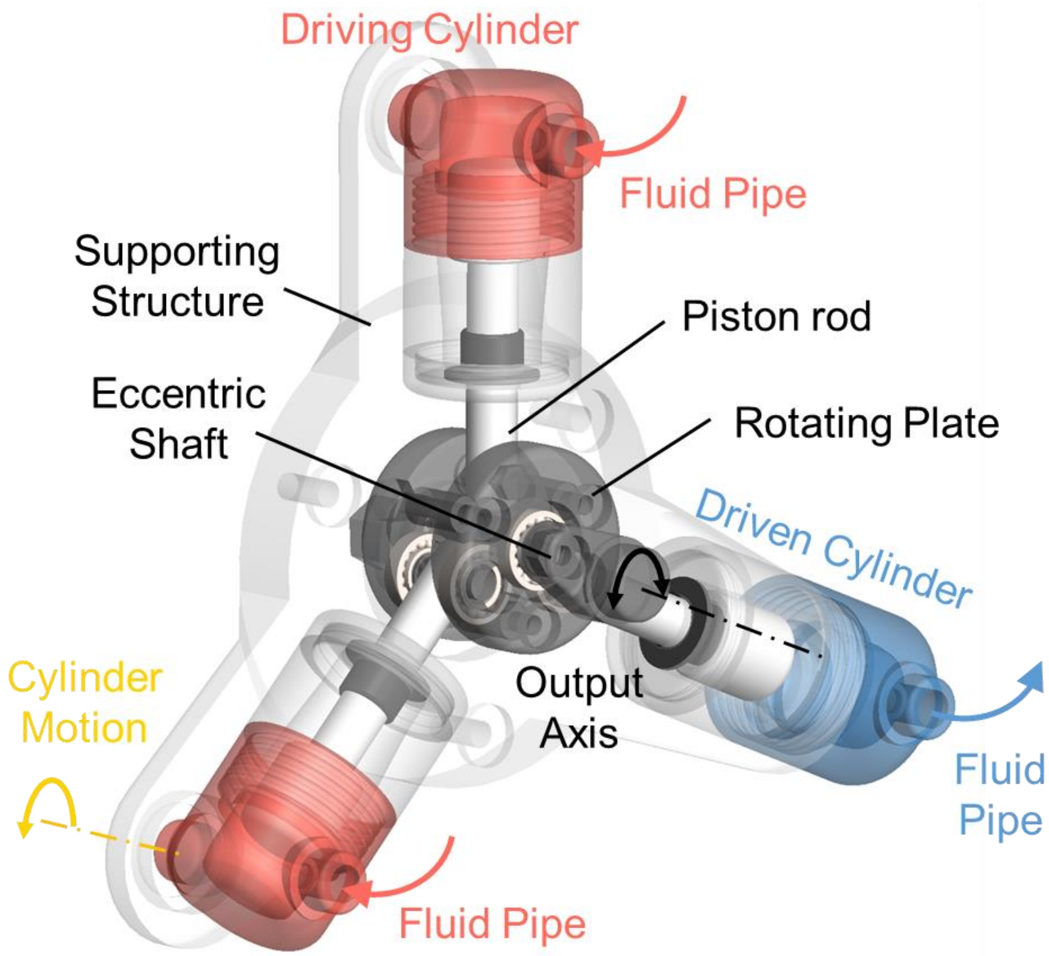

Fig. 4.9 CAD model of the integrated hydraulic transmissions in radial configuration. Similar with the crank-shaft mechanism, a rotating plate and eccentric shaft serve to transfer the linear piston motion to rotation output.

As illustrated in **Fig. 4.10**, three piston rods are coupled with the output shaft via a rotating plate and a crankshaft. Rather than directly attaching all the rods to the crankshaft, the rotating plate connects all the rods within the limited space and allows the cylinders to be arranged in the same plane. However, such mechanical arrangement will introduce an uncontrollable twist of the plate, when the direction of composite force deviate from the center of the rotating plate. To prevent the twist, the rod of cylinder 1 (C1) is fixed with the plate and rods of the other two cylinders (C2, C3) can revolve around the joints. During actuation, each cylinder could sway about the cylinder anchoring joint to keep the axis coincident with the axis of the rod. It can minimize the lateral force between the piston rod and bushing, as well as the possibility of the diaphragm grinding on the cylinder chamber wall. In this way, the friction between the rod and bushing can be reduced and the durability of diaphragm can be enhanced.

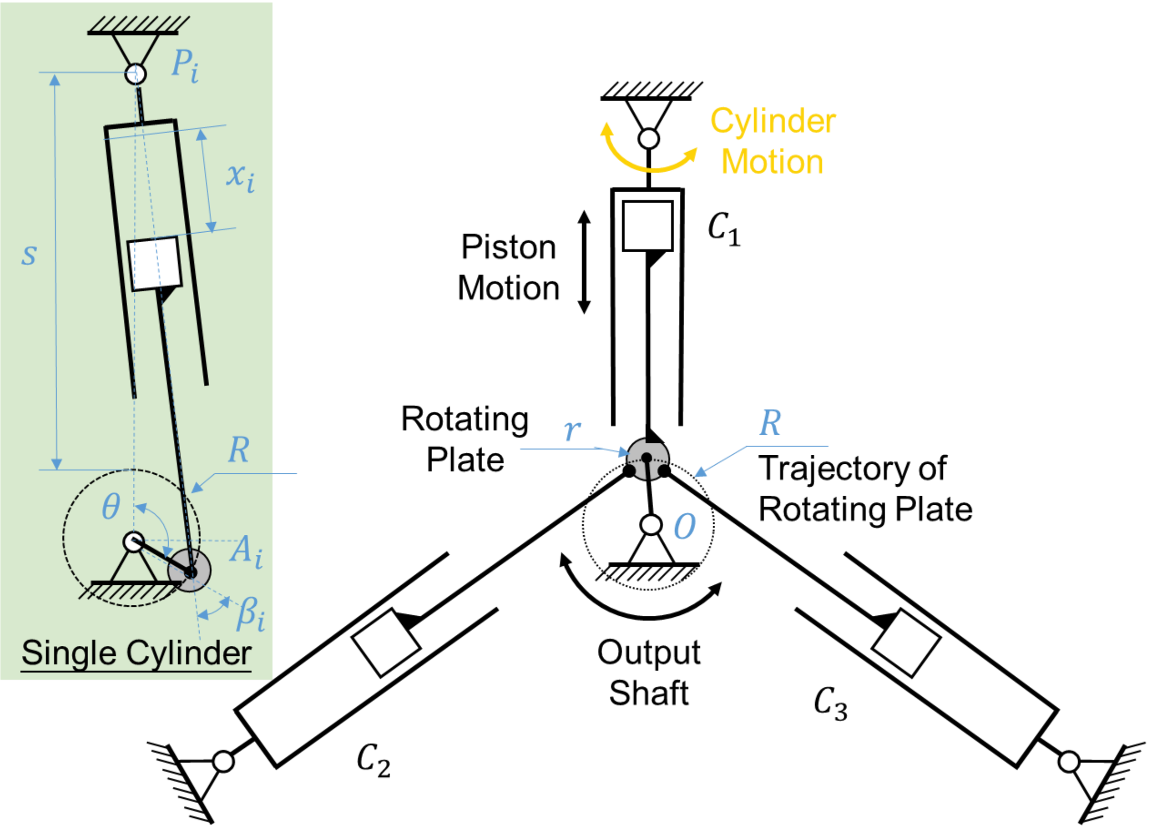

Fig. 4.10 Kinematics diagram of the radial motor. Piston of cylinder $C1$ is fixed with the rotating plate, while the other two may rotate about it. By applying Cosine Law for the triangle ΔOAP in single cylinder, the piston displacement can be calculated as **Eq. 4.1**.

The continuous positional control is achieved by adjusting the combination of output positions of the three pistons. In previous works, such three-cylinder design usually generates step motion with the piston moving end-to-end at full strokes [136] or continuous rotation lack of positional control, which usually presents in hydraulic pumps. With the integration of rolling-diaphragm-sealed cylinders, the displacement of each cylinder rod can be precisely adjusted by the remote-control method through hydraulic pipelines. According to the kinematics, relations of the displacements could be found to generate specific output angle with continuous motion.

4.2.3 Kinematics and Dynamics Modeling

Kinematics model of the three-cylinder configuration can be derived. Key kinematics parameters of a single cylinder are depicted in **Fig. 4.10** and **Table 4.2**. All the components, except for the rolling diaphragm, are considered as rigid bodies. Unique solution of each piston displacement, x_i, is obtainable, corresponding to an angular position θ of the output shaft. By applying Cosine Law for the triangle ΔOAP in **Fig. 4.10**, the piston displacement of the cylinder C1 can be calculated as:

$$x_1(\theta) = \sqrt{(s+R)^2 + R^2 - 2R(s+R)\cos\theta} - s \tag{4.1}$$

where R is the radius of crankshaft and s is the distance from point P to the nearest point on crankshaft trajectory. As the three pistons are evenly placed in a circle, cylinder C2 and C3 have phase differences of $2\pi/3$ and $4\pi/3$ with cylinder C1. Therefore, the piston displacements of cylinder C2 and C3, namely x_2 and x_3, can be derived by re-phasing the θ, respectively, with $(\theta - 2\pi/3)$ and $(\theta - 4\pi/3)$ in **(4.1)**. Note that the misalignment is negligible for the installation of the rotating plate.

Table 4.2 Key Parameters of *Three*-Cylinder Design

Parameter	Description
x_i	Piston displacement
s	Distance from point P to the nearest point on crankshaft trajectory
θ	Angular position of the output shaft
β	Angle between the piston rod and the direction of the rotating plate relative to the output axis
r	Radius of rotating plate
R	Radius of crankshaft

Dynamic model of the integrated transmission system is established and validated in this section to investigate the system properties and optimize the design parameters. Key parameters, that govern the system performance, are identified (**Table 4.3**). System dynamics model can be derived in two parts, namely the slave actuation unit and the hydraulic transmission pipe. For the two-cylinder configuration shown in **Fig. 4.2**, kinematics and dynamics equations could be formulated as $x_t = \pm r_p \cdot \theta$ and $\tau_{t1} - \tau_{t2} = I_p \cdot \ddot{\theta} + \tau_o$, respectively, where the parameters are summarized in **Table 4.3**. Two assumptions are taken into account: **1)** all the components are rigid body, except for the rolling diaphragms and pipelines; **2)** joint friction is negligible.

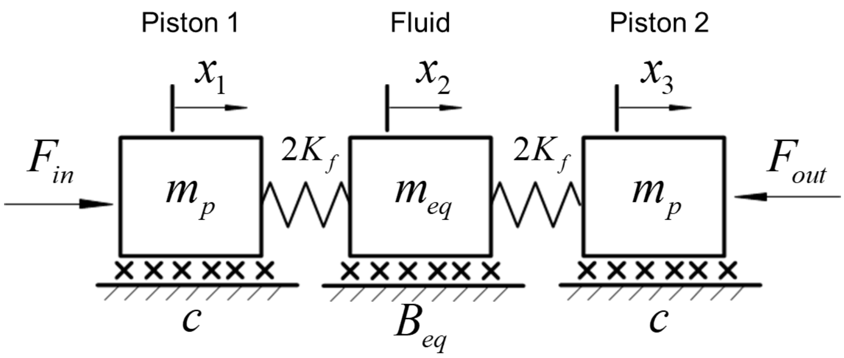

Fig. 4.11 Dynamics parameters of a single transmission line. Input force F_{in} is applied to push the Piston 1 at constant velocity. Output force F_{out} equals to zero. The cross markers "×" under the blocks denote the fluid damping.

Table 4.3 Parameters of Dynamic Model

Parameter	**Description**
x_t	Displacement of the two piston rods
r_p	Radius of the pinion
θ	Angular position of the output shaft
$\ddot{\theta}$	Angular acceleration of the output shaft
τ_{t1}, τ_{t2}	Torques provided by the two cylinders
τ_o	Output torque
I_p	Inertia of the pinion and output shaft

Table 4.4 Values of Major Parameters

Parameter	**Value**
Pipe inner diameter (mm)	4.0
Ratio of pipe inner diameter to thickness	4.0
Pipe material	PA 6
Pipe length (m)	10.0
Piston diameter (mm)	13.0

As for the three-cylinder configuration in **Fig. 4.9**, each cylinder can generate a unidirectional force, which comes from the fluid pressure within the pipeline. The output torque contributed by the i^{th} cylinder, can then be described as $\tau_i = F_i \cdot d_i$, where F_i is the force provided by the cylinder and d_i is the distance between the center line of the i^{th} piston rod and the rotation axis of output shaft. In **Fig. 4.10**, d_i can be calculated as $d_i = R \cdot \sin\beta_i$, where R is the rotational radius and β_i denotes the angle between the axis of the i^{th} piston rod and *AO*. Here $\sin\beta_i$ can be further calculated by Sine Law as:

$$\sin\beta_i = \frac{s\cdot\sin(\theta-\varphi_i)}{\sqrt{s^2+R^2-2s\cdot R\cos(\theta-\varphi_i)}} \tag{4.2}$$

where θ is the angular position of the output shaft and φ_i is the phase for the i^{th} cylinder, with values of $2\pi/3\cdot(i-1)$ for $i=1,2,3$. The torques generated by the three cylinders are summed at the crankshaft as:

$$\sum_{i=1}^{3}\tau_i = I_r\ddot{\theta}+\tau_o \tag{4.3}$$

where I_r is the total inertia of the rotational components, $\ddot{\theta}$ is the angular acceleration of the output shaft. Therefore, the correlation between the output torque and the forces provided by the cylinders, which are governed by fluid pressure, can be described by the dynamics model of the three-cylinder configuration. Torque control is then made possible to be implemented on this actuator.

The second part of the dynamics model describes how the input force F_{in} is transmitted from the master side through the fluid pipeline and hence generating an output force of F_{out} at the slave side (**Fig. 4.2**). A spring-mass-damping system (**Fig. 4.11**) is adopted to approximate the interaction between pistons (mass m_p) and hydraulic fluid (mass m_{eq}). Their interconnection is represented by the spring elements of stiffness $2K_t$, which accounts for the pipeline compliance and fluid compressibility. It is assumed that the system damping is induced by the rolling diaphragm and fluid friction can be described by the coefficients c and B_{eq}. Pipeline compliance is defined at a situation that input force F_{in} is applied at piston 1 and the piston 2 is terminated. The following two equations **(4.4-5)** describe the hoop stress σ_θ and radial stress σ_r at the inner pipe wall in response to the applied pressure P, according to Lamé Formula:

$$\sigma_\theta = P\cdot\frac{D_{pi}^2+D_{po}^2}{D_{po}^2-D_{pi}^2},\ \sigma_r=-P \tag{4.4}$$

where D_{po} and D_{pi} denote the outer and inner diameters of the pipeline. For pipes made of a linear isotropic material, which has material modulus of elasticity E and Poisson's ratio υ, the hoop strain is equivalent to:

$$\varepsilon_\theta = \frac{\Delta D_{pi}}{D_{pi}} = \frac{\sigma_\theta - \upsilon\sigma_r}{E} \quad \textbf{(4.5)}$$

The fluid volume changes inside the cylinder of input equal to the changes in the pipe for a closed system, which gives:

$$\left[(D_{pi} + \Delta D_{pi})^2 - D_{pi}^2\right] L_p = D_{in}^2 \cdot \Delta x_{in} \quad \textbf{(4.6)}$$

where ΔD_{pi} is the change of pipe inner diameter, D_{in} is the diameter of cylinder, Δx_{in} is the displacement of input piston and L_p is the length of pipe. Therefore, the inner diameter change of pipe could be determined by:

$$\Delta D_{pi} \approx \frac{D_{in}^2 \cdot \Delta x_{in}}{2 D_{pi} L_p} \quad \textbf{(4.7)}$$

With **(4.4)** to **(4.7)** and the assumption that the pressure comes from the input force $F_{in} = P \cdot (\pi D_{in}^2/4)$, the pipeline stiffness K_p observed at the piston can be derived as:

$$K_p = \frac{F_{in}}{\Delta x_{in}} = \frac{\pi E D_{in}^4}{8 D_{pi}^2 L_p} \left[\frac{D_{pi}^2 + D_{po}^2 + \upsilon D_{po}^2 - \upsilon D_{pi}^2}{D_{po}^2 - D_{pi}^2}\right]^{-1} \quad \textbf{(4.8)}$$

The fluid stiffness due to compression could be modeled as $K_f = E_v \cdot A_{in}^2/V$, where A_{in} is the cross-sectional area of the input cylinder, V is the total volume of fluid and E_v is the fluid bulk modulus. Hence, the equivalent transmission stiffness K_t of the hydraulic transmission pipe can be calculated as the series of pipeline compliance and fluid stiffness:

$$K_t = \frac{K_p K_f}{K_p + K_f} \quad \textbf{(4.9)}$$

For the system damping factors, it is assumed that the input force at piston 1 is F_{in} and it produces a movement at constant velocity, given that there is *zero* loading at the piston 2 ($F_{out} = 0$).

Derivation begins from establishing the fluid head loss, which is governed by the Bernoulli equation for steady and incompressible flow between any two points in a pipe:

$$\frac{P_{in}}{\rho}+\frac{v_{in}^2}{2}+gz_{in}=\frac{P_{out}}{\rho}+\frac{v_{out}^2}{2}+gz_{out}+h_f \tag{4.10}$$

where P_{in} and P_{out} represent the fluid pressures, v_{in} and v_{out} are the fluid velocities. z_{in} and z_{out} represent elevation at the input and output piston respectively. h_f is the head loss. ρ is the fluid density and g is the gravitational constant.

In this case, pipelines loss mainly contributes to head loss while the local loss at the connection surface between cylinder and tube can be neglected. Due to the fact that the pipeline loss is proportional to the length but *inversely* proportional to the diameters, the head loss in the cylinders is negligible when compared with that in the pipelines. The total pipeline loss can be approximately given as:

$$h_f=\frac{\lambda L_p {v_f}^2}{2D_{pi}} \tag{4.11}$$

where λ is the flow coefficient and v_f is the fluid velocity [160]. For laminar pipe flow, the flow rate is given by $\lambda = 64/Re$, where Re denotes the Reynolds number, $Re = \rho v_f D_{pi}/\mu$, and μ is the dynamic viscosity of fluid.

Since the pipes are put at the same elevation, the term gz_{in} and gz_{out} can be eliminated. The fluid is nearly incompressible so that the velocity at the input piston and output piston is approximately equal, $v_{in} \approx v_{out}$. And the pressure P_{out} is zero in our case with no load applied ($F_{out} = 0$). By observing that $F_{in} = P_{in} \cdot A_{in}$, the equivalent damping coefficient B_{eq} can be obtained as:

$$B_{eq}=\frac{F_{in}}{v_{in}}=8\pi\mu L_P\left(\frac{D_{in}}{D_{pi}}\right)^4 \tag{4.12}$$

For the fluid inertia, an equivalent fluid mass is involved as observed at the piston, which can be determined by energy calculation:

$$m_{eq}v_{in}^2 = m_{cyl}v_{in}^2 + m_f {v_f}^2 \quad \textbf{(4.13)}$$

where m_{eq} is the equivalent mass, m_{cyl} is the fluid mass in cylinder, and m_f is the fluid mass in the pipeline. Then the equivalent mass can be obtained as:

$$m_{eq} = m_{cyl} + m_f \left(\frac{D_{in}}{D_{pi}} \right)^4 \quad \textbf{(4.14)}$$

The dynamics of the hydraulic transmission can be described by a linear differential equation as follows:

$$\mathbf{K}x + \mathbf{C}\dot{x} + \mathbf{M}\ddot{x} = \mathbf{F} \quad \textbf{(4.15)}$$

where

$$\begin{cases} \mathbf{K} = \begin{bmatrix} 2K_t & -2K_t & 0 \\ -2K_t & 4K_t & -2K_t \\ 0 & -2K_t & 2K_t \end{bmatrix} \\ \mathbf{C} = diag\left(c,\, B_{eq},\, c\right) \\ \mathbf{M} = diag(m_p,\, m_{eq},\, m_p) \\ \mathbf{F} = \begin{bmatrix} F_{in} & 0 & -F_{out} \end{bmatrix}^T \end{cases} \quad \textbf{(4.16)}$$

In **(4.15)**, $\mathbf{x} = [x_1 \quad x_2 \quad x_3]^{\mathrm{T}}$ denotes the matrix containing displacements of input piston (x_1), fluid (x_2) and output piston (x_3). Damping coefficient c, is introduced by the rolling diaphragm. F_{in} and F_{out} are the input and output forces, respectively. The state space function can be derived as follows:

$$\begin{bmatrix} \dot{x} \\ \ddot{x} \end{bmatrix} = \begin{bmatrix} 0 & \mathbf{I} \\ -\mathbf{M}^{-1}\mathbf{K} & -\mathbf{M}^{-1}\mathbf{C} \end{bmatrix} \begin{bmatrix} x \\ \dot{x} \end{bmatrix} + \begin{bmatrix} 0 \\ \mathbf{M}^{-1}\mathbf{F} \end{bmatrix} \quad \textbf{(4.17)}$$

4.2.4 Design Optimization

This section presents the design guidelines for the rolling diaphragm-based hydraulic system in regard to the desired system performance, namely: **1)** transmission stiffness; **2)** transmission latency; **3)** pipe bending stiffness. Parametric study is performed by numerical simulation of the dynamics model (**Table 4.3**). The scope of study includes the geometric factors of the pipeline, such as pipe diameter, pipe thickness, pipe material, pipe length and cylinder diameter. *Four* typical types of pipe materials: Polycaprolactam 6 (PA 6), PA 66, Polytetrafluoroethylene (PTFE) and Polyurethane (PU), are examined. I have investigated how these design parameters may contribute to the overall performance by varying their individual values in each analysis. Their nominal values are listed in **Table 4.4** for reference.

4.2.4.1 Stiffness

Transmission stiffness – The transmission stiffness determines the repeatability and accuracy of the hydraulic actuator. The stiffness decreases when the diameter or the length increases, which could be referred to **(4.9)**. The choice of pipe material also imposes a significant influence on the transmission stiffness. PA66 offers the highest transmission stiffness because of it possesses the highest Young's modulus. The enlargement of piston diameter could also enhance the transmission stiffness, accredited to the increased piston diameter to pipe inner diameter ratio.

Bending stiffness – The bending stiffness of the pipe is also an important design consideration. It affects the bending curvature of the pipe and further the arrangement flexibility of the pipelines. As the pipe diameter increases, the pipe will become stiffer. Therefore, it becomes more difficult to be bent and arranged. Different pipe materials have disparate curves of bending stiffness, which varies from 0.05 to 0.17 N·m^2 at a pipe inner diameter of 4 mm.

4.2.4.2 Latency

Transmission latency – the effect of pipe inner diameter, pipe length and material on the transmission latency are discussed in this section. The power transmission in this system could be considered as the simultaneous occurrence of a pressure and velocity changes. Such velocity of pressure transient through the fluid in a closed conduit could be deduced as:

$$c_p = \left(\sqrt{\frac{\rho \psi D_{pi}}{e \cdot E} + \frac{\rho}{E_v}} \right)^{-1} \quad \textbf{(4.18)}$$

where the parameters are summarized in **Table 4.5** [161]. The pipe support factor ψ is a function of the pipe material (υ), the pipe inner diameter (D_{pi}) and the pipe wall thickness (e), which can be calculated as following for the case of thick-walled pipe (D_{pi}/e < 10) without anchorage throughout the length [161]:

$$\psi = \frac{2e}{D_{pi}}(1+\upsilon) + \frac{D_{pi}}{D_{pi}+e} \quad \textbf{(4.19)}$$

The latency with baseline parameter values (with the ratio of pipe inner diameter to thickness varying and pipe thickness fixed at 1 mm) is around 21 ms. The enlargement of pipe inner diameter larger than 2 mm causes slight increase of the latency. But the decline of pipe inner diameter under 1 mm brings significant rise in latency. The latency is proportional to the pipe length. Meanwhile, pipe with more rigid material reduces the transmission latency.

Table 4.5 Physical Parameters

Parameter	**Parameter name**
c_p	Velocity of pressure transient in fluid
E_v	Bulk modulus of fluid
E	Young’s modulus of pipe material
υ	Poisson’s ratio of pipe material
ρ	Fluid density
D_{pi}	Pipe inner diameter
e	Pipe wall thickness
ψ	Pipe support factor

All in all, several design tradeoffs are studied to account for the required dynamics performance and dedicated operating conditions. Shorter pipelines are preferable as a general design rule. Because it can decrease the transmission latency, reduce the fluid inertia and give rise to a higher transmission stiffness. For surgical applications that demands on positional accuracy, such as stereotaxy, pipelines design with smaller diameter and pistons with a larger diameter should be adopted to enhance the transmission stiffness. However, small pipe diameter (<2 mm) can induce transmission latency and damping dramatically, which deteriorates control stability. Therefore, pipeline diameter should be expanded to adapt for applications requiring rapid dynamic response, such as tele-manipulation of a catheter in a master-slave manner. Another practical design concern is that the pipelines also become more flexible to be arranged from the control room to MRI room with smaller bending stiffness by decreasing the pipeline diameter.

4.3 Experiments and Results

In the following performance tests of the proposed rolling-diaphragm-sealed hydraulic actuation, clean water was adopted as working media and pre-pressurized at >0.05 MPa. This is to eliminate the hysteresis induced by gear backlash and the long hydraulic transmission (about 10 m). However, excessive preloading pressure leads to severe gear/pivot friction. This may in return degrade the transmission precision. In this section, force transmission is first evaluated. The effects of preloading levels on the hysteresis are then investigated. Results of position tracking, dynamic response and SNR tests are analyzed to validate the feasibility for driving robot in MR environments.

4.3.1 Force Transmission

Force transmission performance was evaluated with a weight-lifting experiment. A winch of 50-mm radius was coupled to a slave rotary motor depicted in **Fig. 4.2**. With the preloading pressure at 0.10 MPa, this slave motor could lift a 3-kg weight at a constant speed of 100.1 mm/s. This was corresponding to a torque output of 1.47 Nm, and a net power of 2.93 W. A torque sensor was incorporated at the master side to monitor the input torque. The transmission efficiency was calculated as 70%. Such power exertion capability is more than sufficient to manipulate/steer most of the surgical instruments. Actually, the max. torque output of the current prototype is limited by the 3D-printed components, such as the tiny gear teeth and thin shaft. Increasing the mechanical strength of these components will significantly enhance the power transmission performance. An alternative is to fabricate these components with standard industrial machining.

For these procedures, there are still wide choices of MR safe materials, e.g. POM or Nylon. They can all contribute to a more robust structure for enhanced actuation torque and durability.

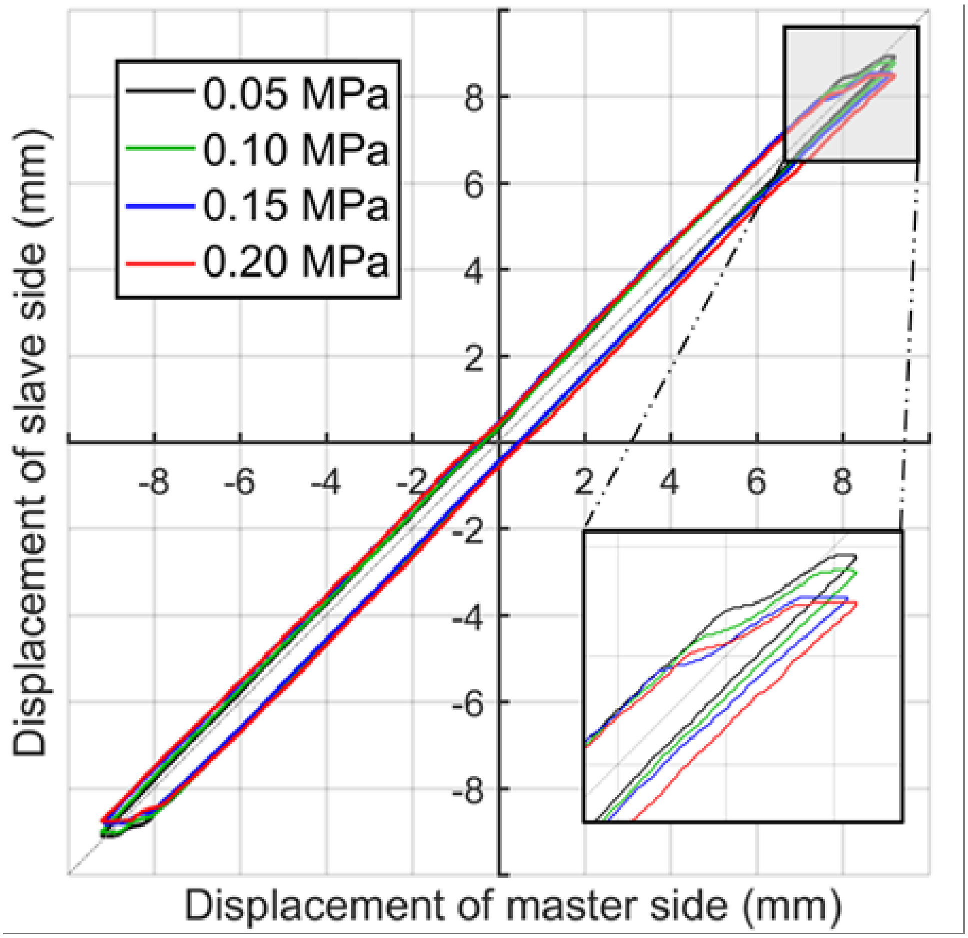

Fig. 4.12 Hysteresis of the proposed hydraulic transmission. The average values of hysteresis, 0.88mm, 0.93mm, 1.02mm and 1.29mm are measured, on condition of preloaded pressure 0.05 MPa, 0.1 MPa, 0.15 MPa and 0.2 MPa, respectively.

4.3.2 Hysteresis

Hysteresis is a primary concern for applications that require reciprocating motion and accurate manipulation with high resolution, e.g. intra-cardiac catheterization for electrophysiological ablation (**Chapter 6**). Hysteresis may attribute to several factors, e.g. transmission friction, component elasticity and residual backlash after preloading. The area of the hysteresis loop represents the energy dissipation in one operation cycle. **Fig. 4.11** depicts the hysteresis of a pair of master-slave rotary actuation unit. Both rotary displacements of master and slave units were measured and computed into the translational displacements of each cylinder pair. This periodic motion at the master side was controlled by an embedded Proportion-Integration-Differentiation (PID) positional controller at the frequency of 0.1 Hz. The motion range was 18 mm, which covered 70% of the 25-mm stoke of rolling diaphragm. Hysteresis tests were conducted with four preloading pressure levels, i.e. 0.05 MPa, 0.1 MPa, 0.15 MPa and 0.2 MPa. There was only slightly increase on the measured hysteresis with higher preloading pressure, owing to the rise in static friction. **Fig. 4.13** shows the slave actuation unit precisely followed the sinusoidal motion of the master unit. The max. absolute error is 0.67 mm.

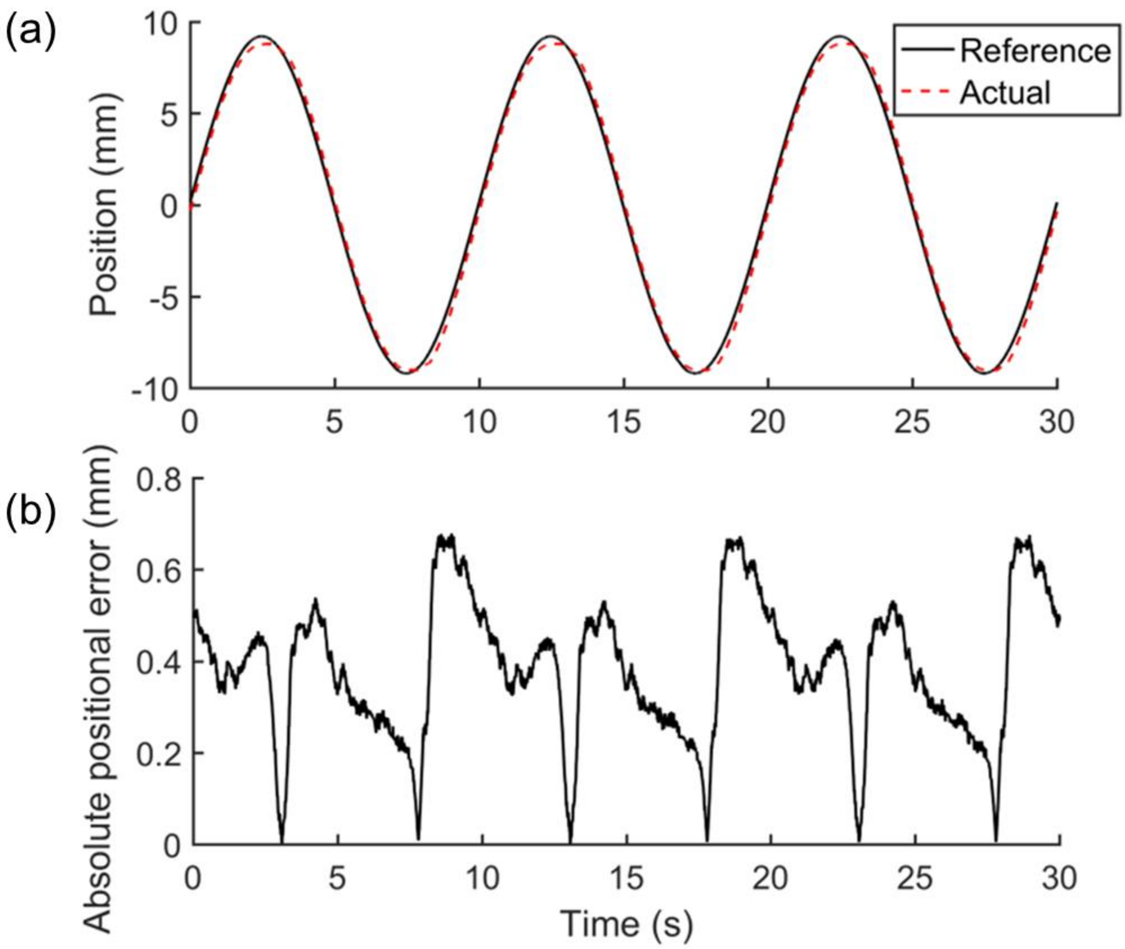

Fig. 4.13 **(a)** Periodic motion of the master-slave actuation. The slave position (dash line) can precisely follow the sinusoidal reference trajectory (concrete line) of the master unit at 0.1 Hz. **(b)** Absolute error has a maximum of 0.67 mm.

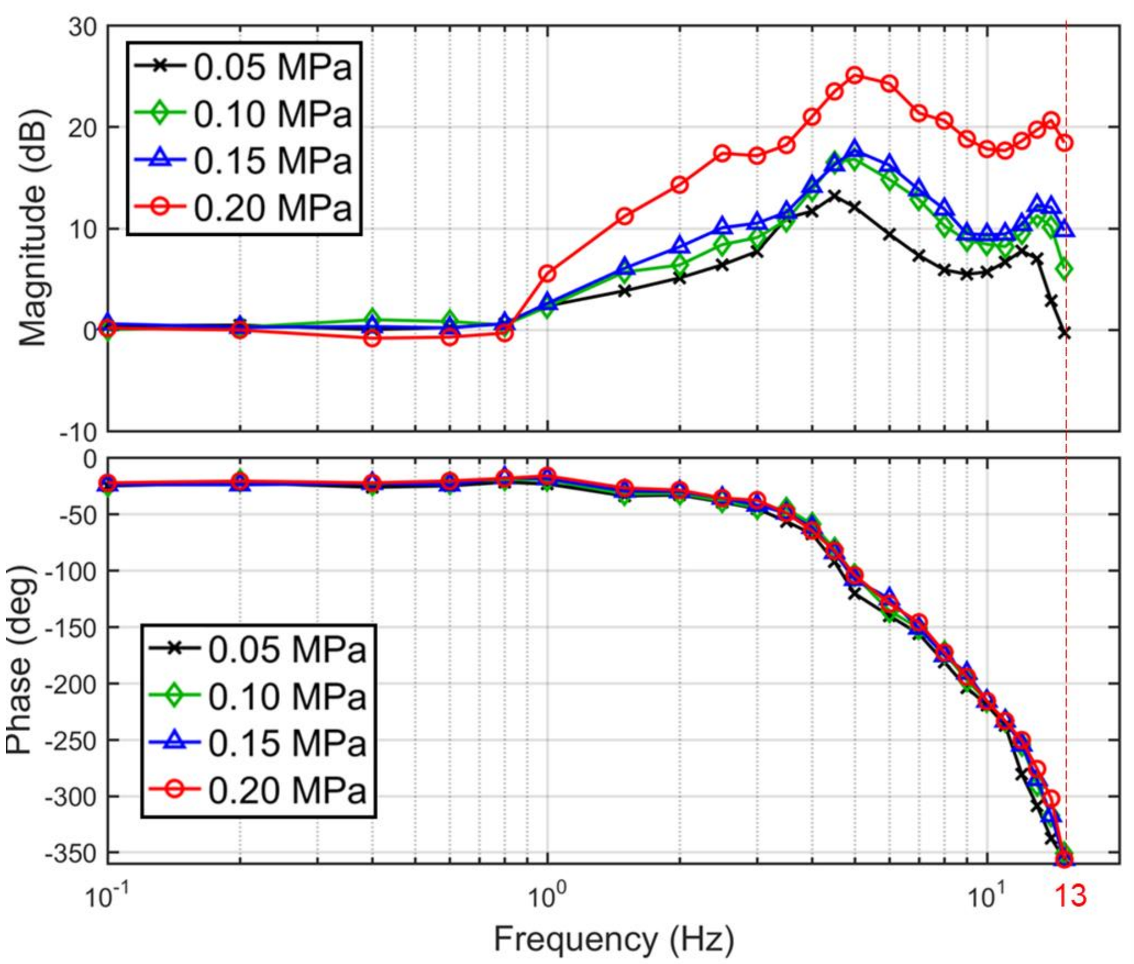

Fig. 4.14 Experimental bode plot showing the torque response of the master-slave hydraulic transmission at four levels of preloaded fluid pressure, namely 0.05, 0.10, 0.15, 0.20 MPa. The magnitude and phase shift are shown in the top and bottom plots respectively. The data are collected at the steady state from 10 cycles. Despite this master-slave hydraulic system is usually operating under <1Hz (delay <45ms). Maximum test frequency reaches 13 Hz to explore the transmission performance at wider bandwidth.

4.3.3 Dynamic Response

The dynamic performance under different preloading pressures was investigated based on a frequency response method. A sinusoidal torque input $\tau = A\sin(\omega t)$ was given to the master actuation unit, where A, ω and t denoted amplitude, frequency and time, respectively. The torque output of slave unit was recorded. Amplitude A was set as 0.1 Nm, within the nominative torque range of motor operation. **Fig. 4.14** depicts the resultant Bode plot, which characterizes the magnification M and phase-shift ξ of the hydraulic transmission system at steady state. Note that the frequency response at steady state becomes $\tau_{ss} = MA\sin(\omega t + \xi)$ in a linear time-invariant system.

The magnitude value peaked at about 5 Hz. This might correspond to the natural frequency of the overall actuation system. The increase of preloading pressure level had no significant impact on the natural frequency. But this pressure increase could induce the rise of magnification. The phase lag of this 10-m hydraulic transmission was kept within approximately $25°$ at low-frequency actuation (≤ 1 Hz). It was not influenced by the variation of preloading pressures. Under the 0.20 MPa pre-pressurization, 45 ms and 74 ms delay was measured at the actuation frequency of 1 Hz and 13 Hz, respectively. The compliance of 10-m long nylon tubes and rolling diaphragms might result in this phase shift.

4.3.4 SNR Test

Referring to the MR safe classification of ASTM standard F2503-13 [162], the slave actuation unit comprised with solely nonmagnetic, nonmetallic and non-conductive materials can be classified as MR safe. Basic operation was simulated inside a 1.5T MRI scanner (SIGNA, General Healthcare) for the compatibility test. The master actuation unit was placed in the control room. The slave actuation unit was placed by an SNR MRI phantom (J8931, J.M. Specialty Parts). The MR images of this phantom were acquired to evaluate the potential EMI introduced by the slave actuation unit.

Fig. 4.15a shows the resultant phantom images under four actuation operating conditions: **i)** *Phantom*: only the phantom was placed at the scanner isocenter, serving as the baseline for evaluation; **ii)** *Static*: the slave actuation unit introduced and its power remained OFF; **iii)** *Powered*: hydraulic and electric power were ON, but the actuation unit kept still; and **iv)** *In motion*: the actuation system was in operation. The reduction of SNR is introduced to quantify the EM-induced effects on MRI. SNR is defined as $J = I/\sigma$, where I represents the mean intensity value of a 40×40-pixel region at the image center, σ is the standard deviation of intensity value in a region at the lower corner with same size [163]. Max. SNR loss was less than 2% as shown in **Fig. 4.15b**. MR images had no observable image artifact even when the actuation unit at full motion.

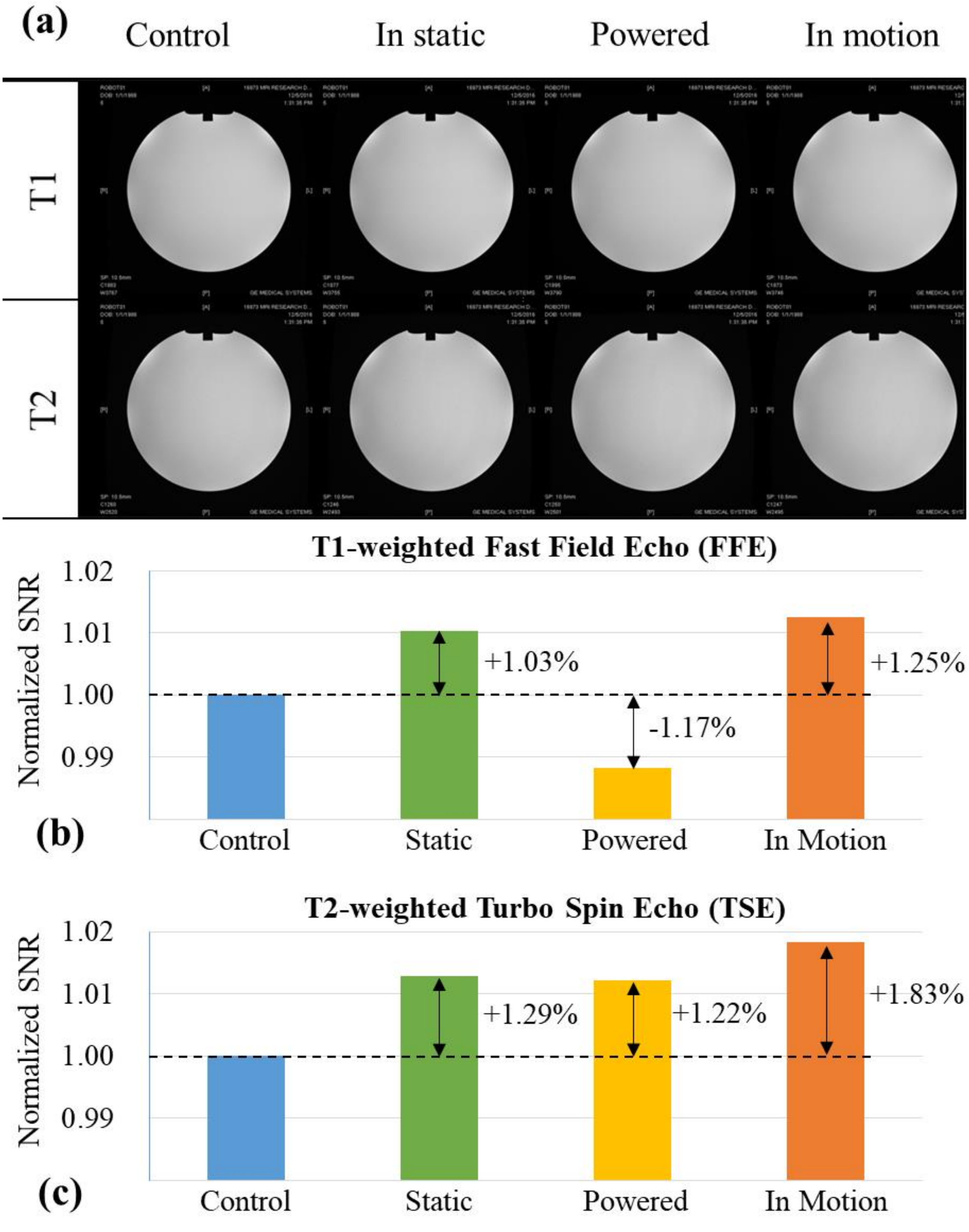

Fig. 4.15 **(a)** MR images of an SNR bottle phantom placed aside, which indicate negligible EMI generated during operation. SNR test results of two imaging sequences: **(b)** T1-weighted FFE, and **(c)** T2-weighted TSE. SNR losses in both sequences are within 2%.

4.4 Conclusions

An integrated hydraulic transmission actuation is proposed, using rolling-diaphragm-sealed cylinders to provide MR safe and high-performance actuation. Through hydrostatic transmission via 10-m long hydraulic tubes, the power from the master actuation unit in control room can be transmitted to the slave unit in MRI room in a remote way. The actuation design can be customized for a wide range of scenarios, with flexible size, motion range and accuracy. The novel three-cylinder design can provide continuous bidirectional rotation with unlimited range. Kinematics and dynamics models of the hydraulic transmission are established to achieve precise open-loop control. The model is also utilized to identify the key design parameters that govern the system performance, namely transmission stiffness, latency and pipe bending stiffness. Design tradeoff is also presented in an analytical study. It is suggested that larger pipe diameter leads to the decrease of fluid friction. It may also result in higher transmission efficiency and smaller phase lag. Shorter tubes are also preferable, which can reduce the fluid inertia and increase the stiffness.

Experiments have demonstrated the proposed hydraulic transmissions have small hysteresis (1.29 mm at 0.1 Hz) and quick response (74 ms at 13 Hz). Despite the hysteresis increasing slightly along with the increase of preloading pressure (0.88 mm at 0.05 MPa, and 1.29 mm at 0.2 MPa), effective force transmission can still be maintained as depicted in the Bode plot. An acceptable system delay, 45 ms at 1 Hz, can be attained within the normative actuation frequency. Distilled water is employed as transmission fluid for its ease of sterilization and availability. In summary, the proposed hydraulic actuation components, particularly the three-cylinder design, which enables high-performance tele-manipulation, would become a benchmark of MR safe robotics. These could be applied to many types of MRI-guided interventions, such as neurosurgery, intra-cardiac catheterization and transoral tumor ablation. The details regarding the incorporation with three different surgical robots will be discussed in the following **Chapter 5**, **Chapter 6** and **Chapter 7.**

Chapter 5
Application of Hydraulic Actuation on Stereotactic Neurosurgery

5.1 Introduction

IN **Chapter 2**, I have reviewed the current state-of-art robotics systems for MRI-guided neurosurgery. Stereotaxy is a technique that can locate targets of surgical interest using an external coordinate system as reference. Deep brain stimulation (DBS) is one of the common stereotactic procedures, which is a surgical treatment for debilitating motor symptoms of Parkinson's disease (PD) and dystonia. *Two* long (e.g. 300mm) slender (≈Ø1.3mm) DBS needles will be individually guided by a stereotactic frame and inserted through burr holes ($\leq \emptyset 14$mm) into the patient's skull. Stimulation electrodes embedded at the tip of needle will then be implanted to the deep brain areas of interest, thus delivering programmed electrical impulses.

5.1.1 MRI-guided High-Intensity Focused Ultrasound (HIFU)

MR-guided focused ultrasound (MRgFUS) is a non-invasive therapy that uses ultrasonic waves to deliver heat or agitation to the targeted tissue/lesion. It may offer alternatives for certain subspecialties of radiation oncology, especially for stereotactic radiation therapy [164]. It has been recently approved by FDA for the treatment of refractory essential tremor (ET). Other applications, such as brain tumor, movement disorders and resistant psychiatric conditions, are under investigation. More than twenty-five clinical trials have now publically registered for the treatment of these neurological disorders [165]. **Fig. 5.1** shows a well-known MRgFUS system, Exablate Neuro® from INSIGHTEC Ltd., consisting of multi-element phased array ultrasound transducers operating at $220-650$ kHz. These transducers are mostly constructed in helmet-shape (~Ø30cm), forming a natural focus. In-between the helmet and patient skull, there is a cooling system supplied with water at constant temperature (approximately 18℃). At low ultrasonic frequency, blood-brain barrier (BBB) can be opened by the focused-ultrasound. Neuronal activities can be thus modulated for the therapeutic compounds delivery. While at high operating frequency, the system can be used to ablate (generally >56℃) discrete brain tissues within the focal region ($\sim 3 \times 15$ mm) at submillimeter accuracy.

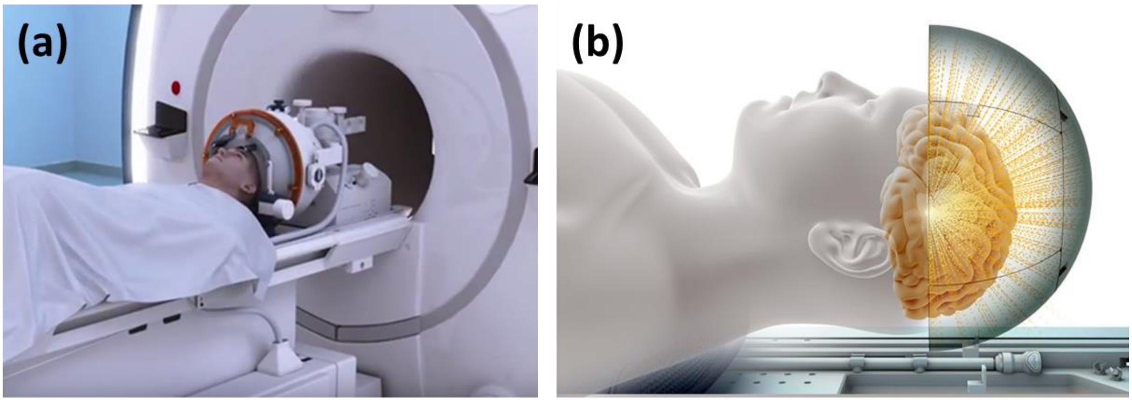

Fig. 5.1 (a) Exablate Neuro® system for MRI-guided HIFU. Patient lying at the MRI table has to wear a helmet, which contains a phase array transducer system composed of over 1,000 individual transducer elements. The space between patient head and transducer is a cooling system filled with constant-temperature (approximately 18℃) water. It is to protect the skull bone temperature remaining within the safe limits. **(b)** Focused ultrasound generating heat and ablating tissue at the focal point.
Image source: INSIGHTEC Ltd.

Despite the promised advantages of non-invasiveness and high accuracy, challenges still exist in HIFU brain applications. **i)** It is difficult to treat targets closely located to the skull surface with high frequencies. Large amount of energy is necessary for coagulative necrosis, but it can also result in bone heating. Non-thermal ablation therapy may be an alternative to circumvent this problem. However, the associated unintended BBB opening may further complicate the procedures. The experience of this therapy is still preliminary and needs more trials. **ii)** For bilateral targets in functional neurosurgeries, MRgFUS can only treat one target at a time. Unlike the conventional DBS, surgeons have to be conservative regarding the irreversible coagulative heating, and wait for longer time to determine the treatment on the other target. **iii)** It needs to await larger amount of clinical trials and longer follow-up to evaluate the efficacy of MRgFUS ablation, especially compared to the conventional open surgery for ET and other indications. **iv)** Current MRgFUS requires patient lying in the MRI machine for several hours. The needs for stereotactic frame and complete head shave may also increase patient uncomfort. Improvements in surgical workflow and sonication protocol are imminent to enhance tolerability and reduce surgical time.

5.1.2 MRI-guided Deep Brain Stimulation (DBS)

In the context of these challenges in the applications of MRgFUS, it is still necessary to further develop DBS in consistent with the conventional approach. Although the standard workflow of stereotactic neurosurgery has been established for over half a century, the operation still remains challenging due to its complicated workflow and high demand for surgical accuracy. The average recorded error of 2-3mm is just barely tolerable [166]. Stereotactic navigation could be further complicated by substantial deformation of intracranial contents, namely “brain shift”, which occurs inevitably after craniotomy. The shift is mainly caused by gravity, CSF leakage, anesthesia and surgical manipulation. It could induce misalignment (as large as 10-30mm [96]) of the pre-op planning path, aiming beyond the actual target. In conventional DBS guided by fluoroscopy/CT, MER is adopted frequently to confirm the acceptable placement of electrodes while assessing the corresponding symptoms with the awake patient under local anesthesia. These complications pose increasing expectation on intra-op MRI-guided stereotaxy. Unlike fluoroscopy/CT, MRI can directly visualize the critical brain structures and targets of interest (e.g. subthalamic nucleus (STN), globus pallidus interna (GPi) or ventral intermediate nucleus).

Currently, there are very limited choices of MR safe stereotactic systems [43, 166] (e.g. NexFrame®, Medtronic Inc., USA and ClearPoint®, MRI Interventions Inc., USA). They generally require intensive manual adjustment of the stereotactic frame, and the patient to be transferred in-and-out of the scanner bore. This eventually disrupts the workflow. To this end, MR safe/conditional robotic platforms have been introduced. An FDA approved prototype, SYMBIS® (formerly called NeuroArm, IMRIS Inc., Canada), is an MRI-compatible robot built predominantly for tele-operated microsurgery, and only one of its robot arms capable of MRI-guided stereotaxy [52]. This MRI-compatible robot arm is actuated by piezoelectric motors and the robot body is made of titanium or PEEK to ensure its MRI compatibility [47]. It can be mounted on the magnet bore, providing constant spatial relation with the magnet isocenter and the patient's anatomy. However, it creates a large footprint in the surgical theater while transferring the intra-op scanner in-and-out for each imaging update, introducing much procedural complexity.

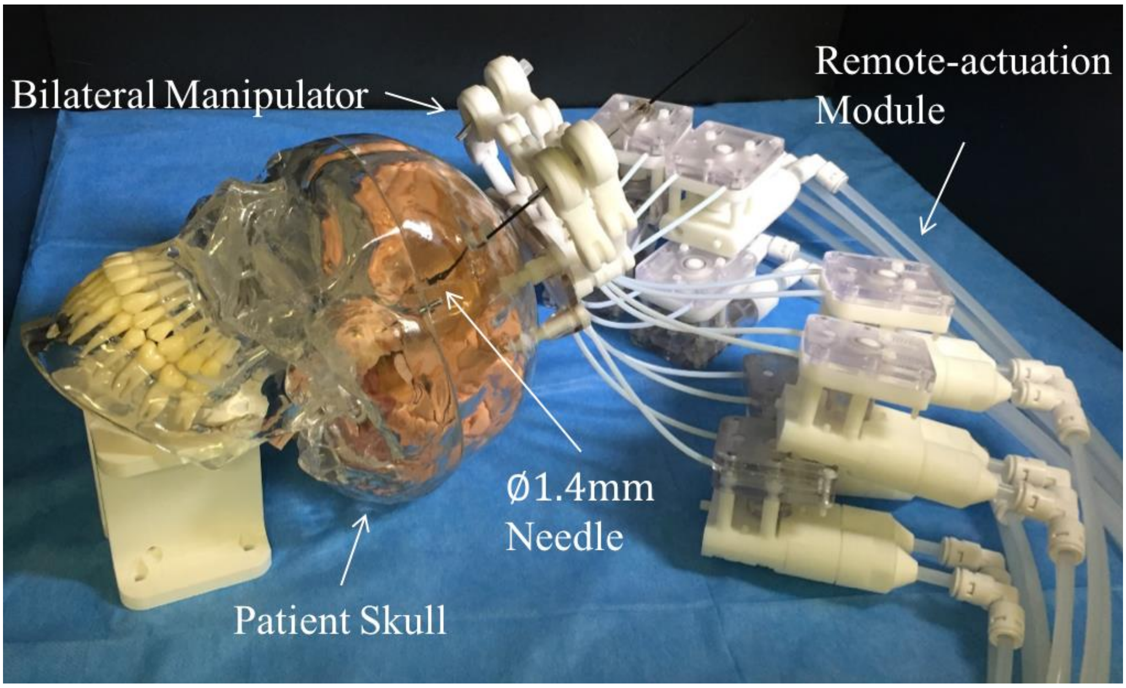

Fig. 5.2 Slave module of the proposed MR safe robot for intra-op MRI-guided bilateral stereotactic procedures.

Neuroblate® (Monteris Medical Inc., USA) is a robotic probe with 2 DoFs (rotation and translation) driven by piezoelectric motors for stereotactic laser ablation [8]. The probe can be passively oriented by AXiiiS stereotactic miniframe, which consists of a ball-socket, three legs and a 360° directional interface. Real-time MR-thermometry data can be provided to ensure safe ablation boundaries from surrounding structures [55]. For multiple surgical paths, the patient will be transferred back to the operating theatre (OT) to remove the probe, relocate/realign the frame and create new craniotomy.

A research prototype developed by Fischer *et al.* [61, 167] towards needle-based neural interventions was reported. The robot is kinematically equivalent with the conventional stereotactic frame (e.g. Leksell frame, Elekta AB, Sweden) and is actuated by piezoelectric motors as well. A control system for these motors is specially designed to allow the simultaneous MR imaging and robot motion, ensuring sufficient image quality for surgical guidance. The robot can be fixed on the surgical table. However, to complete the whole procedure inside the MRI scanner, it may require a specialized MRI head coil or scanner with larger spatial clearance for robot's operation (1.5/3T MRI scanners usually with inner diameter of Ø600 mm).

Compactness and MRI compatibility are two crucial issues regarding the feasibility and adaptability of robots in the regular hospital setup. Very few robotic platforms can fit with the MRI head coil, and also operate during continuous imaging without degrading the image quality. None of the aforementioned platforms can accommodate the trend towards *bilateral* DBS, which becomes the most popular approach for PD [168]. In addition, positional tracking in almost all of them is conducted using either optical tracker or passive MR fiducials, which introduces significant error while registering the robot coordinates with the imaging ones [169]. MR-based tracking involves tiny coils (e.g. Ø3×8 mm^3 [170]) designed to resonate with MR Larmor frequency. It enables real-time localization of robotic instruments. In general, there is no robotic system for functional neurosurgery incorporated with MR safe actuation and MR-based tracking, capable of performing stereotactic manipulation inside the MRI bore [171]. Therefore, the contributions in this chapter[5] can be well-differentiated as follows:

i) Development of the *first* intra-op MRI-guided robot capable of performing *bilateral* neuro-stereotaxy based on a single anchorage on the patient skull. Navigation for both bilateral targets can be performed independently and simultaneously.

---

[5] The work in this chapter has been presented in the following paper and patent:

[1] Z. Guo, Z. Dong, K.H. Lee, C.L. Cheung, H.C. Fu, J.D.L. Ho, H. He, W.S. Poon, D.T.M. Chan, K.W. Kwok. *Compact Design of a Hydraulic Driving Robot for Intra-operative MRI-guided Bilateral Stereotactic Neurosurgery[J].* **IEEE Robotics and Automation Letters**, 2018, 3(3): 2515-2522.

[2] Z. Guo, Z. Dong, K.H. Lee, C.L. Cheung, H.C. Fu, K.W. Kwok. *Robotic stereotactic system for MRI-guided neurosurgery*, US Prov. Patent: **US62/623,280**. [Filed on Jan. 29, 2018]

[3] C.L. Cheung, J.D.L. Ho, Z. Guo, H.C. Chang, V. Vardhanabhuti, K.W. Kwok. *MRI Tracking Device Design, Fabrication, and Methods of use for MRI-guided Robotic System*, US Prov. Patent: **US62/640,798**. [Filed on Mar. 9, 2018]

ii) A light-weight (145.4 g) and compact (110.6×206.8×33.2 mm^3) robot designed to operate within the confined workspace of an MR imaging head coil. It is also actuated by a set of high-performance hydraulic transmissions which are MR safe/induce minimal imaging artifacts.

iii) MRI-guided navigation incorporated with *wireless* MR-based tracking coil units, offering real-time positional feedback directly in MR image coordinates. This avoids any process of offline registration between coordinates of the tracking and imaging space.

5.2 Robot Design Criteria

The proposed robot (**Fig. 5.2**) is designed to perform bilateral instrument navigation in particular for the use of intra-op MRI-guided DBS. Anatomical target, STN, is ellipsoid alike and typically situated in the deep region of brain (90 mm beneath the skull) [172]. Accuracy of the electrode placement must be less than 3 mm in order to maintain optimal stimulation effect. The robot design criteria are stated in the following section.

Two burr holes are created on the skull for the procedure. The proposed robot consists of two manipulators (**Fig. 5.3**) which will be mounted on the middle line of the two burr holes. Each provides 4-DoF manipulation of the instrument access to the corresponding hole, including pitch, roll, and offsets along X-Y plane above the skull surface. This facilitates alignment of the instrument with the desired straight-line trajectory to the STN. Fine adjustments ranged in either X or Y direction of ±2.5 mm, and pitch angle of ±33°, and roll angle of ±26° are more than sufficient to cover the required workspace in many cases [172].

Provided with the intra-op 3D MR images (e.g. acquired by gadolinium-enhanced T1-weighted volumetric scan), surgeons can identify the mid-commissural point (MCP), as well as the STN targets based on the anterior commissure-posterior commissure (AC-PC) line, thereby determining the desired entry point and insertion path to the target. Note that the robot must be operated in the deep brain target coordinates frame, which is defined on the basis of the AC-PC line, such that around 3-4 mm posterior, 5-6 mm inferior and 12mm lateral with respect to (w.r.t.)

the MCP (**Fig. 5.3**) [173].

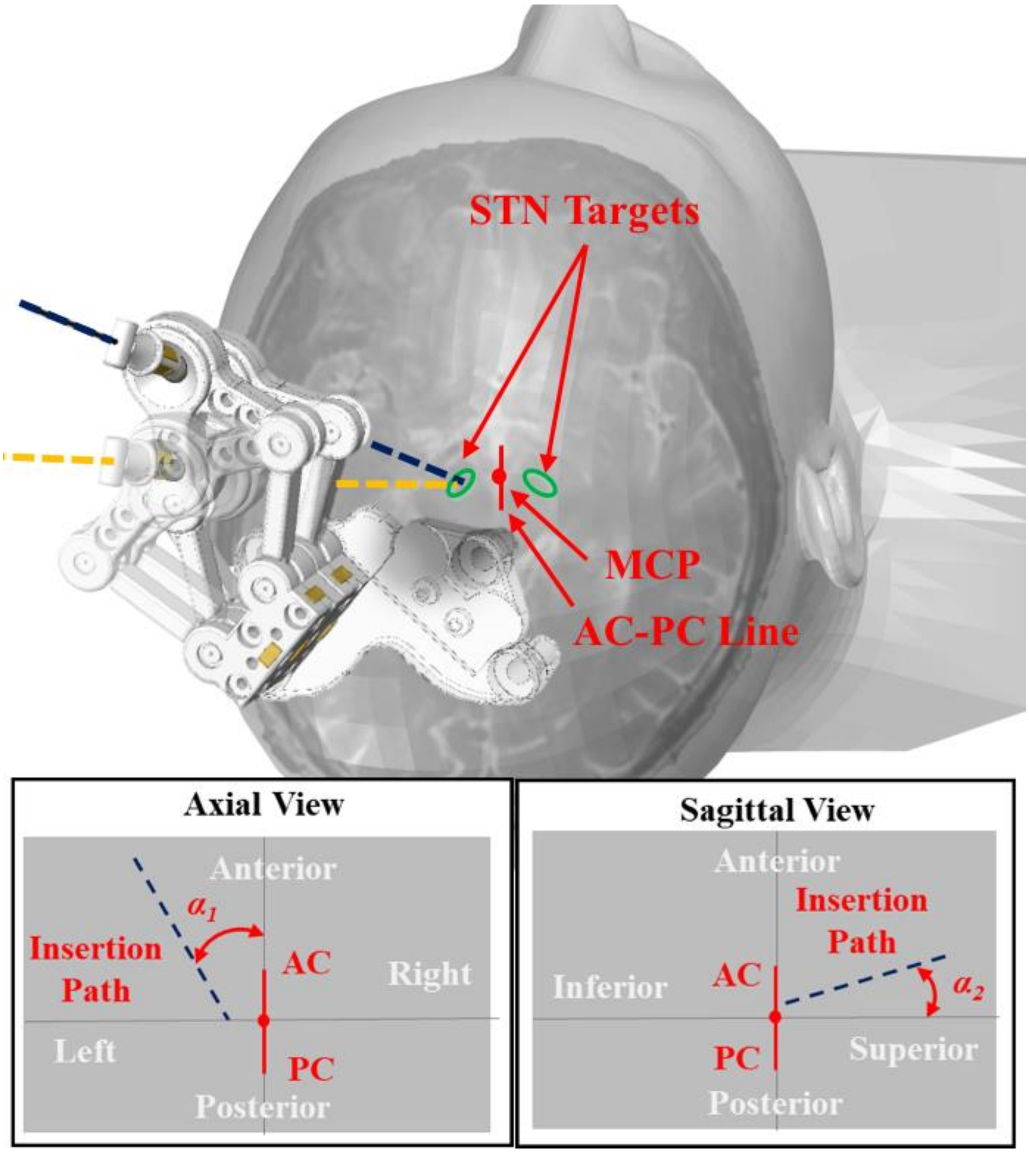

Fig. 5.3 Single manipulator shown with two possible configurations. Boundaries of STN targets highlighted in green, which could be revealed by T2-weighted MRI. The insertion path is the pre-operatively planned trajectory. Its angular inclinations (α_1 and α_2) and projection at axial/sagittal planes are shown in the block at lower left and lower right corners, respectively.

To facilitate the bilateral stereotactic manipulation, the robot is designed:

i) to be compact so that the robot body can be fixed on patient's skull properly within the head coil (inner diameter ~Ø300mm);

ii) to enable automatic trajectory planning and instrument alignment at high accuracy (<2mm);

iii) to perform bilateral manipulation independently with sufficient force (>0.8N);

iv) to fulfill the MRI compatibility upon ASTM F2503-13 standard [174], which defines MR safety, by ensuring no conductive, metallic or magnetic components are involved in the robotic platform. SNR loss is expected to be less than 5%.

5.3 Methodology

5.3.1 Master-slave Actuation Mechanism

Short-tendon-driven design is adopted with the aim to reach stringent criteria, in terms of not only the spatial constraints imposed by the head coil, but also the weight that may cause discomfort to the patient. **Fig. 5.4** shows a slave manipulator in the MRI room, which is wired with a pair of hydraulic transmission units connecting with the other pair in the control room. Such a compact design of the slave can minimize the motion inertia and facilitate manipulation flexibility across the constrained workspace. It is still capable of applying a promising level of torque/force generated by the hydraulic motor. At this stage, the design is mostly prototyped by 3D-printed components made of polymers (VeroClear™, Stratasys Inc., USA).

For a 1-DoF actuation, as depicted in **Fig. 5.4**, the manipulator base joint and the hydraulic units are separated by <200 mm. They are connected with one loop of thin (Ø0.16 mm) tendons (Dyneema polyethylene (PE), Tokushima Inc., Japan) tightly channeled through the Teflon sheaths (outer/inner diameter: Ø2/0.5 mm). The sheath material is axially-incompressible to prevent sudden/excessive pulling force applied on the skull. It also supports the route of tendon with sufficient pliability even under the high tensile strength. The tendon-sheath friction is reduced by proper lubrication. Two idlers are used to pre-load the tension in order to reduce any mechanical backlash.

The master (in control room) and slave (in MRI room) actuation system consists of two identical pinion-and-rack units to transfer the linear motion to rotary (**Fig. 5.4**). The hydraulic power originates from an electric stepper motor (57BYG250-80, Hongfuda Inc., China) and is transmitted via a pair of semi-rigid long pipes made of nylon. The length of this pipe pair is 8m. The outer and inner diameters of the pipes are, respectively, 6mm and 4mm. These design parameters are of importance to the performance of transmission dynamics. It is suggested [175] that using pipes with shorter length and larger diameter can reduce the fluid friction, transmission latency and energy loss. The pipes are filled with incompressible liquid (e.g. water) and are passed through the waveguide in between two rooms. Note that the liquid pressure can be pre-loaded to push the piston towards the pinion-and-rack gear, keeping their teeth in steady contact without backlash.

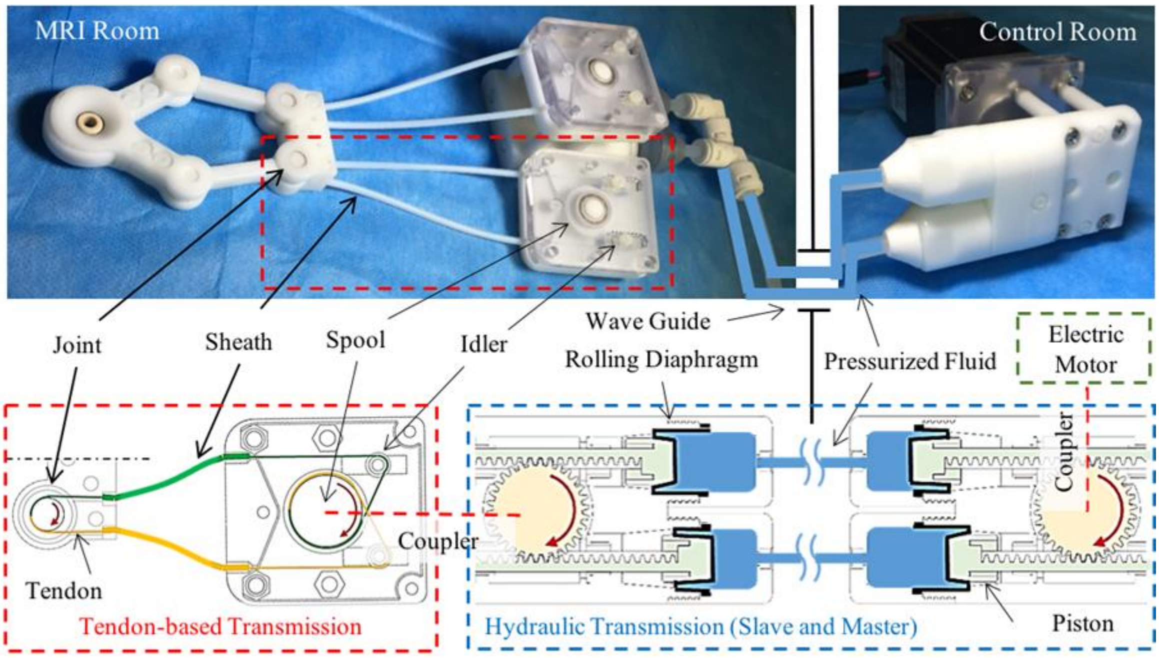

Fig. 5.4 Key components (upper row) and schematic diagram (lower row) of a 1-DoF actuation design.

Rolling-diaphragms (Ø15mm, MCS3014MOP, FEFA Inc., Germany) are used to seal the cylinders with negligible sliding friction during transmission. Let alone the pneumatic actuation approaches [176-178], it is worth noting that the resultant transmission response and power efficiency is already ensured to outperform the use of conventional hydraulic sealing with O-rings, of which the sliding friction is severe [179]. The wall of this rubber diaphragm is reinforced by fabric to withstand the high fluid pressure [180]. Its maximum linear stroke is 20 mm, driving the rotary motion of pinion at most by 100.6°, corresponding to the 201.2° rotation at the base joint.

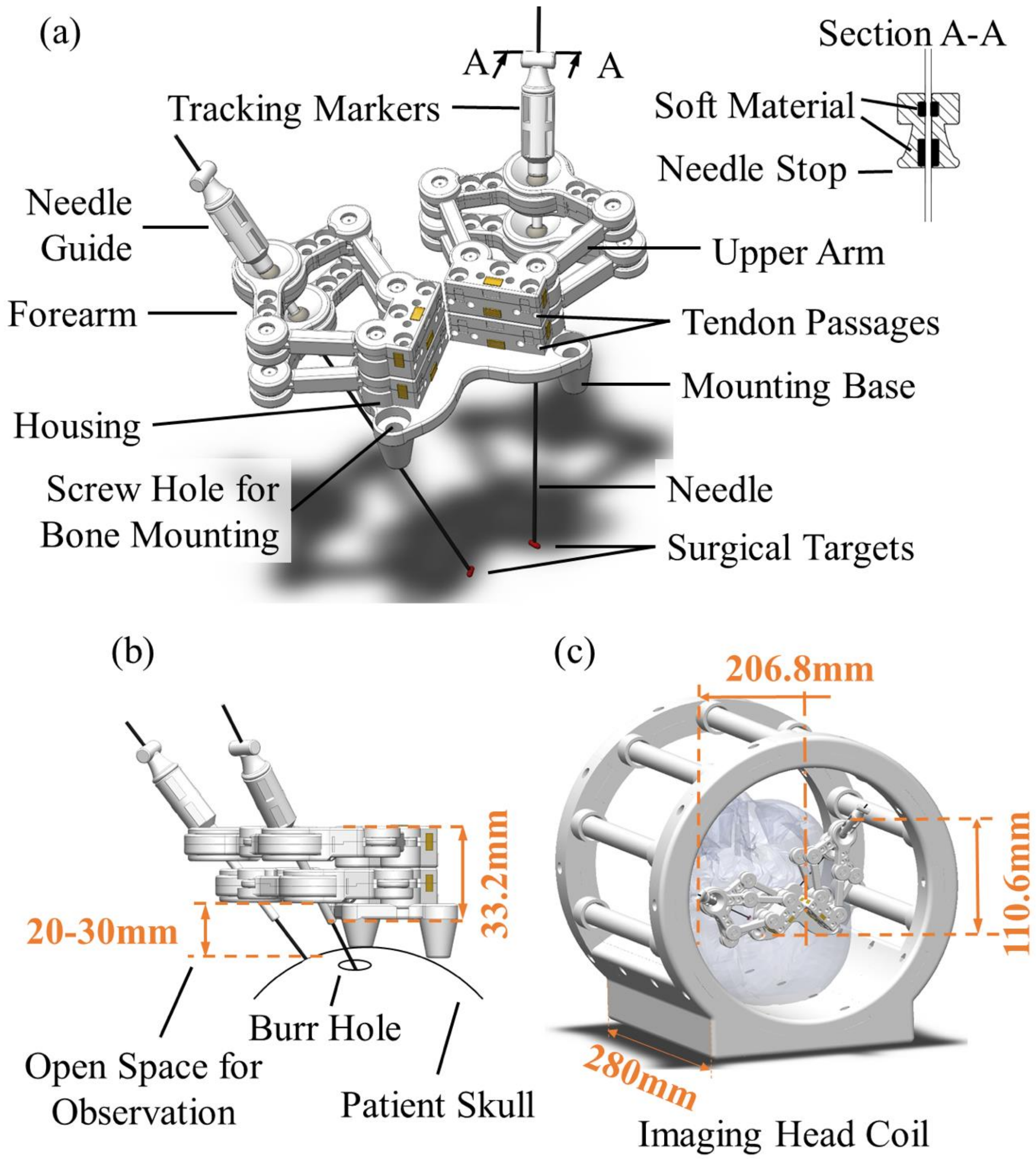

Fig. 5.5 **(a)** CAD model showing the key components of the bilateral stereotactic manipulators. **(b)** Lower layer of the manipulator positioned about 30 mm above the skull surface, which remains the sufficient space for ease of observation around the burr hole. **(c)** Overall dimensions observed, which demonstrates the design is so compact that two (bilateral) manipulators attached on skull can be fully stretched in two extreme configurations within the confined space of a Siemens-style mock head coil (inner diameter Ø265 mm).

5.3.2 Bilateral Manipulator Design

The CAD model and components of the proposed robotic manipulator are illustrated in **Fig. 5.5a**. Parallel mechanisms possess advantages in positioning accuracy and stiffness. Large workspace-to-footprint ratio of a five-bar planar parallel mechanism [181, 182] has also been discussed. Its planar position is controlled by two actuated rotational joints and three passive ones, namely $\underline{R}$RRR$\underline{R}$ mechanism. The above advantages lead to the design of two 4-DoF double-layer five-bar-linkage manipulators in bilateral setting.

The manipulator mainly consists of rigid arms, four housings and a mounting base fixed with the skull via four bone screws, two for each side. All four anchorage sites are away from the sagittal suture to avoid the possible trauma to the critical structures underneath. In the current prototype, lowest surface of the arms is 20-30 mm above the burr hole, depending on the patient-specific skull curvature and its anchorage site (**Fig. 5.5b**). This exposure space at the entry point is reserved for surgeon's observation.

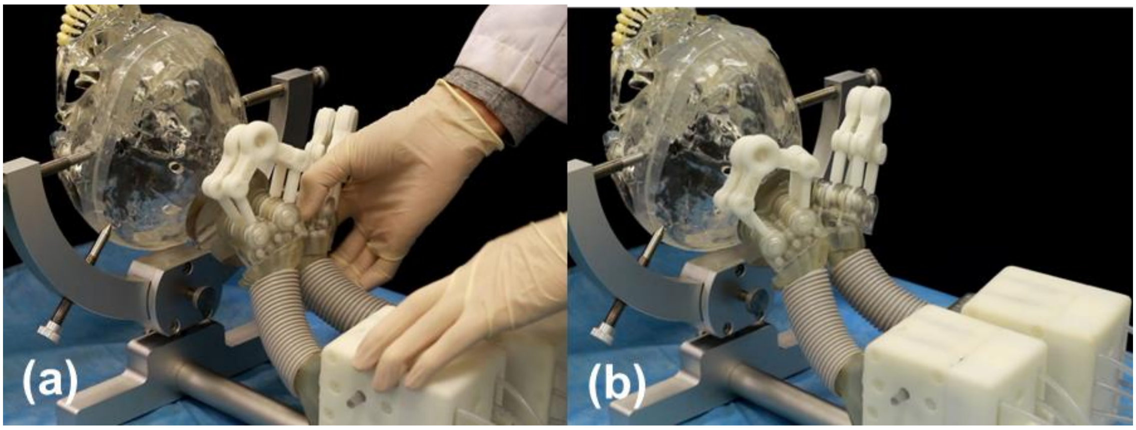

Fig. 5.6 Manual anchorage of the robot to the mounting base without the use of any tool. This design may facilitate the quick robot removal, when any acute emergency occurs and resuscitation has to be performed for the patient.

For versatility, the mounting base can be tailor-made for patient based on the pre-op images. All the housings are rigidly accommodated on the mounting base. Slots on the surface are reserved for the attachment of registration markers. Passages are also created to allow fixture of the sheath's end for better tendon routing. The revolute joints inside the housing can be therefore actuated by the tendons. Two ball joints (igus® Inc., Germany) are incorporated at the distal end of the forearms. A needle guide is oriented by these two joints, and axially fixed with the upper one. In prior to inserting the needle through the cannula held by both end-effectors of the double-layer manipulators, the allowable insertion depth is preset by the needle stop. Soft material is also embedded inside the cannula/needle stop so as to limit the needle linear motion by inducing the sliding friction.

5.3.3 Forward and Inverse Kinematics

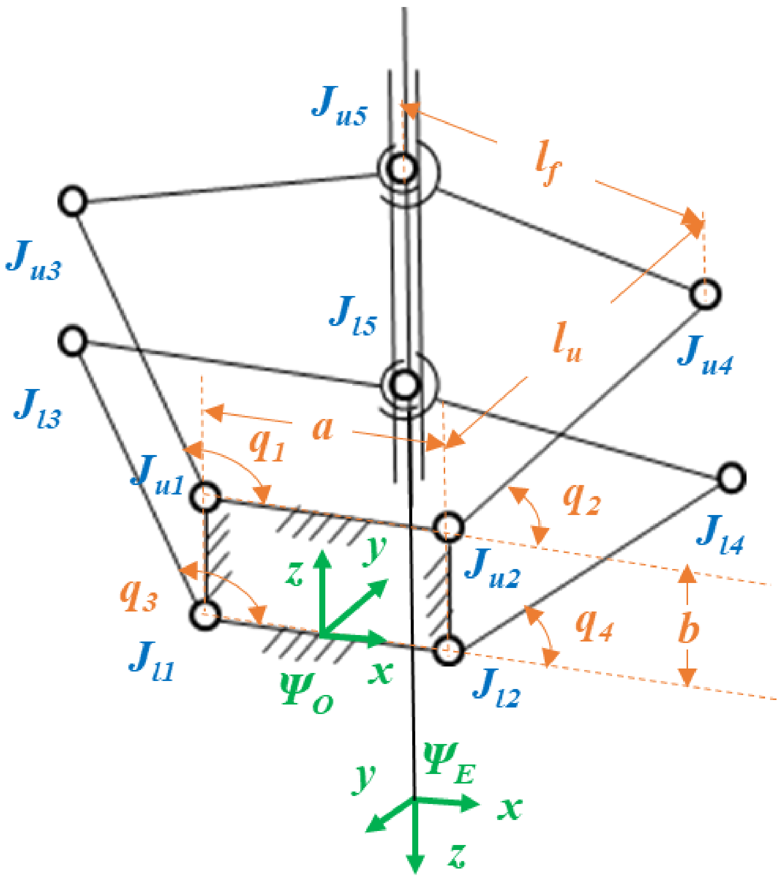

Fig. 5.7 Kinematics diagram of a single manipulator with coordinate frames Ψ_O and Ψ_E defined at the housing base and the needle tip, respectively.

Fig. 5.7 depicts the kinematic diagram of one double-layer manipulator. Two coordinate frames Ψ_O and Ψ_E are defined at the housing base and needle tip, respectively. The cannula is connected by two passive joints J_{u5} and J_{l5} from upper and lower layers, respectively. Its pose can be manipulated by independent (X-Y) planar motion of the upper and lower layers containing the points $p_{uk} = [x_{uk} \quad y_{uk} \quad z_{uk}]^T$ and $p_{lk} = [x_{lk} \quad y_{lk} \quad z_{lk}]^T$ $(k = 1, \dots, 5)$, respectively. Such points denote the 3D coordinates of their corresponding joints J_{uk} and J_{lk} $(k = 1, \dots, 5)$, which can be solved by the following equation sets:

$$\begin{cases} \|p_{u3} - p_{u5}\| = l_f \\ \|p_{u4} - p_{u5}\| = l_f \end{cases} \text{and} \begin{cases} \|p_{l3} - p_{l5}\| = l_f \\ \|p_{l4} - p_{l5}\| = l_f \end{cases} \tag{5.1}$$

Horizontal offset a separating two actuated joints (i.e. J_{u1} and J_{u2} or J_{l1} and J_{l2}) is 25 mm, while the vertical offset b of two layers is 16mm. The array of actuated joint can be defined as $q = [q_1, q_2, q_3, q_4]^T$. Therefore, the angular ranges of active joints J_{u1}, J_{l1} are corresponding to $q_1, q_3 \in [29.7°, 195.3°]$; *f*or joints J_{u2}, J_{l2} are $q_2, q_4 \in [-15.3°, 150.3°]$. The length of two proximal links (upper arms) l_u is 40 mm; for two distal links (forearms) l_f is 35 mm. Two types of singularities can be found in this five-bar linkage mechanism [183]. The first type takes place when forearms are collinear (e.g. joints J_{l3}, J_{l4}, J_{l5} are in one line), and the second one appears only when arms are fully stretched. To prevent collineation of the pair of forearms, a mechanical limit on the relative rotation is adopted. For instance, joint J_{l5} will always locate outside quadrangle area of $J_{l1}J_{l2}J_{l3}J_{l4}$.

To resolve the forward kinematics, the needle's orientation can be denoted by the unit $\vec{r}$ as:

$$\vec{r} = \frac{(p_{l3} - p_{u5})}{\|p_{l3} - p_{u5}\|} \tag{5.2}$$

Assume the insertion depths, d_u and d_l, are defined as the linear distances from joints J_{u5} and J_{l5}, respectively, to the target. The position of needle tip p_t, acting as the ultimate end effector of both manipulators can be calculated:

$$p_t = p_{u5} + d_u \cdot \vec{r} \tag{5.3}$$

Also, the velocity of the end effector of upper layer J_{u5} can be deduced from the above equations:

$$\dot{p}_{u5} = \begin{bmatrix} \dot{x}_{u5} & \dot{y}_{u5} & 0 \end{bmatrix}^T = \begin{bmatrix} \frac{A_1B_2 + B_1B_2}{A_1B_2 + B_1B_2} l_u \sin q_1 - \frac{A_2B_1 + B_1B_2}{A_1B_2 - A_2B_1} l_u \sin q_2 \\ \frac{A_1A_2 + A_1B_2}{A_1B_2 + B_1B_2} l_u \sin q_1 - \frac{A_1A_2 + A_1B_2}{A_1B_2 - A_2B_1} l_u \sin q_2 \\ 0 \qquad\qquad\qquad 0 \end{bmatrix} \begin{bmatrix} \dot{q}_1 \\ \dot{q}_2 \end{bmatrix} \tag{5.4}$$

$$= H_{u5}(q_1, q_2) \begin{bmatrix} \dot{q}_1 \\ \dot{q}_2 \end{bmatrix}$$

where $\begin{cases} A_w(q_1,q_2) = x_{u5}(q_1,q_2) + \frac{a}{2} + l_u \cos q_w \\ B_w(q_1,q_2) = y_{u5}(q_1,q_2) + \frac{a}{2} + l_u \cos q_w \end{cases}, \quad w = 1,2$.

Similarly, the velocity of joint J_{l5} is:

$$\dot{p}_{l5} = H_{l5}(q_3, q_4) \begin{bmatrix} \dot{q}_3 \\ \dot{q}_4 \end{bmatrix} \tag{5.5}$$

Without the trivial details, the velocity of the needle tip $\dot{p}_t$ can be denoted as:

$$\dot{p}_t = J_{3\times 4} \begin{bmatrix} \dot{q} \\ \dot{d}_u \end{bmatrix} \tag{5.6}$$

However, the velocity control may not be a major concern in this robot. Since the velocities of four actuated joints $\dot{q}$ only relates to the speed of trajectory alignment. It is generally limited at low speed (<10°/s) to ensure hydrostatic transmission. The robot then serves as a rigid platform for needle insertion. The inserting speed ($\dot{d}_u$) of needle tip is mainly determined by surgeon's operation or the 1-DoF needle insertion component. Referring to a commercial robot (NeuroArm®) in MRI-guided neurosurgery, this speed should be <50 mm/s [52].

To find the four actuated joint angles $q = [q_1, q_2, q_3, q_4]^T$ based on the desired needle pose w.r.t.

the MR image coordinates, co-registration between the robot and image coordinate system is required. Again, the planned parameters (i.e. p_t and $\vec{r}$) can be defined in Coordinates Ψ_O can be found by calculating the crossing points of needle and two layers using the line equations:

$$p_{u5} = p_t - d_u \cdot \vec{r} \quad \text{and} \quad p_{l5} = p_t - d_l \cdot \vec{r} \tag{5.7}$$

Note that coordinates p_{u5} and p_{l5} belong to triangle $\Delta J_{u1}J_{u3}J_{u5}$ and $\Delta J_{l1}J_{l3}J_{l5}$, respectively. Then, angle $\angle J_{u3}J_{u1}J_{u5}$ and $\angle J_{u4}J_{u2}J_{u5}$ (denoted θ_{u1} as θ_{u2}) can be solved using cosine laws, respectively, in triangle $\Delta J_{u1}J_{u3}J_{u5}$ and $\Delta J_{u2}J_{u4}J_{u5}$:

$$l_f^2 = l_u^2 + p_{u5} - p_{u1}{}^2 - 2l_u p_{u5} - p_{u1} \cos\theta_{u1} \tag{5.8}$$

$$l_f^2 = l_u^2 + p_{u2} - p_{u5}{}^2 - 2l_u p_{u2} - p_{u5} \cos\theta_{u2} \tag{5.9}$$

Angles $\angle J_{u2}J_{u1}J_{u5}$ and $\angle J_{u1}J_{u2}J_{u5}$ (denoted as α_{u1} and α_{u2}) can be obtained similarly in triangle $\Delta J_{u1}J_{u2}J_{u5}$. To avoid the second type of singularity, joint J_{u3}, J_{u4} should be always positioned beyond triangle $\Delta J_{u1}J_{u2}J_{u5}$ such that, $q_1 = \theta_{u1} + \alpha_{u1}$ and $q_2 = \pi - (\theta_{u2} - \alpha_{u2})$. The other actuation angles q_3, q_4 can be solved based on the similar process.

5.3.4 Needle Insertion

The insertion DoF is achieved by a linear actuator driven by the similar master-slave mechanism as introduced in Section **5.3.1** (**Fig. 5.8)**. Two lubricant linear guides constrain the needle in translational motion. A friction drive composed of two rollers is employed, with one powered (driving roller) and the other one passively driven (driven roller). The high friction is ensured by the rough surface of soft material enclosing the rollers. Two rollers are directly 3D printed using digital materials. They can both rotate inwards or outwards for inserting or retrieving the needle. The distance between two roller axes is smaller than the outer diameter of the soft roller, so as to maintain radial pushing forces against each other and increase the gripping force for the needle.

Only nine components are involved in the roller box, namely two rollers, four bearings, two linear guides and one housing. Given the reliable master-slave actuation, only two tendons are connected to driving roller while the remaining slave parts can be all placed on the surgical table. The actuation system of needle insertion cannot interference with the targeting motion. This simple and light-weight design is essential for the integration with such a targeting device, which operates within confined workspace and adjusts its orientation/position frequently.

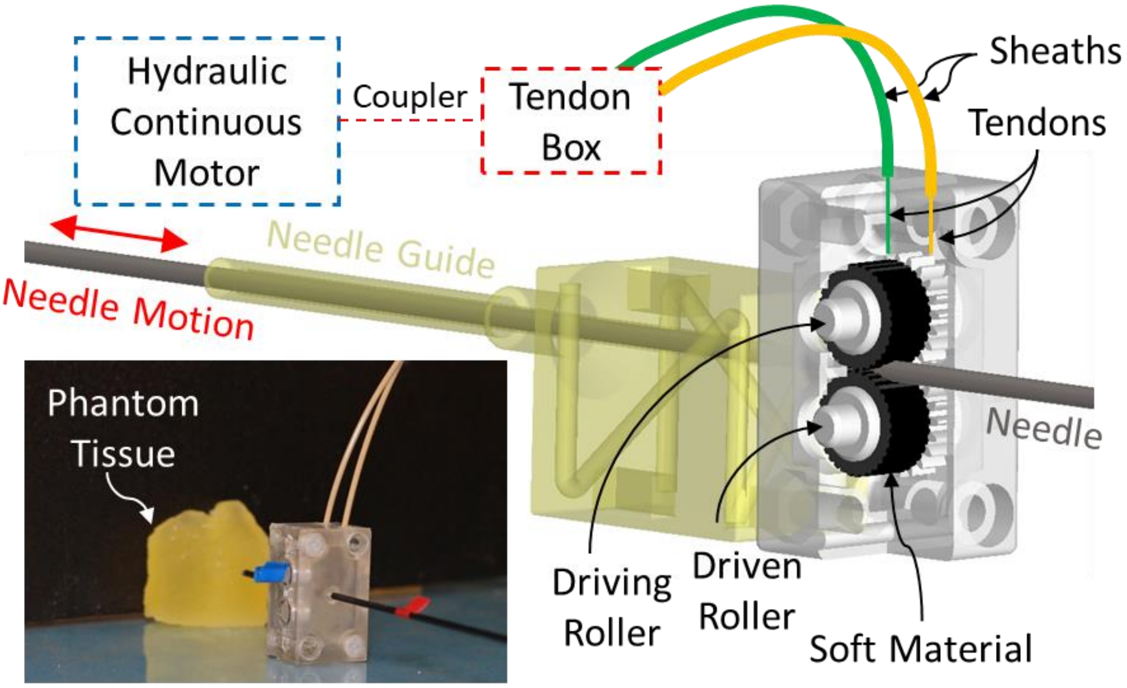

Fig. 5.8 Linear actuator for needle insertion driven by the tendon-sheath mechanism. Two rollers enclosed by high-friction soft material can rotate inwards/outwards and grip the needle for inserting/retrieving motion.

5.3.5 MRI Distortion and Fiducial Marker System

Accuracy is highly demanding in stereotactic neurosurgeries. However, MR images are subject to geometrical distortion from several sources, e.g. inhomogeneous static field, non-linear gradient field and eddy currents [184]. Without proper correction, the discrepancies (e.g. 8 mm) induced by geometrical distortion can lead to mistargeting or considerable under−dosing of the brain tumor. For this reason, optical encoder is not employed in the proposed robotic system. It may provide accurate positional data in Cartesian space, but it cannot project the pose of robot end-effector properly in image domain. Both surgical targets and surgical trajectories are planned pre-operatively in image domain. When the end-effector poses are measured by other trackers different from the MR image coordinates, it may inevitably lead to large discrepancies beyond the surgical plan. To resolve this challenge, MR-based *active* tracking units are deployed to provide real-time positional data for intra-op navigation. Details about the MR-based tracking is discussed in Section **5.4.3**.

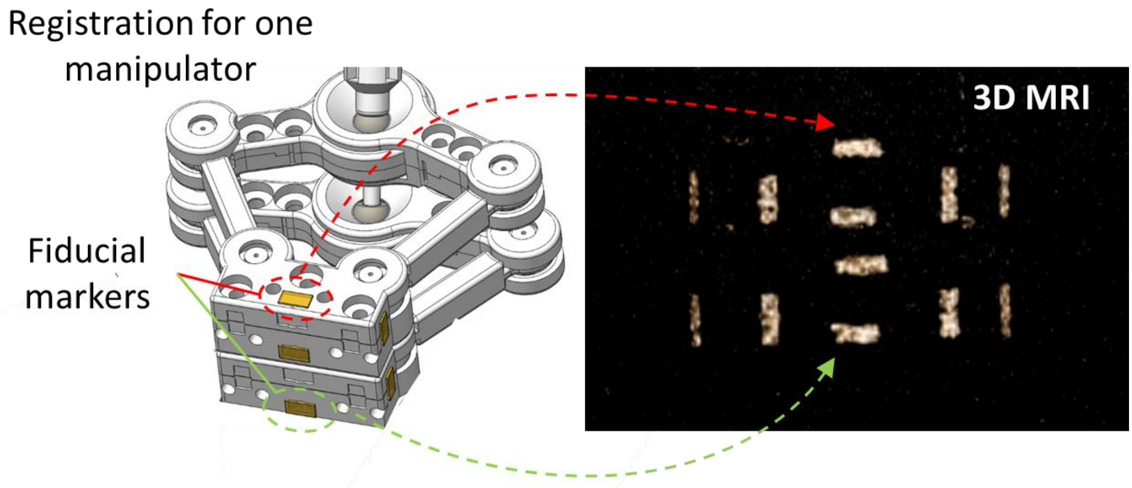

Fig. 5.9 Twelve fiducial markers, filled with Vitamin E or fish oil, which are fixed on the manipulator housing for image registration.

In addition to the MR-based *active* tracking, *passive* fiducial marker systems are also employed. These systems include fiducial points, rings and Z-frames for registration, surgical planning and initial robot pose determination, respectively. Point-based registration may be the most commonly-used method in existing image-guided surgical systems. It generally calls for several predefined fiducial points on the pre-op MRI or CT images, and correlates them with the counterparts on the intra-op images [185]. Registration error has direct implications for the clinical treatment decisions and the risk assessment. Target registration error (TRE), defined as the actual error between the navigation image and the patient anatomy, is the most clinically-relevant measure. It is directly correlated to fiducial localization error (FLE), which is the error in locating the fiducial point coordinates. It has been demonstrated in a clinical neurosurgical navigation setup that FLE distribution is anisotropic, heterogeneous in both direction and magnitude aspects [185]. This study has taken multiple error sources into consideration, such as the inflammatory effect of sedation, human errors in the manual selection of fiducial points, and pairing process. In addition, bias and interdependency with each other might also be included in

FLE. In regard to these complexities, West *et al.* [112] propose three simple guidelines for the fiducial marker distribution: **i)** using as many fiducial markers as possible; **ii)** ensuring that the center of fiducial marker system is close to the target location; and **iii)** avoiding collinear fiducial marker locations. Referring to these guidelines and the practical scenarios, twelve fiducial markers are employed for the rigid registration of one manipulator in the presented robotic system (**Fig. 5.9**).

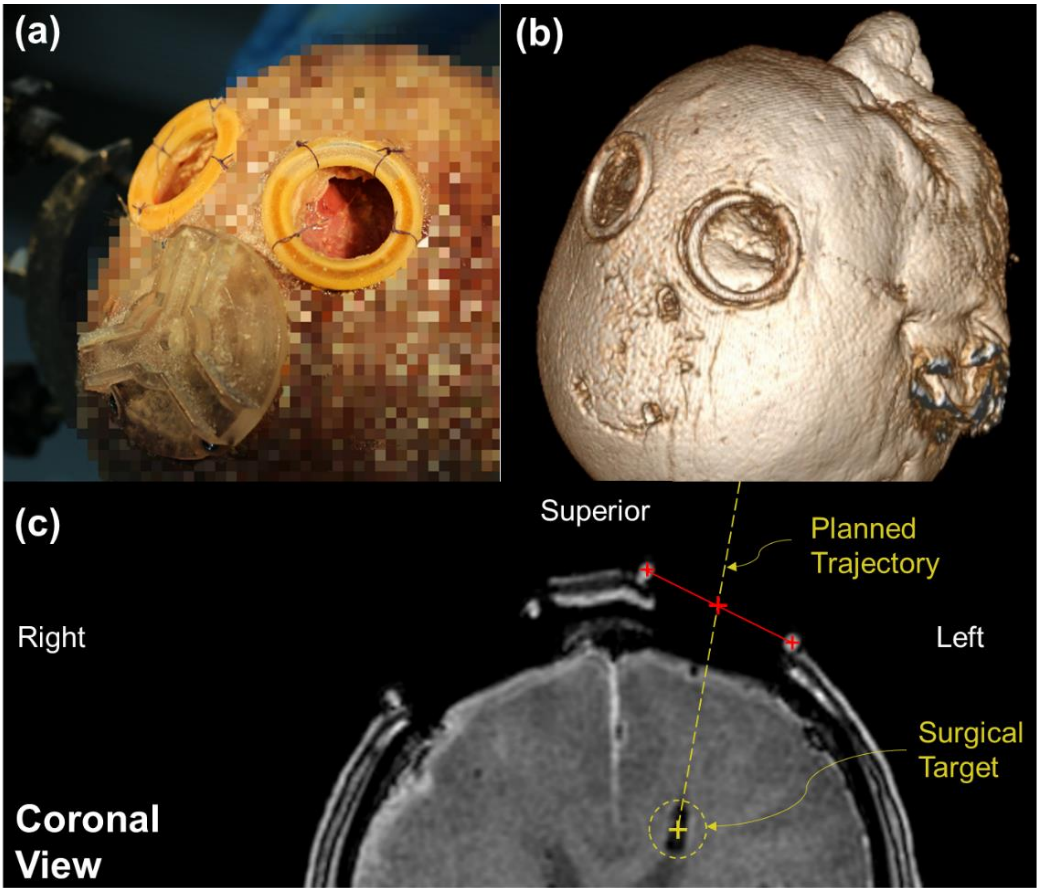

Fig. 5.10 **(a)** Fiducial rings for burr hole localization and trajectory planning. Soft hollow rings are injected with MRI-visible oil (Vitamin-E) and sewed with skin for fixation. **(b)** 3D MRI reconstruction showing the fiducial rings can be clearly identified in the high-resolution anatomical scanning. **(c)** Line trajectory for instrument insertion trajectory defined by the selected target and the center of burr hole, namely the center of fiducial ring.

Another fiducial system adopted is to localize the positions and diameters of the burr holes for immediate trajectory planning. Two soft rings are hollowed and injected with MRI-visible liquid, e.g. Vitamin-E or fish oil. The cross-sectional diameter of the ring is $4\ mm$, sufficient to produce high positive contrast in the image and be well-differentiated from the patient tissue/fat. I have made several sizes (different ring diameters) of such fiducial rings to fit with the created burr holes. These rings are sewed with the skin for temporary fixation, as shown in **Fig. 5.10a**. After the initial high-resolution anatomical MRI scanning, the targets can be identified, as well as the fiducial rings (**Fig. 5.10b**). In the coronal images, a series of scanning planes intersect with the fiducial rings and two pairs of bright spots can be found in images. When the distance between a pair of bright spots reaches the largest, the line segment linking these two points is the diameter of the ring. And the midpoint of that line segment is defined as the entry point of the instrument (**Fig. 5.10c**). Such that, the trajectory can be planned, based on the entry point and selected target. Then, the software checks the planned trajectory is within the workspace (angular range) of the robot.

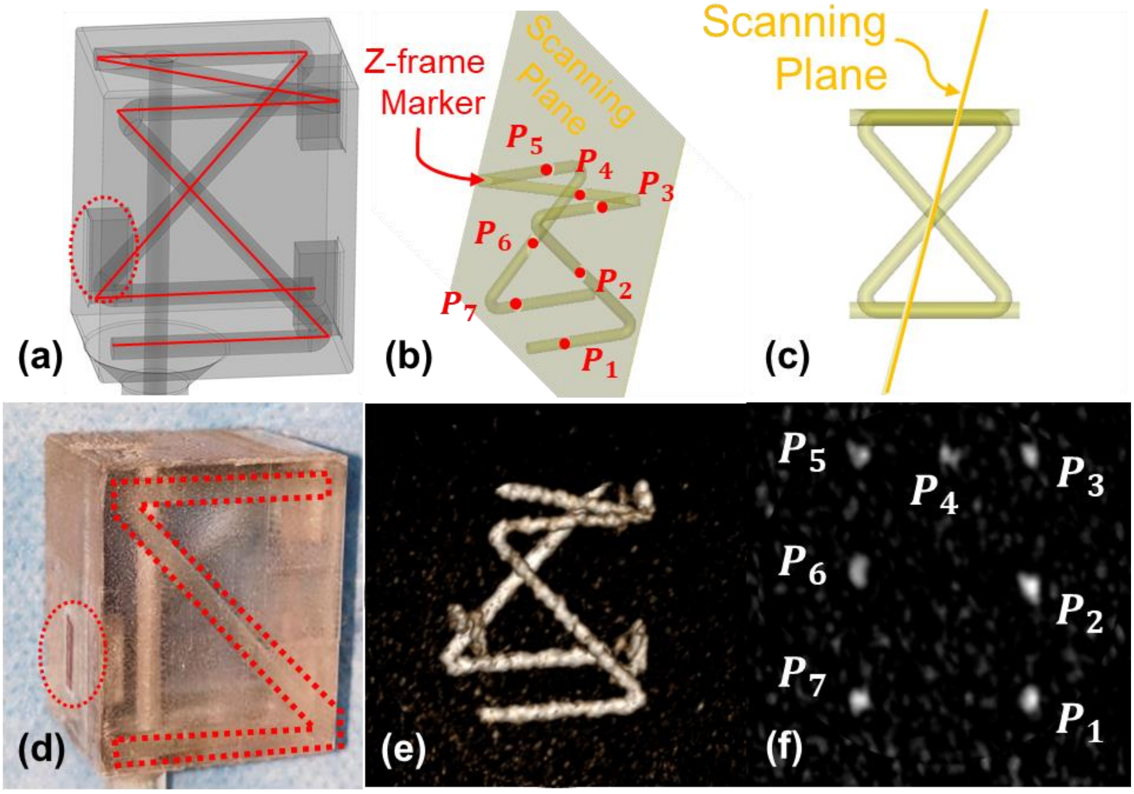

Fig. 5.11 Z-frame fiducial marker system for instrument localization under imaging sequence. **(a)** CAD models of the marker system design, showing the arrangement of seven fiducial lines. Intersection between the scanning plane and Z-frame system, in **(b)** orthogonal view and **(c)** side view. Intersecting points are defined as $p_m, (m = 1,2, \ldots ,7)$. **(d)** Photo of the needle guide embedded with both Z-frame marker (red dash lines) and MR-based wireless trackers (red dash ellipse). **(e)** 3D reconstructed frame marker. **(f)** 2D MRI showing a cross section of the Z-frame. Seven intersecting points are visible in the image and ordered as $p_m, (m = 1,2, \ldots ,7)$.

Besides the registration and immediate trajectory planning, the initial pose of the robot is also important in the first intra-op 3D MRI scanning. This is to calibrate the zero position of the slave robot, as well as to decide the initial movement. Based on the inverse kinematics deduced in the previous section, the robot pose can be calculated from the needle guide pose. Such that, a Z-frame fiducial system is embedded for needle guide localization in imaging sequence. This Z-frame is customized using additive manufacturing, as shown in **Fig. 5.11a**. The MRI-visible material (SUP706, Stratasys, USA) filled inside the seven tubes are printed out at the same time without any post processing. Each of these seven tubes form an MRI-visible line (e.g. $\emptyset 2\ mm \times 20\ mm$) and arranged into three "Z"s.

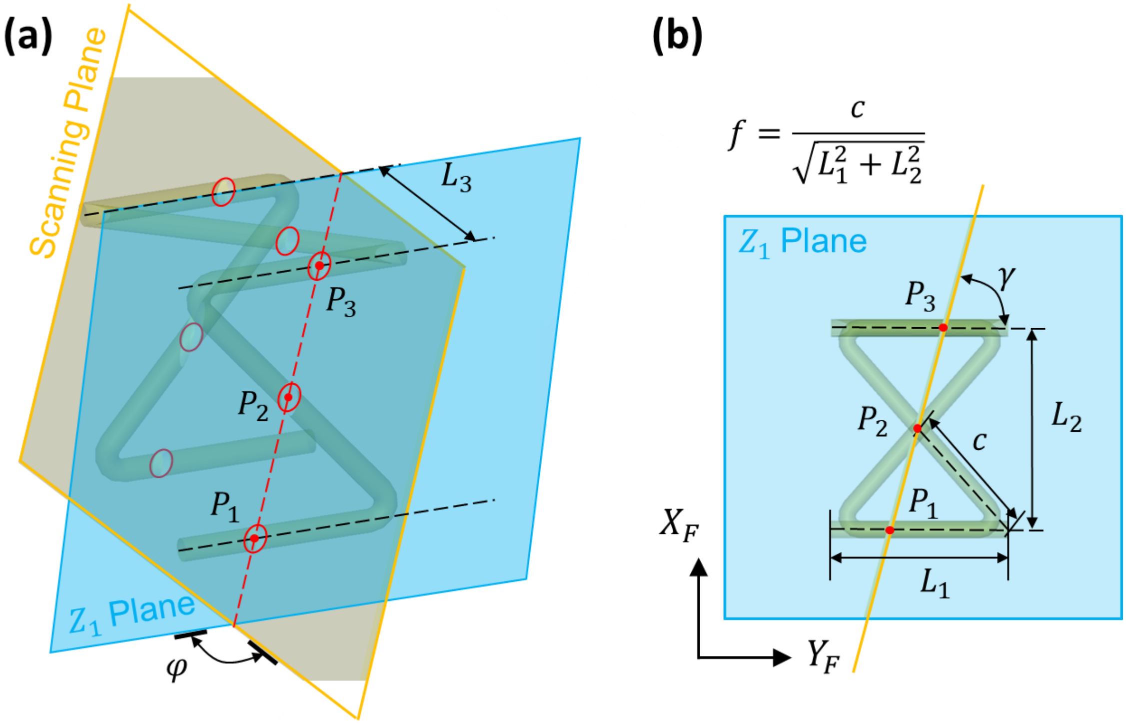

Fig. 5.12 **(a)** Dimension and coordinate systems for the fiducial motif (Z_1 plane). **(b)** Three parameters, φ, γ, f, describing the relationship between the scanning plane and fiducial motif. In the presented Z-frame marker system, $L_1 = 20\ mm, L_2 = 22\ mm, L_3 = 18\ mm$.

Different from the point marker system, there is no concern about the large scanning slice thickness and missing any fiducial lines in the Z frame (**Fig. 5.11b-e**). In any single 2D image intersecting the frame, seven ellipse points corresponding to the intersection points of fiducial lines, can be observed and localized. By finding the centroid of ellipse point, obtained coordinates of seven fiducials are first used for matching. The resultant pattern should be validated against the known geometric constraints and the fiducials are ordered $p_m, (m = 1,2, \dots, 7)$ (**Fig. 5.11f**). Defining one Z as a fiducial motif [186], here I take a motif as an example and describe the method to determine the positions of these three points in both image space, ${}^{IM}p_1, {}^{IM}p_2, {}^{IM}p_3$, and frame space, ${}^{F}p_1$, ${}^{F}p_2$, ${}^{F}p_3$.

The relationship between the scanning plane and fiducial motif (Z_1 plane) can be defined using three parameters (**Fig. 5.12**): φ----the angle between the scanning plane and the Z_1 plane; γ----the angle between the intersection line and the parallel line; and f----the fraction indicating where the intersection occurs:

$$f = \frac{c}{\sqrt{L_1^2 + L_2^2}} \tag{5.10}$$

As the transformation from image space to frame space is rigid body transformation. The distances $\| {}^{F}p_1 - {}^{F}p_2 \|$ and $\| {}^{F}p_2 - {}^{F}p_3 \|$ in frame space are equal with the corresponding distance in image space, $\| {}^{F}p_1 - {}^{F}p_2 \| = \| {}^{IM}p_1 - {}^{IM}p_2 \|$ and $\| {}^{F}p_2 - {}^{F}p_3 \| = \| {}^{IM}p_2 - {}^{IM}p_3 \|$. These distances can be expressed as a function of φ, γ, f.

$$\left\| {}^{IM}p_1 - {}^{IM}p_2 \right\| = fL_2 \csc(\theta) \tag{5.11}$$

$$\left\| {}^{IM}p_3 - {}^{IM}p_2 \right\| = (1 - f) L_2 \csc(\theta) \tag{5.12}$$

The ratio between these distances can be expressed as:

$$\left\| \frac{{}^{IM}p_1 - {}^{IM}p_2}{{}^{IM}p_3 - {}^{IM}p_2} \right\| = \frac{f}{1 - f} \tag{5.13}$$

This ratio is the function of only one parameter f. Such that f can be easily computed, so as parameter c, which determines the position of ${}^{F}p_2$. Based on Law of Cosines, positions of ${}^{F}p_1$ and ${}^{F}p_3$ can be computed as well. Therefore, the coordinates of this intersection in two spaces are obtained. The intersection for the two remaining frame spaces can be calculated by repeating this method.

5.4 Experiments and Results

5.4.1 Transmission Stiffness and Steadiness Analysis

One of the primary factors which determines the system's capability to resist external disturbance is the stiffness of the hydraulic transmission presented. An iterative test was conducted on a 1-DoF actuation, i.e. from the master side to the manipulator's base joint. The upper arms of manipulator were fixed such that rotation of the actuated joint was constrained properly. 10m long pipes filled with distilled water were used to connect both the master-and-slave hydraulic units. The master unit was actuated by an electrical DC motor that provided with 500 encoding pulses feedback. A torque sensor (HLT131, Hualiteng Technology Co. Ltd., China) with 5mNm sensitivity was used to measure the external load. The tests were performed repeatedly (10 cycles) under the bi-directional load. The transmission fluid in the pipes was preloaded at 0.5, 1.0, 1.5 and 2.0 bar in order to investigate the transmission stiffness varying with different fluid pressure levels. The external loads were gradually increased, while recording the corresponding piston displacements.

The force-displacement diagram (**Fig. 5.13)** shows the increasing trend of transmission stiffness with higher fluid pressure pre-loaded. The data was linearly fitted using least-square regression, which indicated the maximum stiffness coefficient can reach 24.35 N/mm under 2 bar pre-loaded pressure.

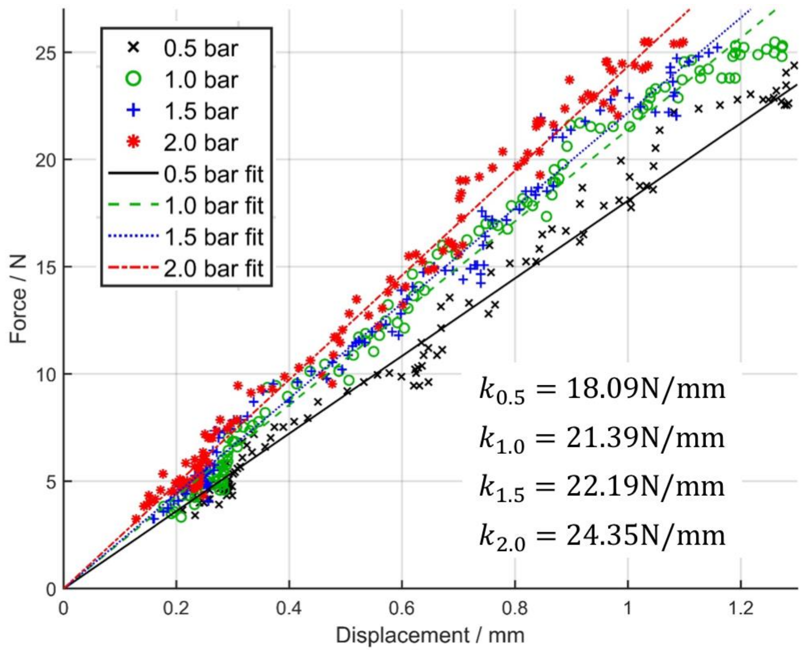

Fig. 5.13 Force-displacement diagram showing the transmission stiffness of the actuation module at four levels (0.5, 1, 1.5 and 2 bar) of pre-loaded pressure on the transmission liquid.

The interaction force between instrument and brain tissue is generally less than 0.8 N [52, 187]. The end effector of the instrument should remain 2 mm accuracy under this disturbance. To find the desired stiffness, I firstly assume the lower ball joint is $h_l = 30\ mm$ away from the trocar (burr hole) and targets locate $h_t = 90\ mm$ deep. Robot may hold a needle guide and adjust its orientation pivoting about the trocar. When the insertion trajectory, i.e. the orientation of needle guide, is confirmed, a rigid needle will be inserted towards the target. In this procedure, I assume the interaction force (max. 0.8 N) between needle and brain tissue is taking effects only on the lower ball joint. This is an extreme case to validate that every single joint/transmission line can sustain the whole interaction force and maintain such accuracy, when all the other joints/transmission lines are out of function. Such that, the maximum interaction torque T_l and force F_l applied on the lower ball joint can be calculated:

$$T_l = F_l \cdot h_l = F_t \cdot h_t \tag{5.14}$$

Straightforwardly, the maximum torque T_{l1} applied on the base joint (e.g. J_{l1}) can be calculated:

$$T_{l1} = F_l \cdot l_u = 48mNm \tag{5.15}$$

To find the displacement of one transmission line and the equivalent force F applied, the radii R_j of base joint and R_s of spool in the tendon box are two critical parameters. In the presented prototype, R_j is set as 8 mm and R_s is 6 mm. Transmission ratio n_T of tendon transmission is:

$$n_T = \frac{R_j}{R_s} \tag{5.16}$$

Then the force F can be calculated:

$$F = T_{l1} \times \frac{1}{n_T} \times \frac{1}{R_s} = 6N \tag{5.17}$$

Based on the inverse kinematics deduced in Section **5.3.3**, the allowable errors of one base joint and one transmission line should be less than $1.86°$ and $0.26\,mm$. The desired transmission stiffness of one line can be deduced:

$$k_{desired} = F / 0.26 = 23.08\,N \cdot mm^{-1} \tag{5.18}$$

It is indicated that the proposed hydraulic transmission (preloaded at 2 bar) is stiff enough to transmit motion for precise tissue manipulation. Compliance in the transmission can be attributed to three major factors: **i)** stretching of the diaphragms, **ii)** deformation of the plastic structural components, and iii) bulging in cross-sectional area of the pipes. To further increase the transmission stiffness, components can be machined by materials with higher rigidity, e.g. polyoxymethylene. Thus, the minimal structural deformation under loading can be ensured. Previous studies [175] have suggested shorter pipes can also contribute to higher stiffness, as well as lower fluid inertia and friction.

5.4.2 Needle Targeting Accuracy

An EM positional tracking system (Aurora, NDI Medical, Canada) was used to measure the 3D coordinates of any point defined in the experimental setup. Ten points were simulated as the STN targets, five at each side on a plastic plate. They were roughly 100mm below the lower-layer of manipulators, which was a typical depth of stereotactic target beneath the human skull. These measured targets coordinates were registered with the robot coordinate system. A phantom needle with similar diameter (Ø1.4 mm) to a DBS cannula was used. A 6-DoF coil sensor was fixed at the needle tip.

Configurations of the robot and needle guide, along with the needle insertion depth, were measured and calculated online. Once aiming at the target point, the needle was then inserted manually. Such trial for each point was repeated 10 times. 100 trials were conducted in total. This targeting task was performed closely to the tracking system, and measurements were taken when the 6-DoF sensor was at rest. These measurements were repeated 500 times at each static location. The average of these 500 measurements was used in the error analysis. Not only was the proximal distance from needle tip to the target measured, but also the distance from the target to the needle axis. The targeting accuracy was quantified by the mean error and its standard deviation (**Table 5.1**). The error is generally less than 2 mm, and its variation also smaller than 1mm. This accuracy is comparable to the current stereotaxy practice [166]. Future work in robot calibration and structural rigidity enhancement may further improve this targeting performance.

Table 5.1 Needle Targeting Accuracy Test

	Needle tip		Normal to the needle	
	Left	Right	Left	Right
Accuracy (mm)	**1.73±0.75**	**1.21±0.63**	**1.61±0.72**	**1.15±0.62**

Table 5.2 MRI Scan Parameters

	w/o needle inserted	w/ needle inserted	SNR test
FOV (mm)	240×240	240×240	280×280
Matrix	256×256	256×256	256×256
Acquisition	FSPGR	FSPGR	T2-FSE
TR (ms)	68.0	68.0	2000.0
TE (ms)	2.8	2.8	76.8
Flip angle (°)	10	10	90

5.4.3 MR-based Navigation

MR-based *wireless* tracking is first introduced to such robotic stereotaxy. It possesses several advantages over the conventional passive tracking [188, 189], in which the real-time and automatic localization cannot be made reliable due to their limited signal contrast to the background. The use of passive tracking could also be time-consuming as visualization of the markers takes place after 2D image reconstruction. The proposed *wireless* and *miniaturized* marker can act as an RF receiver to pick up the MR gradient signal along three principal scanning directions, as well as an inductor to resonate with the signal transmitted to the MRI scanner receiver [123, 190, 191]. Without the need for image reconstruction, they can be rapidly localized using 1D projection techniques [170]. The *wireless* marker cannot be tuned off. But as the number of markers involved in each needle guide is only three, it is easy to identify the correspondency.

The navigation test was carried out under MRI environment. It simulated the conceptual system setup for MRI-guided robotic stereotaxy. To better simulate the surgical scenario, the robot was mounted on the skull model that would be placed and scanned inside a head coil. To reveal the brain phantom in MR image, the “brain” was fabricated and made of agar gel (Biosharp Inc., China) to enhance the image contrast for needle targeting. The two films of MR coil circuits ($1.5 \times 5 \times 0.2$ mm^3) are first employed to perform MR active tracking in 3D for robot control. Both were embedded in the needle guide (**Fig. 5.14(a)**). 3D fast spoiled gradient recalled-echo (FSPGR) sequence was used to assess the location and orientation of the needle guide. The sequence parameters are stated in **Table 5.2.**

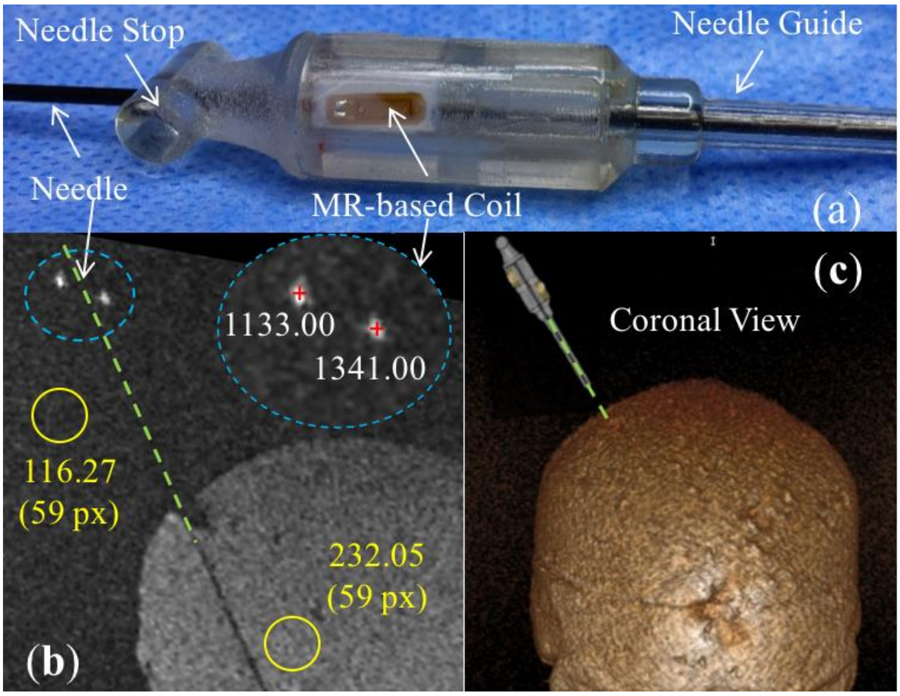

Fig. 5.14 **(a)** Needle guide embedded with two MR-based tracking coil units, one of which is shown on its side wall. **(b)** MR image of the brain phantom (in the coronal view) revealing the two tracking markers by the corresponding bright spots. Dark straight line is the negative artifact of the needle. The two spots are zoomed in (enclosed in the blue dash ellipse). Two red crosses probing at the spots indicate the signal intensity of the coils, in contrast to those intensities average within other two yellow circles: on the background and agar-gel brain phantom. **(c)** Virtual configurations of the instrument augmented on those high-contrast markers, which are posed above the 3D reconstructed brain phantom. Any change of the instrument pose could be detected continuously (at 30-40Hz) under the real-time MR-tracking sequence.

A phantom needle made of carbon fiber was then inserted and scanned with the same imaging sequence. **Fig. 5.14(b)** shows the resultant MR image in coronal view. Both the coils and the inserted needle can be visualized. The signal intensities of two coils are 1133.00 and 1341.00, in the high contrast to those two circular areas comprising 59 pixels, which are sampled on the background and agar-gel brain, respectively, with average signal intensities of 116.27 and 232.05. This contrast can be further enhanced by dedicated excitation at lower flip angles (e.g. 1°), which can minimize the background signals. At a distance of 48mm from the isocenter, the maximum error in marker position was 0.50mm with inherent precision of 0.12 mm. This deviation can be increased when the marker is further from the isocenter due to the nonlinearities of gradient fields.

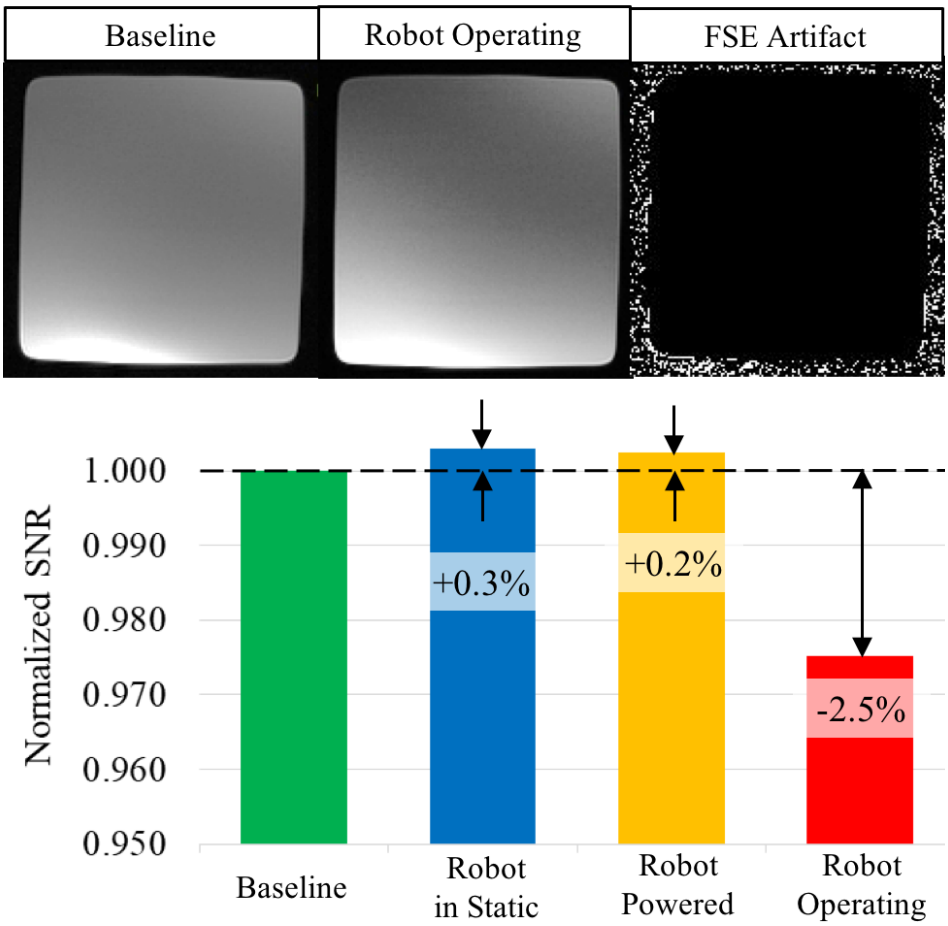

Fig. 5.15 **Upper:** T2-weighted FSE images of an SNR phantom. These images are generated at different stages of robot operation. A binary map for FSE sequence marked the artifacts as white pixels. No artifact is observed within the phantom area. As defined by the ASTM standard, it indicated zero artifact was created by the operation of robot. **Lower:** SNR test results. The existence or operation of the proposed robot is demonstrated to have minimal influence to SNR.

5.4.4 MRI-compatibility Evaluation

The MRI-compatibility test was conducted in a 1.5T MRI scanner (SIGNA™ HDxt, GE Healthcare, USA) at a room temperature of around 20°C. A square SNR phantom (Part Number: 150027, USA Instruments, Inc.) for GE MRI was placed at the isocenter of the scanner. A baseline image without the presence of robot was acquired using T2-weighted fast spin echo (FSE) sequence (**Table II**). This is the acquisition sequence commonly used for localization in stereotactic neurosurgery. Upon introducing the robot right beside the phantom, MR images were obtained under three different robot operating conditions (**Fig. 5.9**), which were: **i)** *Static*: robot was introduced and remained powered off; **ii)** *Powered*: robot remained still, but the hydraulic and electric power was on; **iii)** *Operating*: robot was in full operation. Referring to the guidelines provided by National Electrical Manufacturer's Association (NEMA) [192], the SNR in MR images were evaluated.

As the results shown (**Fig. 5.15**), SNR loss is within 3% even with the robot in full motion. MR image artifacts caused by the presence of robot were quantified based on the ASTM standard test method [193]. The images corresponding to the two conditions, baseline and robot operating, were compared. Pixels with intensity that varied by 30% or above were considered as artifacts [194]. These artifacts would appear as white pixels in the binary map (FSE Artifact, **Fig. 5.15**). No artifact is observed within the phantom area. As defined by the ASTM standard, it indicates the operation of robot generated zero artifact.

5.4.5 Pre-clinical Trial

Pre-clinical trial has been carried out to validate the proposed DBS workflow with MRI-guided bilateral robotic system, which is previously introduced in **Chapter 2 (Fig. 2. 10)**. The detailed system setup (**Fig. 5.16**) and workflow (**Fig. 5.18-19**) with some modification in specific for the testing scenarios is described in this section. A human cadaver was employed. As the delicate DBS targets, e.g. GPi and STN, could not be clearly identified in a long-time frozen brain. MRI scanning and planning in the pre-op stage were eliminated. The targets for this simulated DBS trial were artificial and made of Vitamin-E injected capsules. They were placed into the deep brain immediately when the dura was open, before the subject transferred to the MRI room. The base for the quick anchorage of robotic manipulators was first mounted to the subject. Skin incision, burr hole creation and dural opening were then performed regarding the workspace of the robot. Two fiducial rings were placed at the burr holes and sewed with the skin for the localization of burr hole center. The subject was placed in an MR safe head fixation device (inner/outer diameter: $\emptyset 220/250$ mm) with eight screws, which was specially designed to be fitted into the MRI head coil with inner diameter of Ø300 mm.

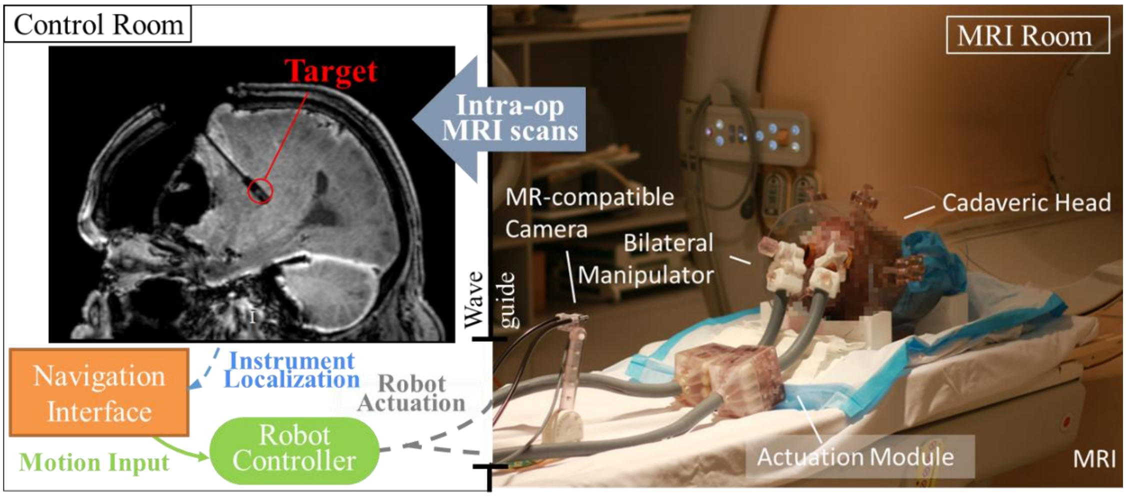

Fig. 5.16 System setup of the presented MRI-guided robot-assisted stereotaxy for cadaver trial. An MRI-compatible camera was placed at about 300 mm away from the subject to monitor subject conditions and robot motions.

The subject with the fixation device was transferred into the MRI room. A 1.5T diagnostic MRI scanner (Achieva, Philips Healthcare) was employed. An overview of the system setup is shown in **Fig. 5.16**. Robotic manipulators could be manually anchored to the base. Their X-Y displacements relative to the burr holes could be slightly adjusted (max. ~20 mm) and then fixed by hands to the base. An MRI-compatible camera (MRC Systems GmbH, Germany) was also setup at about 300 mm away from the subject, to monitor subject conditions and robot motion for safety concerns. Two 10-m optical fibers (inner diameter of Ø12 mm) wrapped by black rubber and a lighting system were incorporated for illumination in the dark MRI bore. A sterile field was created at the patient table with customized drapes. With the imaging coil firmly placed, the subject was moved into the bore such that the superior aspect of forehead was positioned at the isocenter. First 3D volumetric MR scan was carried out with sufficient coverage and resolution to reveal the fiducial markers and the brain structures of interest. The acquired images were sent to the control computers via DICOM link. Fiducial points embedded in the robot base, fiducial rings and targets could be manually selected and localized in the DICOM files. The coordinates of twenty-four fiducial points for bilateral manipulators were input to the control computers for robot registration. With respect to the burr hole center, a line trajectory could be prescribed as a preliminary insertion trajectory. The surgeon might make minor refinement and determine the most appropriate entry points and trajectories to the target region.

Once the preliminary trajectory was selected. MR tracking sequence was then deployed to provide

MR-based needle guide localization for robot navigation. Robot pose could be inversely calculated on the basis of needle guide position and orientation, which were defined by the three *wireless* trackers. A graphical user interface was developed for the intuitive control of robot pose (**Fig. 5.17**) at this stage. An orthogonal view permitted the direct perception of both planned and actual trajectories. Estimated errors and computed desired robot joint motions were displayed at the bottom of the interface. Targeting path could be thus manually adjusted to align with the planned one. It might provide additional guidance as to determine whether planned insertion path was likely to lie beyond the reach of the manipulator. This process was repeated until the guide was aiming at the target.

Once the MR-based navigation completed, the patient table was moved out of the isocenter. Locking screws were inserted to the manipulator to prevent any further changes in robot pose. Insertion depth was displayed in the interface. A needle stop embedded with high-friction material was set to the needle so as to terminate it at the selected target. Needle insertion was completed by surgeon. Then, the subject was moved into the machine isocenter again for the final evaluation to evaluate the targeting errors. This scanning was accomplished using the same MR sequence as the one for target localization.

5.5 Discussion and Conclusions

In this chapter, the design of an MRI-guided robot for stereotactic neurosurgery is presented. Not only is the robot capable to perform bilateral targeting of both STNs independently, but also it is compact in size so as to operate within the confined space of a regular MRI head coil. High-performance hydraulic transmissions are incorporated. Maximum stiffness coefficient of 24.35 N/mm can be achieved. A needle insertion task of DBS has also been simulated, in which the experimental results show the targeting accuracy more than enough in the standard surgical requirement.

The navigation test has been conducted under MRI settings. Advanced MR-based *wireless* tracking is newly developed and incorporated into this robot. Two tracking units are fabricated and embedded inside the instrument guide, marking two very high-contrast bright spots in the image domain. Such marker intensities appear about 10 times of the imaging background and 5 times of the agar-gel brain phantom, thus enabling the accurate and easy instrument localization. It is worth noting that the presented MR-tracking approach could enable a continuous and real-time positional feedback at 30-40 Hz using the proper MR tracking sequences, thus outperforming the use of many passive fiducials only detected using imaging sequence ones. Moreover, compared to the MR-based active tracking, this *wireless* one does not require any cable connection with the scanner receivers. This avoids many technical complications in wiring the co-axial cables with the tracking units as well. MRI-compatibility test shows the minimal imaging interference is generated even when the robot is in full operation.

In stereotactic neurosurgery, the accuracy of instrument placement can be greatly enhanced by coping with brain shift referring to the brain map continuously updated with the intra-op MRI. This brain shift effect could be minimal with this bilateral approach without having to create extra anchorage site on skull. This development of MR safe robotic system, along with the MR-tracking, is timely while taking advantages of current advances of fast MR imaging/tracking sequences. Direct visualization of surgical targets based on this tele-manipulation of the instrument *in situ* under MRI may prevent the risks from damaging the critical brain structures. This would also avoid the complications of local anaesthesia, thus adding confidence by having the post-procedural evaluations of surgical outcome based on images, instead of verbal/physical interaction with the awake patient during the procedure in many current practices. Finally, it is expected to greatly save the operation time from the repeated instrument placement/adjustment, as well as the image alignment with head frame. The overall healthcare expenditure could be significantly reduced, also compensating the high cost of using MRI.

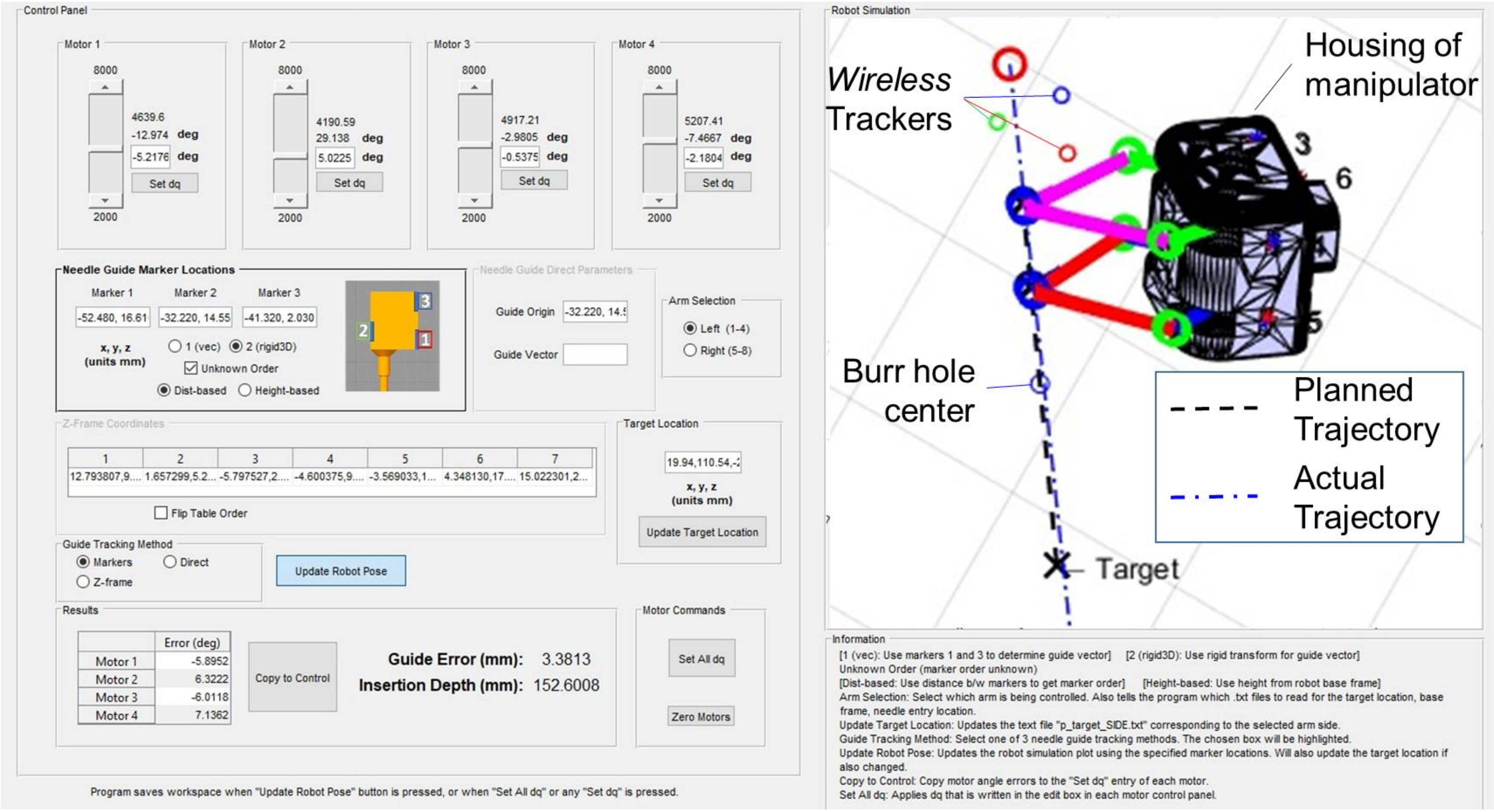

Fig. 5.17 Graphical user interface for robot pose control. The robot is registered with the patient's anatomy, namely the surgical targets and the burr hole centre. Three small circles (in green, red and purple) represent the coordinates of three MR-based *wireless* trackers, which determine the four robot joint angles. Current robot pose (coloured thick lines) and the planned trajectory (black dash line) are shown. Estimated errors and computed robot joint motions are displayed at the bottom of the interface. The targeting trajectory can be manually adjusted to align with the planned trajectory.

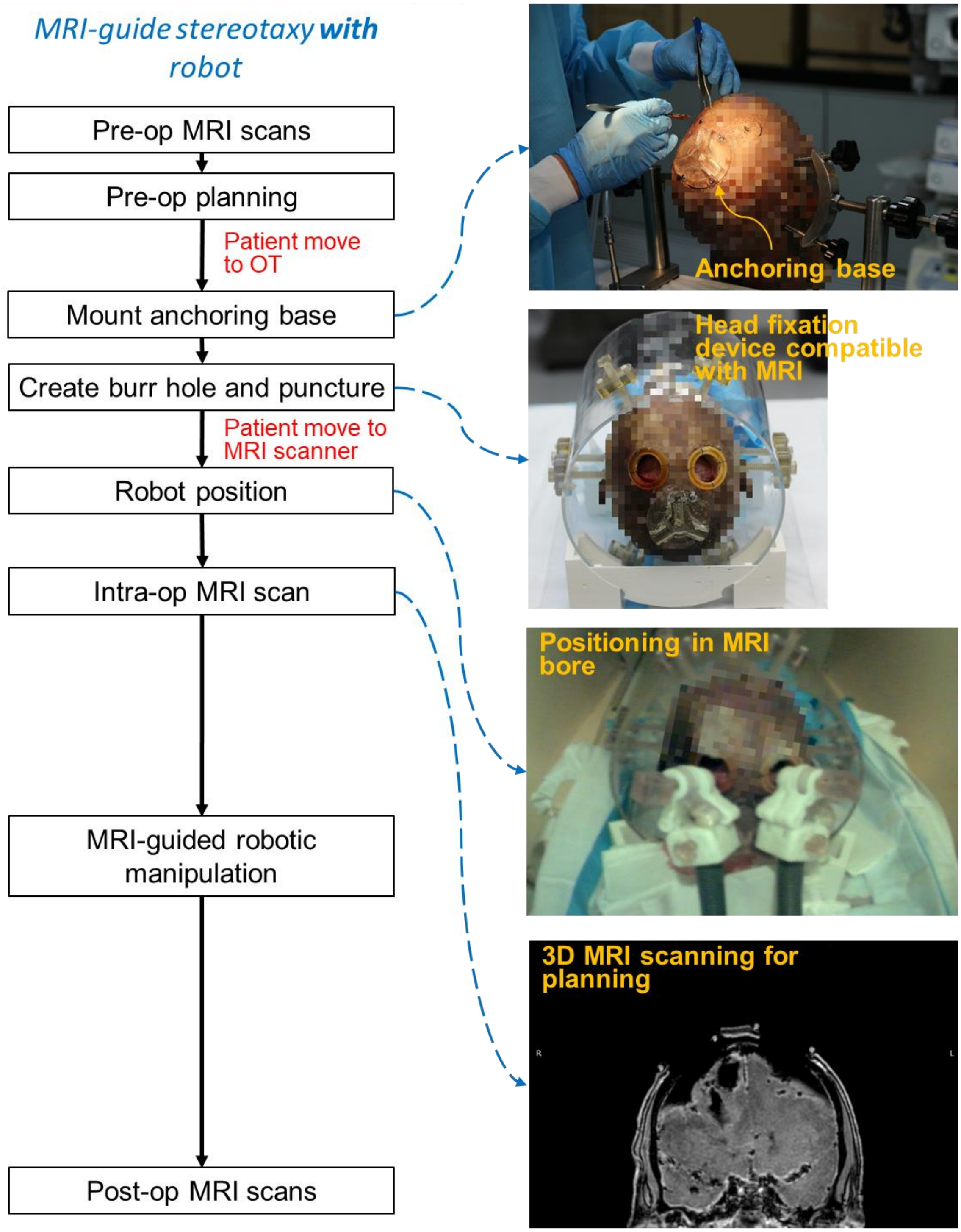

Fig. 5.18 Proposed workflow of the MRI-guided stereotaxy with robot assistance, which is much simpler than the conventional workflow (**Fig. 2.11a**).

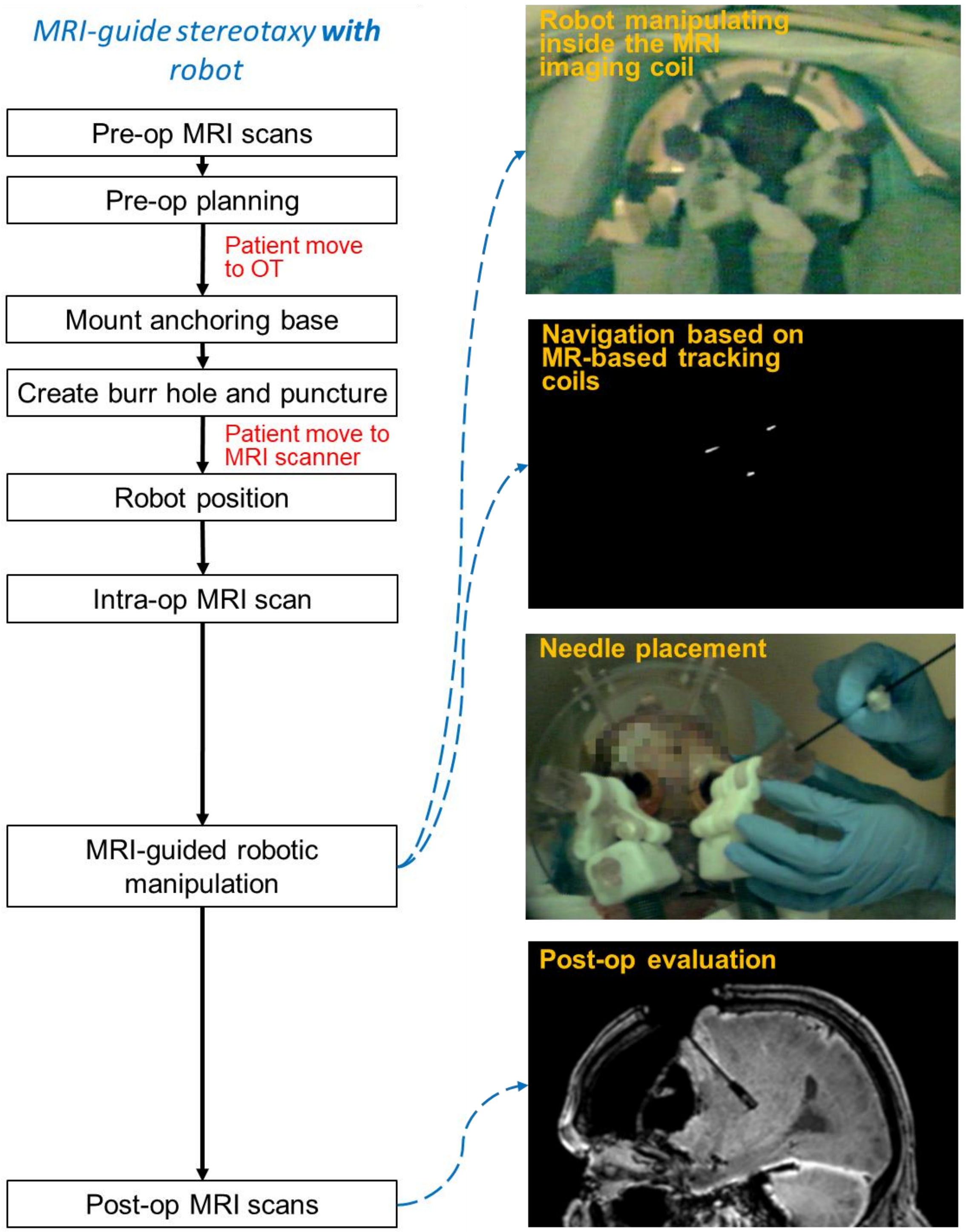

Fig. 5.19 Proposed workflow of the MRI-guided stereotaxy with robot assistance (continued to **Fig. 5.18**).

Chapter 6

Hydraulic-powered Robotic System for Intra-cardiac Catheterization

6.1 Introduction

CATHETERIZATION involves manipulating a thin, long and flexible instrument to pinpoint the anatomical target through intra-luminal, trans-luminal, intra-cranial or intra-cavitary surgical approach. Such manipulation could be used for biopsy, lesion ablation or drug delivery. It has been widely applied to breast biopsy, prostate surgery and cardiovascular interventions. Cardiovascular diseases are one of the major mortality causes in developed countries, which particularly demand on dexterous intra-cardiovascular catheterization. Heart rhythm disorder, also known as arrhythmia, is a typical example. Intra-cardiac EP catheterization is an effective treatment of arrhythmia [195]. In this procedure, a long (over 1.1-m) EP catheter is inserted from femoral vein to the heart chambers. RFA is carried out via the catheter tip, when it gets contact with the lesion tissue. This ablation is to create scar lesion, instead of edema, to isolate the abnormal electrophysiological signals causing the arrhythmia. The safety and efficacy of the EP procedure depend mainly on: 1) the effectiveness of maneuvering catheters to the target lesion for both EAM and RFA, and 2) the ability to assess lesions, their locations and ablation progress intraoperatively.

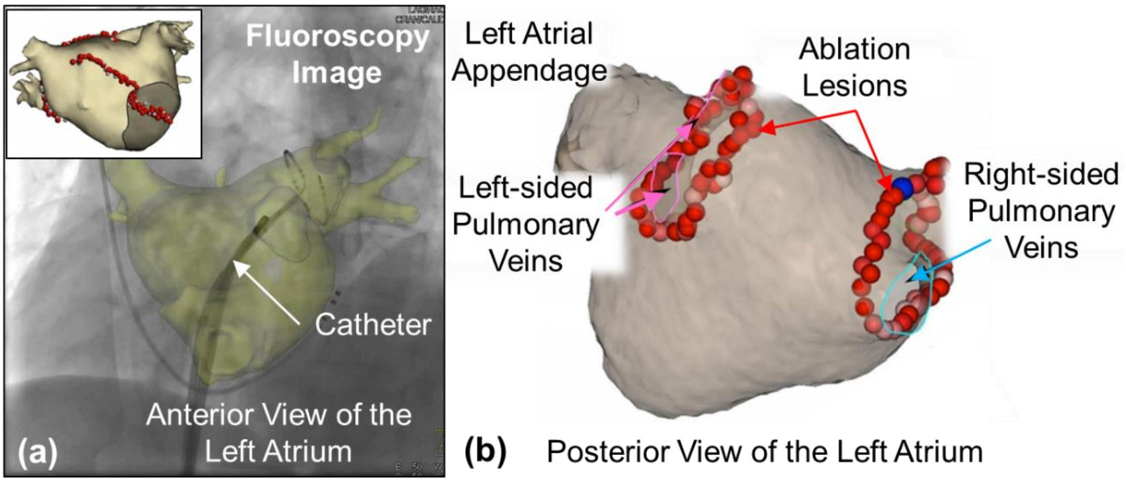

Fig. 6.1 Typical catheter EP ablation roadmap guided by fluoroscopy. **(a)** LA roadmap (syngo® 3D Roadmap) formed by real-time 2D fluoroscopy images augmented with pre-op 3D LA model. **(b)** Posterior view of the LA roadmap for RF ablation. Ablations lesions (red dots) are created around the vein openings to isolate the abnormal electrical impulses from pulmonary veins. Pulmonary vein isolation (PVI) is a treatment for atrial fibrillation (AF).
Image Source: Siemens Healthcare and Hunter Heart [196].

In this chapter[6], an MR conditional catheter robotic system is presented. It integrates an MR safe robotic manipulator, intra-op image processing, real-time positional tracking of catheter in image coordinates, and human-robot control interface to enable MRI-guided cardiac electrophysiological intervention. The robot is powered by hydraulics for effective EP catheterization. The system features a master-slave hydraulic actuation system that has small hysteresis, enabling precise manipulation of standard EP catheter in clinical use. The slave part

[6] The work in this chapter has been presented in the following paper and patent:

[1] Y. Feng, Z. Guo, Z. Dong, X.Y. Zhou, K.W. Kwok, S. Ernst, S.L. Lee. *An Efficient Cardiac Mapping Strategy for Radiofrequency Catheter Ablation with Active Learning[J]*. **International Journal of Computer Assisted Radiology and Surgery**, 2017, 12(7): 1199-1207.

[2] K.H. Lee, Z. Guo, G.C.T. Chow, Y. Chen, W. Luk, K.W. Kwok. *GPU-based Proximity Query Processing on Unstructured Triangular Mesh Model[C]*. **IEEE International Conference on Robotics and Automation 2015** (**ICRA'15**), pp.4405-4411.

[3] K.H. Lee, D.K.C. Fu, Z. Guo, Z. Dong, M.C.W. Leong, C.L. Cheung, A.P.W. Lee, K.W. Kwok. *MR Safe Robotic Manipulator for MRI-Guided Intracardiac Catheterization[J]*. **IEEE/ASME Transactions on Mechatronics**, 2018, 23(2): 586-595.

[4] C.L. Cheung, K.H. Lee, Z. Guo, Z. Dong, M.C.W. Leong, Y. Chen, A.P.W. Lee, K.W. Kwok. *Kinematic-Model-free Positional Control for Robot-assisted Cardiac Catheterization,* Proceedings of **Hamlyn Symposium on Medical Robotics 2016**. London, UK, pp.80-81.

[5] *Robotic Catheter System for MRI-guided Cardiovascular Interventions*, US Utility Patent: **US15/630,406** [Filed on Jun. 22, 2016]; PCT Patent: **PCT/CN2017/089701** [Filed on Jun. 23, 2017].

of the robot is made of MR safe materials, therefore can operate close to or at the isocenter without adversely affecting the imaging quality.

6.2 MR safe Catheter Robot

6.2.1 Motivation and Design Requirements

There are two key procedures repeated in EP when the catheter has been inserted into heart chamber: **i)** EAM – electrode at the catheter tip will be maneuvered in contact with the atrial/ventricle tissue. Numerous catheter-tissue contact points, combined with the measured electrical signals and tracked location of the tip, are collected at different phases of cardiac cycle. The contact points form an EA map which would not be anatomically correct and consistent with the cardiac roadmap obtained by the pre-op imaging (**Fig. 6.1**). **ii)** RFA – electrode at the catheter tip will transfer the RF energy to destroy various small areas of tissue which supposes to be the origins of arrhythmia illustrated on the EA map. In conventional EP, fluoroscopy and ultrasound are adopted to visualize the catheter configuration inside the heart chamber (**Fig. 6.1**). The progress of RFA can only be roughly estimated on the basis of the catheter-tissue contact force, intra-cardiac surface ECGs, ablation temperature and impedance decay at the catheter tip [73].

However, either insufficient RFA of the lesion or inaccurate verification of electrical-circuit isolation [77] can cause edema instead of necrosis, increasing the chances of arrhythmia recurrence. In contrast, excessive heating of tissue would also cause "steam pops", increasing the risk of wall perforation by catheter. MRI can improve intra-op soft-tissue visualization during catheter manipulation, thus reducing complications [197]. Late-gadolinium-enhanced T2W MRI can clearly visualize the pathological/physiological changes of tissues. It can also identify the scar or edema indicating the successful or incomplete RFA, respectively.

Many research groups have performed numerous patient trials. The significant clinical values have been demonstrated with the routine use of intra-op MRI for EP [2-5]. Electrophysiologists are allowed to promptly determine whether the ablation of particular lesion is complete or needs further treatment. Despite intra-op MRI techniques are advantageous to the catheter navigation, the manipulation of the catheter tip to the desired location under such dynamic environment still remains challenging. The control of such a flexible, thin and long EP catheter would be inconsistent, especially within the rapidly-deforming heart chambers, e.g. the LA. Much attention has been drawn to the development of tele-operated robotic platforms to meet these challenges, such as the Sensei® Robotic System for intracardiac EP intervention [198]. Provided with high-quality intra-op MR images to assist cardiac navigation, the safety and effectiveness of robotic EP catheterization can be even further improved.

However, there is still no commercial platform or research prototype of robotic intra-cardiac EP catheterization that is MRI-compatible [197]. For example, the catheter navigation system driven by non-ferromagnetic ultrasonic motors proposed in [199], could only provide two DoFs of catheter manipulation. Similar to piezoelectric motors, these motors are driven by electric current and usually placed close to the MRI scanner. As a result, both the driving and encoding signals would induce EM noise to MRI, thereby deteriorating the image quality. This requires a complex EM-shielding to enclose the motor drivers to minimize the EMI [200]. Therefore, the research focuses have naturally shifted towards actuators driven by MR safe clean energy, e.g. pressurized water [178].

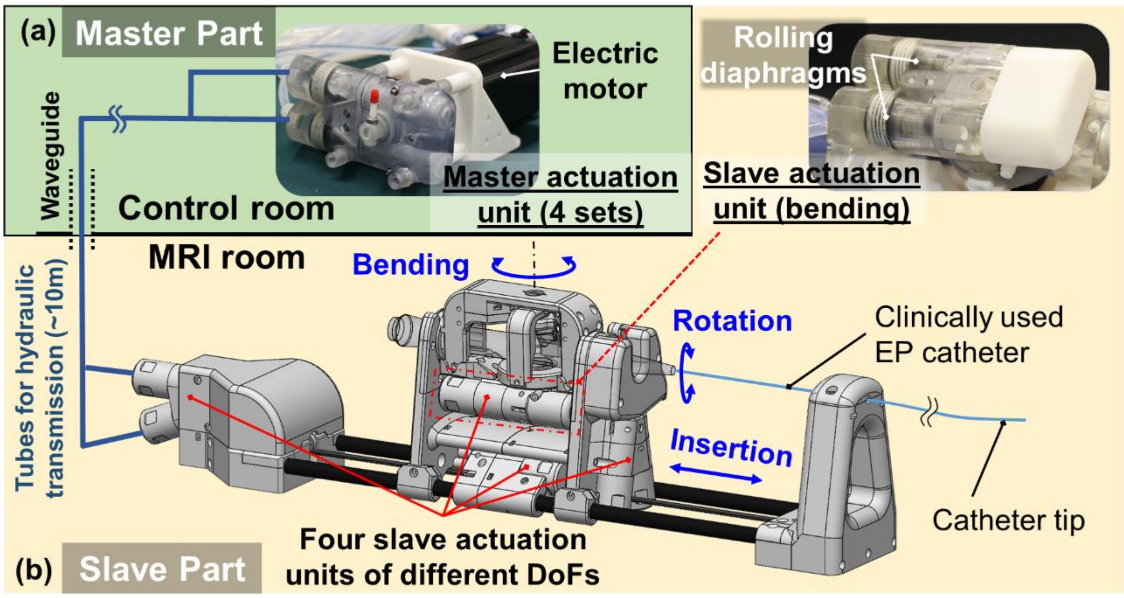

Fig. 6.2 Proposed robotic catheter platform with a clinically-used EP catheter installed. Master actuation unit in control room drives the slave unit in pair, both of which contain rolling-diaphragms for efficient mechanical energy transmission. The robot manipulates the catheter tip in 3-DoF motion, i.e. rotating, bending, coarse/fine insertion.

6.2.2 Robot Description

The catheter robot consists of two parts — the master and slave actuation systems which are placed respectively in the control room and on the patient table in the MRI room (**Fig. 6.2**). The robot has in total 3 DoFs, providing bending of the catheter in two directions of ± 90°, rotating from 0° to 720°, inserting finely in 30 mm and coarsely in 200 mm. These two insertion motions, namely coarse and fine insertions, are actuated by two independent actuation units along the same translational axis. Such design enables both the long vessel-to-chamber navigation, and short-range tip movement inside the heart chamber for EAM and delicate RF ablation.

Four pairs of master-slave hydraulic actuators in 2-cylinder configuration are adopted and each connected by 2 pipelines (**Fig. 6.2)**. The master system is actuated by individual electric motors, which operate in the control room. The motors actively drive the slave system and consequently the catheter tip, via hydraulic transmission along the long pipelines (≈10 m) through a waveguide in-between the control and MRI rooms. The pipelines are filled with pressurized liquids (distilled water) to ensure responsive synchronization between the master and slave. To enhance power transmission efficiency, rolling diaphragms (MCS2018M, FEFA Inc.) are employed for sealing the two ends of pipelines as well as transmitting piston motion. Compared to the traditional O-ring sealing, they can provide sealing with negligible friction during operation by reducing sliding between the seals and the cylinder inner wall as discussed in **Chapter 4**. Hysteresis of actuation is generally a great concern in the feedforward tele-operated robotic systems. In the proposed system, the backlash between gear teeth in actuation units and the compliance of water tubes can all contribute to the hysteresis. To minimize it, pressure in the pipelines is preloaded before starting the robotic operation. The high-pressure water pushes the pistons of cylinders against the gears at both master and slave sides, keeping constant contact of the teeth to reduce backlash. In addition, the pressure in the pipeline can increase the stiffness of water tubes, which also contributes to the decrease of hysteresis.

The slave robot is made of only non-ferromagnetic, non-conductive materials, ensuring MR safety and minimal EMI to the imaging. Main structural components are fabricated by additive manufacturing using polymer materials (Stratasys, USA). Key components for mechanical motion transmission, such as gears, are made of nylon. Other materials involved in the robot are Polyetherimide (PET), PolyVinyl Chloride (PVC), and rubber. The slave system can be mechanically compatible with various types of clinical catheters. An EP ablation catheter can be plugged-in easily and tightly incorporated with the catheter holder, which is tailor-made for steerable bi-directional EP catheters.

Online update of catheter tip position in 3D is necessary in lots of cardiac interventions. Not only does it act as the positional feedback data to close the robot control loop, but it also allows the operator to visualize the catheter configuration with respect to the cardiovascular roadmap constructed by the MR images. Two micro RF coils are incorporated into a clinically-used cardiac catheter (**Fig. 6.3**), which can directly generate signal with the scanner via two pairs of coaxial cables. The cables are connected to a specially-designed receiver interface. Dedicated MR tracking sequences could be applied to acquire the signals from micro-coils along three principle directions of the magnetic field gradient. To correct the inhomogeneity of the static magnetic field, both Hadamard multiplexing and zero-phase-reference methods could be employed. Such MR-based positional tracking is able to achieve a spatial resolution of up to 0.6×0.6×0.6 mm^3, and a sampling rate of up to 40 Hz.

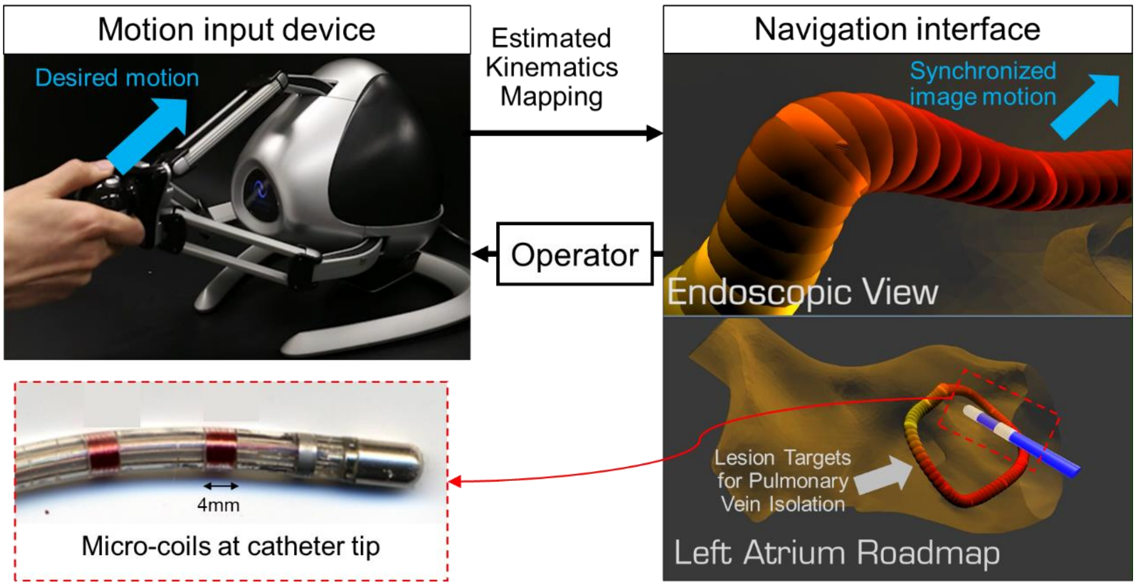

Fig. 6.3 Human-robot navigation interface for precise and effective catheterization. Circular lesion target (red) is indicated in the LA roadmap. Virtual camera is set at the catheter tip to provide endoscopic view from the tip.

Real-time and accurate localization of the catheter tip enables the estimation of its 3D position and orientation. On the basis of MR-based tracking technique, the catheter localization can take place in the image coordinate system. Unlike the conventional EP procedure, it does not need any external tracking reference. Thus the potential co-registration disparity between tracking and imaging coordinate systems can be omitted. In other words, the tracked catheter tip position shares the same coordinate space with the MR images, facilitating precise tip manipulation towards the ablation targets registered on the roadmap.

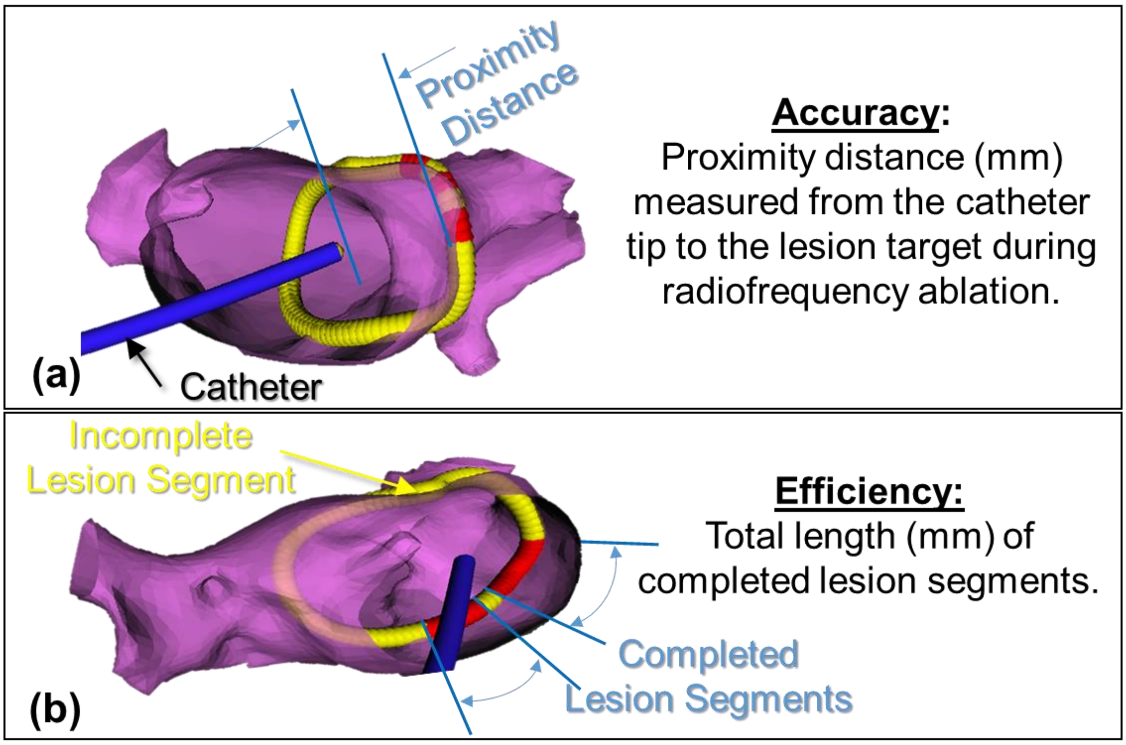

Fig. 6.4 Two major performance indices in the left atrial EP catheterization procedures. **(a)** Accuracy, defined as the proximity distance (mm) measured from catheter tip to lesion target when RF ablation power is on. **(b)** Efficiency, total length (mm) of the completed lesion segments (red).

A navigation interface (**Fig. 6.3**) is developed to provide effective tele-operation control. MR-based tracking can be performed simultaneously with the intra-op imaging, when the tracking sequence is interleaved with the imaging sequence. The continuous positional tracking data is streamed into the control system and displayed at the navigation interface. A reference point-of-view at the catheter tip is simulated and provided. A virtual endoscopic camera view is defined at the catheter tip. It gives the operator a consistent motion reference for catheter manipulation in the unknown/unstructured environment, e.g. inside the heart chambers. This could provide an intuitive visual coordination of catheter, when aiming at the lesion targets, rather than just referring to the fixed point of view.

To assess the EP catheterization procedures, accuracy and efficiency are two major performance indices in terms of the clinical practice. These two indices may be defined as in **Fig. 6.4**. Accuracy is defined as the proximity distance measured from the catheter tip to the lesion target, when the RF ablation power is on. Other factors may also reflect the accuracy, such as the number of ablation times, and the average ablation duration. Efficiency is defined as the total length of completed lesion segments within the prescribed time. But it could also relate to other factors, such as the proportion of missed lesion target segments, and the total tip travel distance. In this context, an algorithm, that can fast compute and update the distance between catheter tip and lesion target (surrounding anatomy), is essential to facilitate accuracy and efficiency. This novel algorithm will be introduced in the following **Section 6.3**.

6.3 Proximity Query (PQ) Algorithm for Intra-Cardiac Catheter Navigation

6.3.1 Background

Proximity Query (PQ) is a process that requests for the relative displacement or configuration among the 3D objects. This computational problem is fundamental in many applications, such as virtual prototyping, robot motion planning, and haptics rendering. One major demand of efficient PQ is driven by the trends of the real-time collision-free trajectories for safe robotic manipulation [201]. A typical example is image-guided surgical robotics, e.g. Virtual Fixtures [202] and Active Constraints [203]. The control concept of it is to impose force/haptics feedback on the basis of anatomical models acquired by continuous imaging data. Triangular meshes are typically used to represent 3D objects.

Previous work can mainly be deployed in convex objects to guarantee global convergence. This hampers the practical values in dynamic environments, especially where irregular or unstructured geometrical details are involved. Despite the low Big-O complexity can be ensured when coping with large samples in the existing approaches [204-207], the computational parallelism is omitted in the algorithm design. One opportunity is these iterative minimization algorithm can take advantage of the parallel computing architecture, which is becoming popular in processing complicated and large data set [201]. The significant computational performance of PQ has been demonstrated using GPU [208] and FPGA [209] on large amount of cloud points in the previous work of my research group.

In this section, the PQ formulation is derived for the analytical calculation of the shortest distance between triangular meshes (environment) and generalized cylinders (catheter or other continuum robotic instruments). This work adopts the logical progression method inspired by the previous work of Kwok *et al.* [208], which computes the shortest distance between the surrounding environments (enclosing segment) and an arbitrary point $x \in \Re^{3\times3}$. The parallelization is enabled by discretizing constraint meshes and robot segments, thus establishing the tight enclosure to improve computational efficiency without an exact robot model [210]. The robotic manipulator can be defined as a chain of finite line segments $P_jP_{j+1}(j = 1,2,\cdots,N_c - 1)$, where N_c is the total number of nodes P_j. The robot segment pathway is defined as the center line along the manipulator. M_j denotes the tangent of the pathway at node P_j. **Fig. 6.5** shows a single segment Ω_j enclosing the manipulator consists of two circles C_j and C_{j+1}, with the center of circle C_j locating at node P_j and the plane normal to tangent M_j. The radius R_j of circle C_j is defined to tightly fit the robot segments. The resolution of this segmentation is correlated to the node interval Δ, where $\Delta = |P_jP_{j+1}|$. With lower node interval Δ, the resolution increases at the cost of extra computational efforts.

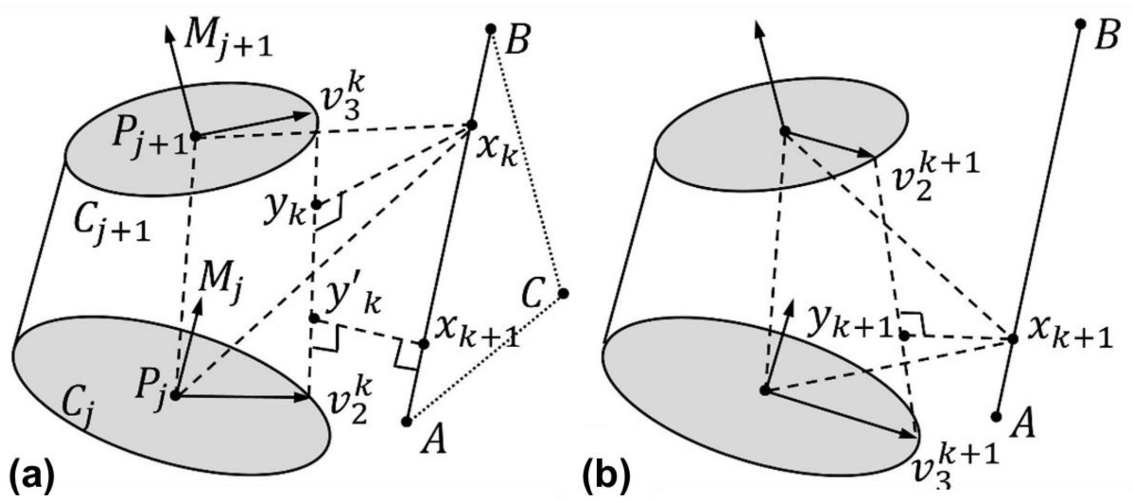

Fig. 6.5 **(a)** Basic structure of a single enclosing segment with two adjacent circular contours. Variables are defined for geometric analysis; **(b)** Newly-added variables following the previous iteration results.

Triangular meshes are commonly adopted in the representations of 3D irregular geometries in computer graphics [211]. The meshes may be constructed based on the synthetic models or using robot sensors. Numbers of tessellation algorithms have been proposed to improve the efficiency of transformation between the non-uniform 3D sensor data and triangular meshes. In these procedures, large amounts of triangles with common vertices T_i^t and edges are involved. When the triangle gets contact with any robot segment, collision occurs. It is implied that the shortest distance d between robot segments and surrounding constraints in this scenario is zero, namely $d = 0$.

The PQ problem can be mathematically simplified as a four-dimensional constrained optimization problem. Most of the optimal value is computed based on an iterative numerical technique. However, it may encounter significant computational burden. To meet this challenge, a novel algorithm is presented to reduce this computational expense by regarding the edges of triangle as independent entities. The edge-segment shortest distance is estimated first; thereby the closest point at the triangle can be searched by evaluating these three distances. The process of each triangle is independent, which leads to more efficient computation compared to the conventional methods. The computational workload can be significantly reduced by averting the repetitive processing of common edge shared by adjacent triangles. In addition, parallel computation can achieve substantial acceleration using independent multiple threads on GPU.

6.3.2 PQ Formulation for Irregular Mesh Model

The formulation algorithm consists of mainly three steps: **i)** analytical formulation of the edge-segment distance; **ii)** approximation of the shortest distance; **iii)** identification of triangle-segment shortest distance.

6.3.2.1 Analytical Formulation of Edge-Segment Closest Point Pairs

To find out the triangle-segment shortest distance, a primary step is to estimate the edge-segment distances of the three triangle edges [212]. For instance, **Fig.6.5** shows that $\overline{AB}$ is the edge of triangle ΔABC**.** Points x and y are parameterized to represent the edge $\overrightarrow{AB}$ and side surface of segment Ω_j, respectively. They are defined as follows:

$$\begin{cases} x = A + \alpha \cdot \overline{AB} \\ y = (1-\eta) \cdot C_j(\theta) + \eta \cdot C_{j+1}(\theta) \end{cases} \quad \textbf{(6.1)}$$

where parameters $\alpha, \eta \in [0,1]$, $\theta \in [0,2\pi)$.

With these parameterized points, this problem can be transformed to search for the closest point pair $x_c y_c$ of segment Ω_j and edge $\overline{AB}$. The corresponding distance can be described as $d_c = \min\{|xy(\alpha,\eta,\theta)|\}$. In terms of the basic geometrical analysis, point pair $x_c y_c$ should meet the three criteria as follows:

1) Point y_c lies in the cross-sectional area containing P_j, P_{J+1}, x_c;
2) The closest point pair $x_c y_c$ is perpendicular to edge $\overline{AB}$, namely $x_c y_c \perp \overline{AB}$;
3) The closest point pair $x_c y_c$ is also perpendicular to segment edge $v_2 v_3$, namely $x_c y_c \perp v_2 v_3$.

Regarding the above criteria, the closest point pair $x_c y_c(\alpha,\eta,\theta)$ can be determined by the solution set (α,η,θ) of equation set below:

$$\begin{cases} \overrightarrow{x_c y_c} \times n_j = 0 \\ \overrightarrow{x_c y_c} \cdot \overline{AB} = 0 \\ \overrightarrow{x_c y_c} \cdot \overrightarrow{v_2 v_3} = 0 \end{cases} \quad \textbf{(6.2)}$$

where n_j denotes the normal of the plane containing points P_j, P_{J+1}, x_c, such that:

$$n_j = (x_c - P_j) \times (x_c - P_{j+1}) \quad \textbf{(6.3)}$$

By substitution of the parameterized vectors $\mathrm{u}(\eta) = [1\ \eta]^T$ and $\omega(\theta) = [1\ \sin\theta\ \cos\theta]^T$ based on **Eq. 6.1** and **Eq. 6.2**, the equation set can be rearranged as below:

$$\begin{cases} \mathrm{u}(\eta)\omega(\theta)^T F_1 \omega(\theta) = \alpha \\ \mathrm{u}(\eta)\omega(\theta)^T F_2 \omega(\theta) = 0 \\ \mathrm{u}(\eta)\omega(\theta)^T F_3 \omega(\theta) = 0 \end{cases} \quad \textbf{(6.4)}$$

where the coefficient matrix $F_1, F_2, F_3 \in \mathfrak{R}^{3\times3}$.

Even though the original problem has been greatly simplified, the analytical special distance between a circle and an edge is already difficult to solve [212]. The analytical formula, i.e. **Eq. 6.2**, has been derived from a mathematical point of view. It can be considered as a reflection of the high geometrical complexity. Furthermore, this formula may lead to extensive computational burdens, making the real-time calculation difficult. To tackle this challenge, a novel algorithm at smaller computational cost is presented. This algorithm might be a promising approach with sufficient accuracy in the closest point pair search.

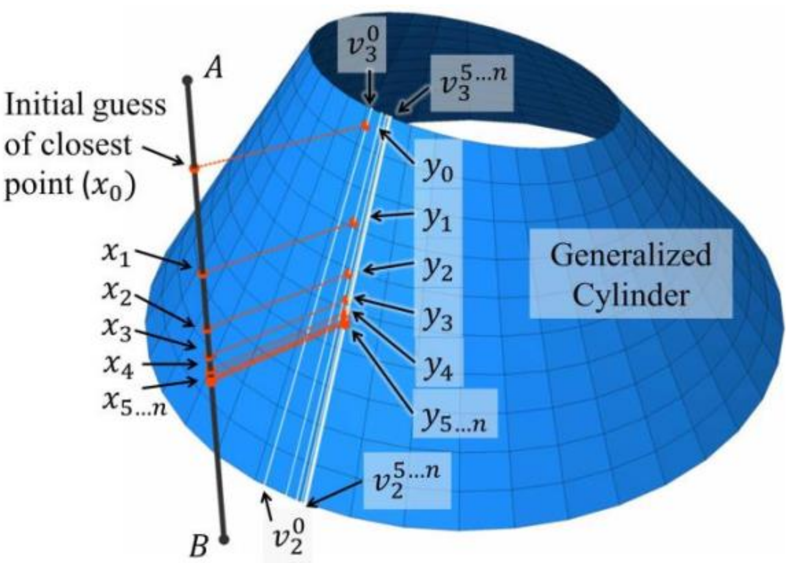

Fig. 6.6 Exemplary configuration showing the closest point pairs of each iteration. It can be considered as an extreme case, which requires more than four iterations for convergence.

6.3.2.2 Optimization-based Edge-Segment Closest Point Pair Estimation

In theory, an exact shortest distance d_c can be obtained by solving **Eq. 6.2**, however, at high computational expense. There is a trade-off between solving a closed-form solution and acquiring the approximation. The latter one is more practical in terms of the computational cost. This problem can be further transformed into the distance calculation of two cylinders by regarding the edge as a zero-radius cylinder. Referring to the cylinder intersection test algorithm proposed by Eberly *et al*. [212], the minimization cost function searching the shortest distance between two cylinders is strictly convex. Furthermore, the global minimum of the object function is either at the line endpoints or at the point at line, where its partial derivatives of variables equal to zero or undefined. In a collision detection system, it works almost only with convex objects since they can force the algorithm converge faster [213]. Such convexity and convergence can guarantee the direction of the presented iterative method (as below), which reaches a point pair with shorter distance than the previous point pair/step. Note that the last two criteria presented in **Section 6.3.2.1** can be used for the accuracy evaluation. The presented optimization-based method is described as below (**Fig. 6.5 and Fig. 6.6**):

Step 1**:** Find the initial point x_0, which is the closest point of edge $\overline{AB}$ to the centreline $P_j P_{J+1}$. This provides an initial guess of the closest point. If segment Ω_j is a right cylinder, $x_c = x_0$. Otherwise, the calculation may proceed.

Step 2**:** Search the corresponding initial point y_0 on the side surface. Referring to [208], corresponding vertices v_2^0 and v_3^0, which lie on both the circular contours and the same plane with points P_j, P_{J+1}, x_0, can be found. Since the segment edge $v_2^0 v_3^0$ contains point y_0, the initial distance can be deduced as the $d_0 = |x_0 y_0|$.

Step 3**:** Find the point x_{k+1} on edge $\overline{AB}$, which is the closest to segment edge $v_2^k v_3^k$, where k is the iteration index, $k = 0,1,2,\cdots$ (**Fig. 6.5a**). Upon the initial guess or resultant point pair $x_k y_k$ of last iteration k settled, the next iteration begins. This step is essentially to apply criteria three (**Section 6.3.2.1**) and come up with the next point pair estimation $x_{k+1} y_k'$ with shorter distance d_k', where d_k' equals to the distance between point x_{k+1} and edge $v_2^k v_3^k$.

$$\left|x_{k+1} y_k'\right| \le \left|x_k y_k\right| \text{, i.e. } d_k' \le d_k \tag{6.5}$$

If x_{k+1} found lying inside the segment, the shortest distance is returned as zero, $d_c = 0$.

Step 4**:** Search the corresponding point y_{k+1} on the side surface (resultant segment edge $v_2^{k+1} v_3^{k+1}$) by applying Kwok's PQ algorithm. The calculated distance of this step is $d_{k+1} = |x_{k+1} y_{k+1}|$. Considering both point y_k' and y_{k+1} on the segment side surface, and $x_{k+1} y_{k+1}$ defined as the shortest distance point pair between point x_{k+1} and segment Ω_j. Therefore,

$$\left|x_{k+1} y_{k+1}\right| \le \left|x_{k+1} y_k'\right| \text{, i.e. } d_{k+1} \le d_k' \tag{6.6}$$

Inequalities 6.5 and 6.6 assure that a shorter vector can be found in each loop, which is $d_{k+1} \leq d_k$. Since this is a convex optimization problem in nature, these calculated distances converge to a global minimum after certain loop number.

Step 5**:** Check if the point pair $x_{k+1}y_{k+1}$ fulfills the criteria two and three (**Section 6.3.2.1**). A threshold value ε, $\varepsilon \in \mathbb{R}^+$, is set to evaluate the dot products of vectors. The two vectors can be approximated as perpendicular when their dot product is less than ε.

$$\begin{cases} \left| \overrightarrow{x_{k+1}y_{k+1}} \cdot \overline{AB} \right| < \varepsilon \\ \left| \overrightarrow{x_{k+1}y_{k+1}} \cdot \overline{v_2^{k+1}v_3^{k+1}} \right| < \varepsilon \end{cases} \tag{6.7}$$

If **inequality set 6.7** not satisfied, repeat ***Step 3*** to ***Step 5*** with k increased by 1 until **inequality set 6.5** is satisfied. For the implementation in GPU, it is more efficient to set a fixed maximum loop number n rather than imposing an ending criteria ε. If **inequality set 6.7** satisfied, the iteration is terminated with the shortest distance d_c found as $d_c = d_{k+1}$.

In summary, the distance approximation between segment Ω_j and edge $\overline{AB}$ is:

$$d_c = \min\left\{ d_k, k = 0,1,2,\cdots,n \right\} \tag{6.8}$$

6.3.2.3 Identification of Shortest Distance from Triangle to Segment

After the computation of closest point pair of each edge, identification is of paramount importance to determine the actual closest point of triangle lying on vertices, edges or faces. Conventional approach, such as Voronoi-Clip [204], usually operates at iterative-wise to search the closest point pair on the whole polyhedral. This approach is limited in the use of convex objects. Its major deficiencies are the slow computation speed for large amounts of meshes, and the incapability of parallelization. In the contrast, the presented identification based on **Theorem I** allows for parallelization so as to achieve higher process speed.

Theorem I Assume that X and Y is a pair of features from each of two disjoint convex polyhedra, containing a pair of closest points for the polyhedra. Let $VR(X)$ and $VR(Y)$ denote their Voronoi Regions, $x \in X$ and $y \in Y$ be the closest points between X and Y. If $x \in VR(Y)$ and $y \in VR(X)$, then x and y are a globally closest pair of points between the polyhedra.

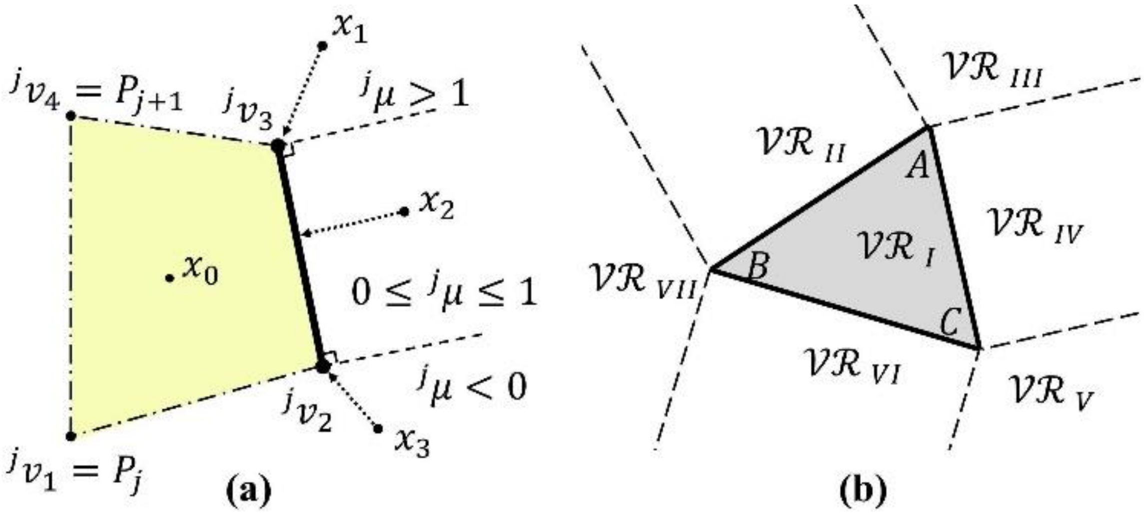

Fig. 6.7 **(a)** Four-vertex polygon extracted from the cross-sectional area of a single segment Ω_j. It is to determine the distance calculation condition by identifying the region containing the point; **(b)** Voronoi Regions of triangle ΔABC in 2D space.

Assume that X and Y represent the features of triangle ΔABC and segment Ω_j respectively, in which features include vertices, edges or surfaces. **Fig. 6.7a** shows a cross-section region defined by ${}^j v_i$, $i = 1,2,3,4$. For point x lying outside the polygon, the paired closest point y of feature Y always lies on the segment edge ${}^j v_2\,{}^j v_3$. A parameter ${}^j\mu \in \mathbb{R}$ is defined by linear interpolation the segment edge ${}^j v_2\,{}^j v_3$, such that $x' = (1 - {}^j\mu)\,{}^j v_2 + {}^j\mu \cdot {}^j v_3$, where x' is the projection of x on that segment edge.

$$ {}^j\mu = -\frac{dot\left\{\left({}^j v_2 - x\right),\left({}^j v_3 - {}^j v_2\right)\right\}}{\left\| {}^j v_3 - {}^j v_2 \right\|^2} \qquad \textbf{(6.9)} $$

For ${}^j\mu \in [0,1]$, point x' is in-between the segment edge ${}^j v_2\,{}^j v_3$. The point-to-line distance is the shortest one to segment Ω_j.

$$d_c = \left\| x - \left[\left(1 - {}^j\mu\right) {}^j v_2 + {}^j\mu \cdot {}^j v_3 \right] \right\| \quad \textbf{(6.10)}$$

Otherwise for ${}^j\mu < 0$, $d_c = \|x - {}^j v_2\|$; if ${}^j\mu > 1$, then $d_c = \|x - {}^j v_3\|$.

Based on the method of edge-segment distance presented above, Voronoi Region (**Theorem I**) is used for extending it to the triangle-segment distance calculation. It can be achieved by rapid identification of the location of closest point x_c in an triangle (e.g. vertices or edges). A triangle, e.g. ΔABC, possesses seven features (three vertices, three edges and one surface) and mutually-exclusive Voronoi Regions (as depicted in **Fig. 6.7b**). Voronoi Regions VR_{III}, VR_V, VR_{VII} are for the vertex features A, B, C respectively $VR_{II}, VR_{IV}, VR_{VI}$ are for the edge features $\overrightarrow{AB}, \overrightarrow{AC}, \overrightarrow{BC}$ respectively and VR_I is for the face feature. For instance, if segment Ω_j falls in a combined region of VR_{III}, VR_{IV} and VR_V, point x_c must locate on the edge $\overrightarrow{AC}$ (containing its two endpoints, i.e. A and C). Then, assume that this edge is denoted as triangle feature X, the closest point within triangle feature X is $x_{c\,min}$, the corresponding point within segment feature Y is $y_{c\,min}$. According to **Theorem I**, the identification is conducted as follows:

$$d = d_{min}, \text{ if } \; y_{c\,min} \in VR(X) \quad (\mathbf{6.11})$$

6.3.3 PQ Implementation for Catheter Navigation

The proposed PQ algorithm for catheter navigation is implemented and evaluated on two kinds of processor, namely multi-core CPU and GPU. CPU-based implementation acts as a reference to demonstrate the computational advantages of GPU-based PQs. Such that, the CPU-based reference platform with detailed kernel source code (CUDA) is designed and complied by Visual Studio 2012 on an AMD Phenom™ II X4 955 Processor@3.20GHz. A typical GPU platform containing 1,536 CUDA cores, nVidia GTX 770, has been employed. The computation power of modern GPUs in floating-point precision is typically ten to one hundred times higher than modern CPUs. GPU speedup can even reach ~200 times faster than the single-core CPU. It enables PQs with thirty segments and about 4M triangle meshes at rate of over 1 Hz. Note that the main memory bandwidth advantage, however, does not scale up accordingly, with only five to ten times higher than CPUs. This is the reason that the speedup magnification cannot maintain at a constant level. Another finding is the positive correlation between the number of times speedup and the number of triangular meshes. This attributes to the more efficient memory access of GPU. In this computational scheme, mesh data is transferred into local memory within every CUDA processor. Such that, only the triangle data is loaded from main memory. It prevents the potential performance degradation because of the insufficient main memory bandwidth.

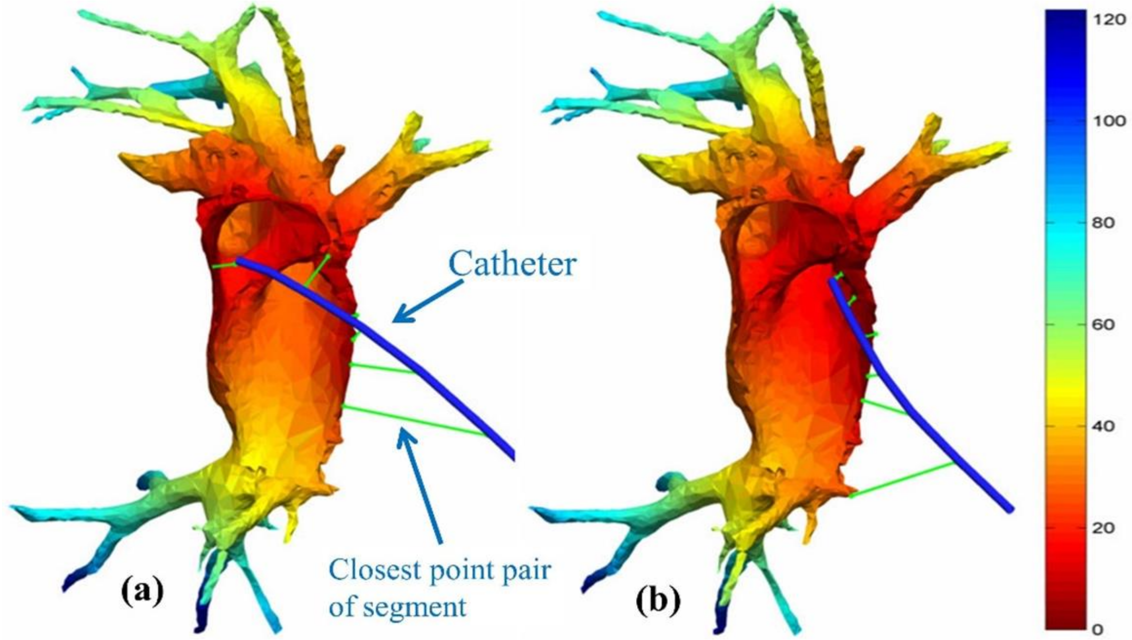

Fig. 6.8 Catheter configurations with two steering curvature. The catheter (7 segments) is inserted inside the LA model (10,658 mesh) for RF ablation during the intra-cardiovascular EP procedure. The sampling rate of PQ is maintained at 1kHz.

Fig. 6.8 shows a left atrial model reconstructed from preoperatively acquired MRI for intra-cardiovascular EP catheterization. This mesh model contains 5372 vertices, 31974 edges and 10658 triangular meshes. It serves as one of the EP catheterization roadmaps for electrophysiologist to efficiently maneuver the catheter tip towards the lesion target and perform tissue ablation. The catheter tip is fitted with 7 generalized-cylinder segments. Its configuration and position are tracked in real-time. The instantaneously-computed PQ distances relative to the mesh surface are indicated in spectrum (**Fig. 6.8**). This PQ process, given an EP roadmap with mesh number less than 10K, can be maintained at rate >1 Hz. Such information is of great potential to be implemented in a robotic catheter control system for safe and precise EP navigation. In addition, image-based haptic feedback may be made possible [214].

6.4 Experiments and Results

RF catheter ablation consists of two stages: **1)** a mapping stage, where the interventional electrophysiologist (operator) collects a number of mapping points sequentially along the endocardium with a mapping catheter. This is to create electrical activation and voltage roadmaps with a mapping system, for instance, CARTO R (BiosenseWebster, USA); and **2)** an ablation stage, where the operator ablates the lesion target via the catheter tip. Therefore the propagation of abnormal electrical signals can be blocked by the resultant scar lesion.

6.4.1 Cardiac Mapping

Mapping stage is an essential step to analyse the cardiac pathology and the lesion point locations. Large amounts of mapping points may facilitate a more precise map, which is preferable. But it may prolong the process by manoeuvring the catheter tips towards such number of mapping points. In addition, it poses potential danger to those patient with hemodynamic instability. This procedure can be especially complicated for certain patients, for instance, those with adult congenital heart diseases (e.g. Tetralogy of Fallot). Their complex anatomy makes it challenging to identify the sources of ventricular tachycardia.

A robotic catheter platform is thus in need to provide dexterous manipulation and access to regions, which are inaccessible by the manual catheters. Combined with an optimized mapping sequence, the procedural time can be greatly reduced. **Fig. 6.9** shows the experimental setup with the proposed tele-operative robotic catheter system implemented with a clinically-used catheter. A cardiac mapping task is simulated in a right ventricle (RV) phantom. The phantom was reconstructed from a pre-op mesh model with 7514 vertices and rapidly fabricated using resin by stereolithography (SLA) with three different mapping sequences (**Fig. 6.9**, **Lower row**) marked, i.e. from implicit exploration (IE) approach, geometry-based approach, and projected expert mapping sequence. IE approach was adapted from the Thompson Sampling [215], in which each step was equally spaced at a generally-consistent forward direction. Geometry-based approach is an existing method presented in [216]. It involved a ratio of point distance and surface curvature into consideration during the path planning. The expert mapping sequence was recorded from the demonstration of an expert operator over the voltage mapping procedures [217]. The voltage data of the dataset was also from previous procedure. Therefore, the mapping sequence was precomputed prior to the experiment. The catheter tip was tele-operated to these points. These tests for the three mapping sequences were carried out in the same environment by a single novice operator to reduce any interoperation factors.

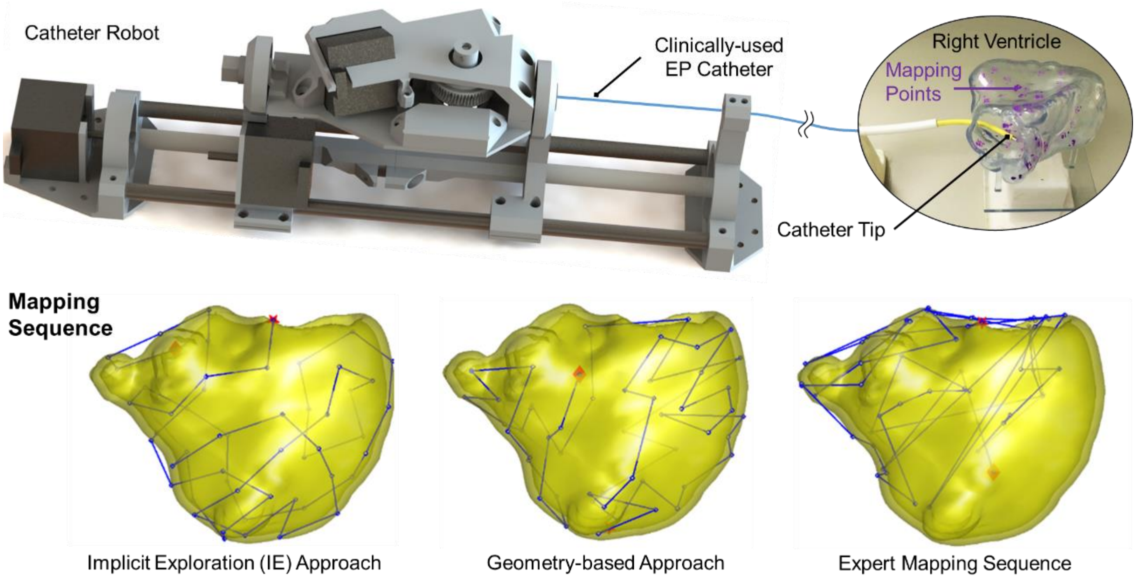

Fig. 6.9 **Upper row:** Experimental setup with the tele-operated robotic catheter system. **Lower row:** Mapping sequences with 52 target points, starting from red star and ending at red diamond. The dataset to be used in the experiment comes from expert mapping of the Tetralogy of Fallot (ToF) right ventricle phantom. The mesh at bottom left corresponds to the right ventricle outflow. And the mesh at bottom right corresponds to the triscupid valve.

Table 6.1 Total time, travel distance and operation cost for three mapping sequences

Mapping sequence	Total time/s	Total travel distance/mm	Total robot operations/no. of steps
Implicit Exploration Approach	579.658	1036.9038	344030
Geometry-based Approach	579.027	1038.5505	378841
Expert Mapping Sequence	627.082	1329.7556	487416

The total procedural time, travel distance and the operation cost for three different mapping sequences were evaluated (**Table 6.1**). The catheter tip trajectories were recorded and summed up as the total travel distances. Robotic operation cost indicated the total number of motor steps at the master side. IE and geometry-based methods had comparable results in terms of three evaluated aspects. It took about 8.3% more time to complete the original expert mapping sequence by the tele-operated robot. This might due to that the mapping points in expert sequence were mostly located in the regions hard to access, e.g. RV outflow. Unlike the equally-distributed mapping points in the previous two sequences, the catheter tip had to bend to 180° now and then to reach those mapping points at the corners. When the catheter configuration had a large bending angle, the catheter itself might possess larger hysteresis and be less responsive. These all led to longer procedural time and complicated operation.

6.4.2 Simulated Pulmonary Vein Isolation

An ablation task for PVI was simulated. The "RF ablation" was conducted inside an LA phantom. It was 3D printed using soft materials (AgliusClear, Stratasys Inc.) (**Fig. 6.10a**). To detect the tip contact with the LA, conductive glue with silver powder was spread at the inner surface of the phantom. A standard EP catheter was plugged in the slave robotic system. Electrodes embedded at the catheter tip and the inner phantom surface were connected via electric wires for contact detection. A 6-DoF EM positional tracker (NDI Medical Aurora) was also attached at the catheter tip for continuous positional feedback. Once the tip-LA contact detected, the instant tip position would be recorded.

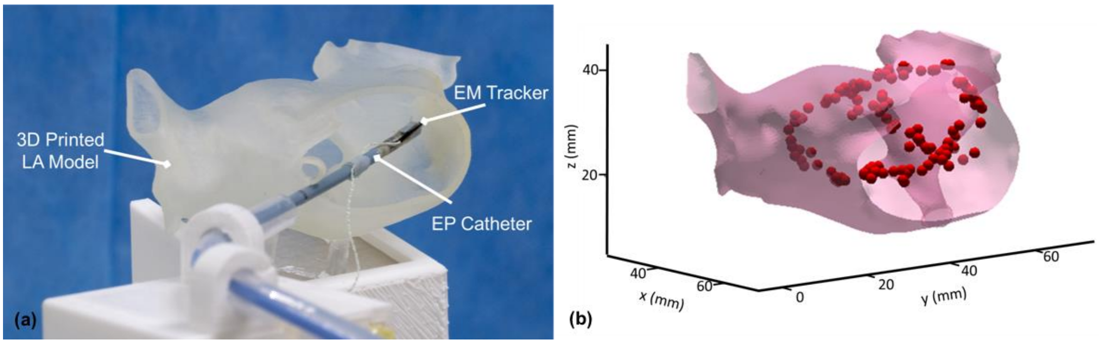

Fig. 6.10 **(a)** Experimental settings of the simulated pulmonary vein isolation task. A clinically-used catheter is tele-manipulated by the proposed robot to perform "ablation" on the LA model. **(b)** Recorded locations (127 points) of ablation in the interior surface.

In this task, operator was required to create lesion scars along the ostia of left-superior and –inferior pulmonary veins (**Fig. 6.1b**). The scars should be consistent to isolate the abnormal electrical signals [218]. Pre-op registration was performed to align the actual LA phantom with the virtual model, as well as the spatial tracking coordinates. The operator could tele-operate the catheter robot using a 6-DoF motion input device. The ablation was triggered by a foot pedal, by which proper tip contact was prescribed on the lesion targets based on the virtual model. **Fig. 6.10b** depicts the locations where "ablations" had been performed. These "ablated" locations were compared with the recorded locations when the tip was detected in contact with the phantom. The results show the catheter tip could be precisely targeted around the pulmonary vein ostia using the presented robotic catheter system. In the real MRI-guided catheterization, MR-based *wireless* coils can be implemented to provide real-time positional feedback in the same imaging coordinate system.

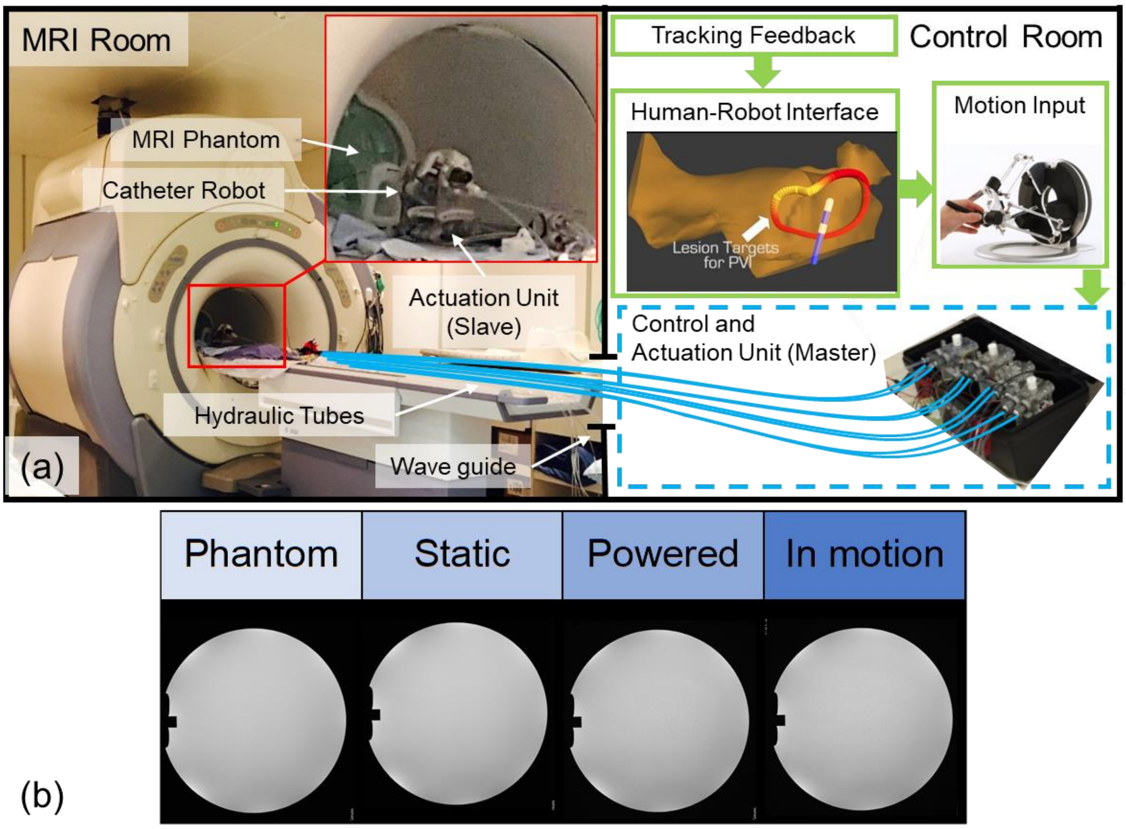

Fig. 6.11 **(a)** Experiment setup of MR-compatibility test. Key components are connected via eight pipelines between MRI and control room. The operator can tele-operate the catheter according to the navigation interface. **(b)** MR images of a SNR bottle phantom placed besides the robot. The EMI generated by the presence of robot or its operation is negligible.

6.4.3 MRI-Compatibility Test

MRI-compatibility test was carried out to validate the performance of robotic system under the MR environment. The system setup is as shown in **Fig. 6.11a**. Slave part was placed besides an MRI phantom filled with distilled water inside the bore of a 1.5T magnet (SIGNA, GE Healthcare); Master part was located in the control room. During the imaging, the water phantom was at the isocenter to verify the EMI, if any, induced by the robot (operation) nearby. **Fig. 6.11b** shows the resultant MR images under four robot operation conditions:

- **i)** *Phantom*: phantom alone placed at the isocenter;
- **ii)** *Static*: robot introduced but power remained OFF;
- **iii)** *Powered*: hydraulic and electric power ON at master side, slave robot kept still;
- **iv)** *In motion*: robot in full motion.

Phantom condition serves as a baseline reference for three other conditions. The EM-induced effects to the MR images were measured based on the changes in the SNR $J = I/\sigma$, where I is the mean intensity value of a 40×40 pixels region at the image center, and σ is the standard deviation of intensity value in a region of 40×40 pixels at the lower corner [163]. MR images in **Fig. 6.11b** had max. SNR loss < 2%. There was no observable artifacts even when the robot was in full motion.

6.5 Conclusion

Currently, there is no such commercialized robotic intra-cardiac catheterization system that is MR-compatible. The presented robotic catheter system that is the first of its kinds to be incorporated with intra-op MRI, real-time positional tracking, human-robot interface, and high-performance actuation. The robot is driven by a master-slave hydraulic actuation system that features with small hysteresis, enabling precise manipulation of standard EP catheter. The slave part is capable of operating close to or even inside the MRI scanner without deteriorating the intra-op imaging quality. This may serve as a benchmark for the design and integration of MR-conditional robotic devices in MR image processing, robot actuation and catheter tracking under MRI.

Realization of MRI-guided cardiac EP intervention requires not only MR-conditional robotic platform, but also other key components such as accurate positional sensing of catheter and intra-op image processing techniques. A control interface is developed, which could integrate advance MR-based catheter tracking and fast image registration techniques, where the catheter tracking was interleaved with the intra-op imaging. This catheter tracking shared the same coordinate system with the MR images, avoiding disparity due to relative registrations between tracking and the imaging systems. This enables construction of virtual endoscopic scene from the viewpoint of the catheter tip, facilitating precise tele-manipulation of the tip towards the ablation targets registered on the cardiac roadmap. Thus, electrophysiologists could have better performance when conducting RF ablations, consequently improving the safety of catheter navigation during the EP procedure.

Chapter 7
Hydraulic Drive Soft Manipulator for Transoral Robotic Laser Ablation

7.1 Introduction

HNCs affect more than 4.6 million people [219]. It is the sixth most common cancer and ninth most frequent cause of death worldwide, with the absolute numbers continuing to increase [220]. Transoral surgery is an approach to treat the HNCs on nasopharynx, oropharynx, larynx and hypopharynx through the oral aperture. Among the other two treatment modalities, i.e. radiotherapy and chemotherapy, transoral surgery has least toxicity and can mitigate the long-term functional sequelae of primary chemoradiation [221]. But this approach may not be able to access some large cancers without specialized techniques or instruments.

7.1.1 Transoral Laser Microsurgery (TLM)

With the advent of minimally invasive endoscope techniques, TLM was introduced in the 1970s. Highly-concentrated laser beam can minimize the carbonization margin and preserve the anatomical/functional integrity [222]. Oncological results reported in many studies [223-225] have demonstrated its excellent local control rates of early laryngeal cancers without compromising vocal function. Carbon dioxide (CO_2) laser (wavelength of $\lambda \approx 10,600$ nm) is the most common laser source in TLM. It can deliver energy at 0.1-100 W and ablate tissue to a depth of 200 μm [221]. Since its introduction, it has largely replaced the conventional electrocautery in advantage of its precise penetration depth and hemostatic control [226]. However, these systems deliver CO_2 laser by a means of rigid optics mechanism that can alter the laser beam projection using adjustable prisms/mirrors. This rigid structure inevitably hinders its use in applications requiring frequent instrument reposition to achieve adequate tumor exposure and cutting effect. To meet this challenge, lasers that can be flexibly guided by optic fiber were introduced. It can provide high-power tissue dissection at much shorter wavelength, e.g. thulium ($\lambda \approx 1,942$ nm) and blue light (445 nm) laser, as well as the excellent hemostasis [226]. These optical fibre-based laser dissection instruments have been currently used in clinical practice [221, 227]. But the difficulties in efficient manual delivery/manipulation of these long flexible instruments has limited its widespread use.

7.1.2 Transoral Robotic Surgery (TORS)

TORS is a kind of MIS that may be incorporated with nonlinear endoscopy and wristed instrumentation, offering the surgeons a much wider view of surgical field and more dexterities in maneuvering the instruments. Very limited number of transoral surgical robot platforms have been currently FDA-approved, i.e. da Vinci robot (Intuitive Surgical Inc., USA) and Flex® Robotic System (Medrobotics, USA) [228]. They are mainly applied for surgical resection of early stage (T1/T2) oropharyngeal lesions. In a controlled prospective study, it has shown that the combination of TORS with thulium laser showed locoregional control, limited injury to internal carotid artery/nerve, decreased postoperative pain and higher surgical safety [227]. However, maneuvering instruments in the confined ONP cavities remains very challenging, Difficulties arose for the resection of deep tumor (5-10 mm) as it closes to the critical neurovascular or muscular structures which affects the speech and swallowing function. Even assisted with robot, lack of adequately pre-surgical plan for the surgery in a three-dimensional approach would heavily relies on the surgeons' experience while dissecting the tumors, particularly their deep aspect that are not readily visible. Evaluating the laser incision/ablation depth beyond the critical artery/nerve is still very difficult due to the disability of real-time, frequent and *in-situ* sampling of tumor margin. Such intra-op evaluation can only be conducted on the basis of pathologic laboratory procedures, e.g. frozen section analysis (FSA) [229], but only right after completion of the tumor resection.

7.1.3 MR Thermometry

MRI offers excellent image contrast for oral and nasopharyngeal soft tissue. It can form a surgical roadmap in 3D, distinguishing even the early stage (T1/T2) of carcinoma/tumor from the healthy tissue, as well as the critical lingual/carotid artery and nerves. Real-time T2/diffusion-weighted MR imagining can also visualize the physiological changes of tissue arising from complete or incomplete cutting/ablation created by laser (tissue temperature <80℃ [230]), thus monitoring the incision depth and progress. By adjusting temperature-sensitive MR parameters, e.g. proton resonance frequency (PRF), the MR susceptibility at high SNR can measure the fine change of temperature in accuracy of <1°C. This capability has been widely employed in MRgFUS procedures [231]. Through the MRI guidance, the 3-D resection margins can be planned, carried out with the laser intra-operatively to protect critical structures yet resect the tumor with adequate margins. Furthermore, intra-op visualization of the HNCs, as well as the laser-induced physiological changes, is made possible by T2-weighed/diffusion-tensor MRI. This may eliminate the need for FSA, thus greatly shorten the operation time.

In this chapter, a soft robotic manipulator for MRI-guided transoral laser ablation is presented. It can be integrated with intra-op MRI and online MR thermometry to realize the high-precision soft robotic/endoscopic navigation for laser microsurgery. Operation time can be greatly reduced from the post-resection margin evaluations, such as frozen section analysis. The contributions of the work is summarized as follows:

i) Development of the *first* MR safe *soft* robotic manipulator for transoral tumor dissection. Its compliance and compact design ensures the safe interaction with patient anatomy and *flexibly* access to the deep ONP lesions.

ii) Hybrid actuation design with three soft actuation chambers reinforced by springs, capable to provide accurate and repeatable manipulation. Covered by a rigid housing, such actuator can still steer the laser collimator at ±30°. This feature indicates its dexterity for lesion targeting within the constrained operating space, i.e. ONP cavities.

iii) Easy fabrication by directly 3D printing using digital materials. It is low-cost and can be disposable for the ease of medical sterilization.

iv) MRI-guided laser ablation on *ex vivo* tissue. This navigation test is incorporated with *wireless* MR trackers to provide direct positional data in imaging coordinates. Ablation progress is monitored by intra-op MR imaging. A smooth, homogeneous, circular trace can be readily identified under the MRI, which has demonstrated the presented soft robotic manipulator capable to perform accurate controllable tissue ablation/cutting.

7.2 Design Requirements

In the current clinical practice of tumor resection, there are two key steps in transoral robotic endoscopic surgery:

i) Instruments docking through the oral cavity: a mechanical oral retractor is positioned non-invasively on the teeth and the maxillary alveolus. This can stabilize the mouth opening (45-55 mm) [232] and enlarge the exposure of surgical field. By pressing the tongue and soft palate, the retractor creates the direct access to the deep ONP cavities and acts as a static frame-of-reference for the surgical instruments (**Fig. 7.1**) [233]. Three rigid long instruments are thus deployed through the retractor, along with a laryngoscope.

ii) Identification of carcinoma margin: margins around the resection have to be marked at least 5-10 mm beyond the actual tumors [234]. Dissection of parapharyngeal space may be required to ensure the adequate exposure of target tumors/lesions [235].

However, the lack of effective manipulation within the confined operating space still makes these procedures time-consuming and complicated. This also limits the conventional approach mostly applied to laryngeal, hypo- or oro-pharyngeal tumors [222]. Although some robotic systems (e.g. da Vinci SP® surgical system and Flex® robotic system) may provide flexible and miniaturized devices through a single cannula (diameter of $\emptyset 25\,\mathrm{mm}$) for dexterous manipulation, e.g. nasopharyngectomy. The resection of relatively large and deep (5-10 mm) tumor still remains challenging without the margin marking in depth, on account of the potential injury to internal carotid artery/nerve.

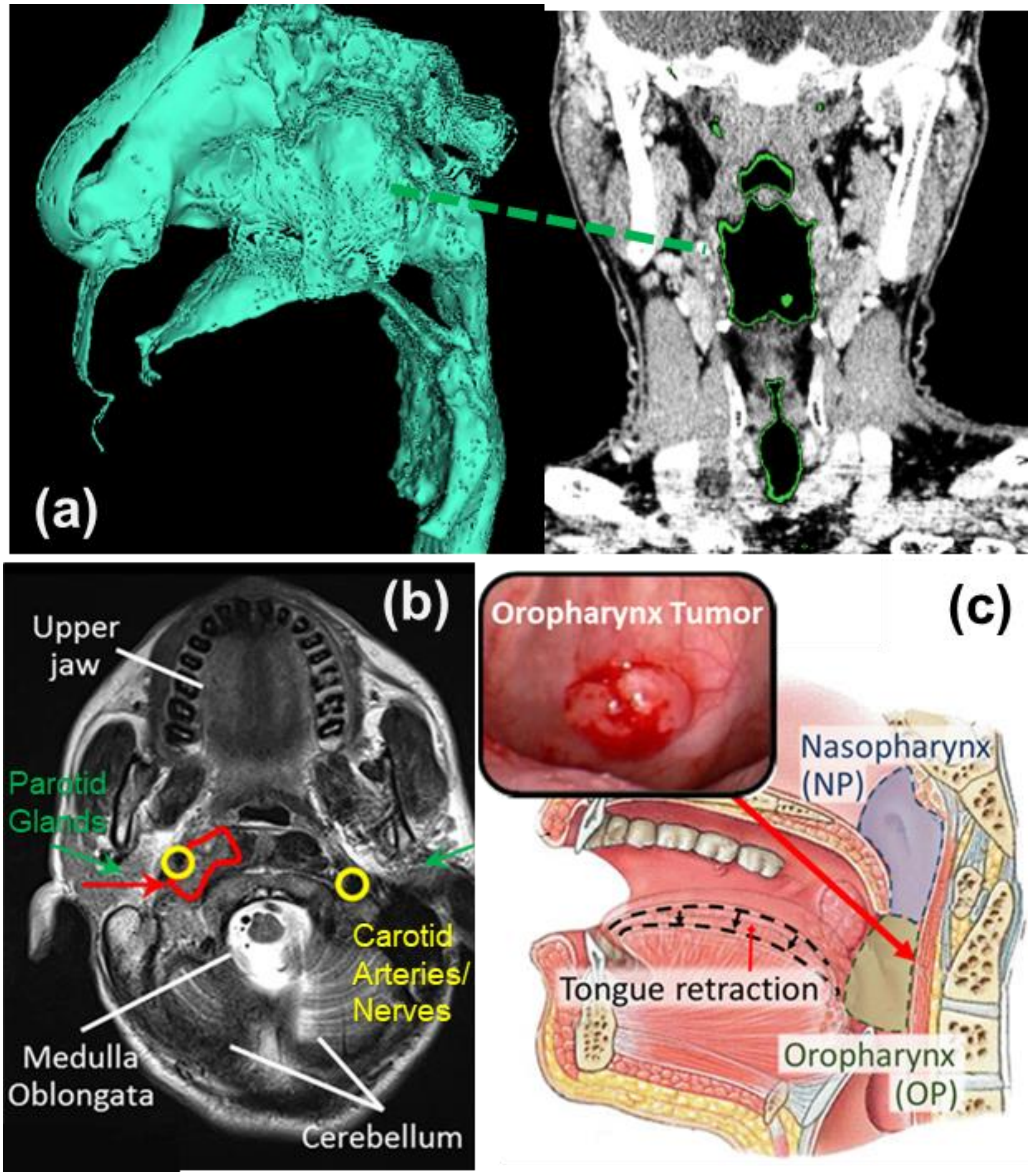

Fig. 7.1 **(a)** Transoral region of interest delineated from CT images in 3D; **(b)** T2-weighted fast spin echo (FSE) MR image of head-and-neck region in the axial scanning plane. Red arrow indicates the tumor located in the parapharyngeal space. Yellow circles and green arrows, respectively, denote the carotid arteries/nerves and parotid (salivary) glands; **(c)** Head-and-neck anatomy indicated with an actual tumor originated from the oropharyngeal cavity.
Image source: Pearson Education Inc.

Table 7.1 Incision power density with its respective effect on tissue

Power Density (PD)	Effect on Tissue
0-500	Heating
500-1500	Contracture, denaturing
1500-5000	Ablation (partial vaporization)
5000-20000	Incision (complete vaporization)
20000-100000	Rapid deep incision

Laser microsurgery is playing an increasingly important role in tumor resection in advantage of its precise incision depth and hemostatic control. Lots of transoral procedures have been performed using the laser surgical systems, e.g. Lumenis® AcuSpot AcuBlade. However, evaluating the laser incision/ablation depth beyond the critical artery/nerve is still very difficult due to the disability of real-time, frequent and in-situ sampling of tumor margin. Such intra-op evaluation can only be conducted on the basis of pathologic laboratory procedures, i.e. FSA, and only right after the completion of tumor resection. The laser effect on tissue is estimated based on the power density as shown in **Table 7.1**. MRI offers excellent image contrast for ONP soft tissue. Provided with intra-op 3D MRI and MR thermometry for guidance, the carcinoma margins can be readily identified and properly planned. Progress of the ablation/incision can be real-time monitored under the MRI as well. It is timely to benefit from these MRI advances for the laser ablation guidance in tumor resection. To facilitate the introduction of MRI into transoral robotic laser microsurgeries, the robot is designed to fulfill the following criteria:

1) The robot has to be *flexibly* introduced through mouth opening, intra-oral and oropharyngeal cavities, even up to nasopharynx, but without having to perform dissection of soft palate. It should ensure the safe interaction with patient anatomy, while offer a stable platform for laser beam projection on ONP lesions.

2) Robotic manipulation should be sufficiently dexterous within the limited operating space. Proximity and differentiation angle from the laser collimator tip towards the ONP lesions have to be promptly adjusted, optimized based on the intra-op MR images and RF-tracking. The repeated workflow of the laser path re-planning should be significantly smoothened, as well as the internal instruments advancement through the endoscope.

7.3 Methodology

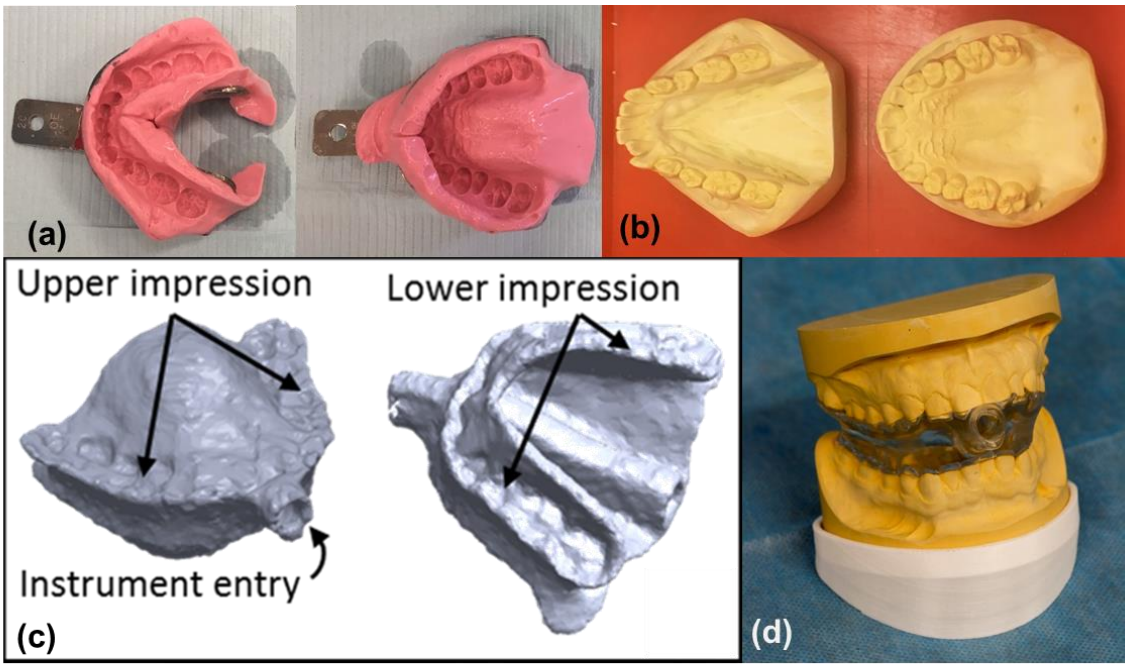

Fig. 7.2 Fabrication procedure of a patient-specific dental guard (docking module); **(a)** Upper and lower impressions of the patient taken by a dentist; **(b)** Master models of the impressions; **(c)** Precise 3D scanned models of the dental arches, including upper and lower impressions. Specific features (e.g. MR-fiducials, instrument channels) are accommodated into the model, of which the shapes, sizes and locations are optimized; **(d)** Dental/surgical guard prototype fabricated using biocompatible material (acrylic resin). It can fix the jaws in open-mouth position so as to provide sufficient workspace ($> 25 \times 25 \times 20$ mm^3) for transoral surgical interventions.

7.3.1 Docking Module

To maximize the cavity space for instrument introduction, a piece of dental surgical guard (docking module) is designed and fabricated using casting models and additive manufacturing (**Fig. 7.2**). Upper and lower oral impression bodies made of fast set alginate (GC Aroma Fine Plus®) are tailor-made by a dentist. Working models casted with plaster is used to form the 3-D CAD models by precise optical scanning. Therefore, the CAD model of a patient-specific dental guard is generated with some adjustments to ensure an open bite of 30mm. Other features are accommodated into the model, including slots ($3 \times 4 \times 8\,mm^3$) for MR fiducials, channels (inner/outer diameter: $\emptyset 11.5/18.3\,mm$) for endoscopic instruments and interlocks to anchor the entire robotic mechanism. The shapes, sizes and locations of these features are optimized considering the material rigidity and strength. MR fiducials (e.g. capsulized with fish oil or MR-based coil-markers) are embedded at the external surface of the dental guard. The minimum number of such fiducials is three to serve as image registration landmarks and offer the steady frame-of-reference relative to the robot base in MR image coordinates. In addition, this dental guard can fix the jaw in open-mouth position so as to create larger oral space (more than $25 \times 25 \times 20\ \mathrm{mm}^3$) for transoral surgical interventions. This avoids the dissection of soft palate, in particular for nasopharyngeal procedure. The dental guard is 3D printed using biocompatible materials (e.g. MED610, Stratasys, Ltd.) at low cost and can be single-use for easy sterilization.

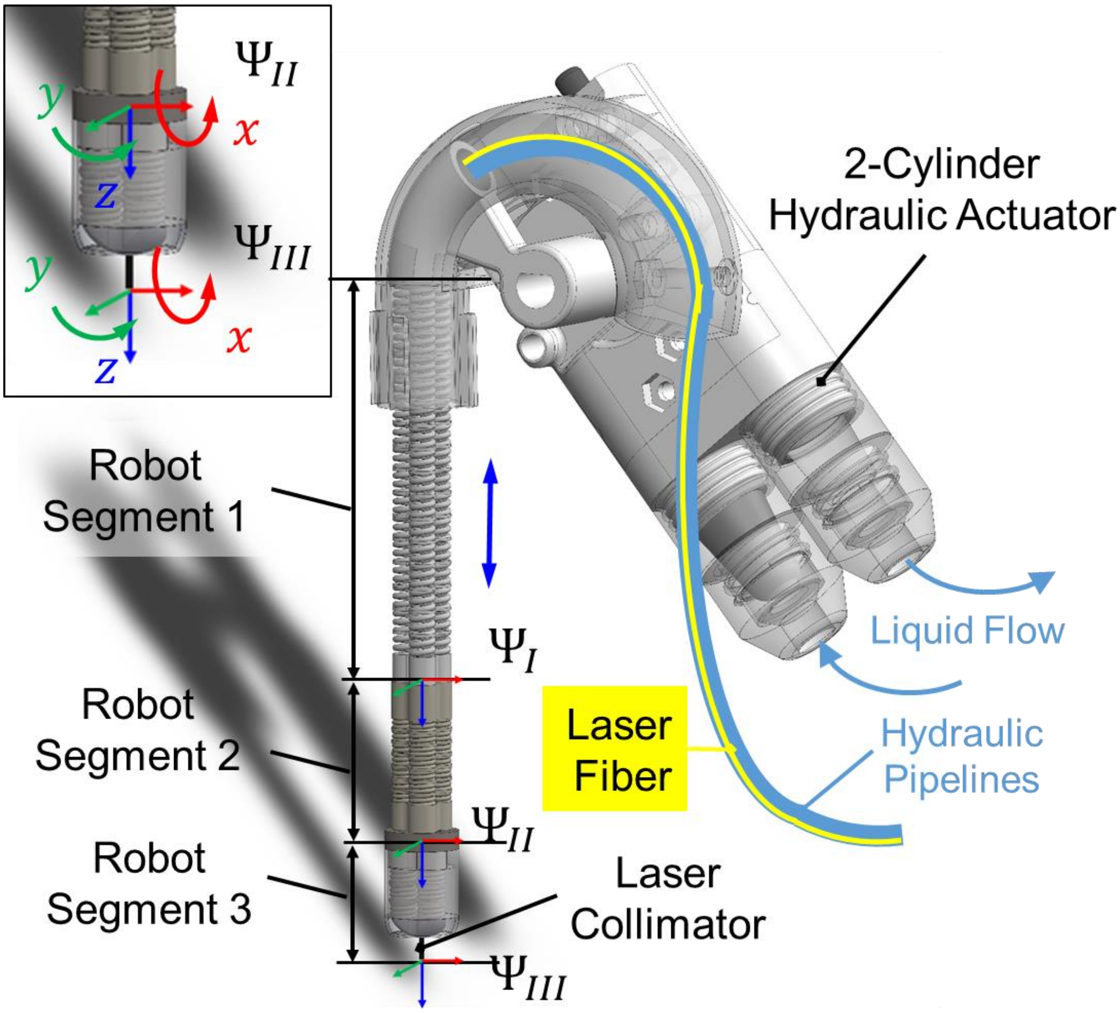

Fig. 7.3 Overview of the proposed transoral robot (slave). Coordinate frames Ψ_I, Ψ_{II} and Ψ_{III} are defined at the distal end of segment 1, 2 and 3, respectively. Segment 1 is a continuum structure for advancement, which is driven by the 2-cylinder actuator and can passively adapt to the curvature of patient natural orifice. Segment 2 and 3 are designed to actively steer the laser collimator, which are actuated by hydraulic power as well.

7.3.2 Advancement Mechanism

The robot can be firmly anchored onto the dental surgical guard, docking/positioning through the oral cavity. Advancement mechanism includes a hydraulic actuator, a curved channel, and the continuum robot segment 1. This segment comprises of three spring-like structures with channels embedded inside for routing of the hydraulic pipes and optical fiber. It is fabricated by 3D printing using soft polymer materials. It can *passively* adapt to the shape of curved channel when it is retrieved from the ONP cavity. The proximal end of segment 1 is coupled with the two-cylinder hydraulic actuator, which is anchored outside the mouth (**Fig. 7.3**). Such hydraulic transmission can push and pull the robot segment 1 to generate translational motion at fine resolution. Note that this resolution will depend on the hysteresis induced by the hydraulic transmission, rather than the pushing/pulling step.

Similar with the setup introduced in **Chapter 2**, rolling-diaphragms are used to seal the cylinders with negligible sliding friction during transmission. The wall of this rubber diaphragm is reinforced by fabric to withstand the high fluid pressure (up to 0.3 MPa). Its maximum linear stroke is 20 mm, driving the rotary motion of pinion at most by 100.6°. This corresponds to 40-mm insertion stroke. Considering the total length of the continuum robot ($\sim\emptyset 12 \times 150$ mm), it is capable of reaching deep laryngeal area. The master and slave actuation systems, located in control and MRI room separately, consists of two identical pinion-and-rack units to transfer the linear motion to rotary. Two 10-m long hydraulic pipes made of Nylon (outer/inner diameters of Ø6/4 mm) connect the master and slave actuators, passing through the waveguide in-between two rooms. Hydraulic power originates from an electric stepper motor (Hong Fu Da Inc., China). Clean water is adopted as transmission working media. Note that the water can be pre-pressurized to push the rack gear teeth towards the pinion teeth, keeping their teeth in steady contact and eliminating backlash.

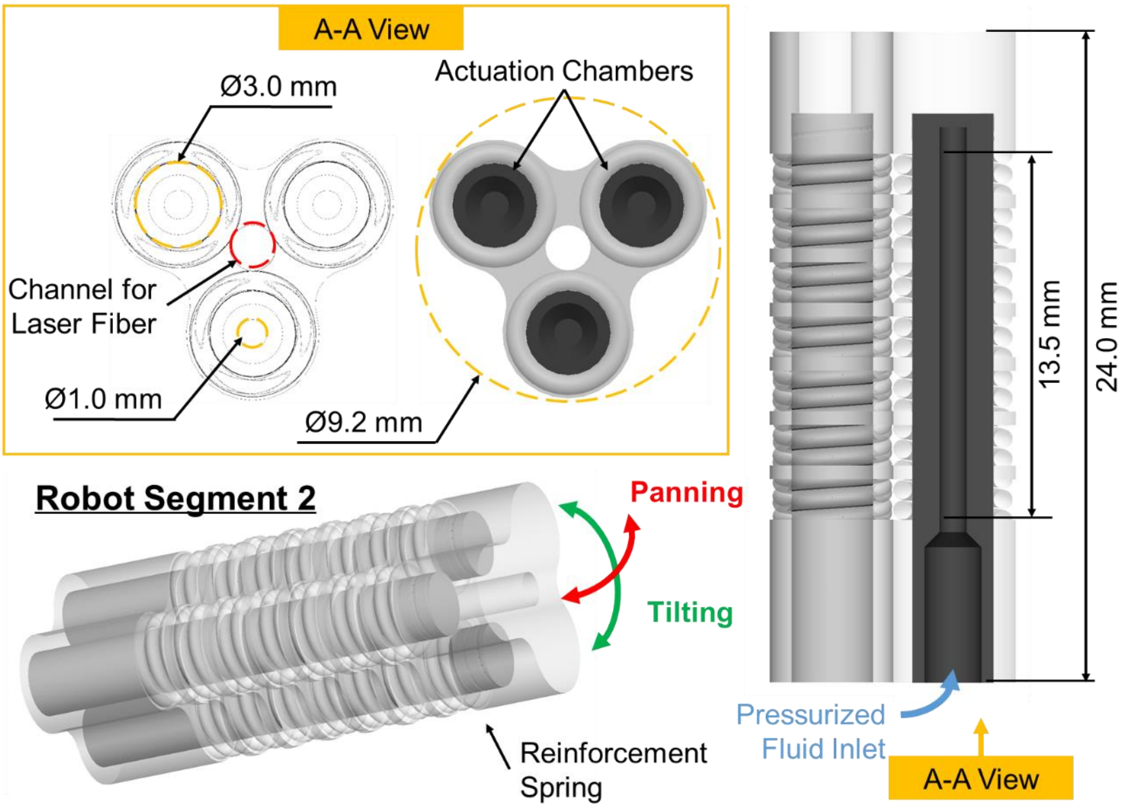

Fig. 7.4 Design and overall dimension of the robot segment 2. Three chambers (black) are actuated by regulated hydraulic pressures. Reinforcement springs with pitch of 0.75 mm tightly enclose the chambers to constrain their radial expansion. Axial elongation of these pressurized slender chambers ($\emptyset 3 \times 13.5$ mm) generate coarse bending motion, max. $\pm 60°$.

7.3.3 Dexterous Laser Steering within Confined Workspace

Accredited to the pliability of soft structure, the manipulation of soft robotics assures relatively high compliance within the confined working space and facilitates versatile interaction with surrounding environments. Such features are especially desired in those applications demanding safe interaction with the dynamic environment. Therefore, a soft robotic manipulator is proposed for transoral laser microsurgery. To dexterously steer the laser collimator, omni-directional bending along the transoral curved pathway is required. Two robot segments are designed and fabricated to generate such pitch-roll displacement, namely segment 2 and 3, for coarse ($\pm 60°$) and fine ($\pm 30°$) steering, separately.

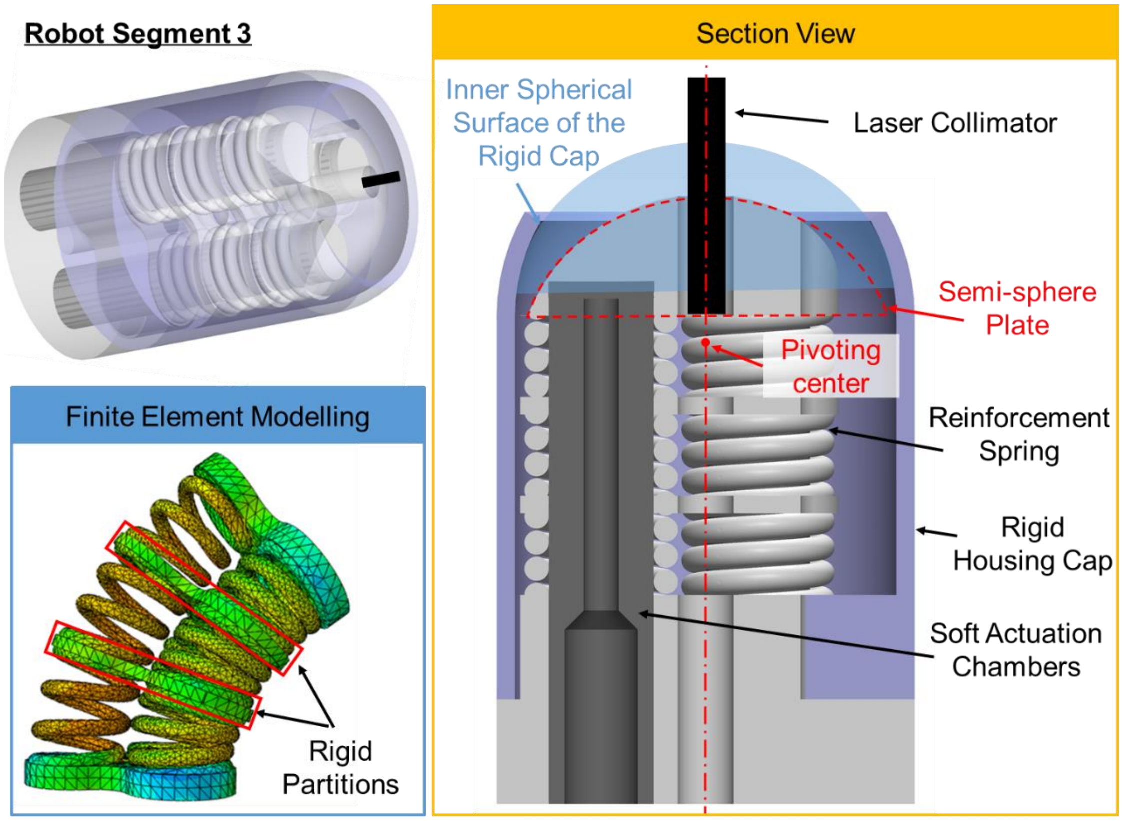

Fig. 7.5 3D model of the robot segment 3. Actuation method of segment 3 is similar with the one of segment 2, but is to provide fine angular adjustment with shorter length of actuation chambers. There are two partitions dividing the reinforcement spring into three segments, in order to reduce the twisting motion and radial inflation during actuation. Different from segment 2, a rigid cap encloses all the actuation structures. This ensures mobility when the curvature of the whole continuum robot is constrained. A semi-sphere plate may interact with the inner spherical surface of the housing cap to form a ball joint. The laser collimator is fixed with the semi-sphere plate and can be pivoted to perform laser projection ablation.

Fig. 7.4 shows the CAD/CAM designs of robot segment 2 for large-angle bending. Elastic/linear strain-stress control is currently exploited in many soft continuum robots. These soft structures generally lacks of rigidity or stiffness to offer a stable platform for accurate targeting. It limits their applications in the procedures, e.g. microsurgeries, which demand on precise manipulation at submillimeter scale accuracy. Considering the trade-offs of compliance and stability, a hybrid actuation mechanism with both soft and rigid components is presented. All these components can be directly printed out without assembly using digital material 3D printing (Object360, Stratasys Ltd.). Elastomer material (Agilus 30, Stratasys Ltd.) is used for actuation chambers, while reinforcement springs are fabricated by rigid material (MED610, Strarasys Ltd.). Three hydraulic tubes are plugged in to supply the regulated hydraulic pressures. Elongation of the slender chambers (inner/outer diameter: $\emptyset 1/3$mm, length: 13.5 mm) results in the segment bending. The max. angular displacement of segment 2 is about $\pm 60°$ at 6 bar. The radial expansion of the chambers are constrained by the reinforcement springs. Innovated by fiber and paper reinforcement mechanisms, these springs serve as strain wrapping and enhance the radial stiffness. Six partition plates divide the springs into separate seven segments. This can eliminate the radial inflation and twisting instability during actuation. The total diameter of segment 2 is $\emptyset 9.2$ mm with a through channel at the center for laser fiber, smaller than the diameter ($\emptyset 12$mm) of the other two segments. This reserves space for the channeling of the remaining three hydraulic tubes for segment 3.

Fig. 7.5 shows the CAD/CAM designs of robot segment 3. Similar with the design of segment 2, this segment consists of three separated elastic chambers situated $120°$ apart. Each chamber is fully enclosed by a reinforcement spring with three partition plates (thickness: 0.5 mm). The chamber length of segment 3 is shorter than that of segment 2, i.e. 8.6 mm. Different from the coarse angular adjustment of segment 2, segment 3 is designed to provide fine panning/tilting motion in the constrained operating space. A rigid housing covers all the actuation structures. Even when the curvature of whole continuum robot is fixed, there is still mobility to tuning the laser projection orientation. At the distal end of the reinforcement-spring mechanism, a semi-sphere plate is designed to hold the laser collimator and interact with the inner surface of the housing, thus forming a ball joint. The laser collimator can pivot about the virtual sphere center for projection ablation.

7.4 Experiments and Results

7.4.1 Path-following Test

Path-following tasks were conducted to evaluate the accuracy and repeatability of the presented soft robotic manipulator. Experimental setup is shown in **Fig. 7.6**. The pressure changes of chambers are regulated to be smooth and gradual (**Fig. 7.8** and **Fig. 7.11**). It allows the reaching of equilibrium for each pose and minimizes the residual motion generated during the fluidic actuation. Such quasi-static motion can facilitate steady targeting of the laser collimator or other interventional tools at the regions of surgical interests. Thereby the inadvertent damage to delicate tissues and potential discomfort of patient can be avoided.

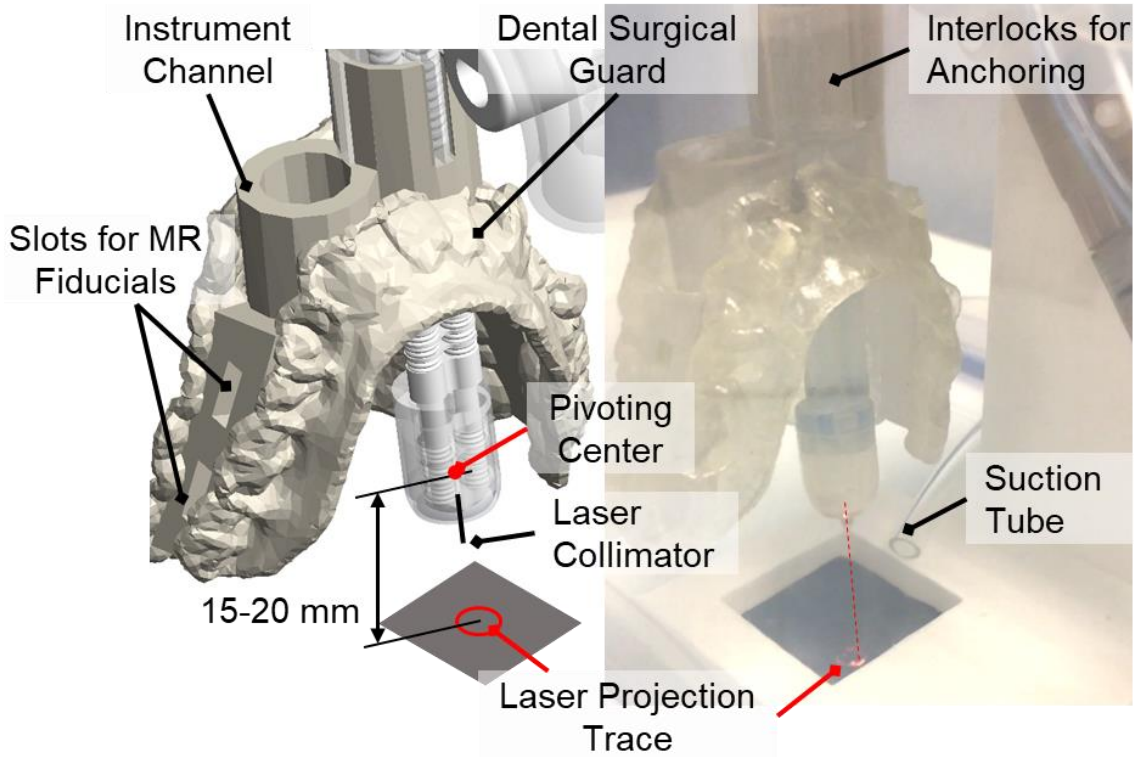

Fig. 7.6 Experimental setup of the path-following test. An EM tracking system (NDI Medical Aurora) is employed to provide the real-time position and orientation data feedback. The projection plane is placed about 15-20 mm away from the pivoting centre of the laser collimator. A circular ablation trace (Ø5 mm) can be observed in the projection plane.

Actively-bending segment 2 and 3 are tested separately. To mathematically describe the state space, $u_k \in U$ is defined as the chamber water pressure at equilibrium at time step k, where U is the control space. s_k represents the projected point coordinates when the robot chambers are pressurized with u_k and at equilibrium status. This task space coordinate s_k corresponds to the robot state x_k, namely $s_k = f(x_k)$. $x_k = [p, n]^T \in \Re^6$, where $p_k \in \Re^3$ denotes the distal end position and $n_k \in \Re^3$ denotes the orientation normal vector in the Cartesian space. Robot state is determined by the control space, $x_k = h(u_k)$. Unlike the rigid-link robots, of which the state can be well-defined by the joint kinematics, it is hard to describe the state of soft continuum robot. Such that, a learning-based feedforward control, i.e. neural network, is adopted to establish the mapping between control space u_k and task space s_k. Pre-training is conducted with 3512 inputs. Inverse kinematics can be thus calculated by the mapping of forward kinematics.

Projection planes were placed at a distance of 20 mm from the pivoting center of the laser collimator (**Fig. 7.7** and **Fig. 7.10**). A 6-DoF EM tracking coil (Ø0.8 × 9 mm) replaced the laser collimator to record the continuous (at 40 Hz) positional data. The EM tracking system employed can provide position and orientation data with root mean square accuracy of $0.7\ \text{mm}$ and $0.2°$. The robot was anchored with a dental guard and performed the spiral trajectory tracking task in free space. The tracking errors are defined as the distances between the targeted points and actual projection points, as shown in **Fig. 7.9** and **Fig. 7.12**. Optimal control parameters were obtained for the subsequent MRI-based trials to coordinate robotic motions including advancing and steering the laser collimator.

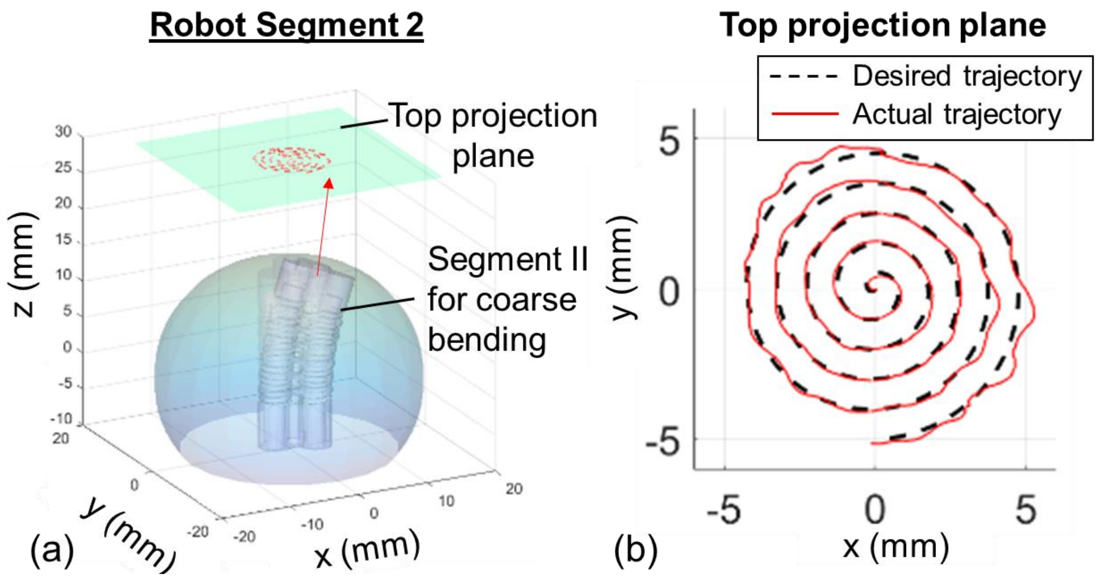

Fig. 7.7 **(a)** Isometric view of robot segment 2 projecting a spiral trajectory at the plane; **(b)** Plot of desired (black) and actual (red) trajectories on the projection plane.

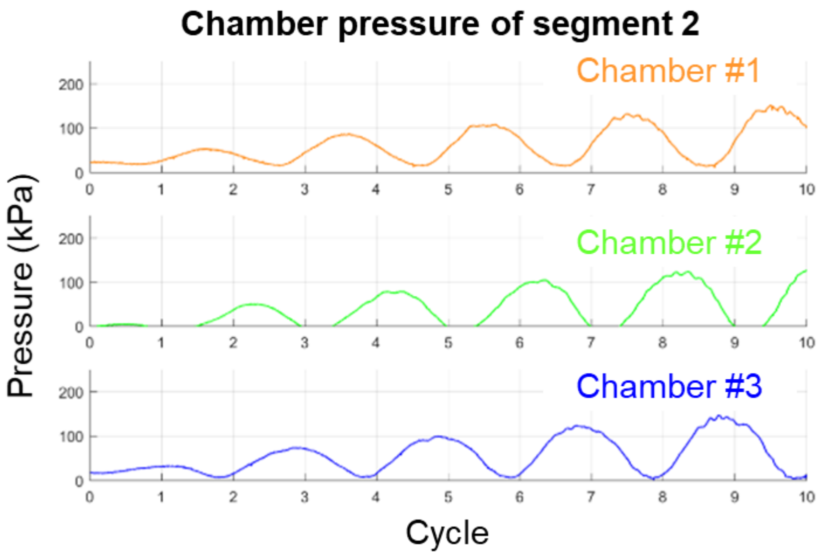

Fig. 7.8 Pressure variation of three actuation chambers through the whole journey of spiral path following.

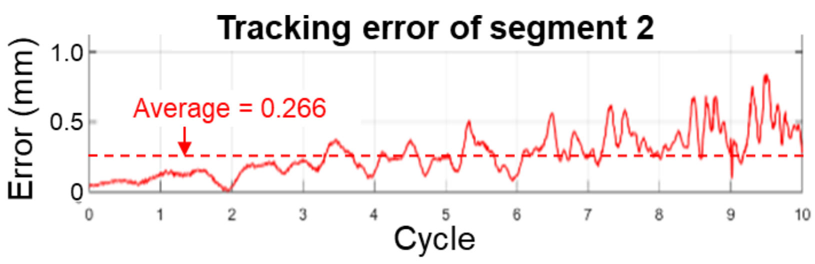

Fig. 7.9 Path following errors calculated in the projection plane. Tracking errors are defined as the distances between the target and actual projection points. The accuracy is 0.266 ± 0.155 mm, with max. absolute error of 0.843 mm.

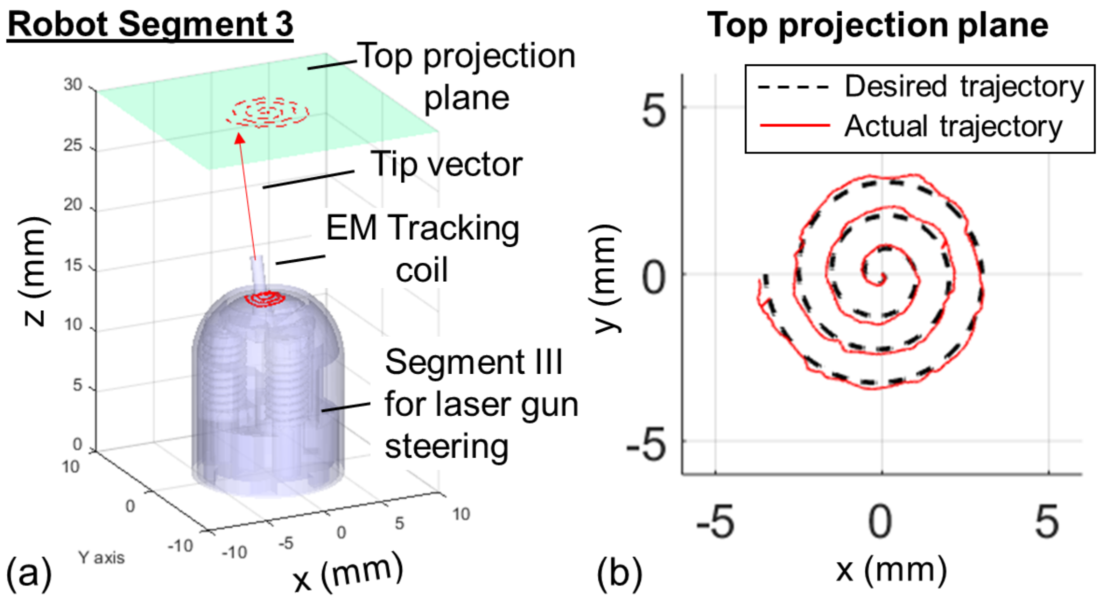

Fig. 7.10 (a) Isometric view of robot segment 3 projecting a spiral trajectory on the plane; **(b)** Plot of desired (black) and actual (red) trajectories on the projection plane.

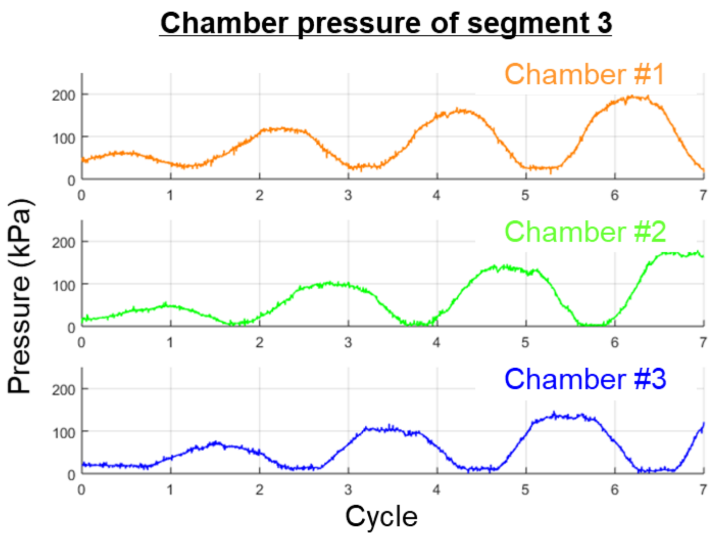

Fig. 7.11 Pressure variation of three actuation chambers through the whole journey of spiral path following.

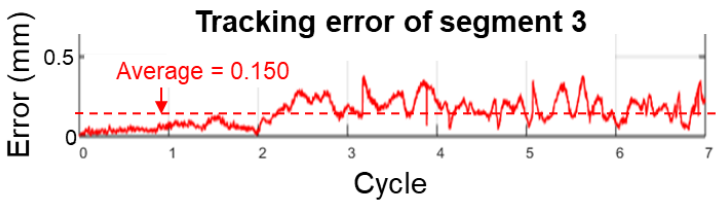

Fig. 7.12 Path following errors calculated in the projection plane. The accuracy is 0.150 ± 0.084 mm, with max. absolute error of 0.375 mm.

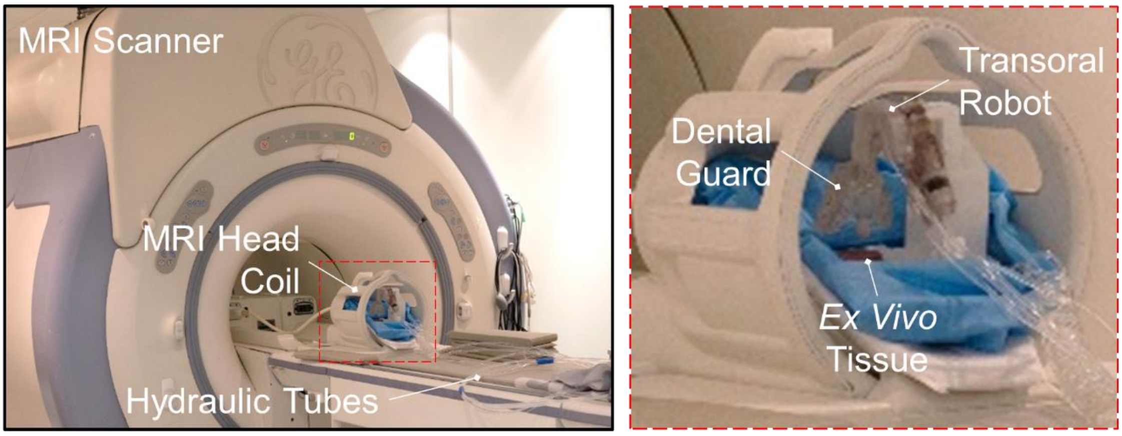

Fig. 7.13 System setup in a 1.5T MRI scanner (SIGNA™ HDxt, GE Healthcare). Transoral robot operated inside an MRI head coil for MRI-based tissue ablation test.

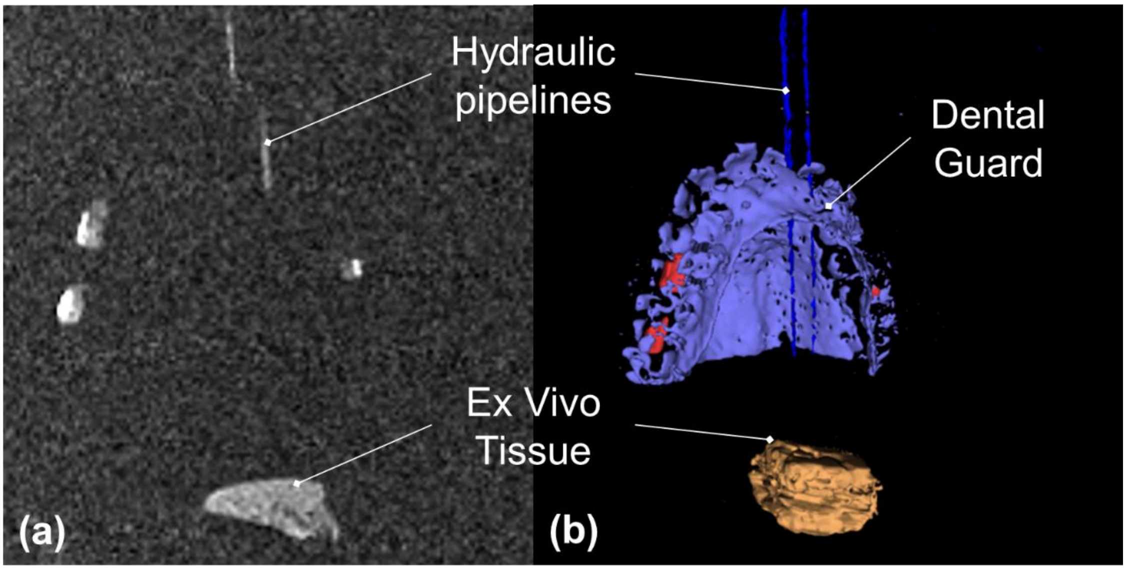

Fig. 7.14 **(a)** MR image of robot and target tissue under the imaging sequence, flip angle = 10°. This scanning was performed pre-operatively for target lesion localization and robot planning. Target tissue, water lines, supporting material of the dental guard can be all visualized under this scanning sequence. **(b)** 3D MRI reconstruction showing the delicate robot structures.

7.4.2 MRI-based Validation

Fig. 7.13 shows the experimental setup of MRI-based validation. The navigation was conducted under the MR environment. It simulated the surgical scenario with the robot anchored to the dental guard and the whole setup placed inside an imaging head coil. To reveal the surgical target in MR images, an *ex vivo* tongue tissue was placed at the distance of about 20 mm away from the laser collimator for ablation (**Fig. 7.14**). A tube was channelled through the other entrance of the dental guard for suction. 3D GRE sequence with flip angel of 10° was first performed to assess the initial location of target tissue and robot. Besides the target tissue, delicate structures of the robot including water lines and supporting materials of the dental guard could be also visualized in this sequence.

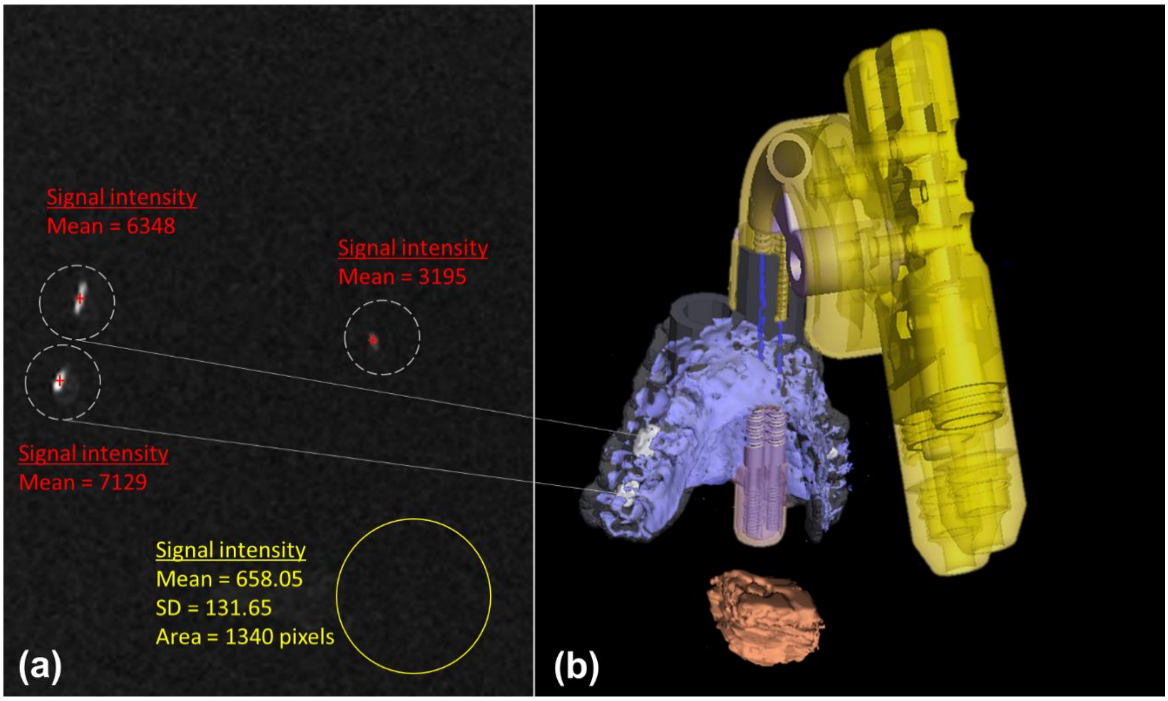

Fig. 7.15 **(a)** MR image under the tracking sequence, flip angle = 2°. Three tiny bright spots indicate the 3D locations of tracking coils. Compared to the images obtained under the imaging sequence, the signal of tissue/water is weakened while the coil signal is being amplified in the tracking sequence. **(b)** 3D robot model augmented in image space based upon the *active* MR tracking feedback.

Three MRI-based *wireless* markers were embedded in the dental guard to provide active 3D tracking. 3D GRE imaging with lower flip angle of 2° was used to clearer visualize and localize the marker locations. The background signals can be minimized by the dedicated excitation sequence with lower flip angle. This can be also observed by the comparison between two MR images in **Fig. 7.14a** and **Fig. 7.15a**. **Fig. 7.15** shows the resultant MR image with three tiny bright spot indicating the *wireless* markers. The signal intensities of the tracked markers are 3195, 6348 and 7129, in contrast to the background signal at a 1340-pixel circular area with an average intensity of 658. A circular pattern was selected for target lesion trajectory. Thirty-cycle ablation was carried out in total and the ablation time was ten minutes. To monitor the ablation progress, MR imaging was performed to update the physiological changes of target lesion, as shown in **Fig. 7.16**. A smooth circular slot can be observed in the images. Dexterity and precision of the presented robotic manipulation has been demonstrated.

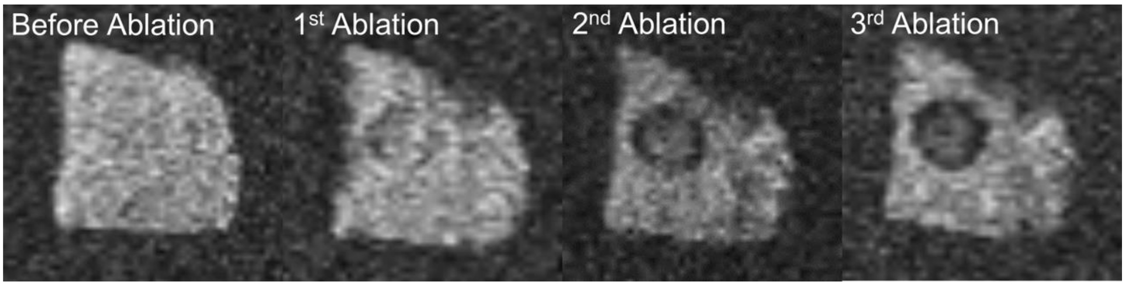

Fig. 7.16 MR images of the target lesion showing the ablation progress. The robot ran ten ablation cycles and stopped for one imaging update. Thirty ablation cycles were performed. Total ablation time was 10 min. A smooth, homogeneous, and circular trace could be readily identified.

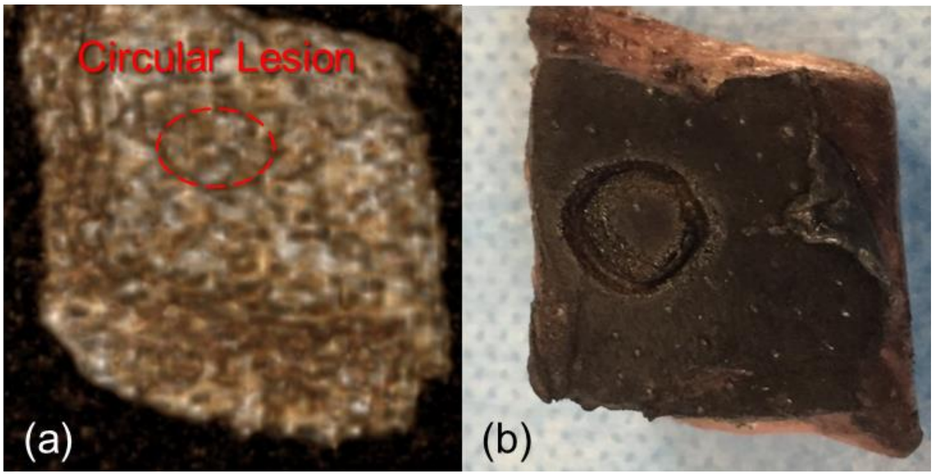

Fig. 7.17 Post-mortem evaluation. **(a)** 3D MRI reconstruction, showing the circular ablation trace. **(b)** *Ex vivo* tissue photo with the circular lesion.

Table 7.2 Scan Parameters for MRI-based Ablation and MRI Compatibility Test

	Pre-op Planning	**Intra-op Tracking**	**SNR test**	**SNR test**
FOV (mm)	100×100	100×100	100×100	100×100
Matrix	256×256	256×256	256×256	256×256
Scanning Sequence	3D GRE	3D GRE	T1-GRE	T2-FSE
TR (ms)	6.1	6.2	100.0	2000.0
TE (ms)	2.4	2.4	5.4	88.6
Flip angle (°)	10	2	1	90

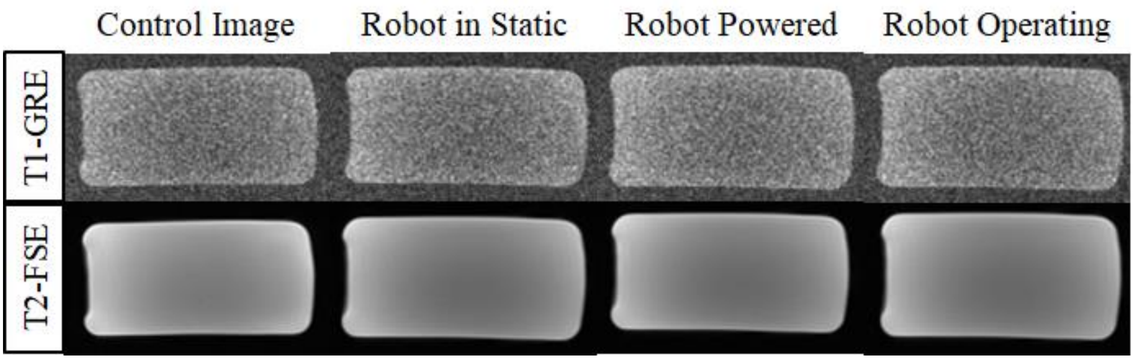

Fig. 7.18 MR images of four different robot operating conditions, scanned by two sequences: T1W- GRE and T2W- FSE.

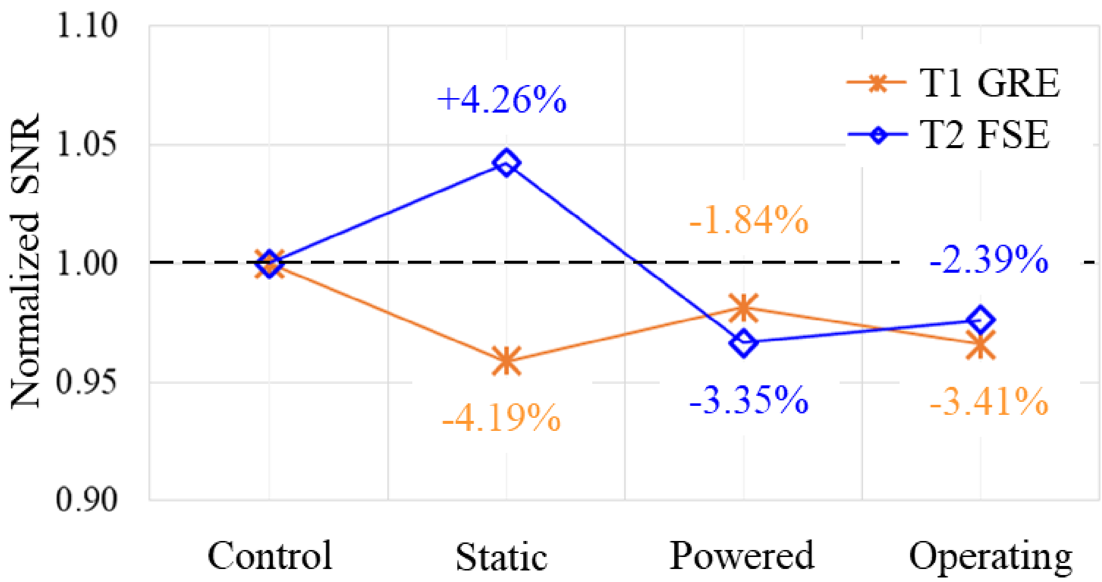

Fig. 7.19 Results of MRI compatibility test. Max. SNR loss reached 4.19% in T1-weighted FSE scanning. This may due to the existence of aluminium coupler of the laser collimator.

7.4.3 MRI-compatibility Evaluation

As the guidelines of NEMA instructed, MRI compatibility test has been conducted and the SNR reduction of resultant MR images were evaluated. The test was performed in the same 1.5T MRI scanner as in the MRI-based validation test at a room temperature, about 20°C. An SNR bottle phantom was placed right beside the robot at the scanner isocenter. Two scanning sequences were employed: T1-weighted GRE and T2-weighted FSE sequence (**Table 7.2**). For each scanning sequence, images were acquired under four different conditions, which were: **1)** control image –

robot not introduced into the MRI scanner; **2)** robot in static – all the power was off; **3)** robot powered **-** hydraulic and electric power was on, but robot remained still; **4)** robot operating – robot in full motion. **Fig. 7.17** shows the corresponding MR images. Image artifact is negligible with the presence of robot motion. SNR reduction is within 5% in all robot operating conditions, **Fig. 18**. This result exceeds the ones of neurosurgical robot and catheter robot as introduced in previous chapters, which excluded additional instruments during the testing, e.g. implant electrodes and catheter. Possible reason of this relatively-large SNR reduction may be the aluminum coupler between the laser fiber and collimator. This can be improved by the proper selection of totally MR safe laser collimator and any other supplementary tools.

7.5 Discussion and Conclusions

In this chapter, a soft continuum robotic manipulator is presented for the transoral laser microsurgery. The continuum robot can be divided into three segments regarding the functionalities. Segment 1 is a continuum structure for advancement, which can passively adapt to the curvature of patient natural orifice. Six water tubes and one laser fiber are channelled through. Segment 2 and 3 are designed for actively steering. They feature with the hybrid structure design, comprising of both soft actuation chambers and rigid spring enclosure for reinforcement. Segment 2 has longer chambers for coarse angular bending, max. ±60°. While segment 3 fully covered by a rigid housing is designed for fine tuning of the bending angle within the confined operating space. Sufficient accuracy, 0.266±0.155 mm, has been demonstrated in a series of spiral-trajectory-following tests controlled by a learning-based algorithm. Low-error (<0.5 mm), high-frequency (>30 Hz) positional tracking using miniaturized RF-semi-active coils, along with intra-op MRI guidance, has been incorporated for an MRI-based laser ablation task. The steady, smooth and consistent motion control of this long, thin and flexible continuum robot has been validated. MRI compatibility test has also been performed to validate the minimal imaging interference during robot operation.

There are two crucial goals of oncological management for HNCs: to achieve loco-regional and distant tumor control; and to preserve breathing, vocal and swallowing functions. The achievements in this chapter might represent an important step toward several ultimate clinical goals: **i)** preserving best the anatomical and functional integrity with enhanced accuracy of tumor resection margins. The expected accuracy (±1mm) will be accomplished by monitoring laser beam projection and its ablation progress using instantly-updated MR images and MR-tracked instruments; **ii)** decreasing the risks of damages to the critical neurovascular and muscular structures; **iii)** avoiding the complications of instruments docking through the intraoral cavity using conventional retractors; **iv)** saving the operation time from the post-resection margin evaluations, such as frozen section analysis. The procedural time would be reduced from approximately 120 to 60 minutes. The aforementioned outcomes would give rise to a new standard treatment of early-stage carcinoma, alternative to the conventional radiotherapy and current surgical modalities that inevitably associate with damage to muscles, bones, nerves and salivary glands with the resultant morbidity of dysphagia, dysphonia, worse quality of life and poor self-esteem from the injury.

Chapter 8
Conclusions and Future Work

8.1 Achievement of this Thesis

IN this thesis, several major challenges related to the MRI-guided robot-assisted surgery have been investigated, involving the high-performance MR safe actuation development, compact and dexterous robotic manipulator design, and the lab/MRI-based experimental validation based on the relevant clinical requirements. It is anticipated that the introduction of MRI-guided robotics will significantly enable future advances of image-guided surgery. The material presented in this thesis constitutes improved MR-based surgical manipulation, allowing enhanced efficiency and accuracy for complex procedures. Technically, a number of novel designs have been proposed and the contribution of the thesis can be summarised by the five objectives as follows:

The original technical contribution of this thesis includes:

- *Customizable pneumatic stepper motor:* a novel air stepper motor has been design, which comprises of only seven components and can be directly fabricated by 3D printing process. The cost is low, such that the motor can be disposable eliminating the needs for complicated sterilization. A small-size and self-lockable pneumatic motor designed to operate inside the limited space of MRI scanner. It can be incorporated with the robotic systems for applications demanding on high stall torque/steady positioning. Easy customization of the motor with regards to its dynamic performance. Mapping between design parameters and dynamic performance has been established. It is believed that a family of motors can be easily generated and cover a wide range of application scenarios. Experimental validation on motor performance and MRI compatibility has demonstrated its potential to be adopted in MRI-guided robotic interventions. A unique feature is, compared to the existing pneumatic motors, the torque output at a certain pressure supply level does not compromise with the increasing speed.

- *High-fidelity integrated hydraulic actuation:* low-friction hydraulic transmissions have been developed, allowing high-fidelity quick-response master-slave manipulation over a long (10 m) distance. The integration methods can be customized for different robot DoFs. Novel three-cylinder designs can provide smooth bidirectional rotation with unlimited range. Both position and torque controls can be further applied on it. Dynamics model for design optimization. Experimental validation of transmission force, hysteresis, dynamic response is performed to ensure dexterous robotic manipulation.

- *Robotic catheterization system for intra-cardiac EP ablation:* a high-performance robotic platform, integrated with MR safe actuation unit and MR-based *wireless* tracking, is capable of operating under the real-time MRI guidance and dexterously manipulating the long, thin, flexible EP catheter. A human-machine interface has been developed to provide the operator with steady and accurate tele-manipulation of the catheter, which is localized with respect to the registered EP roadmap. Multiple simulated clinical tasks have also been carried out to demonstrate the robot performances.

- *Bilateral robotic manipulator for stereotactic neurosurgery:* A light-weight (145.4 g) and compact (110.6×206.8×33.2 mm^3) robot designed to operate within the confined workspace of an MR imaging head coil. It is also actuated by a set of high-performance hydraulic transmissions which are MR safe/induce minimal imaging artifacts. MRI-guided navigation incorporated with *wireless* MR-based tracking coil units, can offer real-time positional feedback directly in MR image coordinates. This avoids any process of offline registration between coordinates of the tracking and imaging space. This is the *first* intra-op MRI-guided robot capable of performing *bilateral* neuro-stereotaxy based on a single anchorage on the patient skull. Navigation for both bilateral targets can be performed independently and simultaneously.

- *Soft transoral robot for tumor laser dissection:* this is the *first* MR safe *soft* robotic manipulator for transoral tumor dissection. Its compliance and compact design ensure the safe interaction with patient anatomy and *flexibly* access to the deep ONP lesions. Novel hybrid actuation has been designed, which features with three soft actuation chambers reinforced by springs. It is capable to provide accurate and repeatable manipulation. Covered by a rigid housing, such actuator can still steer the laser collimator at ±30°. This feature indicates its dexterity for lesion targeting within the constrained operating space, i.e. ONP cavities. The fabrication is easy and can be accomplished by directly 3D printing using digital materials. It is low-cost and can be disposable for the ease of medical sterilization. MRI-guided laser ablation on *ex vivo* tissue has been performed. This navigation test is incorporated with wireless MR trackers to provide direct positional data in imaging coordinates. Ablation progress is monitored by intra-op MR imaging. A smooth, homogeneous, circular trace can be readily identified under the MRI, which has demonstrated the presented soft robotic manipulator capable to perform accurate controllable tissue ablation/cutting.

8.2 Future Directions

Despite of the benefits of the work presented in this thesis, there are still several areas that deserve further improvement. In **Chapter 3** and **Chapter 4**, the work on MR safe fluidic actuation represents a fundamental component of the proposed MRI-guided robotic systems in the following chapters. Rolling-diaphragm-sealed hydraulic transmission can be expected to be incorporated in many other MRI-based applications, such as prostate interventions and breast biopsy. To strengthen its application flexibility and feasibility, design parameters can be standardized and multiple motor models can be generated to cover a spectrum of dynamic scenarios. Further enhancement on the motor performance will be also meaningful. This will involve tailor-made rolling diaphragm design to minimize the motor dimension; high-stiffness structural component selection/fabrication to enhance the transmission stiffness and reduce backlash; high-performance transmission media exploration, e.g. oil; hydraulic circuit optimization to smooth the robot setup procedure; positional/torque sensor incorporation to conduct close-loop control. More tests will be carried out to validate these improvements, such as durability test and safety tests as required by FDA. Three robotic systems are introduced in **Chapter 5-7**. One of them, neurosurgical robot, has started cadaveric trials. More trials would be necessary to validate its clinical benefits before it enters the next stage, namely animal trial and human trial. It demands on the seamless collaboration with clinical partners and requires a long-term follow-up to finally determine the surgical outcomes. Another challenge would be accessible facilities for such research purpose, e.g. an intra-op MRI. The other two robots, catheter robot and transoral robot, are currently at the lab-based stage. Tests on static phantom/*ex vivo* tissue may indicate the sufficient functionalities/accuracy to target the prescribed lesion. But for *in vivo* tissue, several concerns should be addressed, such as dynamic anatomical environment, patient movement and tissue inhomogeneity. Dynamic phantom test and cadaveric trial could be an intermediate step toward the animal/human trials. At the meantime, a thorough surgical paradigm design is imperative to integrate the robotic systems with clinical procedures. Since the advancements in surgical robotics usually come with the development/modification of conventional workflow. In sum, the hardware platform of these three robots has set a solid foundation to incorporate with more navigation techniques. Imaging and navigation would be another research opportunities in MRI-guided surgical robotics. Advance imaging sequences for real-time MRI navigation are crucial parts to close the image guidance and feedback control loop. Image processing and computer vision may play an important role for the future development.

References

[1] J. H. Kaouk, R. K. Goel, G. P. Haber, S. Crouzet, and R. J. Stein, "Robotic single-port transumbilical surgery in humans: initial report," *BJU international,* vol. 103, pp. 366-369, 2009.

[2] D. P. Devito, L. Kaplan, R. Dietl, M. Pfeiffer, D. Horne, B. Silberstein*, et al.*, "Clinical acceptance and accuracy assessment of spinal implants guided with SpineAssist surgical robot: retrospective study," *Spine,* vol. 35, pp. 2109-2115, 2010.

[3] G. A. Antoniou, C. V. Riga, E. K. Mayer, N. J. Cheshire, and C. D. Bicknell, "Clinical applications of robotic technology in vascular and endovascular surgery," *Journal of vascular surgery,* vol. 53, pp. 493-499, 2011.

[4] A. Mert, L. S. Gan, E. Knosp, G. R. Sutherland, and S. Wolfsberger, "Advanced cranial navigation," *Neurosurgery,* vol. 72, pp. A43-A53, 2013.

[5] T. Kahn and H. Busse, *Interventional magnetic resonance imaging*: Springer, 2012.

[6] S.-E. Song, N. B. Cho, G. Fischer, N. Hata, C. Tempany, G. Fichtinger*, et al.*, "Development of a pneumatic robot for MRI-guided transperineal prostate biopsy and brachytherapy: New approaches," in *IEEE International Conference on Robotics and Automation 2010* 2010, pp. 2580-2585.

[7] G. Rahmathulla, P. F. Recinos, K. Kamian, A. M. Mohammadi, M. S. Ahluwalia, and G. H. Barnett, "MRI-guided laser interstitial thermal therapy in neuro-oncology: a review of its current clinical applications," *Oncology,* vol. 87, pp. 67-82, 2014.

[8] M. J. LaRiviere and R. E. Gross, "Stereotactic Laser Ablation for Medically Intractable Epilepsy: The Next Generation of Minimally Invasive Epilepsy Surgery," *Frontiers in surgery,* vol. 3, 2016.

[9] J. Fritz, C. Thomas, S. Clasen, C. D. Claussen, J. S. Lewin, and P. L. Pereira, "Freehand real-time MRI-guided lumbar spinal injection procedures at 1.5 T: feasibility, accuracy, and safety," *American Journal of Roentgenology,* vol. 192, pp. W161-W167, 2009.

[10] M. Kinoshita, N. McDannold, F. A. Jolesz, and K. Hynynen, "Targeted delivery of antibodies through the blood–brain barrier by MRI-guided focused ultrasound," *Biochemical and biophysical research communications,* vol. 340, pp. 1085-1090, 2006.

[11] A. Tzifa, G. A. Krombach, N. Krämer, S. Krüger, A. Schütte, M. von Walter*, et al.*, "Magnetic Resonance–Guided Cardiac Interventions Using Magnetic Resonance–Compatible Devices," *Circulation: Cardiovascular Interventions,* vol. 3, pp. 585-592, 2010.

[12] Y. Feng, Z. Guo, Z. Dong, X.-Y. Zhou, K.-W. Kwok, S. Ernst*, et al.*, "An efficient cardiac mapping strategy for radiofrequency catheter ablation with active learning," *International Journal of Computer Assisted Radiology and Surgery,* pp. 1-9, 2017.

[13] R. Blanco Sequeiros, R. Ojala, J. Kariniemi, J. Perälä, J. Niinimäki, H. Reinikainen*, et al.*, "MR-guided interventional procedures: a review," *Acta Radiologica,* vol. 46, pp. 576-586, 2005.

[14] K. Masamune, E. Kobayashi, Y. Masutani, M. Suzuki, T. Dohi, H. Iseki*, et al.*, "Development of an MRI-compatible needle insertion manipulator for stereotactic neurosurgery," *Journal of Image Guided Surgery,* vol. 1, pp. 242-248, 1995.

[15] K. M. Pondman, J. J. Fütterer, B. ten Haken, L. J. S. Kool, J. A. Witjes, T. Hambrock*, et al.*, "MR-guided biopsy of the prostate: an overview of techniques and a systematic review," *European urology,* vol. 54, pp. 517-527, 2008.

[16] A. N. Sridhar, A. Hughes-Hallett, E. K. Mayer, P. J. Pratt, P. J. Edwards, G.-Z. Yang*, et al.*, "Image-guided robotic interventions for prostate cancer," *Nature reviews Urology,* vol. 10, pp. 452-462, 2013.

[17] D. B. Comber, E. B. Pitt, H. B. Gilbert, M. W. Powelson, E. Matijevich, J. S. Neimat*, et al.*, "Optimization of curvilinear needle trajectories for transforamenal hippocampotomy," *Operative Neurosurgery,* vol. 13, pp. 15-22, 2016.

[18] M. Uecker, S. Zhang, D. Voit, A. Karaus, K. D. Merboldt, and J. Frahm, "Real-time MRI at a resolution of 20 ms," *NMR in Biomedicine,* vol. 23, pp. 986-994, 2010.

[19] H. E. Cline, J. Schenek, K. Hynynen, and R. D. Watkins, "MR-guided focused ultrasound surgery," *Journal of computer assisted tomography,* vol. 16, pp. 956-956, 1992.

[20] W. F. Block and B. P. Grabow, "Pulse sequences for interventional MRI," in *Interventional Magnetic Resonance Imaging*, ed: Springer, 2012, pp. 17-34.

[21] A. E. Campbell-Washburn, M. A. Tavallaei, M. Pop, E. K. Grant, H. Chubb, K. Rhode*, et al.*, "Real-time MRI guidance of cardiac interventions," *Journal of Magnetic Resonance Imaging,* vol. 46, pp. 935-950, 2017.

[22] K.-J. F. Jansson, B. Håkansson, S. Reinfeldt, C. Rigato, and M. Eeg-Olofsson, "Magnetic resonance imaging investigation of the bone conduction implant–a pilot study at 1.5 Tesla," *Medical Devices (Auckland, NZ),* vol. 8, p. 413, 2015.

[23] P.-M. L. Robitaille, R. Warner, J. Jagadeesh, A. M. Abduljalil, A. Kangarlu, R. E. Burgess*, et al.*, "Design and assembly of an 8 tesla whole-body MR scanner," *Journal of computer assisted tomography,* vol. 23, pp. 808-820, 1999.

[24] E. Stikova, "Magnetic resonance imaging safety: principles and guidelines," *Contributions of Macedonian Academy of Sciences & Arts,* vol. 33, 2012.

[25] R. Galloway and R. J. Maciunas, "Stereotactic neurosurgery," *Critical reviews in biomedical engineering,* vol. 18, pp. 181-205, 1989.

[26] K. L. Holloway, S. E. Gaede, P. A. Starr, J. M. Rosenow, V. Ramakrishnan, and J. M. Henderson, "Frameless stereotaxy using bone fiducial markers for deep brain stimulation," *Journal of neurosurgery,* vol. 103, pp. 404-413, 2005.

[27] J. M. Henderson, "Frameless localization for functional neurosurgical procedures: a preliminary accuracy study," *Stereotactic and functional neurosurgery,* vol. 82, pp. 135-141, 2004.

[28] R. J. Maciunas, J. M. Fitzpatrick, R. Galloway, and G. S. Allen, "Beyond stereotaxy: extreme levels of application accuracy are provided by implantable fiducial markers for interactive image-guided neurosurgery," *Interactive image-guided neurosurgery,* pp. 259-270, 1993.

[29] R. J. Maciunas, R. L. Galloway Jr, and J. W. Latimer, "The application accuracy of stereotactic frames," *Neurosurgery,* vol. 35, pp. 682-695, 1994.

[30] R. Dammers, I. Haitsma, J. Schouten, J. Kros, C. Avezaat, and A. Vincent, "Safety and efficacy of frameless and frame-based intracranial biopsy techniques," *Acta neurochirurgica,* vol. 150, pp. 23-29, 2008.

[31] N. Dorward, T. Paleologos, O. Alberti, and D. Thomas, "The advantages of frameless stereotactic biopsy over frame-based biopsy," *British journal of neurosurgery,* vol. 16, pp. 110-118, 2002.

[32] D. L. Lunsford, R. Parrish, and L. Albright, "Intraoperative imaging with a therapeutic computed tomographic scanner," *Neurosurgery,* vol. 15, pp. 559-561, 1984.

[33] P. M. Black, T. Moriarty, E. Alexander III, P. Stieg, E. J. Woodard, P. L. Gleason*, et al.*, "Development and implementation of intraoperative magnetic resonance imaging and its neurosurgical applications," *Neurosurgery,* vol. 41, pp. 831-845, 1997.

[34] M. Hadani, R. Spiegelman, Z. Feldman, H. Berkenstadt, and Z. Ram, "Novel, compact, intraoperative magnetic resonance imaging-guided system for conventional neurosurgical operating rooms," *Neurosurgery,* vol. 48, pp. 799-809, 2001.

[35] T. Foltynie, L. Zrinzo, I. Martinez-Torres, E. Tripoliti, E. Petersen, E. Holl*, et al.*, "MRI-guided STN DBS in Parkinson's disease without microelectrode recording: efficacy and safety," *Journal of Neurology, Neurosurgery & Psychiatry,* vol. 82, pp. 358-363, 2011.

[36] D. G. Southwell, J. A. Narvid, A. J. Martin, S. E. Qasim, P. A. Starr, and P. S. Larson, "Comparison of Deep Brain Stimulation Lead Targeting Accuracy and Procedure Duration between 1.5-and 3-Tesla Interventional Magnetic Resonance Imaging Systems: An Initial 12-Month Experience," *Stereotactic and functional neurosurgery,* vol. 94, pp. 102-107, 2016.

[37] S. Chabardes, S. Isnard, A. Castrioto, M. Oddoux, V. Fraix, L. Carlucci*, et al.*, "Surgical implantation of STN-DBS leads using intraoperative MRI guidance: technique, accuracy, and clinical benefit at 1-year follow-up," *Acta neurochirurgica,* vol. 157, pp. 729-737, 2015.

[38] R. Clarke, "THE STRUCTURE AND FUNCTIONS OF THE CEREBELLUM EXAMINED BY A NEW METHOD. By SIR VICTOR HORSLEY, FRS, FRCS, AND," *Brain: A Journal of Neurology,* p. 45, 1908.

[39] E. A. Spiegel, H. T. Wycis, M. Marks, and A. Lee, "Stereotaxic apparatus for operations on the human brain," *Science,* vol. 106, pp. 349-350, 1947.

[40] Y. S. Kwoh, J. Hou, E. A. Jonckheere, and S. Hayati, "A robot with improved absolute positioning

accuracy for CT guided stereotactic brain surgery," *IEEE Transactions on Biomedical Engineering,* vol. 35, pp. 153-160, 1988.

[41] S. P. DiMaio, N. Archip, N. Hata, I. Talos, S. K. Warfield, A. Majumdar*, et al.*, "Image-guided neurosurgery at Brigham and Women's Hospital," *IEEE Engineering in Medicine and Biology Magazine,* vol. 25, pp. 67-73, 2006.

[42] P. Larson, P. A. Starr, J. L. Ostrem, N. Galifianakis, M. S. L. Palenzuela, and A. Martin, "203 Application Accuracy of a Second Generation Interventional MRI Stereotactic Platform: Initial Experience in 101 DBS Electrode Implantations," *Neurosurgery,* vol. 60, p. 187, 2013.

[43] C. Sidiropoulos, R. Rammo, B. Merker, A. Mahajan, P. LeWitt, P. Kaminski*, et al.*, "Intraoperative MRI for deep brain stimulation lead placement in Parkinson's disease: 1 year motor and neuropsychological outcomes," *Journal of neurology,* vol. 263, pp. 1226-1231, 2016.

[44] D. L. Drane, D. W. Loring, N. L. Voets, M. Price, J. G. Ojemann, J. T. Willie*, et al.*, "Better object recognition and naming outcome with MRI‐guided stereotactic laser amygdalohippocampotomy for temporal lobe epilepsy," *Epilepsia,* vol. 56, pp. 101-113, 2015.

[45] P. Chittiboina, J. D. Heiss, and R. R. Lonser, "Accuracy of direct magnetic resonance imaging-guided placement of drug infusion cannulae," *Journal of neurosurgery,* vol. 122, pp. 1173-1179, 2015.

[46] K. Chinzei, N. Hata, F. A. Jolesz, and R. Kikinis, "MR compatible surgical assist robot: System integration and preliminary feasibility study," in *MICCAI*, 2000, pp. 921-933.

[47] J. W. Motkoski and G. R. Sutherland, "Why Robots Entered Neurosurgery," *Experimental Neurosurgery in Animal Models,* pp. 85-105, 2016.

[48] A. J. Golby, *Image-Guided Neurosurgery*: Elsevier Science, 2015.

[49] K. Masamune, E. Kobayashi, Y. Masutani, M. Suzuki, T. Dohi, H. Iseki*, et al.*, "Development of an MRI-compatible needle insertion manipulator for stereotactic neurosurgery," *Computer Aided Surgery,* vol. 1, pp. 242-248, 1995.

[50] K. Chinzei and K. Miller, "Towards MRI guided surgical manipulator," *Medical science monitor,* vol. 7, pp. 153-163, 2001.

[51] J. S. Lewin, A. Metzger, and W. R. Selman, "Intraoperative magnetic resonance image guidance in neurosurgery," *Journal of Magnetic Resonance Imaging,* vol. 12, pp. 512-524, 2000.

[52] G. R. Sutherland, Y. Maddahi, L. S. Gan, S. Lama, and K. Zareinia, "Robotics in the neurosurgical treatment of glioma," *Surgical neurology international,* vol. 6, p. S1, 2015.

[53] G. R. Sutherland, P. B. McBeth, and D. F. Louw, "NeuroArm: an MR compatible robot for microsurgery," in *International congress series*, 2003, pp. 504-508.

[54] C. Faria, W. Erlhagen, M. Rito, E. De Momi, G. Ferrigno, and E. Bicho, "Review of robotic technology for stereotactic neurosurgery," *Biomedical Engineering, IEEE Reviews in,* vol. 8, pp. 125-137, 2015.

[55] A. H. Hawasli, W. Z. Ray, R. K. Murphy, R. G. Dacey Jr, and E. C. Leuthardt, "Magnetic resonance imaging-guided focused laser interstitial thermal therapy for subinsular metastatic adenocarcinoma: technical case report," *Operative Neurosurgery,* vol. 70, pp. onsE332-onsE338, 2011.

[56] A. M. Mohammadi, A. H. Hawasli, A. Rodriguez, J. L. Schroeder, A. W. Laxton, P. Elson*, et al.*, "The role of laser interstitial thermal therapy in enhancing progression-free survival of difficult-to-access high-grade gliomas: a multicenter study," *Cancer medicine,* vol. 3, pp. 971-979, 2014.

[57] M. Ho, Y. Kim, S. S. Cheng, R. Gullapalli, and J. P. Desai, "Design, development, and evaluation of an MRI-guided SMA spring-actuated neurosurgical robot," *The International journal of robotics research,* vol. 34, pp. 1147-1163, 2015.

[58] Y. Kim, S. S. Cheng, M. Diakite, R. P. Gullapalli, J. M. Simard, and J. P. Desai, "Toward the Development of a Flexible Mesoscale MRI-Compatible Neurosurgical Continuum Robot," *IEEE Transactions on Robotics,* 2017.

[59] S. S. Cheng, Y. Kim, and J. P. Desai, "New Actuation Mechanism for Actively Cooled SMA Springs in a Neurosurgical Robot," *IEEE Transactions on Robotics,* 2017.

[60] G. Li, H. Su, G. Cole, W. Shang, K. Harrington, A. Camilo*, et al.*, "Robotic System for MRI-Guided Stereotactic Neurosurgery," *Biomedical Engineering, IEEE Transactions on,* vol. 62, pp. 1077-1088, 2015.

[61] C. J. Nycz, R. Gondokaryono, P. Carvalho, N. Patel, M. Wartenberg, J. G. Pilitsis*, et al.*, "Mechanical Validation of an MRI Compatible Stereotactic Neurosurgery Robot in Preparation for Pre-Clinical Trials," presented at the IEEE/RSJ International Conference on Intelligent Robots and Systems (IROS), 2017.

[62] G. R. Sutherland, P. B. McBeth, and D. F. Louw, "NeuroArm: an MR compatible robot for microsurgery," *International Congress Series,* vol. 1256, pp. 504-508, 2003.

[63] D. F. Louw, T. Fielding, P. B. McBeth, D. Gregoris, P. Newhook, G. R. Sutherland*, et al.*, "Surgical robotics: A review and neurosurgical prototype development," *Neurosurgery,* vol. 54, pp. 525-537, 2004.

[64] S. Manjila, K. E. Knudson, C. Johnson Jr, and A. E. Sloan, "Monteris AXiiiS stereotactic miniframe for intracranial biopsy: precision, feasibility, and ease of use," *Operative Neurosurgery,* vol. 12, pp. 119-127, 2016.

[65] D. B. Comber, J. E. Slightam, V. R. Gervasi, J. S. Neimat, and E. J. Barth, "Design, additive manufacture, and control of a pneumatic mr-compatible needle driver," *IEEE Transactions on Robotics,* vol. 32, pp. 138-149, 2016.

[66] Y. Koseki, R. Kikinis, F. A. Jolesz, and K. Chinzei, "Precise evaluation of positioning repeatability of MR-compatible manipulator inside MRI," in *International Conference on Medical Image Computing and Computer-Assisted Intervention*, 2004, pp. 192-199.

[67] Z. Guo, Z. Dong, K.-H. Lee, C. L. Cheung, H. C. Fu, J. D.-L. Ho, *et al.*, "Compact Design of a Hydraulic Driving Robot for Intra-operative MRI-guided Bilateral Stereotactic Neurosurgery," *IEEE Robotics and Automation Letters,* 2018.

[68] C. Jun, S. Lim, J.-P. Wolinsky, T. Garzon-Muvdi, D. Petrisor, K. Cleary, *et al.*, "MR Safe Robot Assisted Needle Access of the Brain: Preclinical Study," *Journal of Medical Robotics Research,* vol. 3, p. 1850003, 2018.

[69] N. Miyata, E. Kobayashi, D. Kim, K. Masamune, I. Sakuma, N. Yahagi, *et al.*, "Micro-grasping forceps manipulator for MR-guided neurosurgery," *Medical Image Computing and Computer-Assisted Intervention—MICCAI 2002,* pp. 107-113, 2002.

[70] Y. Koseki, T. Washio, K. Chinzei, and H. Iseki, "Endoscope manipulator for trans-nasal neurosurgery, optimized for and compatible to vertical field open MRI," *Medical Image Computing and Computer-Assisted Intervention—MICCAI 2002,* pp. 114-121, 2002.

[71] C. Raoufi, A. A. Goldenberg, and W. Kucharczyk, "Design and control of a novel hydraulically/pneumatically actuated robotic system for MRI-guided neurosurgery," *Journal of Biomedical Science and Engineering,* vol. 1, p. 68, 2008.

[72] Z. Hong, C. Yun, L. Zhao, and Y. Wang, "Design and optimization analysis of open-MRI compatibile robot for neurosurgery," presented at the 2nd International Conference on Bioinformatics and Biomedical Engineering, iCBBE, 2008.

[73] T. Reichlin, S. Knecht, C. Lane, M. Kuhne, E. Nof, N. Chopra, *et al.*, "Initial impedance decrease as an indicator of good catheter contact: Insights from radiofrequency ablation with force sensing catheters," *Heart Rhythm,* vol. 11, pp. 194-201, Feb 2014.

[74] M. Shurrab, R. Schilling, E. Gang, E. M. Khan, and E. Crystal, "Robotics in invasive cardiac electrophysiology," *Expert Rev Med Devices,* vol. 11, pp. 375-81, Jul 2014.

[75] T. Datino, A. Arenal, M. Pelliza, J. Hernandez-Hernandez, F. Atienza, E. Gonzalez-Torrecilla, *et al.*, "Comparison of the safety and feasibility of arrhythmia ablation using the Amigo Robotic Remote Catheter System versus manual ablation," *Am J Cardiol,* vol. 113, pp. 827-31, Mar 1 2014.

[76] A. Aryana, A. d'Avila, E. K. Heist, T. Mela, J. P. Singh, J. N. Ruskin, *et al.*, "Remote magnetic navigation to guide endocardial and epicardial catheter mapping of scar-related ventricular tachycardia," *Circulation,* vol. 115, pp. 1191-200, Mar 13 2007.

[77] A. C. Lardo, E. R. McVeigh, P. Jumrussirikul, R. D. Berger, H. Calkins, J. Lima, *et al.*, "Visualization and temporal/spatial characterization of cardiac radiofrequency ablation lesions using magnetic resonance imaging," *Circulation,* vol. 102, pp. 698-705, 2000.

[78] E. M. Aliot, W. G. Stevenson, J. M. Almendral-Garrote, F. Bogun, C. H. Calkins, E. Delacretaz, *et al.*, "EHRA/HRS Expert Consensus on Catheter Ablation of Ventricular Arrhythmias: developed in a partnership with the European Heart Rhythm Association (EHRA), a Registered Branch of the European Society of Cardiology (ESC), and the Heart Rhythm Society (HRS); in

collaboration with the American College of Cardiology (ACC) and the American Heart Association (AHA)," *Heart Rhythm,* vol. 6, pp. 886-933, Jun 2009.

[79] S. Nazarian, A. Kolandaivelu, M. M. Zviman, G. R. Meininger, R. Kato, R. C. Susil*, et al.*, "Feasibility of real-time magnetic resonance imaging for catheter guidance in electrophysiology studies," *Circulation,* vol. 118, pp. 223-229, 2008.

[80] E. J. Schmidt, R. P. Mallozzi, A. Thiagalingam, G. Holmvang, A. d'Avila, R. Guhde*, et al.*, "Electroanatomic Mapping and Radiofrequency Ablation of Porcine Left Atria and Atrioventricular Nodes Using Magnetic Resonance Catheter Tracking," *Circulation-Arrhythmia and Electrophysiology,* vol. 2, pp. 695-+, Dec 2009.

[81] D. C. Peters, J. Hsing, K. V. Kissinger, B. Goddu, R. Nezafat, J. E. Taclas*, et al.*, "T2-Weighted Imaging of the Left Atrium Acutely After Pulmonary Vein Isolation Demonstrates Wall Thickening and Edema," *ISMRM Proceedings,* 2009.

[82] J. Ren, K. A. McIsaac, R. V. Patel, and T. M. Peters, "A Potential Field Model Using Generalized Sigmoid Functions," *IEEE Trans on Systems, Man, and Cybernetics, Part B: Cybernetics,* vol. 37, pp. 477-484, 2007.

[83] A. N. Raval, P. V. Karmarkar, M. A. Guttman, C. Ozturk, R. Desilva, R. J. Aviles*, et al.*, "Real-time MRI guided atrial septal puncture and balloon septostomy in swine," *Catheterization and cardiovascular interventions : official journal of the Society for Cardiac Angiography & Interventions,* vol. 67, pp. 637-643, 2006.

[84] S. R. Dukkipati, R. Mallozzi, E. J. Schmidt, G. Holmvang, A. d'Avila, R. Guhde*, et al.*, "Electroanatomic Mapping of the Left Ventricle in a Porcine Model of Chronic Myocardial Infarction With Magnetic Resonance-Based Catheter Tracking," *Circulation,* vol. 118, pp. 853-862, 2008.

[85] R. C. Susil, C. J. Yeung, H. R. Halperin, A. C. Lardo, and E. Atalar, "Multifunctional interventional devices for MRI: a combined electrophysiology/MRI catheter," *Magnetic resonance in medicine : official journal of the Society of Magnetic Resonance in Medicine / Society of Magnetic Resonance in Medicine,* vol. 47, pp. 594-600, 2002.

[86] R. Razavi, D. L. Hill, S. F. Keevil, M. E. Miquel, V. Muthurangu, S. Hegde*, et al.*, "Cardiac catheterisation guided by MRI in children and adults with congenital heart disease," *Lancet,* vol. 362, pp. 1877-1882, 2003.

[87] S. Zuehlsdorff, R. Umathum, S. Volz, P. Hallscheidt, C. Fink, W. Semmler*, et al.*, "MR coil design for simultaneous tip tracking and curvature delineation of a catheter," *Magn Reson Med,* vol. 52, pp. 214-8, Jul 2004.

[88] W. Wang, A. Damato, T. Penzkofer, L. Pan, W. Gilson, R. Seethamraju*, et al.*, "Real-Time Catheter Localization Using An Active MR Tracker for Interstitial Brachytherapy," *Medical Physics,* vol. 41, p. 525, 2014.

[89] Y. Ishihara, R. Nazafat, J. V. Wylie, M. G. Linguraru, M. E. Josephson, R. D. Howe, *et al.*, "MRI Evaluation of RF Ablation Scarring for Atrial Fibrillation Treatment," in *Proceedings of the SPIE*, 2007, p. 65090.

[90] J. Relan, M. Pop, H. Delingette, G. A. Wright, N. Ayache, and M. Sermesant, "Personalization of a Cardiac Electrophysiology Model Using Optical Mapping and MRI for Prediction of Changes With Pacing," *Biomedical Engineering, IEEE Transactions on*, vol. 58, pp. 3339-3349, 2011.

[91] N. Archip, O. Clatz, S. Whalen, D. Kacher, A. Fedorov, A. Kot, *et al.*, "Non-rigid alignment of pre-operative MRI, fMRI, and DT-MRI with intra-operative MRI for enhanced visualization and navigation in image-guided neurosurgery," *Neuroimage*, vol. 35, pp. 609-624, Apr 1 2007.

[92] J. Dong, H. Calkins, S. B. Solomon, S. Lai, D. Dalal, A. C. Lardo, *et al.*, "Integrated electroanatomic mapping with three-dimensional computed tomographic images for real-time guided ablations," *Circulation*, vol. 113, pp. 186-94, Jan 17 2006.

[93] J. U. N. Dong, T. Dickfeld, D. Dalal, A. Cheema, C. R. Vasamreddy, C. A. Henrikson, *et al.*, "Initial Experience in the Use of Integrated Electroanatomic Mapping with Three-Dimensional MR/CT Images to Guide Catheter Ablation of Atrial Fibrillation," *Journal of Cardiovascular Electrophysiology*, vol. 17, pp. 459-466, 2006.

[94] J. Ector, S. De Buck, J. Adams, S. Dymarkowski, J. Bogaert, F. Maes, *et al.*, "Cardiac three-dimensional magnetic resonance imaging and fluoroscopy merging: a new approach for electroanatomic mapping to assist catheter ablation," *Circulation*, vol. 112, pp. 3769-76, Dec 13 2005.

[95] T. A. Mattei, A. H. Rodriguez, D. Sambhara, and E. Mendel, "Current state-of-the-art and future perspectives of robotic technology in neurosurgery," *Neurosurgical review*, vol. 37, pp. 357-366, 2014.

[96] C. Nimsky, O. Ganslandt, P. Hastreiter, and R. Fahlbusch, "Intraoperative compensation for brain shift," *Surgical neurology*, vol. 56, pp. 357-364, 2001.

[97] N. Archip, O. Clatz, S. Whalen, D. Kacher, A. Fedorov, A. Kot, *et al.*, "Non-rigid alignment of pre-operative MRI, fMRI, and DT-MRI with intra-operative MRI for enhanced visualization and navigation in image-guided neurosurgery," *Neuroimage*, vol. 35, pp. 609-624, 2007.

[98] O. Škrinjar, A. Nabavi, and J. Duncan, "Model-driven brain shift compensation," *Medical image analysis*, vol. 6, pp. 361-373, 2002.

[99] J. Hu, X. Jin, J. B. Lee, L. Zhang, V. Chaudhary, M. Guthikonda, *et al.*, "Intraoperative brain shift prediction using a 3D inhomogeneous patient-specific finite element model," *Journal of neurosurgery*, vol. 106, pp. 164-169, 2007.

[100] W. M. Tavares, F. Tustumi, C. da Costa Leite, L. F. Gamarra, E. Amaro Jr, M. J. Teixeira, *et al.*, "An image correction protocol to reduce distortion for 3-T stereotactic MRI," *Neurosurgery*, vol. 74, pp. 121-127, 2014.

[101] L. N. Baldwin, K. Wachowicz, S. D. Thomas, R. Rivest, and B. G. Fallone, "Characterization, prediction, and correction of geometric distortion in 3T MR images," *Medical Physics,* vol. 34, pp. 388-399, 2007.

[102] R. Mallozzi, "Geometric Distortion in MRI," ed: The Phantom Laboratory, Inc, 2015.

[103] A. Walker, G. Liney, P. Metcalfe, and L. Holloway, "MRI distortion: considerations for MRI based radiotherapy treatment planning," *Australasian Physical & Engineering Sciences in Medicine,* vol. 37, pp. 103-113, 2014.

[104] C. Bhushan, J. P. Haldar, S. Choi, A. A. Joshi, D. W. Shattuck, and R. M. Leahy, "Co-registration and distortion correction of diffusion and anatomical images based on inverse contrast normalization," *NeuroImage,* vol. 115, pp. 269-280, 2015.

[105] M. K. Murgasova, G. Lockwood-Estrin, R. G. Nunes, S. Malik, M. Rutherford, D. Rueckert*, et al.*, "Distortion correction in fetal EPI using non-rigid registration with a Laplacian constraint," *IEEE Transactions on Medical Imaging,* 2017.

[106] K.-W. Kwok, G. C. Chow, T. C. Chau, Y. Chen, S. H. Zhang, W. Luk*, et al.*, "FPGA-based acceleration of MRI registration: an enabling technique for improving MRI-guided cardiac therapy," *Journal of Cardiovascular Magnetic Resonance,* vol. 16, p. W11, 2014.

[107] K.-W. Kwok, Y. Chen, T. C. Chau, W. Luk, K. R. Nilsson, E. J. Schmidt*, et al.*, "MRI-based visual and haptic catheter feedback: simulating a novel system's contribution to efficient and safe MRI-guided cardiac electrophysiology procedures," *Journal of Cardiovascular Magnetic Resonance,* vol. 16, p. O50, 2014.

[108] X. Gu, H. Pan, Y. Liang, R. Castillo, D. Yang, D. Choi*, et al.*, "Implementation and evaluation of various demons deformable image registration algorithms on a GPU," *Physics in medicine and biology,* vol. 55, p. 207, 2009.

[109] M. Moche, R. Trampel, T. Kahn, and H. Busse, "Navigation concepts for MR image-guided interventions," *Journal of Magnetic Resonance Imaging,* vol. 27, pp. 276-291, 2008.

[110] G. B. Chavhan, P. S. Babyn, B. Thomas, M. M. Shroff, and E. M. Haacke, "Principles, techniques, and applications of T2-based MR imaging and its special applications," *Radiographics,* vol. 29, pp. 1433-1449, 2009.

[111] R. M. Richardson, A. P. Kells, A. J. Martin, P. S. Larson, P. A. Starr, P. G. Piferi*, et al.*, "Novel platform for MRI-guided convection-enhanced delivery of therapeutics: preclinical validation in nonhuman primate brain," *Stereotactic and functional neurosurgery,* vol. 89, pp. 141-151, 2011.

[112] C. Truwit, A. J. Martin, and W. A. Hall, "MRI guidance of minimally invasive cranial applications," in *Interventional Magnetic Resonance Imaging*, ed: Springer, 2011, pp. 97-112.

[113] S. Weiss, T. Kuehne, F. Brinkert, G. Krombach, M. Katoh, T. Schaeffter*, et al.*, "In vivo safe catheter visualization and slice tracking using an optically detunable resonant marker," *Magnetic resonance in medicine,* vol. 52, pp. 860-868, 2004.

[114] W. Wang, C. L. Dumoulin, A. N. Viswanathan, Z. T. Tse, A. Mehrtash, W. Loew, *et al.*, "Real-time active MR-tracking of metallic stylets in MR-guided radiation therapy," *Magnetic resonance in medicine,* vol. 73, pp. 1803-1811, 2015.

[115] S. Elayaperumal, J. C. Plata, A. B. Holbrook, Y.-L. Park, K. B. Pauly, B. L. Daniel, *et al.*, "Autonomous real-time interventional scan plane control with a 3-D shape-sensing needle," *Medical Imaging, IEEE Transactions on,* vol. 33, pp. 2128-2139, 2014.

[116] S. C. Strother, J. R. Anderson, X.-L. Xu, J.-S. Liow, D. C. Bonar, and D. A. Rottenberg, "Quantitative comparisons of image registration techniques based on high-resolution MRI of the brain," *Journal of computer assisted tomography,* vol. 18, pp. 954-962, 1993.

[117] D. Wang, W. Strugnell, G. Cowin, D. M. Doddrell, and R. Slaughter, "Geometric distortion in clinical MRI systems: Part I: evaluation using a 3D phantom," *Magnetic resonance imaging,* vol. 22, pp. 1211-1221, 2004.

[118] C. Dumoulin, S. Souza, and R. Darrow, "Real-time position monitoring of invasive devices using magnetic resonance," *Magnetic resonance in medicine,* vol. 29, pp. 411-415, 1993.

[119] R. Werner, S. Krueger, A. Winkel, C. Albrecht, T. Schaeffter, M. Heller, *et al.*, "MR-guided breast biopsy using an active marker: A phantom study," *Journal of Magnetic Resonance Imaging,* vol. 24, pp. 235-241, 2006.

[120] H. Zimmermann, S. Müller, B. Gutmann, H. Bardenheuer, A. Melzer, R. Umathum, *et al.*, "Targeted-HASTE imaging with automated device tracking for MR-guided needle interventions in closed-bore MR systems," *Magnetic resonance in medicine,* vol. 56, pp. 481-488, 2006.

[121] G. A. Coutts, D. J. Gilderdale, M. Chui, L. Kasuboski, and N. M. Desouza, "Integrated and interactive position tracking and imaging of interventional tools and internal devices using small fiducial receiver coils," *Magnetic resonance in medicine,* vol. 40, pp. 908-913, 1998.

[122] M. K. Konings, L. W. Bartels, H. F. Smits, and C. J. Bakker, "Heating around intravascular guidewires by resonating RF waves," *Journal of Magnetic Resonance Imaging,* vol. 12, pp. 79-85, 2000.

[123] M. A. Rube, A. B. Holbrook, B. F. Cox, J. G. Houston, and A. Melzer, "Wireless MR tracking of interventional devices using phase-field dithering and projection reconstruction," *Magnetic resonance imaging,* vol. 32, pp. 693-701, 2014.

[124] W. Wang, C. L. Dumoulin, A. N. Viswanathan, Z. T. Tse, A. Mehrtash, W. Loew, *et al.*, "Real-time active MR-tracking of metallic stylets in MR-guided radiation therapy," *Magnetic Resonance in Medicine,* vol. 73, pp. 1803-1811, 2015.

[125] A. Krieger, S.-E. Song, N. B. Cho, I. I. Iordachita, P. Guion, G. Fichtinger, *et al.*, "Development and evaluation of an actuated MRI-compatible robotic system for MRI-guided prostate intervention," *Mechatronics, IEEE/ASME Transactions on,* vol. 18, pp. 273-284, 2013.

[126] K. El Bannan, B. A. Chronik, and S. P. Salisbury, "Development of an MRI-Compatible, Compact,

Rotary-Linear Piezoworm Actuator," *Journal of Medical Devices*, vol. 9, p. 014501, 2015.

[127] Y. Wang, G. A. Cole, H. Su, J. G. Pilitsis, and G. S. Fischer, "MRI compatibility evaluation of a piezoelectric actuator system for a neural interventional robot," in *Engineering in Medicine and Biology Society, 2009. EMBC 2009. Annual International Conference of the IEEE*, 2009, pp. 6072-6075.

[128] H. Su, D. C. Cardona, W. Shang, A. Camilo, G. A. Cole, D. C. Rucker*, et al.*, "A MRI-guided concentric tube continuum robot with piezoelectric actuation: a feasibility study," in *2012 IEEE International Conference on Robotics and Automation (ICRA), ,* pp. 1939-1945.

[129] D. Stoianovici, A. Patriciu, D. Petrisor, D. Mazilu, and L. Kavoussi, "A new type of motor: Pneumatic step motor," *IEEE/ASME Transactions on Mechatronics,* vol. 12, pp. 98-106, 2007.

[130] H. Sajima, H. Kamiuchi, K. Kuwana, T. Dohi, and K. Masamune, "MR-safe pneumatic rotation stepping actuator," *Journal of Robotics and Mechatronics,* vol. 24, pp. 820-826, 2012.

[131] Y. Chen, C. D. Mershon, Z. Tsz, and H. Tse, "A 10-mm MR-Conditional Unidirectional Pneumatic Stepper Motor," *Mechatronics, IEEE/ASME Transactions on,* vol. 20, pp. 782-788, 2015.

[132] Y. Chen, K. W. Kwok, and Z. T. H. Tse, "An MR-Conditional High-Torque Pneumatic Stepper Motor for MRI-Guided and Robot-Assisted Intervention," *Annals of Biomedical Engineering,* vol. 1, 2014.

[133] H. Su, G. A. Cole, and G. S. Fischer, "High-field MRI-compatible needle placement robots for prostate interventions: pneumatic and piezoelectric approaches," *Advances in robotics and virtual reality,* pp. 3-32, 2012.

[134] G. R. Sutherland, I. Latour, A. D. Greer, T. Fielding, G. Feil, and P. Newhook, "An Image-guide Magnetic Resonance-compatible Surgical Robot," *Neurosurgery,* vol. 62, pp. 286-293, 2008.

[135] G. R. Sutherland, I. Latour, and A. D. Greer, "Integrating an image-guided robot with intraoperative MRI," *IEEE engineering in medicine and biology magazine*, vol. 27, pp. 59-65, 2008.

[136] D. Stoianovici, A. Patriciu, D. Petrisor, D. Mazilu, and L. Kavoussi, "A new type of motor: pneumatic step motor," *IEEE/ASME Transactions On Mechatronics,* vol. 12, pp. 98-106, 2007.

[137] D. Stoianovici, C. Kim, D. Petrisor, C. Jun, S. Lim, M. W. Ball*, et al.*, "MR safe robot, FDA clearance, safety and feasibility of prostate biopsy clinical trial," *IEEE/ASME Transactions on Mechatronics,* vol. 22, pp. 115-126, 2017.

[138] O. Felfoul, A. Becker, C. Bergeles, and P. E. Dupont, "Achieving commutation control of an MRI-powered robot actuator," *Robotics, IEEE Transactions on,* vol. 31, pp. 387-399, 2015.

[139] H. Su, W. Shang, G. Cole, G. Li, K. Harrington, A. Camilo*, et al.*, "Piezoelectrically Actuated Robotic System for MRI-Guided Prostate Percutaneous Therapy," *IEEE/ASME Transactions on Mechatronics,* vol. 20, pp. 1920-1932, 2015.

[140] ASTM, *Designation: F2503-13, Standard Practice for Marking Medical Devices and Other Items*

for Safety in the Magnetic Resonance Environment. West Conshohocken, PA: American Society for Testing and Materials (ASTM) International 2013.

[141] *Product Specifications of PAD7344 from Noliac Company*. Available: http://www.noliac.com/products/motors/pad7344/

[142] R. Gassert, A. Yamamoto, D. Chapuis, L. Dovat, H. Bleuler, and E. Burdet, "Actuation methods for applications in MR environments," *Concepts in Magnetic Resonance Part B: Magnetic Resonance Engineering,* vol. 29, pp. 191-209, 2006.

[143] D. Stoianovici, A. Patriciu, D. Petrisor, D. Mazilu, and L. Kavoussi, "A new type of motor: pneumatic step motor," *Mechatronics, IEEE/ASME Transactions on,* vol. 12, pp. 98-106, 2007.

[144] H. Sajima, H. Kamiuchi, K. Kuwana, T. Dohi, and K. Masamune, "MR-safe pneumatic rotation stepping actuator," *Journal of Robotics and Mechatronics,* vol. 24, pp. 820-827, 2012.

[145] R. Secoli, M. Robinson, M. Brugnoli, and F. Rodriguez y Baena, "A low-cost, high-field-strength magnetic resonance imaging–compatible actuator," *Proceedings of the Institution of Mechanical Engineers, Part H: Journal of Engineering in Medicine,* vol. 229, pp. 215-224, 2015.

[146] V. Groenhuis and S. Stramigioli, "Laser-cutting pneumatics," *IEEE/ASME transactions on mechatronics,* vol. 21, pp. 1604-1611, 2016.

[147] D. G. H. Bosboom, J. J. Fütterer, and J. Bosboom, "Motor system, motor, and robot arm device comprising the same," ed: Google Patents, 2016.

[148] M. E. Abdelaziz, V. Groenhuis, J. Veltman, F. Siepel, and S. Stramigioli, "Controlling the Stormram 2: An MRI-compatible robotic system for breast biopsy," in *Robotics and Automation (ICRA), 2017 IEEE International Conference on*, 2017, pp. 1746-1753.

[149] V. Groenhuis, F. J. Siepel, J. Veltman, and S. Stramigioli, "Design and characterization of Stormram 4: an MRI-compatible robotic system for breast biopsy," in *Intelligent Robots and Systems (IROS), 2017 IEEE/RSJ International Conference on*, 2017, pp. 928-933.

[150] K. Chinzei, R. Kikinis, and F. A. Jolesz, "MR compatibility of mechatronic devices: Design criteria," *Medical Image Computing and Computer-Assisted Intervention, Miccai'99, Proceedings,* vol. 1679, pp. 1020-1030, Jan 1999.

[151] G. Ganesh, R. Gassert, E. Burdet, and H. Bleuler, "Dynamics and control of an MRI compatible master-slave system with hydrostatic transmission," in *IEEE International Conference on Robotics and Automation 2004* 2004, pp. 1288-1294.

[152] J. P. Whitney, T. Chen, J. Mars, and J. K. Hodgins, "A hybrid hydrostatic transmission and human-safe haptic telepresence robot," in *IEEE International Conference on Robotics and Automation 2016* 2016, pp. 690-695.

[153] N. Burkhard, S. Frishman, A. Gruebele, J. P. Whitney, R. Goldman, B. Daniel*, et al.*, "A rolling-diaphragm hydrostatic transmission for remote MR-guided needle insertion," in *IEEE International Conference on Robotics and Automation 2017* 2017, pp. 1148-1153.

[154] K. H. Lee, D. K. C. Fu, Z. Guo, Z. Dong, M. C. W. Leong, C. L. Cheung, *et al.*, "MR Safe Robotic Manipulator for MRI-guided Intra-cardiac Catheterization," *IEEE/ASME Transactions on Mechatronics*, vol. (Accepted), 2018.

[155] T. Helbich, M. Rudas, A. Haitel, P. Kohlberger, M. Thurnher, M. Gnant, *et al.*, "Evaluation of needle size for breast biopsy: comparison of 14-, 16-, and 18-gauge biopsy needles," *AJR. American journal of roentgenology,* vol. 171, pp. 59-63, 1998.

[156] M. A. G. Maldon, "Crankless mechanism," ed: Google Patents, 1927.

[157] G. Mohn and T. Nafz, "Swash plate pumps–the key to the future," in *10. Internationales Fluidtechnisches Kolloquium*, 2016.

[158] W. R. Martini, *Stirling engine design manual*: US Department of Energy, Office of Conservation and Solar Applications, Division of Transportation Energy Conservation, 1978.

[159] R. C. Benjamin, "Swash plate mechanism for engines," ed: Google Patents, 1934.

[160] R. W. Fox, A. T. McDonald, and P. J. Pritchard, *Introduction to fluid mechanics* vol. 5. New York: John Wiley & Sons 1998.

[161] D. A. Thorley, *Fluid transients in pipeline systems*: ASME Press, 2004.

[162] W. C. ASTM International, PA, "ASTM F2503-13, Standard Practice for Marking Medical Devices and Other Items for Safety in the Magnetic Resonance Environment, ASTM International, West Conshohocken, PA," vol. ASTM F2503-13, ed, 2013, www.astm.org.

[163] K. Chinzei, R. Kikinis, and F. A. Jolesz, "MR compatibility of mechatronic devices: design criteria," in *International Conference on Medical Image Computing and Computer-Assisted Intervention*, 1999, pp. 1020-1030.

[164] P. Ghanouni, K. B. Pauly, W. J. Elias, J. Henderson, J. Sheehan, S. Monteith, *et al.*, "Transcranial MRI-guided focused ultrasound: a review of the technologic and neurologic applications," *American Journal of Roentgenology,* vol. 205, pp. 150-159, 2015.

[165] Y. Meng, S. Suppiah, K. Mithani, B. Solomon, M. L. Schwartz, and N. Lipsman, "Current and emerging brain applications of MR-guided focused ultrasound," *Journal of therapeutic ultrasound,* vol. 5, p. 26, 2017.

[166] R. A. Vega, K. L. Holloway, and P. S. Larson, "Image-guided deep brain stimulation," *Neurosurgery Clinics*, vol. 25, pp. 159-172, 2014.

[167] W. Wang, C. L. Dumoulin, A. N. Viswanathan, Z. T. Tse, A. Mehrtash, W. Loew, *et al.*, "Real-time active MR-tracking of metallic stylets in MR-guided radiation therapy," *Magnetic resonance in medicine,* vol. 73, pp. 1803-1811, 2015.

[168] F. W. Petraglia, S. H. Farber, J. L. Han, T. Verla, J. Gallis, Y. Lokhnygina, *et al.*, "Comparison of bilateral vs. staged unilateral deep brain stimulation (DBS) in Parkinson's disease in patients under 70 years of age," *Neuromodulation: Technology at the Neural Interface,* vol. 19, pp. 31-37, 2016.

[169] G. Widmann, "Image-guided surgery and medical robotics in the cranial area," *Biomedical*

imaging and intervention journal, vol. 3, 2007.

[170] F. Galassi, D. Brujic, M. Rea, N. Lambert, N. Desouza, and M. Ristic, "Fast and accurate localization of multiple RF markers for tracking in MRI-guided interventions," *Magnetic Resonance Materials in Physics, Biology and Medicine,* vol. 28, pp. 33-48, 2015.

[171] Z. Guo, Z. Dong, K.-H. Lee, H. C. Fu, C. L. Cheung, and K.-W. Kwok, "Robotic stereotactic system for mri-guided neurosurgery," ed: Patent US 62/623,280, 2018.

[172] P. S. Larson, P. A. Starr, G. Bates, L. Tansey, R. M. Richardson, and A. J. Martin, "An optimized system for interventional magnetic resonance imaging-guided stereotactic surgery: preliminary evaluation of targeting accuracy," *Operative Neurosurgery,* vol. 70, pp. ons95-ons103, 2011.

[173] D. Tarsy, J. L. Vitek, and A. M. Lozano, *Surgical treatment of Parkinson's disease and other movement disorders*: Springer Science & Business Media, 2002.

[174] ASTM, "ASTM F2503-13: Standard Practice for Marking Medical Devices and Other Items for Safety in the Magnetic Resonance Environment," ed: ASTM International.

[175] G. Ganesh, R. Gassert, E. Burdet, and H. Bleuler, "Dynamics and control of an MRI compatible master-slave system with hydrostatic transmission," in *IEEE International Conference on Robotics and Automation (ICRA'04)* 2004, pp. 1288-1294.

[176] D. B. Comber, E. J. Barth, and R. J. Webster, "Design and control of an magnetic resonance compatible precision pneumatic active cannula robot," *Journal of Medical Devices,* vol. 8, p. 011003, 2014.

[177] Z. Guo, T. Lun, Y. Chen, H. Su, D. Chan, and K. Kwok, "Novel design of an MR-safe pneumatic stepper motor for MRI-guided robotic interventions," in *Proceedings of The Hamlyn Symposium on Medical Robotics*, 2016.

[178] Y. Chen, K.-W. Kwok, and Z. T. H. Tse, "An MR-conditional high-torque pneumatic stepper motor for MRI-guided and robot-assisted intervention," *Annals of biomedical engineering*, vol. 42, pp. 1823-1833, 2014.

[179] J. P. Whitney, T. Chen, J. Mars, and J. K. Hodgins, "A hybrid hydrostatic transmission and human-safe haptic telepresence robot," in *IEEE International Conference on Robotics and Automation (ICRA'16)*, 2016, pp. 690-695.

[180] K. H. Lee, K.-C. D. Fu, Z. Guo, Z. Dong, M. C. W. Leong, C. Cheung, *et al.*, "MR Safe Robotic Manipulator for MRI-guided Intra-cardiac Catheterization," *IEEE/ASME Transactions on Mechatronics*, 2018.

[181] J.-P. Merlet, "Parallel robots: open problems," in *Robotics research*, ed: Springer, 2000, pp. 27-32.

[182] L. Campos, F. Bourbonnais, I. A. Bonev, and P. Bigras, "Development of a five-bar parallel robot with large workspace," in *Proceedings of the International Design Engineering Technical Conferences and Computers and Information in Engineering Conference IDETC/CIE*, 2010, pp. 15-18.

[183] A. Figielski, I. A. Bonev, and P. Bigras, "Towards development of a 2-DOF planar oparallel robot with optimal workspace use," in *IEEE International Conference on Systems, Man and Cybernetics (ISIC'07)*, 2007, pp. 1562-1566.

[184] T. M. Seibert, N. S. White, G.-Y. Kim, V. Moiseenko, C. R. McDonald, N. Farid*, et al.*, "Distortion inherent to magnetic resonance imaging can lead to geometric miss in radiosurgery planning," *Practical radiation oncology,* vol. 6, pp. e319-e328, 2016.

[185] R. R. Shamir, L. Joskowicz, and Y. Shoshan, "Fiducial optimization for minimal target registration error in image-guided neurosurgery," *IEEE transactions on medical imaging,* vol. 31, pp. 725-737, 2012.

[186] R. C. Susil, J. H. Anderson, and R. H. Taylor, "A single image registration method for CT guided interventions," in *International Conference on Medical Image Computing and Computer-Assisted Intervention*, 1999, pp. 798-808.

[187] Ö. Bebek, M. J. Hwang, and M. C. Cavusoglu, "Design of a parallel robot for needle-based interventions on small animals," *IEEE/ASME Transactions on Mechatronics,* vol. 18, pp. 62-73, 2013.

[188] H. Busse, R. Trampel, W. Gründer, M. Moche, and T. Kahn, "Method for automatic localization of MR-visible markers using morphological image processing and conventional pulse sequences: Feasibility for image-guided procedures," *Journal of Magnetic Resonance Imaging,* vol. 26, pp. 1087-1096, 2007.

[189] Y. Chen, W. Wang, E. J. Schmidt, K.-W. Kwok, A. N. Viswanathan, R. Cormack*, et al.*, "Design and fabrication of MR-tracked metallic stylet for gynecologic brachytherapy," *IEEE/ASME Transactions on Mechatronics,* vol. 21, pp. 956-962, 2016.

[190] M. B. Ooi, M. Aksoy, J. Maclaren, R. D. Watkins, and R. Bammer, "Prospective motion correction using inductively coupled wireless RF coils," *Magnetic resonance in medicine,* vol. 70, pp. 639-647, 2013.

[191] Z. Guo, Z. Dong, K.-H. Lee, C. L. Cheung, K. C. D. FU, and K. W. Kwok, "Robotic catheter system for mri-guided cardiovascular interventions," ed: Patent US 15/630,406; PCT/CN 2017/089,701, 2017.

[192] NEMA, "Determination of signal-to-noise ratio (SNR) in diagnostic magnetic resonance images," ed: National Electrical Manufacturers Association, 2008.

[193] ASTM, "ASTM F2119-07: Standard Test Method for Evaluation of MR Image Artifacts from Passive Implants," ed: ASTM International, 2006.

[194] M. A. Tavallaei, M. Lavdas, D. Gelman, and M. Drangova, "Magnetic resonance imaging compatible remote catheter navigation system with 3 degrees of freedom," *International journal of computer assisted radiology and surgery,* vol. 11, pp. 1537-1545, 2016.

[195] M. Haïssaguerre, M. Hocini, P. Sanders, F. Sacher, M. Rotter, Y. Takahashi*, et al.*, "Catheter

ablation of long-lasting persistent atrial fibrillation: clinical outcome and mechanisms of subsequent arrhythmias," *Journal of cardiovascular electrophysiology*, vol. 16, pp. 1138-1147, 2005.

[196] N. Jackson. Available: https://www.hunterheart.com.au/content/atrial-flutter-and-atrial-fibrillation-af

[197] S. Nazarian, A. Kolandaivelu, M. M. Zviman, G. R. Meininger, R. Kato, R. C. Susil*, et al.*, "Feasibility of real-time magnetic resonance imaging for catheter guidance in electrophysiology studies," *Circulation*, vol. 118, pp. 223-229, 2008.

[198] M. Shurrab, R. Schilling, E. Gang, E. M. Khan, and E. Crystal, "Robotics in invasive cardiac electrophysiology," *Expert review of medical devices*, vol. 11, pp. 375-381, 2014.

[199] M. A. Tavallaei, Y. Thakur, S. Haider, and M. Drangova, "A magnetic-resonance-imaging-compatible remote catheter navigation system," *IEEE Transactions on Biomedical Engineering*, vol. 60, pp. 899-905, 2013.

[200] H. Su, D. C. Cardona, W. Shang, A. Camilo, G. A. Cole, D. C. Rucker*, et al.*, "A MRI-guided concentric tube continuum robot with piezoelectric actuation: a feasibility study," in *Robotics and Automation (ICRA), 2012 IEEE International Conference on*, 2012, pp. 1939-1945.

[201] J. Pan, L. Zhang, and D. Manocha, "Collision-free and Smooth Trajectory Computation in Cluttered Environments," *International Journal of Robotics Research*, vol. 31, pp. 1155-1175, 2012.

[202] M. Li, M. Ishii, and R. H. Taylor, "Spatial motion constraints using virtual fixtures generated by anatomy," *IEEE Trans. on Robotics*, vol. 23, pp. 4-19, 2007.

[203] B. Davies, M. Jakopec, S. J. Harris, F. R. Y. Baena, A. Barrett, A. Evangelidis*, et al.*, "Active-constraint robotics for surgery," *Proceedings of the IEEE*, vol. 94, pp. 1696-1704, 2006.

[204] B. Mirtich, "V-Clip: Fast and robust polyhedral collision detection," *ACM Trans. on Graphics*, vol. 17, pp. 177-208, 1998.

[205] E. Gilert, D. Johnson, and S. S. Keerthi, "A fast procedure for computing the distance between complex objects in three dimensional space," *IEEE Journal of Robotics and Automation*, vol. 4, pp. 193-203, 1988.

[206] S. Cameron, "A Comparison of Two Fast Algorithms for Computing the Distance between Convex Polyhedra," *IEEE Trans. on Robotics*, vol. 13, pp. 915-920, 1997.

[207] N. Chakraborty, J. Peng, S. Akella, and J. E. Mitchell, "Proximity Queries Between Convex Objects: An Interior Point Approach for Implicit Surfaces," *IEEE Trans. on Robotics*, vol. 24, pp. 211-220, 2008.

[208] K. W. Kwok, K. H. Tsoi, V. Vitiello, J. Clark, G. C. T. Chow, W. Luk*, et al.*, "Dimensionality Reduction in Controlling Articulated Snake Robot for Endoscopy Under Dynamic Active Constraints," *Ieee Transactions on Robotics*, vol. 29, pp. 15-31, Feb 2013.

[209] T. C. P. Chau, K. Ka-Wai, G. C. T. Chow, T. Kuen Hung, L. Kit-Hang, Z. Tse, *et al.*, "Acceleration of real-time Proximity Query for dynamic active constraints," in *Field-Programmable Technology (FPT), 2013 International Conference on*, 2013, pp. 206-213.

[210] K. W. Kwok, G. P. Mylonas, L. W. Sun, M. Lerotic, J. Clark, T. Athanasiou, *et al.*, "Dynamic Active Constraints for Hyper-Redundant Flexible Robots," *Medical Image Computing and Computer-Assisted Intervention - Miccai 2009, Pt I, Proceedings,* vol. 5761, pp. 410-417, 2009.

[211] S. Ilic and P. Fua, "Implicit meshes for surface reconstruction," *IEEE Trans on Pattern Analysis and Machine Intelligence,* vol. 28, pp. 328-333, Feb 2006.

[212] D. Eberly, "Intersection of cylinders," 2010.

[213] C. Fares and Y. Hamam, "Collision detection for rigid bodies: A state of the art review," *GraphiCon 2005,* 2005.

[214] K. W. Kwok, Y. Chen, T. C. P. Chau, W. Luk, K. Nilsson, E. J. Schmidt, *et al.*, "MRI-based visual and haptic catheter feedback: simulating a novel system's contribution to efficient and safe MRI-guided cardiac electrophysiology procedures," *Journal of Cardiovascular Magnetic Resonance,* vol. 16, p. O50, 2014.

[215] W. R. Thompson, "On the likelihood that one unknown probability exceeds another in view of the evidence of two samples," *Biometrika,* vol. 25, pp. 285-294, 1933.

[216] X.-Y. Zhou, S. Ernst, and S.-L. Lee, "Path planning for robot-enhanced cardiac radiofrequency catheter ablation," in *Robotics and Automation (ICRA), 2016 IEEE International Conference on*, 2016, pp. 4172-4177.

[217] Y. Feng, Z. Guo, Z. Dong, X.-Y. Zhou, K.-W. Kwok, S. Ernst, *et al.*, "An efficient cardiac mapping strategy for radiofrequency catheter ablation with active learning," *International journal of computer assisted radiology and surgery,* vol. 12, pp. 1199-1207, 2017.

[218] H. Oral, C. Scharf, A. Chugh, B. Hall, P. Cheung, E. Good, *et al.*, "Catheter ablation for paroxysmal atrial fibrillation," *Circulation,* vol. 108, pp. 2355-2360, 2003.

[219] T. Vos, R. M. Barber, B. Bell, A. Bertozzi-Villa, S. Biryukov, I. Bolliger, *et al.*, "Global, regional, and national incidence, prevalence, and years lived with disability for 301 acute and chronic diseases and injuries in 188 countries, 1990–2013: a systematic analysis for the Global Burden of Disease Study 2013," *The Lancet,* vol. 386, pp. 743-800, 2015.

[220] H.-H. Liu, L.-J. Li, B. Shi, C.-W. Xu, and E. Luo, "Robotic surgical systems in maxillofacial surgery: a review," *International journal of oral science,* vol. 9, p. 63, 2017.

[221] J. Attra and N. Kokot, "Transoral Robotic Surgery and Lasers," in *Biomedical Optics in Otorhinolaryngology,* ed: Springer, 2016, pp. 183-201.

[222] C. Arens, "Transoral treatment strategies for head and neck tumors," *GMS current topics in otorhinolaryngology, head and neck surgery,* vol. 11, p. Doc05, 2012 2012.

[223] M. K. Bhayani and S. Y. Lai, "A shifting paradigm for patients with head and neck cancer: transoral

robotic surgery (TORS)," *Oncology,* vol. 24, p. 1010, 2010.

[224] D. G. Grant, M. L. Hinni, J. R. Salassa, W. C. Perry, R. E. Hayden, and J. D. Casler, "Oropharyngeal cancer: a case for single modality treatment with transoral laser microsurgery," *Archives of Otolaryngology–Head & Neck Surgery,* vol. 135, pp. 1225-1230, 2009.

[225] W. Steiner, O. Fierek, P. Ambrosch, C. P. Hommerich, and M. Kron, "Transoral laser microsurgery for squamous cell carcinoma of the base of the tongue," *Archives of Otolaryngology–Head & Neck Surgery,* vol. 129, pp. 36-43, 2003.

[226] J. A. Burns, J. B. Kobler, J. T. Heaton, G. Lopez-Guerra, R. R. Anderson, and S. M. Zeitels, "Thermal damage during thulium laser dissection of laryngeal soft tissue is reduced with air cooling: ex vivo calf model study," *Annals of Otology, Rhinology & Laryngology,* vol. 116, pp. 853-857, 2007.

[227] K. M. Van Abel, E. J. Moore, M. L. Carlson, J. A. Davidson, J. J. Garcia, S. M. Olsen*, et al.*, "Transoral robotic surgery using the thulium: YAG laser: a prospective study," *Archives of Otolaryngology–Head & Neck Surgery,* vol. 138, pp. 158-166, 2012.

[228] D. T. Friedrich, M. O. Scheithauer, J. Greve, T. K. Hoffmann, and P. J. Schuler, "Recent advances in robot-assisted head and neck surgery," *The International Journal of Medical Robotics and Computer Assisted Surgery,* vol. 13, p. e1744, 2017.

[229] S. M. Olson, M. Hussaini, and J. S. Lewis, "Frozen section analysis of margins for head and neck tumor resections: reduction of sampling errors with a third histologic level," *Mod Pathol,* vol. 24, pp. 665-670, 05//print 2011.

[230] A. A. Oraevsky, S. L. Jacques, R. O. Esenaliev, F. K. J. L. i. S. Tittel, M. T. O. J. o. t. A. S. f. L. Medicine, and Surgery, "Pulsed laser ablation of soft tissues, gels, and aqueous solutions at temperatures below 100 C," vol. 18, pp. 231-240, 1996.

[231] M. Marx, P. Ghanouni, and K. Butts Pauly, "Specialized volumetric thermometry for improved guidance of MRgFUS in brain," *Magnetic resonance in medicine,* vol. 78, pp. 508-517, 2017.

[232] R. K. Tsang and F. C. Holsinger, "Transoral endoscopic nasopharyngectomy with a flexible next-generation robotic surgical system," *The Laryngoscope,* vol. 126, pp. 2257-2262, 2016.

[233] J. Y. K. Chan, R. J. Li, and J. D. Richmon, "Transoral approaches to the oropharynx: The revival of surgery for oropharyngeal carcinoma," *Otorinolaringologia,* vol. 62, pp. 149-159, 2012.

[234] W. I. Wei and W.-K. Ho, "Transoral Robotic Resection of Recurrent Nasopharyngeal Carcinoma," *The Laryngoscope,* vol. 120, pp. 2011-2014, 2010.

[235] J. Y. K. Chan, R. K. Tsang, D. W. Eisele, and J. D. Richmon, "Transoral robotic surgery of the parapharyngeal space: A case series and systematic review," *Head & Neck,* vol. 37, pp. 293-298, 2015.